2026-01

Investigation of Magnetohydrodynamic Non-Newtonian Nanofluid Flow over Stretching Surfaces with Hall and Ion Slip Effects

Wubale, Demis

BAHIR DAR UNIVERSITY

College of Science

Department of Mathematics

Investigation of Magnetohydrodynamic Non-Newtonian Nanofluid Flow over Stretching Surfaces with Hall and Ion Slip Effects

By:

Wubale Demis Alamirew

January, 2026

Bahir Dar, Ethiopia

BAHIR DAR UNIVERSITY
College of Science
Department of Mathematics

Investigation of Magnetohydrodynamic Non-Newtonian Nanofluid Flow over Stretching Surfaces with Hall and Ion Slip Effects

By:

Wubale Demis Alamirew

A Dissertation Submitted to the School of Graduate Studies, Bahir Dar University, in Partial Fulfillment of the Requirements for the Degree of **Doctor of Philosophy** in **Applied Mathematics (Fluid Dynamics)**

Principal Advisor: **Dr. Gurju Awgichew** (Asso. Professor)
Co-Advisor: **Dr. Eshetu Haile** (Asso. Professor)

January, 2026

Bahir Dar, Ethiopia

Declaration

I declare that the dissertation entitled "**Investigation of Magnetohydrodynamic Non-Newtonian Nanofluid Flow over Stretching Surfaces with Hall and Ion Slip Effects**", submitted in partial fulfillment of the requirements for the degree of Doctor of Philosophy in Applied Mathematics (Fluid Dynamics) of Department of Mathematics, Bahir Dar University, is a record of original work carried out by me and has never been submitted to this or any other institution to get any other degree or certificates. The assistance and help I received during the course of this investigation have been duly acknowledged.

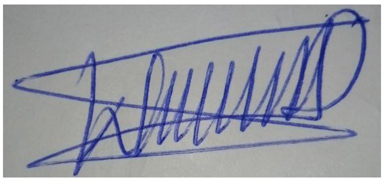

January, 2026

Date

Wubale Demis Alamirew

BAHIR DAR UNIVERSITY

College of Science

Department of Mathematics

Approval of Dissertation for Defense

We hereby certify that we have supervised, read, and evaluated this dissertation titled "**Investigation of Magnetohydrodynamic Non-Newtonian Nanofluid Flow over Stretching Surfaces with Hall and Ion Slip Effects**" prepared by Wubale Demis Alamirew under our guidance. I recommend the thesis to be submitted for oral defense.

Dr. Gurju Awgichew (Associate Professor)		January, 2026
Advisor's Name	Signature	Date
Dr. Eshetu Haile (Associate Professor)		January, 2026
Co-Advisor's Name	Signature	Date
Dr. Hunegnaw Dessie (Associate Professor)		January, 2026
Department Head	Signature	Date
Prof. Tsegaye Kassa		January, 2026
Postgraduate Head	Signature	Date

BAHIR DAR UNIVERSITY

College of Science

Department of Mathematics

Approval of Dissertation for Defense Result

As members of the the board of examiners, we examined this dissertation entitled "**Investigation of Magnetohydrodynamic Non-Newtonian Nanofluid Flow over Stretching Surfaces with Hall and Ion Slip Effects**" by Wubale Demis Alamirew. We hereby certify that the dissertation is accepted for fulfilling the requirements for the award of the degree of "**Doctor of Philosophy** in Applied Mathematics (Fluid Dynamics)".

Board of Examiners

Prof. Wubshet Ibrahim		January 05, 2026
External examiner name I	Signature	Date
Dr. Gossaye Aliy (Asso. Professor)		January 05, 2026
External examiner name II	Signature	Date
Dr. Hunegnaw Dessie (Asso. Professor)		January, 2026
Internal examiner name	Signature	Date
Dr. Tesfahun Birhane (Asso. Professor)		January, 2026
Chair person's name	Signature	Date

Acknowledgements

First and foremost, I would like to express my sincere gratitude to the Almighty God and His Mother, the Virgin Mary. I thank my supervisors, Dr. Gurju Awgichew (PhD, Associate Professor) and Dr. Eshetu Haile (PhD, Associate Professor), for their guidance, constructive feedback, and support throughout the development of this PhD dissertation. I am deeply grateful to Bahir Dar University and Debre Berhan University for their financial, academic, and technical support, which made this research possible. I also extend my heartfelt thanks to my friends—Tadele Ambaye (Tade Philo), Dr. Zemenu Bires, Sabom Melkamu Geremew, Arefayne Mesfen Dessye, Bukayaw K, Dagnaw T, Habtamu G, Gizachew B, Eyaya B, Girma Desu, Dagnachew J, and Asfaw T—for their encouragement and support. Most importantly, I express my deepest gratitude to my family: my father, Demis Alamirew; my mother, Melkam Mele; my cousin, Workiye Alemayehu; my cousin, Aytenew (Nius) Teshome; my sister, Tseganesh Demis; my brother, Getaneh Demis; my wife, Wudie Fekadie Kassa; and my daughters, Seblewongel Wubale and Elleni Wubale, for their unconditional love, patience and understanding throughout this endeavor. This acknowledgment would be incomplete without recognizing their immeasurable contribution to my life and work.

Abstract

This dissertation presents a theoretical investigation of magnetohydrodynamic (MHD) flow of non-Newtonian nanofluids over stretching surfaces, with particular focus on the combined effects of Hall currents and ion slip under strong magnetic fields. The study employs the Buongiorno nanofluid model to analyze four distinct non-Newtonian fluid types—Williamson, Casson, tangent hyperbolic, and Jeffrey fluids—incorporating key physical phenomena such as nonlinear thermal radiation, viscous dissipation, Joule heating, chemical reaction, and heat generation/absorption subject to porous medium. Using appropriate similarity transformations, the governing partial differential equations are converted into a system of nonlinear ordinary differential equations. These equations are solved numerically using a fifth-order and sixth-order Runge–Kutta method combined with the shooting technique, implemented in the Python programming language. To ensure the reliability of numerical solutions, the results are validated by comparing them with standard previously published studies under specific limiting conditions. The excellent agreement confirms the accuracy and robustness of the computational methods employed. The results are presented through detailed graphs and tables that illustrate the influence of various physical parameters on the velocity, temperature, and concentration profiles. In addition, important engineering quantities such as the skin friction coefficient, the Nusselt number, and the Sherwood number are evaluated and interpreted. The impact of each parameter is analyzed to provide a clear physical insight into how it affects the behavior of the fluid within the boundary layer. Among the various outcomes, the findings reveal that for all the considered fluid models, the Hall and ion slip parameters consistently enhance the principal (streamwise) velocity profiles within the boundary layer, indicating a reduction in the Lorentz-force resistance due to the modified current density. In contrast, these parameters exert a suppressive effect on both the temperature and the nanoparticle concentration distributions, leading to thinner thermal and concentration boundary layers. Furthermore, the nonlinear thermal radiation parameter demonstrates a positive influence by significantly increasing the fluid temperature and nanoparticle concentration, thereby intensifying the thermal transport and diffusion processes. Overall, the dissertation provides valuable contributions to the theoretical understanding of MHD non-Newtonian nanofluid flows and provides practical insight for engineering applications.

Keywords: Hall current; ion slip; porous medium; Runge-Kutta method; shooting technique; viscous dissipation; Joule heating; nonlinear thermal radiation.

Contents

Acknowledgements v

Abstract vi

List of Figures xi

List of Tables xiv

List of Symbols xvi

1 Introduction 1
- 1.1 Background . . . 1
- 1.2 Basic Concepts . . . 2
  - 1.2.1 The Idea of Continuum Hypothesis . . . 2
  - 1.2.2 Incompressible and Compressible Fluid Flow . . . 3
  - 1.2.3 Viscous and Inviscid Fluid Flow . . . 4
  - 1.2.4 Laminar and Turbulent Flow . . . 5
  - 1.2.5 Eulerian and Lagrangian Approaches . . . 6
- 1.3 Review of Related Literature . . . 6
  - 1.3.1 Introduction to Non-Newtonian Fluids . . . 7
  - 1.3.2 Nanofluids and their Importance . . . 9
  - 1.3.3 Magnetohydrodynamics and the Lorentz Force . . . 10
  - 1.3.4 Flow over Stretching Surfaces . . . 11
  - 1.3.5 Flow through Porous Medium . . . 11
  - 1.3.6 Physical Flow Properties . . . 12
  - 1.3.7 Rotating Flow . . . 13
  - 1.3.8 Flow over Permeable Surface . . . 14
  - 1.3.9 Hall and Ion slip Effects . . . 14
  - 1.3.10 Conclusion . . . 15
- 1.4 Statement of the Problem . . . 16
- 1.5 Objectives of the Study . . . 17
- 1.6 Significance of the Study . . . 18
- 1.7 Scope of the Study . . . 18

1.8 Outlines of the Dissertation 19

2 Mathematical Descriptions of Non-Newtonian Fluids, Heat and Mass Transfer, Boundary Layer Flows and Basic Governing Laws 21

2.1 Mathematical Descriptions of Non-Newtonian Fluids and MHD 21
2.1.1 Constitutive Equations of some Non-Newtonian Fluids 21
2.1.2 Magnetohydrodynamics 29
2.2 Heat and Mass Transfer 31
2.2.1 Heat Transfer 31
2.2.2 Mass Transfer 34
2.2.3 Coupled Heat and Mass Transfer 35
2.2.4 Brownian Diffusion and Thermophoresis 37
2.3 Boundary Layer Flow and Some Prominent Dimensionless Prameters . 39
2.3.1 The Concept of Boundary Layer Theory 39
2.3.2 Skin Friction Coefficients 41
2.3.3 Nusselt Number 42
2.3.4 Sherwood Number 42
2.4 Governing Equations and Conservation Laws 43
2.4.1 Continuity Equation 44
2.4.2 Momentum Equation 44
2.4.3 Energy Equation 45
2.4.4 Concentration Equation 46

3 Research Methodology 47

3.1 Introduction 47
3.2 Review of Related Numerical Methods 47
3.3 Shooting Technique 49
3.4 Higher Order Runge-Kutta Method 50
3.4.1 Fifth Order Runge-Kutta Method 51
3.4.2 Sixth Order Runge-Kutta Method 51
3.5 Numerical Simulation 52
3.6 Implementation 53
3.7 Used Software 53
3.8 Validation 54
3.9 Numerical Solution Procedure 54

4 Effects of Hall, Ion Slip, Viscous Dissipation and Nonlinear Thermal Radiation on MHD Williamson Nanofluid Flow Past a Stretching Sheet 56

4.1 Introduction 56
4.2 Mathematical Formulation 57
4.2.1 Model Assumptions 57
4.2.2 Conservation Equations 58
4.2.3 Coupled Governing Equations and Boundary Conditions 62
4.2.4 Similarity Transformation 63
4.2.5 Engineering Relevant Quantities in Boundary Layer 70
4.3 Method of Solution 74
4.4 Results and Discussion 75

4.4.1 Validation of the Numerical Method 76
4.4.2 Profiles of Velocity, Temperature and Nanoparticle concentration with Prominent Flow Parameters 77
4.4.3 Effects of Pertinent Flow Parameters on Skin Friction Coefficients, Nusselt Number and Sherwood Number 86
4.5 Conclusion 92

5 Mixed Convection Flow of MHD Casson Nanofluid over a Vertically Extending Sheet with Effects of Hall, Ion Slip and Nonlinear Thermal Radiation 94
5.1 Introduction 94
5.2 Mathematical Formulation 95
5.2.1 Model Assumptions 95
5.2.2 Conservation Equations 96
5.2.3 Coupled Governing Equations and Boundary Conditions 100
5.2.4 Similarity Transformation 101
5.2.5 Engineering Relevant Quantities in Boundary Layer 107
5.3 Method of Solutions 110
5.4 Results and Discussion 112
5.4.1 Validation of the Numerical Method 112
5.4.2 Profiles of Velocity, Temperature and Nanoparticle Concentration with Prominent Flow Parameters 113
5.4.3 Effects of Pertinent Flow Parameters on Skin Friction Coefficients, Nusselt Number and Sherwood Number 127
5.5 Conclusion 131

6 Investigation on Rotating Flow of MHD Tangent Hyperbolic Nanofluid over a Stretching Permeable Sheet: Impacts of Hall, Ion Slip and Suction velocity 133
6.1 Introduction 133
6.2 Mathematical Formulation 134
6.2.1 Model Assumptions 134
6.2.2 Conservation Equations 135
6.2.3 Coupled Governing Equations and Boundary Conditions 138
6.2.4 Similarity Transformation 139
6.2.5 Engineering Relevant Quantities in Boundary Layer 144
6.3 Method of Solutions 146
6.4 Results and Discussion 148
6.4.1 Validation of the Numerical Method 148
6.4.2 Profiles of Velocity, Temperature and Nanoparticle Concentration with Prominent Flow Parameters 148
6.4.3 Effects of Pertinent Flow Parameters on Skin Friction Coefficients, Nusselt Number and Sherwood Number 166
6.5 Conclusion 170

7 Python-Based Simulation on Rotating MHD Jeffrey Nanofluid Flow over a Permeable Stretching Surface Subject to Hall and Ion Slip Effects 172
7.1 Introduction 172
7.2 Mathematical Formulation 173

7.2.1 Model Assumptions . . . 173
7.2.2 Conservation Equations . . . 175
7.2.3 Coupled Governing Equations and Boundary Conditions . . . 177
7.2.4 Similarity Transformation . . . 178
7.2.5 Engineering Relevant Quantities in Boundary Layer . . . 185
7.3 Method of Solution . . . 187
7.4 Results and Discussion . . . 189
7.4.1 Validation of the Numerical Method . . . 189
7.4.2 Profiles of Velocity, Temperature and Nanoparticle Concentration with Prominent Flow Parameters . . . 190
7.4.3 Effects of Pertinent Flow Parameters on Skin Friction Coefficients, Nusselt Number and Sherwood Number . . . 203
7.5 Conclusion . . . 207

8 Conclusions, Recommendations and Future Works 208
8.1 Conclusions . . . 208
8.2 Recommendations . . . 210
8.3 Future Research Work . . . 211

Bibliography 213

A Mesh Independence Analysis 236
A.1 Mesh Independence Analysis for Principal and Spanwise Velocity Components . . . 236
A.1.1 Principal Velocity Profile . . . 236
A.1.2 Spanwise Velocity Profile . . . 238
A.2 Temperature Profile and Gradient . . . 239
A.3 Concentration Profile and Gradient . . . 240

B Computational Performance and Accuracy 241

List of Figures

3.1 Research framework . . . 55

4.1 A schematic of the physical model . . . 57
4.2 The principal velocity profile $f'(\eta)$ with Hall parameter β_e. . . . 77
4.3 The secondary velocity profile $h(\eta)$ with Hall parameter β_e. . . . 78
4.4 Temperature profile $\theta(\eta)$ with Hall parameter β_e. . . . 78
4.5 Concentration profile $\phi(\eta)$ with Hall parameter β_e. . . . 79
4.6 The principal velocity profile $f'(\eta)$ with ion slip parameter β_i. . . . 79
4.7 The secondary velocity profile $h(\eta)$ with ion slip parameter β_i. . . . 80
4.8 Temperature profile $\theta(\eta)$ with ion slip parameter β_i. . . . 80
4.9 Concentration profile $\phi(\eta)$ with ion slip parameter β_i. . . . 81
4.10 Temperature profile $\theta(\eta)$ with nonlinear thermal radiation parameter R_n. 81
4.11 Concentration profile $\phi(\eta)$ with nonlinear thermal radiation parameter R_n. 82
4.12 The principal velocity profile $f'(\eta)$ with Williamson parameter We. . . 83
4.13 The secodary velocity profile $h(\eta)$ with Williamson parameter We. . . . 83
4.14 Temperature profile $\theta(\eta)$ with Williamson parameter We. . . . 84
4.15 Concentration profile $\phi(\eta)$ with Williamson parameter We. . . . 84
4.16 Temperature profile $\theta(\eta)$ with Eckert number, Ec. . . . 85
4.17 Concentration profile $\phi(\eta)$ with Eckert number, Ec. . . . 85
4.18 Impact of the chemical reaction parameter, C_r, on the distribution of concentration (nanoparticles volume fraction), $\phi(\eta)$ . . . 86
4.19 Influences of β_e and β_i on $-\left(f''(0) + \frac{We}{2} f''^2(0)\right)$ . . . 87
4.20 Influences of β_e and β_i on $h'(0) + \frac{We}{2} h'^2(0)$ . . . 87
4.21 Influences of β_e and β_i on $-\left(1 + R\theta_w^3\right)\theta'(0)$ . . . 88
4.22 Influences of β_e and β_i on $-\phi'(0)$ . . . 88
4.23 Influences of R_n and Ec on $-\left(1 + R_n\theta_r^3\right)\theta'(0)$ . . . 89
4.24 Influences of R_n and Ec on $-\phi'(0)$ . . . 89

5.1 Physical model . . . 96
5.2 Effects of Hall parameter β_e on the principal velocity $f'(\eta)$. . . . 114
5.3 Effects of Ion slip parameter β_i on the principal velocity $f'(\eta)$. . . . 115

5.4 Effects of β (Casson parameter) on the principal velocity $f'(\eta)$. 115
5.5 Effects of λ_t (mixed convection parameter) on the principal velocity $f'(\eta)$. 116
5.6 Effects of λ_c (modified mixed convection parameter) on the principal velocity $f'(\eta)$. 116
5.7 Effects of β_e (Hall parameter) on the secondary velocity $h(\eta)$. 117
5.8 Effects of β_i (Ion slip) on the secondary velocity $h(\eta)$. 118
5.9 Effects of β (Casson parameter) on the secondary velocity $h(\eta)$. 118
5.10 Effects of λ_t on the secondary velocity $h(\eta)$. 119
5.11 Effects of λ_c on the secondary velocity $h(\eta)$. 119
5.12 Impacts of Hall parameter β_e on temperature $\theta(\eta)$. 121
5.13 Impacts of ion slip parameter β_i on $\theta(\eta)$. 121
5.14 Impacts of Casson parameter β on $\theta(\eta)$. 122
5.15 Impacts of λ_t on $\theta(\eta)$. 122
5.16 Impacts of nonlinear thermal radiation Rn on temperature profile $\theta(\eta)$. . 123
5.17 Impacts of θ_r on temperature profile $\theta(\eta)$. 123
5.18 Impacts of Ec on temperature profile $\theta(\eta)$. 124
5.19 Influences of β on nanoparticle concentration $\phi(\eta)$. 125
5.20 Influences of modified mixed convection parameter λ_c on $\phi(\eta)$. 125
5.21 Influences of Eckert number Ec on nanoparticle concentration $\phi(\eta)$. . . 126
5.22 Influences of Cr on nanoparticle concentration $\phi(\eta)$. 126
5.23 Influences of Schmidt number Sc on nanoparticle concentration $\phi(\eta)$. . 127

6.1 Physical model 135
6.2 Profiles of principal velocity $f'(\eta)$ with Hall parameter β_e. 150
6.3 Profiles of secondary velocity $h(\eta)$ with β_e. 150
6.4 Profiles of Temperature $\theta(\eta)$ with β_e. 151
6.5 Profiles of nanoparticle concentration $\phi(\eta)$ with β_e. 151
6.6 Profiles of principal velocity $f'(\eta)$ with ion slip parameter β_i. 152
6.7 Profiles of secondary velocity $h(\eta)$ with β_i. 152
6.8 Profiles of Temperature $\theta(\eta)$ with β_i. 153
6.9 Profiles of nanoparticle concentration $\phi(\eta)$ with β_i. 153
6.10 Profiles of principal velocity $f'(\eta)$ with power index parameter n. 154
6.11 Profiles of secondary velocity $h(\eta)$ with n. 155
6.12 Profiles of Temperature $\theta(\eta)$ with n. 155
6.13 Profiles of nanoparticle concentration $\phi(\eta)$ with n. 156
6.14 Profiles of principal velocity $f'(\eta)$ with Weissenberg number (We). . . . 156
6.15 Profiles of secondary velocity $h(\eta)$ with We. 157
6.16 Profiles of Temperature $\theta(\eta)$ with We. 157
6.17 Profiles of nanoparticle concentration $\phi(\eta)$ with We. 158
6.18 Profiles of principal velocity $f'(\eta)$ with Suction Velocity parameter (V_0). 159
6.19 Profiles of secondary velocity $h(\eta)$ with V_0. 159
6.20 Profiles of Temperature $\theta(\eta)$ with V_0. 160
6.21 Profiles of nanoparticle concentration $\phi(\eta)$ with V_0. 160
6.22 Profiles of leading velocity $f'(\eta)$ with rotation parameter (ω). 161
6.23 Profiles of auxiliary velocity $h(\eta)$ with ω. 161
6.24 Profiles of Temperature $\theta(\eta)$ with ω. 162

6.25 Profiles of Temperature $\theta(\eta)$ with nonlinear thermal radiation parameter R_t. . . . 163
6.26 Profiles of nanoparicle concentration $\phi(\eta)$ with R_t. . . . 163
6.27 Profiles of Temperature $\theta(\eta)$ with ratio of temperature parameter θ_r. . . . 164
6.28 Profiles of nanoparicle concentration $\phi(\eta)$ with θ_r. . . . 164
6.29 Profiles of Temperature $\theta(\eta)$ with Eckert number Ec. . . . 165
6.30 Profiles of Temperature $\theta(\eta)$ with chemical reaction parameter Cr. . . . 165
6.31 Profiles of nanoparicle concentration $\phi(\eta)$ with Cr. . . . 166

7.1 A schematic of the physical model 174
7.2 Principal velocity profiles with magnetic parameter M. . . . 191
7.3 Principal velocity profiles with Hall parameter β_e. . . . 192
7.4 Streamwise velocity profiles with ion slip parameter β_i. . . . 192
7.5 Principal velocity profiles with λ_1. . . . 193
7.6 Principal velocity profiles with Deborah number β_1. . . . 193
7.7 Principal velocity profiles with rotation parameter ω. . . . 194
7.8 Secondary velocity profiles with λ_1. . . . 195
7.9 Secondary velocity profiles with Diborah number ($beta_1$). . . . 195
7.10 Secondary velocity profiles with rotation parameter (ω). . . . 196
7.11 Secondary velocity profiles with suction parameter (V_0). . . . 196
7.12 Temperature ($\theta(\eta)$) profiles for Hall parameter (β_e). . . . 198
7.13 Temperature ($\theta(\eta)$) profiles for Hall parameter (β_e). . . . 198
7.14 Temperature ($\theta(\eta)$) profiles for ion slip parameter (β_i). . . . 199
7.15 Temperature ($\theta(\eta)$) profiles for nonlinear thermal radiation parameter (Rn). . . . 199
7.16 Temperature ($\theta(\eta)$) profiles for ratio of temperature parameter (θ_r). . . . 200
7.17 Temperature ($\theta(\eta)$) profiles for Eckert number(Ec). . . . 200
7.18 Nanoparticle concentration profiles for Hall parameter (β_e). . . . 201
7.19 Nanoparticle concentration profiles for ion slip parameter (β_i). . . . 202
7.20 Nanoparticle concentration profiles for chemical reaction parameter (Cr). 202

A.1 Mesh independence of the principal velocity profile $f'(\eta)$ for different grid resolutions 237
A.2 Mesh independence of the spanwise velocity profile $h(\eta)$ for different grid resolutions 238
A.3 Mesh independence of the temperature profile for different grid resolutions 239
A.4 Mesh independence of the concentration profile for different grid resolutions 240

List of Tables

4.1 Dimensionless parameters and their definitions 70

4.2 Comparison of $-\theta'(0)$ values with Khan and Pop [1], Bouslimi et al. [2] and the current investigation for $Pr = Sc = 10$, and in the absence of M, Da, Ec, C_r, Q_h, R_n, θ_r, We, β_i, and β_e. 76

4.3 Numerical values of the skin friction coefficients, Nusselt number and Sherwood number of some values of parameters for $Pr = 5$, $C_r = 0.6$, $N_b = N_t = Da = 0.5$, $Sc = 2$, $R_n = \theta_r = 1.2$, $Ec = 0.4$, $We = 0.2$, $Q_h = -0.1$, $\beta_i = 0.2$, $\beta_e = 1$ 91

5.1 Dimensionless parameters and their definitions 107

5.2 The numerical value comparison of Nadeem et al. [3], Sahoo and Nandkeolyar [4] and the current findings by analyzing the values of $-(1 + \frac{1}{\beta})f''(0)$ against M for $\beta = 1$, $Pr = 10$, $Nb = Nt = 0.1$ and the absence of Da, Ec, C_r, S, R_n, θ_r, Sc, β_i, β_e, λ_t, and λ_c. 112

5.3 A comparison of results of Khan and Pop [1], Sahoo and Nandkeolyar [4] and current study by examining the values of $-\theta'(0)$ and $-\phi'(0)$ under the conditions $Pr = Sc = 10$, $\beta \to \infty$, $Nb = 0.1$ and $M = Da = Ec = C_r = Q_h = R_n = \theta_r = Sc = \beta_i = \beta_e = \lambda_t = \lambda_c = 0$. 112

5.4 Numerical values of the primary $-(1 + \frac{1}{\beta})f''(0)$ and secondary $-(1 + \frac{1}{\beta})h'(0)$ skin friction coefficients of some values of parameters for $N_b = 0.2$, $N_t = Ec = Q_h = 0.1$, $Sc = 1.5$, $Da = \lambda_t = \lambda_c = \beta = Rn = Cr = 0.5$, $Pr = 6$, $M = 7$, $\beta_i = \theta_r = 1$ and $\beta_e = 2$. 128

5.5 The Nusselt number and Sherwood number corresponding to specific parameter values for $N_b = 0.2$, $N_t = Ec = Q_h = 0.1$, $Sc = 1.5$, $Da = \lambda_t = \lambda_c = \beta = Rn = Cr = 0.5$, $Pr = 6$, $M = 7$, $\beta_i = \theta_r = 1$ and $\beta_e = 2$. . . 130

6.1 Definitions of Dimensionless Parameters 143

6.2 Numerical value comparison between Fathizadeh et al. [5], Ibrahim [6], Atif et al. [7] and the findings of our study by evaluating the values of $-f''(0)$ against M for $Pr = 1$, $Nb = 0.0001$, $Nt = 0.0$ and the absence of Da, Ec, Cr, Q_h, R_n, θ_r, Sc, V_0, We, n, β_i, β_e and ω. 148

6.3 Numerical values of the skin friction coefficients of some values of parameters for $Pr = 3,\ M = 5,\ Sc = 1.5,\ We = 0.2,\ \beta_e = 2,\ n = 0.3,\ V_0 = 0.7,\ \beta_i = \omega = \theta_r = 1,\ Ec = 0.1,\ R_n = Cr = N_b = N_t = D_a = Q_h = 0.5.$ 167
6.4 Numerical values of the rate of heat transfer and rate of mass transfer of some parameters values for $Pr = 3,\ M = 5,\ Sc = 1.5,\ We = 0.2,\ \beta_e = 2,\ n = 0.3,\ V_0 = 0.7,\ \beta_i = \omega = \theta_r = 1,\ Ec = 0.1,\ R_n = Cr = N_b = N_t = D_a = Q_h = 0.5.$ 169

7.1 Definitions of Dimensionless Parameters 184
7.2 Comparison of Nu_r and Sh_r with N_t for $Pr = Le = 10$, $Nb = 0.1$, and $Ec = Cr = Da = \lambda_1 = V_0 = Rn = Qh = M = \beta_i = \omega = \theta_r = \beta_1 = \beta_e = 0$ 189
7.3 Numerical values of the skin friction coefficients of some values of parameters for $N_b = N_t = Ec = Cr = 0.1$, $Sc = 10$, $Da = \lambda_1 = V_0 = Rn = Qh = 0.5$, $Pr = 7$, $M = 5$, $Cr = 0.1$ $\beta_i = 1 = \omega$, $\theta_r = 1.2$, $\beta_1 = 0.5$ and $\beta_e = 2$. 204
7.4 Numerical values of the rate of heat transfer $\left(1 + R_n\theta_r^3\right)\theta'(0)$ and rate of mass transfer $(-\phi'(0))$ of some parameters values for $N_b = N_t = Ec = Cr = 0.1$, $Sc = 10$, $Da = \lambda_1 = V_0 = Rn = Qh = 0.5$, $Pr = 7$, $M = 5$, $Cr = 0.1$ $\beta_i = 1 = \omega$, $\theta_r = 1.2$, $\beta_1 = 0.5$ and $\beta_e = 2$. 206

8.1 Effect of the magnetic parameter M on the wall shear stress $-f''(0)$ for different non-Newtonian fluid models 210

A.1 Grid convergence study for principal velocity gradient and velocity profile 237
A.2 Grid convergence study for the spanwise velocity profile $h(\eta)$ 238
A.3 Grid convergence study for temperature gradient and temperature profile 239
A.4 Grid convergence study for concentration gradient and concentration profile 240

B.1 Computational performance and accuracy for different domain truncations of chapter 5 241

List of Symbols

Symbol	Description
B_0	External magnetic field
C	Nanoparticle concentration
C_w	Nanoparticle fraction at wall
C_p	Specific heat at constant pressure
C_r	Dimensionless chemical reaction parameter,
Da	Darcy number
D_B	Coefficient of Brownian motion
D_T	Thermophoresis coefficient
$\vec{E}$	Electric field intensity
Ec	Eckert number
Gr_x	Thermal Grashof number
Gr_m	Mass Grashof number
$\vec{J}$	Current density
J_x, J_y, J_w	Currents along x, y and z directions
K	Parameter of porous medium ,
$k*$	Mean absorption coefficient
M	Dimensionless magnetic field parameter.
N_b	Dimensionless Brownian motion parameter,
N_t	Dimensionless thermophoretic parameter,
Nu	Nusselt number
Pr	Prandtl number
Q_h	Dimensionless Heat source/sink parameter
qm	Nonlinear mass flux
Q_0	heat absorption/ generation
qr	Nonlinear heat flux
R_n	Thermal radiation parameter (Non-linear)
Re_x	Local Reynolds number
R_0	Chemical reaction parameter,
Sc	Schmidt number,
Sh_x	Local Sherwood number
T	Dimensional Fluid temperature
T_w	Fluid temperature at wall
T_∞	Free stream (Ambient) fluid temperature
u, v, w	velocity components along x, y and z axes
U_w	Velocity of Stretching Sheet

V	velocity vector,
V_0	Suction factor,
V_w	Suction velocity,
We	Weissenberg number,
x, y, z	Space coordinates

Greek Symbols

α	Thermal diffusivity
β	Casson parameter
β_1	Deborah number
β_C	Coefficient of concentration expansion
β_e	Hall effect parameter
β_i	Ion slip parameter
β_T	Coefficient of the thermal expansion
η	Similarity variable
θ	Dimensionless fluid temperature
θ_r	Temperature ratio
κ	Thermal conductivity of the fluid
Λ	Ratio of heat capacities,
λ_1	Ratio of relaxation and retardation times
λ_2	Relaxation time
λ_c	Modified mixed convection parameters
λ_t	Mixed convection parameters
μ	Dynamic viscosity of fluid
μ_0	Zero shear rate viscosity,
μ_∞	Infinite shear rate viscosity,
ρ	Fluid Density
σ	Electrical conductivity
$\sigma*$	Stefan-Boltzmann constant
τ_e	electron collision time,
τ_w	Shear stress along stretching surface
υ	Momentum diffusivity
ϕ	Dimensionless concentration
ψ	Dimensionless stream function
ω_e	Cyclotron frequency,
Ω	Angular velocity,
ω	Rotational parameter.

Subscripts

∞	Far from the sheet
w	At the wall (sheet surface)

Chapter 1

Introduction

1.1 Background

Fluids, which are substances that continuously change shape when subjected to shear stress, are fundamental to both natural processes and technological applications. They encompass liquids, gasses, and even plasmas and are ubiquitous in our everyday life. Common examples include water flowing from a faucet (valve), air circulating in a room, blood circulating in the human body, fuel injected into engines, or the transfer of coolants in industrial heat exchangers. The behavior of fluids governs a wide range of practical systems, such as weather patterns, aircraft aerodynamics, chemical mixing processes, and biomedical transport phenomena. These real-world applications highlight the importance of understanding the mechanics of fluids in diverse settings. Despite their widespread presence, the complex nature of fluid interactions, especially under the influence of various physical forces and boundary conditions, still poses significant challenges. Traditional experimental techniques, while insightful, are often limited by high costs and practical constraints and fail to capture intricate behaviors under extreme or coupled physical effects, which necessitates the application of mathematical modeling and computational simulations for a deeper analysis.

The need for robust and realistic modeling becomes even more pronounced when dealing with complex fluids exhibiting non-Newtonian behavior, nanofluid characteristics, or interactions with electromagnetic fields. Non-Newtonian fluids, such as polymer solutions, blood, paints and slurries, deviate from Newton's law of viscosity and require more advanced constitutive models to describe their flow behavior. Nanofluids, engineered by dispersing nanoparticles in base fluids, demonstrate enhanced thermal conductivity and are widely investigated in fields such as microfluidics, energy systems, and medical diagnostics. When such fluids interact with magnetic fields, their flow becomes governed by additional electromagnetic forces. This is especially relevant in systems such as magnetic drug targeting, nuclear cooling processes, and electromechanical devices. Moreover, the study of fluid flow over stretching sheets arises in the extrusion, metal spinning, and polymer processing industries, where the control of surface stretching affects product quality. The complexities increase further when considering porous media, which model real-world environments like biological tissues or filtration systems. Phenomena such as Joule heating, nonlinear thermal radiation, Hall effects, and ion slip introduce new layers of coupled behavior between thermal, chemical, and electromagnetic variables. Each of these aspects reveals a research gap capturing non-linear thermal transport, or quantifying surface forces, which current literature often treats in isolation or under simplifying assumptions.

Given these challenges and research opportunities, the present study focuses on a comprehensive mathematical and numerical analysis of MHD non-Newtonian nanofluid flows over stretching surfaces, with special emphasis on the Hall and ion slip effects. This work addresses several coupled physical mechanisms by incorporating realistic thermophysical models and exploring the non-linear interactions among fluid velocity, temperature, and nanoparticle concentration in porous media. Particular attention is paid to the influence of nonlinear thermal radiation, heat generation or absorption, chemical reactions, and viscous dissipation on flow characteristics. By employing appropriate similarity transformations and advanced numerical methods (notably higher-order Runge–Kutta methods with shooting techniques), the dissertation offers insight into how these parameters affect skin friction, Nusselt number, and Sherwood number. Through the detailed examination of four distinct non-Newtonian models of Williamson, Casson, tangent hyperbolic, and Jeffrey fluids, this study provides a broad yet deep understanding of the fluid behavior under diverse and realistic engineering conditions, ultimately contributing to both theoretical advancements and applied engineering practices.

1.2 Basic Concepts

1.2.1 The Idea of Continuum Hypothesis

The continuum hypothesis is a foundational concept in fluid mechanics that enables the mathematical treatment of fluids as continuous media, rather than discrete collections of molecules. This assumption posits that properties such as density, velocity, pressure, and temperature are continuous smooth functions of space and time, allowing the application of differential calculus to derive governing equations, such as the Navier–Stokes equations, to describe fluid motion [8, 9].

The validity of the continuum hypothesis is governed by the Knudsen number (Kn), defined as the ratio of the molecular mean free path to a characteristic physical length scale of the flow [10]. The hypothesis is generally considered applicable for $Kn < 0.01$, a condition satisfied in most engineering applications where the flow scale (e.g., a boundary layer) is vastly larger than the molecular scale [11, 12]. Despite its widespread use, the continuum hypothesis has limitations. For example, in micro- and nanoscale flows, such as gas flows in microchannels, the molecular effects become significant, and continuum models break down [13]. Similarly, in cases where the Knudsen number approaches unity or greater ($Kn \geq 1$), such as in rarefied gas flows, the continuum hypothesis breaks down. Under such circumstances, molecular dynamics or kinetic theory approaches, including the Boltzmann equation, become necessary [14]. However, for most engineering and physical applications involving liquids and dense gases, the continuum hypothesis remains robust and forms the backbone of fluid mechanics. For non-Newtonian nanofluid flows considered in this dissertation, the continuum hypothesis remains applicable because the working scale is sufficiently larger than the molecular scale, despite the addition of nanoparticles. All analyses presented in this dissertation are based on the continuum hypothesis. The governing equations, which are systems of non-linear partial differential equations, are formulated under this assumption, enabling the study of field variables such as velocity, temperature, and concentration distributions across the boundary layer.

1.2.2 Incompressible and Compressible Fluid Flow

Fluids are often classified as incompressible or compressible depending on whether changes in density are considered significant in the analysis. An incompressible fluid is one in which the density is assumed constant, regardless of changes in pressure or temperature. This assumption is appropriate for most liquids, as their densities vary negligibly with pressure and temperature under ordinary conditions [15]. Mathematically, for an incompressible flow, the substantial derivative of the density is $\frac{D\rho}{Dt} = 0$. This simplifies to the divergence-free velocity field $\nabla \cdot V = 0$, which is the famous continuity equation for incompressible flow [16]. In contrast, a compressible fluid experiences significant density changes as a result of variations in pressure [17]. The compressibility is quantified by the Mach number (M), the ratio of the flow speed to the speed of sound in that fluid. When the Mach number exceeds 0.3, compressibility effects cannot be ignored. In such cases, the governing equations must account for variations in density, and phenomena such as shock waves, expansion fans, and acoustic waves are prevalent [18]. The incompressibility assumption greatly simplifies the governing equations, making the analysis feasible for a wide range of engineering applications. For example, most water flow problems in hydraulics and civil engineering are modeled as incompressible flows.

In particular, the incompressible–compressible classification is not strictly related to the physical nature of the fluid, but rather to the assumptions made in modeling. For example, air is inherently compressible, but at low velocities ($M < 0.3$), it can be treated as incompressible without significant loss of accuracy. Thus, the choice between incompressible and compressible models depends on the flow regime and the requirements of the problem [19].

This study mainly considers incompressible fluids, as density variations are assumed to be negligible for the flow problems investigated. Both the base fluid and the nanofluid are treated as incompressible within the boundary layer approximations. This assumption simplifies the governing equations and aligns with the fact that most liquid-based nanofluids (e.g., water and ethylene glycol) exhibit minimal density variations under moderate pressure and temperature changes.

1.2.3 Viscous and Inviscid Fluid Flow

Viscosity is the property of a fluid that resists deformation due to shear stress, and it plays a fundamental role in distinguishing between viscous and inviscid flows. Viscous flows account for internal frictional forces caused by molecular interactions and are mathematically governed by the Navier–Stokes equations, which include viscous stress terms [20]. Such effects become particularly important in regions near solid boundaries, where velocity gradients are steep and shear stresses are significant. In contrast, inviscid flow assumes negligible viscosity, leading to a simplification of the governing equations into the Euler equations [12].

The Reynolds number, defined as the ratio of inertial to viscous forces, provides a fundamental criterion to distinguish between viscous and inviscid dominated regimes. Low Reynolds number flows are strongly influenced by viscous effects, while high Reynolds number flows can often be approximated as inviscid, except near solid boundaries, where shear stresses remain significant [21].

For non-Newtonian and nanofluid systems, the viscosity exhibits complex, non-linear behavior that cannot be ignored. Rheological models such as the Williamson, Casson, tangent hyperbolic, and Jeffrey fluid models are commonly employed to capture these variations. In such cases, the governing equations explicitly retain viscous terms along with additional resistive forces, including those arising from MHD effects. In this dissertation, viscous fluid flow is considered, rather than inviscid flow, because the influence of viscosity is central to the formulation of boundary layer equations. The viscous shear stresses play a significant role in the velocity profiles near the stretching sheet. Ignoring viscosity would eliminate the concept boundary layer itself, which is the basis of this study.

1.2.4 Laminar and Turbulent Flow

Laminar and turbulent flows represent two distinct regimes of fluid motion. Laminar flow is characterized by a smooth, ordered, and layered motion of fluid particles, with minimal mixing between adjacent layers. It occurs when viscous forces dominate over inertial forces, typically at low Reynolds numbers. In laminar flow, the velocity, temperature, and concentration profiles remain well-structured and predictable. Examples include blood flow in capillaries and oil flow in narrow pipes. Turbulent flow, on the contrary, exhibits chaotic and irregular motion, characterized by eddies, vortices, and intense mixing. It occurs at high Reynolds numbers, where inertial forces overwhelm the viscous damping [21].

The transition between laminar and turbulent flow is not abrupt but depends on both the Reynolds number and external disturbances. For example, in pipe flow, laminar flow persists for Reynolds numbers below approximately 2300, while turbulence dominates above 4000, with a transition region in between [21]. Boundary layer theory also highlights that surface roughness and pressure gradients significantly influence the onset of turbulence. In flow over a flat plate, laminar behavior is generally sustained for $Re < 5 \times 10^5$, while higher values typically lead to a transition into turbulence [22].

Understanding the laminar–turbulent distinction is essential in fluid mechanics, as it determines the choice of governing equations, modeling techniques, and numerical methods. Laminar flows can be well described by deterministic equations, whereas turbulent flows need further modeling. The study of turbulence remains one of the most challenging problems in classical physics [23]. The laminar flow regime is considered throughout this dissertation. Since the mathematical models are formulated within the boundary layer framework and the solutions are obtained under assumptions valid for laminar conditions, turbulence is excluded. This assumption is supported by the parameter ranges of magnetic field, non-Newtonian and other parameter effects, which are selected to ensure that the flows remain laminar and stable.

1.2.5 Eulerian and Lagrangian Approaches

The analysis of fluid motion is fundamentally described by two distinct frameworks: the Eulerian and Lagrangian approaches. In the Eulerian description, the flow field is analyzed by defining fluid properties such as velocity, pressure, and temperature at fixed points in space as functions of time. This perspective is highly effective for continuum-level modeling, naturally aligns with experimental measurement techniques, and is the predominant framework for deriving and solving the governing partial differential equations, such as the Navier-Stokes equations [24]. In contrast, the Lagrangian description tracks the history of individual fluid particles as they move through space and time [25]. Although this approach provides direct insight into particle trajectories and residence times, making it invaluable for studies of dispersion or particle-laden flows, it is often computationally prohibitive for analyzing entire flow fields at the continuum scale [26, 27].

The choice between these mathematically related yet conceptually different approaches is dictated by the specific problem. The Eulerian method is overwhelmingly preferred for analyzing flows in boundary layer and flow through fixed control volumes, such as channels or around airfoils, as it allows for a straightforward application of boundary conditions at fixed spatial locations [28]. In contrast, the Lagrangian method excels in applications where tracking discrete elements is paramount, such as in molecular dynamics, pollutant dispersion, or the simulation of droplet dynamics in multiphase flows [25, 29]. To take advantage of both, hybrid Eulerian-Lagrangian schemes are frequently employed in complex simulations like combustion or sediment transport, where a continuous phase is modeled Eulerially and discrete particles are tracked in a Lagrangian frame [30].

In this dissertation, the entire analysis is conducted within the Eulerian framework, where fluid properties are described at fixed spatial locations relative to the stretching sheet, making this approach appropriate for boundary layer analysis. Although the Lagrangian perspective is useful for particle tracking, the focus of this study lies on field distributions of velocity, temperature, and nanoparticle concentration rather than individual particle paths.

1.3 Review of Related Literature

In recent years, the study of fluid flow problems involving non-Newtonian nanofluids under MHD influences has attracted considerable attention. Key motivations include enhanced heat and mass transfer properties, wide industrial and engineering applications such as cooling systems, materials processing, energy devices, etc., and the complex physics introduced by effects such as Hall currents, ion slip, nonlinear thermal radiation, viscous dissipation, chemical reactions, and rotation. The inclusion of these effects with different non-Newtonian fluid models (such as Williamson, Casson, tangent hyperbolic, Jeffrey) over stretching or permeable surfaces in porous media or with permeable boundaries has been a rich field of investigation.

This review surveys the theoretical and numerical findings of non-newtonian fluids, nanofluids, MHD and Lorentz forces, Hall and ion slip effects, flows over stretching surfaces, porous media, rotating flows, permeable surface flows, and relevant physical phenomena (like viscous dissipation, Joule heating, chemical reaction, thermal radiation). The aim is to see what has been done, what gaps remain, and how the four fluid models fit and extend the existing literature.

1.3.1 Introduction to Non-Newtonian Fluids

Viscosity, a property of fluids that resists the relative motion of fluid layers, plays a critical role in the behavior of fluids under stress. In fluid dynamics, the behavior of fluids is classified on the basis of how they respond to shear stress, either following or deviating from Newton's law of viscosity. Newton's law of viscosity states that the shear stress between two fluid layers is directly proportional to the velocity gradient between those layers [31], expressed as follows.

$$\tau = \mu \left(\frac{du}{dy} \right), \tag{1.1}$$

where τ represents the shear stress, μ the dynamic viscosity, and $\frac{du}{dy}$ is the velocity gradient perpendicular to the flow direction. Fluids that obey this law are termed Newtonian fluids, while those that do not are categorized as non-Newtonian fluids. Newtonian fluids, such as water, air, motor oil, common gases, and simple liquids, exhibit constant viscosity regardless of the shear rate. Their predictable behavior and linear response to shear make them easier to model and analyze using the Navier-Stokes equations. However, non-Newtonian fluids do not follow this linear stress-strain relationship. Common examples include blood, ketchup, toothpaste, and polymer solutions. The mathematical treatment of these fluids involves modifying the stress tensor in the momentum equations to reflect non-linear behavior.

Non-Newtonian fluids [32], as opposed to Newtonian fluids, exhibit a more complex relationship between shear stress and shear rate. In these fluids, the viscosity is not constant, and it may vary depending on factors such as shear rate, time, or applied stress. This unique behavior makes non-Newtonian fluids a significant area of study, particularly in industries where complex fluids, such as polymer melts, slurries, and biological fluids, are involved. The flow of non-Newtonian fluids is commonly classified into several categories based on their rheological properties [33]. These categories include shear-thinning (pseudoplastic), shear-thickening (dilatant), viscoelastic (showing elastic memory effects), and viscoplastic fluids [34]. Shear-thinning fluids, such as blood and paints, become less viscous as the shear rate increases, making them easier to flow under high shear conditions. In contrast, shear-thickening fluids become more viscous as the shear rate increases [35], often resulting in the fluid becoming solid-like under rapid deformation. Viscoelastic fluids exhibit both viscous and elastic characteristics, which means that they behave like solids under certain conditions and like liquids under others. On the other hand, certain fluids may start to flow only if the external stress exceeds a certain threshold value [36]; such fluids are called viscoplastic fluids. For this type of behavior, there is a minimum stress threshold, called yield stress, that must be exceeded for the fluid to flow or deform. The study of non-Newtonian fluids involves developing constitutive equations that model these complex behaviors, providing insight into how the fluids will react to various flow and external conditions, such as temperature, pressure, magnetic fields, and particle concentrations.

The study of fluids encompasses a wide array of applications in science, engineering, and manufacturing processes. In recent years, the study of non-Newtonian fluids has attracted significant attention because of their unique rheological characteristics and relevance in practical applications. Researching the flow characteristics of non-Newtonian fluids and their uses in several industrial domains has garnered significant attention in the past few years. A wide range of mathematical models, such as the Carreau-Yasuda, Williamson, Casson, K-L, Cross, generalized power-law, tangent hyperbolic, Prandtl-Eyring, Powell-Eyring, Ellis, Maxwell, and Jeffery models, have been developed to capture the complex rheological behavior of non-Newtonian fluids, as reported in the literature [37, 38]. These models have been successfully applied in numerous studies to investigate the flow characteristics of non-Newtonian fluids under various geometric configurations and boundary conditions.

In the context of this dissertation, non-Newtonian fluid models, including the Williamson, Casson, tangent hyperbolic and Jeffrey fluid models, are employed to better understand the effects of magnetic fields, thermal gradients, and nanoparticle dispersion in nanofluid flows. The behavior of these complex fluids under the influence of such external factors is a key to optimizing industrial processes such as heat exchangers, drug delivery systems, and lubrication mechanisms. By examining the properties of these fluids through the lens of MHD and boundary layer theory, this work contributes valuable insights into the flow characteristics, heat transfer, and mass transfer phenomena that arise in applications involving non-Newtonian fluids.

1.3.2 Nanofluids and their Importance

Nanofluids represent a class of fluids consisting of a base fluid, typically water, oil, or ethylene glycol, with suspended nanoparticles. Metallic solids like copper(Cu), silver(Ag), gold(Au,); metallic oxides like alumina (Al_2O_3), CuO, nonmetallic solids such as titanium oxide (TiO_2), silica (SiO_2), etc.; and metallic liquids like sodium (Na) are used as nanoparticles [39, 40]. The inclusion of nanoparticles in the base fluid significantly enhances its thermal conductivity and heat transfer capabilities. Nanofluids have emerged as promising candidates for various applications, including heat exchangers, cooling systems, and microfluidics. The investigation of nanofluids offers opportunities to explore novel fluid flow phenomena and optimize heat transfer processes. The use of nanoparticles to improve the thermal conductivity of fluids was presented by Choi and Eastman.

The importance of nanofluids stems from their remarkable thermo-physical properties, which make them highly attractive for a multitude of engineering applications. They offer a notable improvement in the cooling performance of systems such as automotive radiators, nuclear reactors, heat exchangers, and electronic cooling devices, where efficient heat removal is critical for performance and safety [41]. Beyond enhanced thermal conductivity, nanofluids can improve the convective heat transfer coefficient, boiling critical heat flux, and overall energy efficiency of thermal systems. This has profound implications for energy conservation, equipment miniaturization, and the development of new technologies in biomedicine (e.g., drug delivery, hyperthermia) and material processing [42].

Many writers have also suggested models and techniques for studying convective fluxes of nanofluid, including the most well-liked models put forth by Buongiorno [43] and Tiwari and Das [44]. A comparison of the relative velocities of the nanoparticles and the base fluid was explained in detail by Buongiorno [43] using seven different slip mechanisms. These include the Magnus effect, fluid drainage, inertia, Brownian diffusion, thermophoresis, diffusiophoresis, and gravity. The investigation led to the conclusion that the only significant slip mechanisms are thermophoresis and Brownian diffusion. Brownian diffusion accounts for the random motion of nanoparticles due to collisions with base fluid molecules, whereas thermophoresis describes the migration of particles from hotter to cooler regions under temperature gradients. These mechanisms significantly influence the distribution of the nanoparticles and, consequently, the thermal conductivity and convective heat-transfer behavior of nanofluids. The model is widely regarded for its ability to capture essential microscale effects in heat and mass transfer, particularly under external forces or complex boundary conditions. Its efficacy has been demonstrated in various configurations, notably by Hayat et al. [45], who applied it to three-dimensional boundary layer flows and showed that thermophoretic forces dominate nanoparticle migration at high temperature gradients.

1.3.3 Magnetohydrodynamics and the Lorentz Force

MHD refers to the dynamics of electrically conducting fluids in the presence of magnetic fields. In most boundary layer MHD flow problems, the external magnetic field (often uniform) induces currents in the fluid, which interact with the magnetic field to produce Lorentz force, usually opposing motion (i.e. acting as a drag). In non-Newtonian fluids, this force is coupled with the rheological stress relations, leading to modified momentum equations. Sometimes a magnetic parameter (Hartmann number), or magnetic field parameter appears, scaling the Lorentz force. Ohmic heating also arises when there is finite electrical conductivity. MHD has been a vibrant area of research for several decades, with applications across various scientific and engineering domains. The foundational work on MHD dates back to when Hannes Alfvén developed the basic theory of magnetohydrodynamics and introduced the concept of Alfvén waves [46]. In the more recent decades, MHD research has expanded to encompass a wide range of applications, including MHD power generation, plasma confinement in fusion reactors, liquid metal cooling for nuclear reactors, and MHD propulsion for spacecraft [47, 48].

The fluid equations in the MHD model incorporate the Lorentz force term in addition to the Maxwell equations. So, the inclusion of MHD can significantly influence the flow behavior and heat transfer characteristics of the fluid. Furthermore, the behavior of nanofluids also becomes increasingly intricate and demanding to analyze when they are subjected to an external magnetic field, owing to the complex interplay between the applied magnetic field and the interactions of the suspended nanoparticles within the fluid. Farzin et al. [49] studied that magnetic nanoparticles have been developed for localized drug delivery for patients with cancers. These are directed to the tumor, by acting as a carrier of the drug. Once the drug has reached the patient's bloodstream, a magnetic field is applied to retain the particles in the targeted site of the tumor. Besides, magnetic nanoparticles can control nanoparticle delivery where nanoparticle hyperthermia is used for confined cancer tumors.

The application of a transverse magnetic field to a non-Newtonian nanofluid flow over a stretching sheet typically results in a resistive Lorentz force that decelerates the flow in the primary direction. This retarding effect enhances the apparent viscosity and leads to a rise in temperature and concentration within the boundary layer due to the conversion of the kinetic energy into Joule heating [50]. Numerous studies, including those on Williamson, Casson, tangent hyperbolic, and Jeffrey fluids by Raza et al. [51], Mohamed et al. [52], Ashraf et al. [53] and Abdullah et al. [54], have consistently shown that an increasing magnetic parameter leads to a decrease in primary velocity and an increase in temperature. Some pertinent and creative concerns about MHD conducted under various circumstances are discussed by several authors [52, 55–57].

1.3.4 Flow over Stretching Surfaces

Flow over a stretching sheet is a classical problem in fluid mechanics that is of great significance in numerous industrial processes. The analysis of flow over a stretching sheet is particularly important for understanding the behavior of fluids near solid surfaces, which significantly influences heat transfer and flow characteristics. The idea of boundary layer flow across a continuously stretching surface was proposed by Sakiadis [58]. Following Sakiadis, numerous fluid dynamics researchers, including Nadeem et al. [59], Ullah et al. [60], and others, have conducted research on fluid motions in the context of stretching surfaces.

The study of heat transfer over a stretching sheet has numerous applications, as discussed by Iqbal et al. [61] and Muzara and Shateyi [62]. Surfaces with stretching properties find significant applications in areas such as metallurgical processes, polymer extrusion, plastic films, metal spinning, paper manufacturing, wire drawing, hot rolling, and fiber production [63]. The flow over stretching surfaces has been investigated by researchers, considering factors such as magnetic fields, nanofluids, chemical reactions, and convective boundary conditions, as discussed by Kumar et al. [64] and Irshad et al. [65]. The comprehensive understanding of boundary layer flow across stretched sheets is a subject of intense interest for a large number of researchers driven by its extensive applications in various industrial sectors.

1.3.5 Flow through Porous Medium

Fluid flow through porous media is a critical phenomenon in both natural and engineered systems, occurring in materials such as soil, biological tissues, and filtration systems. The presence of a porous medium introduces additional complexity to the flow behavior, as it creates resistance to fluid motion and alters the heat and mass transfer characteristics. Understanding these dynamics is essential for optimizing applications in groundwater hydrology, petroleum engineering, oil recovery, geothermal energy extraction, and chemical processes [66].

Darcy's law provides a fundamental description of flow through porous media, stating that the flow rate is proportional to the pressure gradient. Recent studies have explored the behavior of non-Newtonian nanofluids in porous media, particularly under MHD effects. For example, research by Razi et al. [67] examined the impact of wall thickness, slip parameters, and velocity power index on the MHD boundary layer flow of the Williamson nanofluid over a stretched sheet in porous media. Similarly, Kebede et al. [68] conducted an analytical study on heat and mass transfer in time-dependent Williamson nanofluid flow over a permeable stretching sheet embedded in a porous medium. A nonlinear stretching sheet embedded in a porous medium was studied by Abbas et al. [69] to investigate the behavior of magnetohydrodynamic Williamson nanofluid flow and heat transfer. Abdal et al. [70] also studied the transport of MHD Casson nanofluid to an extending cylinder through porous media. Further investigations by Abbas et al. [69] highlighted how porous media influence the flow and heat transfer characteristics, particularly for tangent hyperbolic nanofluids. Additional contributions from [71–77] have expanded the understanding of fluid dynamics in porous media, emphasizing its importance in industrial applications such as filtration, catalysis, and energy systems.

1.3.6 Physical Flow Properties

In real-world scenarios, several physical phenomena influence fluid flow (momentum transfer), heat transfer, and mass transfer processes. Factors such as viscous dissipation, Ohmic heating, thermal radiation, heat generation/absorption, and chemical reactions significantly affect the overall behavior of the system. Viscous dissipation refers to the energy loss due to internal friction or viscosity within a fluid. Ohmic heating, or Joule heating, arises from the passage of an electric current through a conducting fluid, generating heat due to the resistance of the fluid. Heat generation/absorption accounts for the production or consumption of heat within the fluid, alters the thermal boundary conditions, while chemical reactions impact the concentration distribution and overall fluid properties. Tarakaramu et al. [78], Ibrahim and Anbessa [79], Bouslimi et al. [2], Abbas et al. [69], Taj and Salahuddin [80], Walelign et al. [81], Hunegnaw [82], Khan et al. [83], Qamar [84], Shahzad et al. [85], Sohail et al. [86], Muduly et al. [87], Waqas et al. [88], Nandi and Kumbhakar [89], Nagaraja et al. [90], Tarakaramu et al. [91] Younas and Sagheer [92] extensively studied these phenomena, providing a comprehensive understanding of how each factor influences fluid flow and heat and mass transfer.

Thermal radiation, which is essential to the processes of conveying heat in high-temperature systems, follows linear models like the Stefan-Boltzmann law for small temperature differences, but as these differences increase, the thermal radiation becomes nonlinear, exhibiting a more complex, exponential dependence on temperature that cannot be captured by simple linear models. Therefore, the effects of nonlinear thermal radiation have to be incorporated in the study to accurately model the heat transfer processes in such systems. Researchers from several studies, including Archana et al. [93], Ghadikolaei et al. [94], Akaje and Olajuwon [95], Shamshuddin et al. [96], Li et al. [97], have conducted research on the effects of nonlinear thermal radiation in various fluid flow scenarios. The findings of these studies highlight the need to account for this phenomenon when analyzing and modeling heat transfer in different fluid flow situations.

1.3.7 Rotating Flow

Rotational flows, which are prevalent in geophysical processes and rotating machinery, generate Coriolis forces that substantially alter velocity distributions, induce secondary flows, and influence overall flow stability. These effects extend beyond purely mechanical alterations, as they directly impact heat and mass transfer processes, mixing efficiency, and boundary layer development. Previous investigations, such as the foundational work of Hayat et al. [98] on rotating Jeffrey fluids, have provided governing frameworks, which were later extended to nanofluids by Veera Krishna [99] and Krishna and Chamkha [100], who incorporated Hall currents and ion slip effects. These studies demonstrated that Coriolis forces not only amplify electromagnetic interactions but also significantly reshape thermal and concentration profiles through modifications of thermal boundary layers.

More recent contributions reinforce these findings in broader physical contexts. Anand Kumar et al. [101] and Preetham and Kumbinarasaiah [102] examined the combined influence of rotation and magnetic fields, while Hani and Ali [103] highlighted how the Coriolis effect alters boundary layer characteristics, driving natural convective heat transfer in MHD flows. Similarly, Vaddemani et al. [104] explored rotational impacts on non-Newtonian fluids, uncovering critical changes in flow patterns and thermal behavior. Collectively, these studies emphasize that rotational dynamics through the coupling of Coriolis forces with Hall current, ion slip, and electromagnetic effects are indispensable in accurately modeling non-Newtonian nanofluids.

1.3.8 Flow over Permeable Surface

The suction velocity of fluid through a permeable surface can significantly alter the boundary layer thickness, velocity profiles, and rates of heat and mass transfer. Research by Ishak et al. [105] demonstrated that suction can stabilize the boundary layer, while injection tends to destabilize it. These effects are utilized in various engineering applications, such as boundary layer control in aerodynamics and cooling of electronic devices. More recent studies, such as those by Shahzad et al. [106] and Alkaoud et al. [107], have further investigated the effects of suction and injection in different flow configurations and their practical implications. Amer et al. [108] proved that the suction parameter $(-V_w)$ critically controls the boundary layer and has a significant impact on profiles of nanofluid velocity. These works underscore the role of medium permeability in altering momentum and energy transport.

1.3.9 Hall and Ion slip Effects

The investigation of Hall and ion slip effects in MHD flows has gained attention because of their significant influence on flow behavior. These phenomena are also important in the design of devices such as Hall sensors, magnetic accelerators, and centrifugal pumps, as they influence the flow behavior of conducting fluids in the presence of strong magnetic fields. The Hall effect refers to the interaction between charged particles and magnetic fields, resulting in the development of electric fields perpendicular to the current and magnetic field directions. The ion slip effect accounts for the relative motion between the charged particles and the neutral fluid. These effects can alter flow characteristics, heat transfer rates, and mass transfer rates; this requires investigation of these effects to understand and optimize MHD flows. When the magnetic field is large, the strong electromagnetic force causes Hall current and ion-slip phenomena to be more pronounced. Hall current and ion slip effects are being studied by numerous researchers. The effects of ion-slip and Hall currents on the steady magneto-micropolar of an electrically conducting viscous incompressible fluid were examined by Seddeek [109]. Taking into account the impacts of Hall and ion-slip currents, Su [110] analyzed the problem of unsteady MHD mixed convective flow of a Cu-water nanofluid across a vertical convectively heated plate. Opanuga et al. [111] examined the effects of suction/injection and Hall current on a third-grade fluid that was steady, viscous, incompressible, and electrically conducting as it passed a semi-infinite plate with entropy generation. Ibrahim and Anbessa [112] have addressed the Hall and ion-slip effects on a mixed convection flow of an electrically conducting nanofluid over a stretching sheet in a permeable medium. Krishna [99] investigated the effects of thermal radiation, Hall, and ion slip on the unsteady MHD-free convective rotating flow of Jeffrey fluid through an infinite vertical porous plate with a ramped wall temperature. In a semi-infinite vertical moving permeable surface, Krishna et al. [100] theoretically investigated the effects of Hall and ion slip on an unsteady laminar MHD convective rotating flow of heat-generating or absorbing second-grade fluid.

The literature strongly supports the idea that incorporation of Hall and ion slip effects adds significant depth to MHD boundary layer studies. These effects are pronounced in ionized fluids and plasma environments, where the conductivity of the fluid changes due to the presence of electric and magnetic fields. Hall current alters the Lorentz force direction, affecting the velocity components, while ion slip accounts for ion inertia, which modifies the current density and electric field behavior. Together, they influence the thickness of the boundary layer, the heat transfer rate, and the flow stability.

1.3.10 Conclusion

In summary, recent investigations have significantly advanced the understanding of MHD Non-Newtonian nanofluid flows by incorporating various physical mechanisms and rheological models. Krishna and Kumar [114] analyzed unsteady MHD Jeffreys nanofluid flow over a stretching sheet with velocity slip, nonlinear radiation, and chemical reaction, while neglecting Hall and ion slip effects, viscous dissipation, porosity, and Joule heating. Abbas et al. [115] investigated chemically reactive Williamson nanofluid flow with nonlinear radiation and variable thermal conductivity over stretching and shrinking surfaces, revealing dual solution behavior, yet Hall and ion slip mechanisms were not incorporated. Kumari et al. [116] studied MHD Jeffrey nanofluid flow over an inclined porous stretching sheet and demonstrated the suppressing role of magnetic fields on velocity and the enhancing effect of thermal radiation on heat transfer, while Brownian motion and thermophoresis influenced thermal and concentration boundary layers; however, Hall and ion slip effects were excluded. Mingliang et al. [117] explored electrically conducting tangent hyperbolic nanofluid flow and reported strong sensitivity of flow resistance and heat and mass transfer to rheological and nanoparticle parameters, but nonlinear thermal radiation and Hall and ion slip effects were not considered. Khalil et al. [118] analyzed slip effects on MHD Casson nanofluid flow over a vertical stretching surface and found that buoyancy and magnetic forces enhance heat and mass transfer while velocity slip reduces wall shear stress, although Hall and ion slip mechanisms were omitted. Ahmad et al. [119] investigated unsteady MHD Williamson nanofluid flow between rotating disks, providing insights into shear-thinning behavior and transport characteristics, but without accounting for Hall and ion slip effects. Collectively, these studies demonstrate substantial progress in modeling MHD Non-Newtonian nanofluid flows; nevertheless, they consistently overlook the combined influence of Hall and ion slip currents, particularly in conjunction with nonlinear thermal radiation, viscous dissipation, Joule heating, chemical reaction, porous media, and multiple non-Newtonian fluid models. This clearly identified gap motivates the present dissertation, which aims to develop a unified and comprehensive framework that systematically incorporates these neglected electromagnetic and thermophysical mechanisms to enhance the physical realism and applicability of MHD nanofluid flow models.

1.4 Statement of the Problem

The analysis of MHD flows involving Non-Newtonian nanofluids over stretching surfaces constitutes a fundamental research area with profound implications for advanced engineering applications, including polymer extrusion, electromagnetic materials processing, thermal management of high-power electronic and nuclear systems, and targeted drug delivery. Numerous industrially and biologically relevant fluids—such as polymer solutions, biological fluids, lubricants, and colloidal suspensions—exhibit intrinsically non-Newtonian rheological characteristics, including shear-thinning, shear-thickening, yield stress, and viscoelastic behaviors. The interaction of such complex fluids with applied magnetic fields introduces intricate multiphysical couplings among electromagnetic, thermal, species transport, and rheological phenomena.

A critical examination of existing literature reveals that contemporary investigations on non-Newtonian nanofluid flows frequently employ simplifying assumptions that limit their physical realism, particularly under strong magnetic field conditions. Specifically, the Hall and ion-slip effects are routinely neglected despite their dominance in regimes characterized by high magnetic intensity or low fluid density. Furthermore, prevailing studies typically examine isolated non-Newtonian models under simplified thermal and chemical boundary conditions, thereby precluding systematic cross-rheological comparisons and hindering the identification of universal magneto-rheological transport principles. The synergistic interplay of these electromagnetic slip mechanisms with other relevant phenomena—including nonlinear thermal radiation, porous media resistance, viscous dissipation, chemical reaction, and convective transport of nanoparticles—remains markedly underexplored for multi-class non-Newtonian systems.

Consequently, while individual physical effects have been studied in isolation, the integrated response of different non-Newtonian nanofluid families to concurrent electromagnetic, thermal, and chemical stimuli remains largely uncharted. The present research is formulated to systematically investigate and quantify the combined influence of Hall and ion-slip currents, nonlinear radiation, porous media, chemical reaction, and nanoparticle transport on the MHD flow and heat/mass transfer characteristics of four prominent non-Newtonian models: Casson, Williamson, Tangent Hyperbolic, and Jeffrey nanofluids.

Accordingly, this study seeks to answer the following research questions:

1. How can mathematical models for MHD flow of non-Newtonian nanofluids past a stretching sheet be formulated?

2. How do the embedded physical parameters affect the velocity, temperature, and nanoparticle concentration profiles?

3. How do non-Newtonian parameters, nonlinear thermal radiation, viscous dissipation, rotation, chemical reaction, suction, magnetic field, Hall currents, and ion-slip affect flow characteristics? What are the physical interpretations of such factors?

4. How are skin friction, Nusselt number, and Sherwood number affected due to the presence of physical parameters?

5. How can the momentum, thermal, and concentration boundary layer problems be solved by using the higher-order Runge-Kutta method with shooting?

1.5 Objectives of the Study

The primary objective of this study is to investigate and analyze the effects of Hall and ion slip currents on the flow behavior, heat transfer, and mass transfer characteristics of MHD Non-Newtonian nanofluids over a stretching sheet under the influence of relevant physical parameters.

The study also has the following specific objectives:

1. Analyze the influence of Hall current, ion slip, viscous dissipation, and nonlinear thermal radiation on the boundary layer flow of MHD Williamson nanofluid past a stretching sheet.

2. Examine the mixed convection flow of MHD Casson nanofluid over a vertically stretching sheet embedded in a porous medium, accounting for the combined effects of Hall and ion slip, nonlinear thermal radiation, and Ohmic heating.

3. Investigate the rotating flow behavior of MHD tangent hyperbolic nanofluid over a stretching permeable sheet, with special attention to the impacts of suction velocity, Hall current, ion slip, and nonlinear thermal radiation.

4. Conduct numerical simulations on the three-dimensional rotating flow of MHD Jeffrey nanofluid over a permeable stretching surface, accounting for the influence of Hall/ion slip currents, viscous dissipation, and nonlinear thermal radiation on the thermo-physical properties of the flow.

1.6 Significance of the Study

The significance of this study lies in its theoretical, practical, and applied contributions to the understanding of MHD Non-Newtonian nanofluid flows over stretching surfaces. Specifically, the study makes the following important contributions:

i. Enhances fundamental understanding of MHD non-Newtonian nanofluid flows with Hall/ion slip effects, offering a more realistic model of transport phenomena.

ii. Fills a gap by systematically analyzing coupled Hall/ion slip effects on momentum, heat, and mass transfer in non-Newtonian nanofluids.

iii. Applicable to electronics cooling, polymer processing, metallurgical operations, energy systems, and MHD flow control technologies.

iv. Guides engineers in optimizing thermal/mass transfer processes, improving efficiency and reducing operational costs.

v. Serves as a reference for advanced fluid models, numerical simulations, and future studies.

vi. Improves predictive capabilities for complex nanofluid systems and supports development of advanced heat/mass transfer technologies.

1.7 Scope of the Study

The scope of this dissertation is defined as follows:

- The study is restricted to steady, laminar, viscous, homogeneous, and incompressible MHD flows of non-Newtonian nanofluids (Williamson, Casson, tangent hyperbolic, and Jeffrey) past a stretching sheet embedded in a porous medium.

- A strong magnetic field is applied perpendicular to the sheet, inducing Hall and ion-slip effects that result in a three-dimensional force acting on the fluid.

- The Buongiorno nanofluid model is employed to describe the dynamics of nanoparticles in the base fluid.

- The study incorporates the effects of Joule heating (Ohmic heating), viscous dissipation, nonlinear thermal radiation, rotation, suction, heat generation/absorption, and chemical reactions.

- Excluded from the study: Turbulent flows, compressible effects, variable fluid properties, non-uniform magnetic fields, and surface slip effects are not considered.

1.8 Outlines of the Dissertation

This dissertation investigates MHD non-Newtonian nanofluid flows over a stretching sheet, incorporating the Hall current, ion-slip effects, and influences of other pertinent flow parameters. The research combines theoretical derivations, numerical simulations, and parametric analyses to explore heat and mass transfer characteristics in four distinct non-Newtonian fluid models. The structure of the dissertation is organized as follows.

Chapter 1 presents the research problem and provides a contextual background. The chapter includes subsections on the background, basic concepts, review of related literature, problem statement, research objectives, significance, scope, and organization of the dissertation.

Chapter 2 incorporates constitutive equations of non-Newtonian fluids, with particular focus on the mathematical descriptions of Williamson, Casson, tangent hyperbolic, and Jeffrey fluid models. Boundary layer assumptions and the coupling of heat- and mass-transfer phenomena are also discussed. Furthermore, it also presents the fundamental governing equations of fluid flow, including the continuity equation (mass conservation), the momentum equations (Newton's second law), the energy equation (first law of thermodynamics), and the concentration equation.

The third chapter details the numerical approach adopted in the study, including a review of related numerical methods, a detailed explanation of the shooting technique, and the implementation of higher-order Runge–Kutta methods (fifth and sixth order variants). It also covers the simulation setup, software tools (Python), validation techniques, and step-by-step numerical procedures adopted to obtain accurate solutions.

Chapter 4 examines the effects of Hall current, ion slip, viscous dissipation, and nonlinear thermal radiation on the flow of the MHD Williamson nanofluid through a stretching sheet. This study, the most important findings published in the International Journal of Thermofluids (2024, DOI: 10.1016/j.ijft.2024.100646) [120], highlights how prominent parameters influence the velocity, temperature, and nanoparticle concentration profiles, with implications for industrial cooling technologies and energy systems. The effects of various physical parameters on the skin friction coefficient, the local Nusselt number, and the Sherwood number are also investigated.

Chapter 5 analyzes the mixed convection flow of MHD Casson nanofluid over a vertically stretching sheet, emphasizing Hall, ion-slip, and non-linear thermal radiation effects. Published in the International Journal of Thermofluids (2024, DOI: 10.1016/j.ijft.2024.100762) [121], this chapter explores the role of porous media, chemical reactions, and other physical phenomena in heat and mass transfer, offering insights for biomedical and geothermal applications.

Chapter 6 investigates the rotating flow of MHD tangent hyperbolic nanofluid over a permeable stretching sheet, focusing on suction, Hall current, and ion-slip effects. Published in the Journal of Nanofluids (2024, DOI: 10.1166/jon.2024.2208) [122], this study demonstrates how rotation and suction alter flow dynamics, with relevance for aerospace and coating technologies. Detailed graphical and numerical discussions on flow fields, surface drag, and heat and mass transfer rates are provided.

Chapter 7 presents a comprehensive numerical investigation into the three-dimensional rotating flow of an electrically conducting Jeffrey nanofluid on a permeable stretching surface. The study incorporates the combined effects of Hall and ion slip currents, viscous dissipation, Joule heating, nonlinear thermal radiation, and chemical reaction, while employing the Buongiorno model for nanoparticle transport. The results of this chapter are published in the International Journal of Thermofluids (2025, DOI: 10.1016/j.ijft.2025.101517) [123]. A detailed discussion of the graphical profiles for the velocity, temperature, and nanoparticle concentration distributions under the influence of various dimensionless parameters, complemented by tabulated data for key engineering quantities such as the skin friction coefficients and the local Nusselt and Sherwood numbers, are incorporated.

Chapter 8 concludes the dissertation by summarizing the major contributions and proposing future research directions in MHD nanofluid dynamics.

Chapter 2

Mathematical Descriptions of Non-Newtonian Fluids, Heat and Mass Transfer, Boundary Layer Flows, and Basic Governing Laws

2.1 Mathematical Descriptions of Non-Newtonian Fluids and MHD

2.1.1 Constitutive Equations of some Non-Newtonian Fluids

Constitutive equations define the dependence of stress on the rate of strain. Although Newtonian fluids have a linear relationship between shear stress and shear rate (governed by a constant viscosity), Non-Newtonian fluids exhibit more complex behavior. Because of these deviations from classical Newtonian behavior, different fluid models are used, each with their own constitutive equations, to accurately describe Non-Newtonian flows. These equations are crucial for understanding the behavior of industrial, biological, and engineering fluids such as polymer melts, blood, and paints, especially when combined with external effects such as magnetic fields and nanoparticle suspensions.

In MHD nanofluid flows involving Non-Newtonian fluids over stretching sheets, accurate constitutive modeling is essential. The four non-Newtonian models considered in this dissertation, Williamson, Casson, tangent hyperbolic and Jeffrey, each capture unique rheological characteristics. In particular, the Williamson model describes shear-thinning behavior typical of pseudoplastic fluids without yield stress, while the Casson model describes a shear-thinning fluid that is considered to have a very high viscosity when no shear is applied, does not flow until a certain yield stress is exceeded, and exhibits negligible viscosity at extremely high shear rates [124]. The tangent hyperbolic fluid model is a pseudoplastic fluid model, characterized by a mathematical formulation that uses the hyperbolic tangent function to describe the relationship between shear stress and shear rate. The Jeffrey fluid model, on the other hand, belongs to the class of rate-type fluid models that account for the effects of relaxation and retardation times. It exhibits linear viscoelastic properties, making it widely applicable in the polymer industry, and is regarded as one of the simplest and most common non-Newtonian models, distinguished by the presence of a time derivative rather than a convective derivative in its constitutive equation [125].

These models alter the structure of the stress tensor in the momentum equations and therefore have a direct impact on the velocity distributions, shear stress, and skin friction coefficients. The application of these models in conjunction with MHD and nanofluid physics provides a more realistic and nuanced view of how advanced fluids behave under simultaneous thermal, mass, and electromagnetic forces.

2.1.1.1 Constitutive Equation of Williamson Fluid Model

The Cauchy stress tensor τ for a Williamson fluid is given as follows.

$$\tau = -PI + \tau_{ij}, \tag{2.1}$$

where P is its normal component, usually called the pressure (which prevents volume shrinking), $\tau_{\mathbf{ij}}$ is the deviatoric extra stress tensor, and $\mathbf{I}$ is the unit tensor.

The constitutive equation for the deviatoric extra stress tensor is given by

$$\tau_{\mathbf{ij}} = \left(\mu_\infty + \frac{\mu_0 - \mu_\infty}{1 - \Gamma\dot{\gamma}}\right)\mathbf{A}_1, \tag{2.2}$$

where μ_0 is limiting viscosity at zero shear rate, and μ_∞ is the limiting viscosity at infinite shear rates, $\Gamma > 0$ is a relaxation time constant, and $\mathbf{A}_1$ is the first Rivlin-Ericksen tensor (rate of strain tensor), and $\dot{\gamma}$ is the shear rate.

The first Rivlin-Ericksen tensor is given by:

$$\mathbf{A}_1 = \nabla\mathbf{V} + (\nabla\mathbf{V})^T, \tag{2.3}$$

with $\nabla\mathbf{V}$ denoting the gradient of the velocity vector (a tensor quantity) and T denoting the transpose operator.

The shear rate is also defined as

$$\dot{\gamma} = \sqrt{\frac{\Pi}{2}}, \tag{2.4}$$

where Π is the second invariant of strain tensor given by

$$\Pi = \frac{1}{2}\,\mathrm{tr}(\mathbf{A}_1^2). \tag{2.5}$$

It is considered the case for pseudo-plastic fluids $\mu_\infty = 0$; thus, Eq. (2.2) reduced to

$$\tau_{\mathbf{ij}} = \left(\frac{\mu_0}{1-\Gamma\dot{\gamma}}\right)\mathbf{A}_1. \tag{2.6}$$

Using the Taylor series expansion of first-order term, Eq. (2.6) can be approximated for $\Gamma\dot{\gamma} < 1$ as follow.

$$\tau_{\mathbf{ij}} \approx \mu_0(1+\Gamma\dot{\gamma})\mathbf{A}_1. \tag{2.7}$$

In three-dimensional Cartesian coordinates (x, y, z), the velocity field is $\mathbf{V}(u, v, w)$ and the velocity gradient tensor is

$$\nabla\mathbf{V} = \begin{bmatrix} \frac{\partial u}{\partial x} & \frac{\partial u}{\partial y} & \frac{\partial u}{\partial z} \\ \frac{\partial v}{\partial x} & \frac{\partial v}{\partial y} & \frac{\partial v}{\partial z} \\ \frac{\partial w}{\partial x} & \frac{\partial w}{\partial y} & \frac{\partial w}{\partial z} \end{bmatrix} \tag{2.8}$$

Then, the component form of the first Rivlin-Ericksen tensor becomes

$$\boldsymbol{A}_1 = \nabla\mathbf{V} + (\nabla\mathbf{V})^T = \begin{bmatrix} 2\frac{\partial u}{\partial x} & \frac{\partial u}{\partial y}+\frac{\partial v}{\partial x} & \frac{\partial u}{\partial z}+\frac{\partial w}{\partial x} \\ \frac{\partial u}{\partial y}+\frac{\partial v}{\partial x} & 2\frac{\partial v}{\partial y} & \frac{\partial v}{\partial z}+\frac{\partial w}{\partial y} \\ \frac{\partial u}{\partial z}+\frac{\partial w}{\partial x} & \frac{\partial v}{\partial z}+\frac{\partial w}{\partial y} & 2\frac{\partial w}{\partial z}. \end{bmatrix} \tag{2.9}$$

Squaring $\mathbf{A}_1$ and taking the sum of the diagonal elements as the trace of $\mathbf{A}_1^2$, computing the trace explicitly as

$$\begin{aligned} \mathrm{tr}(\mathbf{A}_1^2) =& 4\left(\left(\frac{\partial u}{\partial x}\right)^2 + \left(\frac{\partial v}{\partial y}\right)^2 + \left(\frac{\partial w}{\partial z}\right)^2\right) \\ &+ 2\left(\left(\frac{\partial u}{\partial y}+\frac{\partial v}{\partial x}\right)^2 + \left(\frac{\partial u}{\partial z}+\frac{\partial w}{\partial x}\right)^2 + \left(\frac{\partial v}{\partial z}+\frac{\partial w}{\partial y}\right)^2\right). \end{aligned} \tag{2.10}$$

Thus,

$$\Pi = \frac{1}{2}\operatorname{tr}(\boldsymbol{A}_1^2) = 2\left(\left(\frac{\partial u}{\partial x}\right)^2 + \left(\frac{\partial v}{\partial y}\right)^2 + \left(\frac{\partial w}{\partial z}\right)^2\right) + \left(\frac{\partial u}{\partial y} + \frac{\partial v}{\partial x}\right)^2 + \left(\frac{\partial u}{\partial z} + \frac{\partial w}{\partial x}\right)^2 + \left(\frac{\partial v}{\partial z} + \frac{\partial w}{\partial y}\right)^2. \tag{2.11}$$

Consequently, the shear rate can be obtained as follows:

$$\dot{\gamma} = \sqrt{\left(\frac{\partial u}{\partial x}\right)^2 + \left(\frac{\partial v}{\partial y}\right)^2 + \left(\frac{\partial w}{\partial z}\right)^2 + \frac{1}{2}\left[\left(\frac{\partial u}{\partial y} + \frac{\partial v}{\partial x}\right)^2 + \left(\frac{\partial u}{\partial z} + \frac{\partial w}{\partial x}\right)^2 + \left(\frac{\partial v}{\partial z} + \frac{\partial w}{\partial y}\right)^2\right]}. \tag{2.12}$$

The full deviatoric stress tensor can thus be written as

$$\boldsymbol{\tau_{ij}} = \begin{bmatrix} \tau_{xx} & \tau_{xy} & \tau_{xz} \\ \tau_{yx} & \tau_{yy} & \tau_{yz} \\ \tau_{zx} & \tau_{zy} & 2\tau_{zz} \end{bmatrix} = \mu_0(1 + \Gamma\dot{\gamma}) \begin{bmatrix} 2\frac{\partial u}{\partial x} & \frac{\partial u}{\partial y} + \frac{\partial v}{\partial x} & \frac{\partial u}{\partial z} + \frac{\partial w}{\partial x} \\ \frac{\partial u}{\partial y} + \frac{\partial v}{\partial x} & 2\frac{\partial v}{\partial y} & \frac{\partial v}{\partial z} + \frac{\partial w}{\partial y} \\ \frac{\partial u}{\partial z} + \frac{\partial w}{\partial x} & \frac{\partial v}{\partial z} + \frac{\partial w}{\partial y} & 2\frac{\partial w}{\partial z} \end{bmatrix} \tag{2.13}$$

This concludes the three-dimensional tensor formulation of the Williamson fluid model.

2.1.1.2 Constitutive Equation of Casson Fluid Model

The constitutive equation describing the Cauchy stress tensor for a Casson fluid is given by [126]

$$\tau = \tau_0 + \mu\dot{\gamma}, \tag{2.14}$$

where τ is the shear stress, τ_0 is the Casson yield stress, μ is the dynamic viscosity, and $\dot{\gamma}$ is the shear rate. Equivalently,

$$\tau_{ij} = \begin{cases} 2\left(\mu_B + \dfrac{\tau_0}{\sqrt{2\pi}}\right)e_{ij}, & \pi > \pi_c, \\ 2\left(\mu_B + \dfrac{\tau_0}{\sqrt{2\pi_c}}\right)e_{ij}, & \pi \le \pi_c, \end{cases} \tag{2.15}$$

where τ_{ij} is the (i, j)-th component of the stress tensor, τ_0 denotes the yield stress of fluid, $\pi = e_{ij}e_{ij}$ is the product of the components of the deformation rate tensor with itself, e_{ij} is the (i, j)-th component of the deformation rate tensor, π_c denotes a critical value of this product based on the non-Newtonian fluid model, and μ_B is the plastic dynamic viscosity of the non-Newtonian fluid.

The yield stress of the fluid, denoted by τ_0, is given by

$$\tau_0 = \frac{\mu_B\sqrt{2\pi}}{\beta}, \tag{2.16}$$

where β denotes the Casson fluid parameter.

When a shear stress lower than the yield stress is applied to the fluid, it behaves like an elastic solid (plug flow), exhibiting no flow. Once the applied shear stress exceeds the yield stress threshold, the fluid begins to deform and flow. This characteristic behavior is a defining feature of yield stress fluids. Furthermore, certain non-Newtonian fluids, known as rheopectic fluids, require a progressively increasing shear stress to maintain a constant strain rate over time. In the context of Casson fluid flow, particularly when the deformation rate parameter π exceeds its critical value π_c (i.e., when $\pi > \pi_c$), the effective viscosity can be expressed as

$$\mu = \mu_B + \frac{\tau_0}{\sqrt{2\pi}}. \tag{2.17}$$

By utilizing Eq. (2.16) and (2.17), the kinematic viscosity of the Casson fluid can be expressed as

$$\upsilon = \frac{\mu}{\rho} = \frac{\mu_B + \frac{\tau_0}{\sqrt{2\pi}}}{\rho} = \frac{\mu_B}{\rho}\left(1 + \frac{1}{\beta}\right), \tag{2.18}$$

where υ is the kinematic viscosity, ρ is the fluid density, and β is a parameter related to the Casson fluid behavior.

The Casson parameter can also be derived from Eq. (2.16) and is defined by

$$\beta = \frac{\mu_B\sqrt{2\Pi}}{\tau_0}. \tag{2.19}$$

In the limit as $\beta \to \infty$ (i.e., $\tau_0 \to 0$), the Casson model reduces to the Newtonian form with constant viscosity.

So, a Casson fluid is a type of non-Newtonian, shear-thinning liquid that exhibits infinite viscosity at zero shear rate, possesses a finite yield stress below which no deformation occurs, and approaches zero viscosity as the shear rate tends toward infinity.

Furthermore, the components of the shear stress tensor in the Casson fluid model are expressed as follows, where the three-dimensional rate of deformation tensor $\boldsymbol{e_{ij}}$ is defined as

$$e_{ij} = \frac{1}{2}\left(\frac{\partial u_i}{\partial x_j} + \frac{\partial u_j}{\partial x_i}\right). \tag{2.20}$$

Explicitly in Cartesian coordinates (x, y, z):

$$\boldsymbol{e_{ij}} = \begin{bmatrix} \frac{\partial u}{\partial x} & \frac{1}{2}\left(\frac{\partial u}{\partial y} + \frac{\partial v}{\partial x}\right) & \frac{1}{2}\left(\frac{\partial u}{\partial z} + \frac{\partial w}{\partial x}\right) \\ \frac{1}{2}\left(\frac{\partial v}{\partial x} + \frac{\partial u}{\partial y}\right) & \frac{\partial v}{\partial y} & \frac{1}{2}\left(\frac{\partial v}{\partial z} + \frac{\partial w}{\partial y}\right) \\ \frac{1}{2}\left(\frac{\partial w}{\partial x} + \frac{\partial u}{\partial z}\right) & \frac{1}{2}\left(\frac{\partial w}{\partial y} + \frac{\partial v}{\partial z}\right) & \frac{\partial w}{\partial z} \end{bmatrix} \tag{2.21}$$

The stress tensor for Casson fluid has two regimes.

- Yielded Regime ($\pi > \pi_c$)

$$\tau_{ij} = 2\left(\mu_B + \frac{\tau_0}{\sqrt{2\pi}}\right)e_{ij}. \tag{2.22}$$

- Unyielding Regime ($\pi \leq \pi_c$)

$$\tau_{ij} = 2\left(\mu_B + \frac{\tau_0}{\sqrt{2\pi_c}}\right)e_{ij}. \tag{2.23}$$

The complete stress tensor components in 3D are

$$\begin{cases} \tau_{xx} = 2\left(\mu_B + \frac{\tau_0}{\sqrt{2\Pi}}\right)\frac{\partial u}{\partial x}, \ \ \tau_{yy} = 2\left(\mu_B + \frac{\tau_0}{\sqrt{2\Pi}}\right)\frac{\partial v}{\partial y}, \\ \tau_{zz} = 2\left(\mu_B + \frac{\tau_0}{\sqrt{2\Pi}}\right)\frac{\partial w}{\partial z}, \ \ \tau_{xy} = \tau_{yx} = \left(\mu_B + \frac{\tau_0}{\sqrt{2\Pi}}\right)\left(\frac{\partial u}{\partial y} + \frac{\partial v}{\partial x}\right), \\ \tau_{xz} = \tau_{zx} = \left(\mu_B + \frac{\tau_0}{\sqrt{2\Pi}}\right)\left(\frac{\partial u}{\partial z} + \frac{\partial w}{\partial x}\right), \ \ \tau_{yz} = \tau_{zy} = \left(\mu_B + \frac{\tau_0}{\sqrt{2\Pi}}\right)\left(\frac{\partial v}{\partial z} + \frac{\partial w}{\partial y}\right). \end{cases} \tag{2.24}$$

Finally, the stress tensor components in Eq. (2.24) can be rewritten as follows.

$$\begin{cases} \tau_{xx} = 2\mu_B\left(1 + \frac{1}{\beta}\right)\frac{\partial u}{\partial x}, \ \ \tau_{yy} = 2\mu_B\left(1 + \frac{1}{\beta}\right)\frac{\partial v}{\partial y}, \ \ \tau_{zz} = 2\mu_B\left(1 + \frac{1}{\beta}\right)\frac{\partial w}{\partial z}, \\ \tau_{xy} = \tau_{yx} = \mu_B\left(1 + \frac{1}{\beta}\right)\left(\frac{\partial u}{\partial y} + \frac{\partial v}{\partial x}\right), \\ \tau_{yz} = \tau_{zy} = \mu_B\left(1 + \frac{1}{\beta}\right)\left(\frac{\partial v}{\partial z} + \frac{\partial w}{\partial y}\right), \\ \tau_{xz} = \tau_{zx} = \mu_B\left(1 + \frac{1}{\beta}\right)\left(\frac{\partial u}{\partial z} + \frac{\partial w}{\partial x}\right). \end{cases} \tag{2.25}$$

2.1.1.3 Constitutive Equation of Tangent Hyperbolic Fluid

The rheological equation of Tangent hyperbolic fluid can be written as [7]

$$\tau_{ij} = [\mu_\infty + (\mu_0 + \mu_\infty)\, tanh(\Gamma\dot{\gamma})^n]\, \mathbf{A}_1, \tag{2.26}$$

where Γ is the time constant, n is the power law index, τ_{ij} = is extra stress tensor, μ_0 zero shear rate viscosity, μ_∞ =infinite shear rate viscosity and $\mathbf{A}_1$ is the first Rivlin-Ericksen tensor. Also, $\dot{\gamma}$ is described as

$$\dot{\gamma} = \sqrt{\frac{1}{2}\sum_i \sum_j \dot{\gamma}_{ij}\dot{\gamma}_{ji}} = \sqrt{\frac{1}{2}\Pi}, \tag{2.27}$$

where Π is the second invariant of the strain rate tensor and is given by

$$\Pi = \frac{1}{2}\mathrm{tr}({A_1}^2) = \frac{1}{2}\mathrm{tr}\left(\nabla\mathbf{V} + (\nabla\mathbf{V})^T\right)^2. \tag{2.28}$$

Since the analysis at infinite shear rate viscosity is not feasible, we adopt assumption $\mu_\infty = 0$, which is appropriate with our focus on shear-thinning behavior and then Eq. (2.26) is reduced to

$$\tau_{ij} = [\mu_0 tanh(\Gamma\dot{\gamma})^n]\, \mathbf{A}_1. \tag{2.29}$$

We consider the case where $\Gamma\dot{\gamma} < 1$, in which the hyperbolic tangent function can be expanded as

$$\tanh(\Gamma\dot{\gamma}) = \Gamma\dot{\gamma} - \frac{(\Gamma\dot{\gamma})^3}{3} + \frac{2(\Gamma\dot{\gamma})^5}{15} - \frac{17(\Gamma\dot{\gamma})^7}{315} + \frac{62(\Gamma\dot{\gamma})^9}{2835} - \cdots \tag{2.30}$$

Taking the first-order term of the tangent hyperbolic function series expansion, Eq. (2.29) can be approximated for $\Gamma\dot{\gamma} < 1$ as follows.

$$\tau_{ij} = \mu_0\, [(\Gamma\dot{\gamma})^n]\, \mathbf{A}_1. \tag{2.31}$$

Rewriting Eq. (2.31), and based on the tangent line approximation the stress tensor τ_{ij} will be reduced to:

$$\tau_{ij} = \mu_0[(\Gamma\dot{\gamma})^n]\dot{A}_1 = \mu_0[(1 + \Gamma\dot{\gamma} - 1)^n]\dot{A}_1 \approx \mu_0\, [1 + n(\Gamma\dot{\gamma} - 1)]\, \mathbf{A}_1. \tag{2.32}$$

Finally, we have

$$\tau_{ij} = \mu_0\, [1 + n(\Gamma\dot{\gamma} - 1)]\, \mathbf{A}_1. \tag{2.33}$$

In three-dimensional Cartesian coordinates (x, y, z), the stress tensor is

$$\boldsymbol{\tau_{ij}} = \begin{bmatrix} \tau_{xx} & \tau_{xy} & \tau_{xz} \\ \tau_{yx} & \tau_{yy} & \tau_{yz} \\ \tau_{zx} & \tau_{zy} & 2\tau_{zz} \end{bmatrix} = \mu_0 \left[1 + n(\Gamma\dot{\gamma} - 1)\right] \begin{bmatrix} 2\frac{\partial u}{\partial x} & \frac{\partial u}{\partial y} + \frac{\partial v}{\partial x} & \frac{\partial u}{\partial z} + \frac{\partial w}{\partial x} \\ \frac{\partial u}{\partial y} + \frac{\partial v}{\partial x} & 2\frac{\partial v}{\partial y} & \frac{\partial v}{\partial z} + \frac{\partial w}{\partial y} \\ \frac{\partial u}{\partial z} + \frac{\partial w}{\partial x} & \frac{\partial v}{\partial z} + \frac{\partial w}{\partial y} & 2\frac{\partial w}{\partial z} \end{bmatrix} \tag{2.34}$$

This non-Newtonian model, tangent hyperbolic fluid, will be reduced to the Newtonian whenever $\Gamma = 0$ and $n = 0$.

2.1.1.4 Constitutive Equations of the Jeffrey Fluid Model

The Cauchy stress tensor τ for a Jeffrey fluid is given by

$$\tau = -P\mathbf{I} + \tau_{ij}, \tag{2.35}$$

where P is the pressure (preventing volume shrinkage), τ_{ij} is the deviatoric extra stress tensor, and $\mathbf{I}$ is the unit tensor.

The constitutive equation for the deviatoric extra stress tensor is written as [127]

$$\tau_{ij} = \frac{\mu}{1 + \lambda_1}\left(\mathbf{A}_1 + \lambda_2 \frac{d\mathbf{A}_1}{dt}\right), \tag{2.36}$$

where μ is the dynamic viscosity, λ_1 is the ratio of relaxation to retardation times, λ_2 is the retardation time, $\mathbf{A}_1$ is the first Rivlin–Ericksen tensor defined in Eq. (2.3), and $\frac{d}{dt}$ denotes the material derivative. For steady flow, the material derivative reduces to the convective derivative

$$\frac{d}{dt} = \mathbf{V} \cdot \nabla = u\frac{\partial}{\partial x} + v\frac{\partial}{\partial y} + w\frac{\partial}{\partial z}. \tag{2.37}$$

In three-dimensional Cartesian coordinates (x, y, z), the velocity field is $\mathbf{V} = (u, v, w)$, and $\mathbf{A}_1$ has the component form as (defined in Eq. (2.9))

$$\mathbf{A}_1 = \begin{bmatrix} 2\frac{\partial u}{\partial x} & \frac{\partial u}{\partial y} + \frac{\partial v}{\partial x} & \frac{\partial u}{\partial z} + \frac{\partial w}{\partial x} \\ \frac{\partial v}{\partial x} + \frac{\partial u}{\partial y} & 2\frac{\partial v}{\partial y} & \frac{\partial v}{\partial z} + \frac{\partial w}{\partial y} \\ \frac{\partial w}{\partial x} + \frac{\partial u}{\partial z} & \frac{\partial w}{\partial y} + \frac{\partial v}{\partial z} & 2\frac{\partial w}{\partial z} \end{bmatrix}. \tag{2.38}$$

Applying Eq. (2.36) to each component of $\mathbf{A}_1$ for steady flow yields

$$
\begin{cases}
\tau_{xx} = \dfrac{\mu}{1+\lambda_1}\left[2\dfrac{\partial u}{\partial x} + \lambda_2\left(u\dfrac{\partial}{\partial x}\left(2\dfrac{\partial u}{\partial x}\right) + v\dfrac{\partial}{\partial y}\left(2\dfrac{\partial u}{\partial x}\right) + w\dfrac{\partial}{\partial z}\left(2\dfrac{\partial u}{\partial x}\right)\right)\right], \\
\tau_{yy} = \dfrac{\mu}{1+\lambda_1}\left[2\dfrac{\partial v}{\partial y} + \lambda_2\left(u\dfrac{\partial}{\partial x}\left(2\dfrac{\partial v}{\partial y}\right) + v\dfrac{\partial}{\partial y}\left(2\dfrac{\partial v}{\partial y}\right) + w\dfrac{\partial}{\partial z}\left(2\dfrac{\partial v}{\partial y}\right)\right)\right], \\
\tau_{zz} = \dfrac{\mu}{1+\lambda_1}\left[2\dfrac{\partial w}{\partial z} + \lambda_2\left(u\dfrac{\partial}{\partial x}\left(2\dfrac{\partial w}{\partial z}\right) + v\dfrac{\partial}{\partial y}\left(2\dfrac{\partial w}{\partial z}\right) + w\dfrac{\partial}{\partial z}\left(2\dfrac{\partial w}{\partial z}\right)\right)\right], \\
\tau_{xy} = \tau_{yx} = \dfrac{\mu}{1+\lambda_1}\left[\dfrac{\partial u}{\partial y} + \dfrac{\partial v}{\partial x} + \lambda_2\left(u\dfrac{\partial}{\partial x}\left(\dfrac{\partial u}{\partial y} + \dfrac{\partial v}{\partial x}\right) + v\dfrac{\partial}{\partial y}\left(\dfrac{\partial u}{\partial y} + \dfrac{\partial v}{\partial x}\right)\right.\right. \\
\qquad\qquad \left.\left. + w\dfrac{\partial}{\partial z}\left(\dfrac{\partial u}{\partial y} + \dfrac{\partial v}{\partial x}\right)\right)\right], \\
\tau_{yz} = \tau_{zy} = \dfrac{\mu}{1+\lambda_1}\left[\dfrac{\partial v}{\partial z} + \dfrac{\partial w}{\partial y} + \lambda_2\left(u\dfrac{\partial}{\partial x}\left(\dfrac{\partial v}{\partial z} + \dfrac{\partial w}{\partial y}\right) + v\dfrac{\partial}{\partial y}\left(\dfrac{\partial v}{\partial z} + \dfrac{\partial w}{\partial y}\right)\right.\right. \\
\qquad\qquad \left.\left. + w\dfrac{\partial}{\partial z}\left(\dfrac{\partial v}{\partial z} + \dfrac{\partial w}{\partial y}\right)\right)\right], \\
\tau_{xz} = \tau_{zx} = \dfrac{\mu}{1+\lambda_1}\left[\dfrac{\partial u}{\partial z} + \dfrac{\partial w}{\partial x} + \lambda_2\left(u\dfrac{\partial}{\partial x}\left(\dfrac{\partial u}{\partial z} + \dfrac{\partial w}{\partial x}\right) + v\dfrac{\partial}{\partial y}\left(\dfrac{\partial u}{\partial z} + \dfrac{\partial w}{\partial x}\right)\right.\right. \\
\qquad\qquad \left.\left. + w\dfrac{\partial}{\partial z}\left(\dfrac{\partial u}{\partial z} + \dfrac{\partial w}{\partial x}\right)\right)\right].
\end{cases}
\tag{2.39}
$$

The full deviatoric stress tensor is therefore

$$
\tau_{ij} = \begin{bmatrix} \tau_{xx} & \tau_{xy} & \tau_{xz} \\ \tau_{yx} & \tau_{yy} & \tau_{yz} \\ \tau_{zx} & \tau_{zy} & \tau_{zz} \end{bmatrix}. \tag{2.40}
$$

This concludes the three-dimensional tensor formulation of the Jeffrey fluid model.

2.1.2 Magnetohydrodynamics

MHD concerns the behavior of electrically conducting fluids such as plasmas, liquid metals, and nanofluids in the presence of magnetic fields. In MHD, the fluid motion and magnetic field are dynamically coupled through the Lorentz force, which arises due to the interaction between the fluid's electric current and the magnetic field. The governing equations of MHD combine the principles of fluid dynamics with Maxwell's equations of electromagnetism. These include the modified Navier-Stokes equations incorporating electromagnetic body forces and the magnetic induction equation, which describes how the magnetic field evolves with fluid motion. The Lorentz force, denoted as $\mathbf{J} \times \mathbf{B}$, where $\mathbf{J}$ is the current density and $\mathbf{B}$ is the magnetic field, acts as a resistance to fluid motion and is particularly significant in high-conductivity fluids.

Ohm's law provides the starting point for describing the current density in a moving conducting fluid.

$$j = \sigma E', \tag{2.41}$$

where σ is electric conductivity and E' is the electric field experienced by the fluid element in its rest frame. When the plasma is moving with respect to the external magnetic field at the velocity V, applying the Lorentz transformation, we obtain the equation:

$$E' = E + V \times B. \tag{2.42}$$

Substituting into Eq. (2.41) yields:

$$\frac{1}{\sigma} j = E + V \times B. \tag{2.43}$$

For the ideal MHD case of perfect conductivity ($\sigma \to \infty$), this simplifies to:

$$E = -V \times B. \tag{2.44}$$

Taking the curl of the electric field in Eq. (2.44) and applying Faraday's law:

$$\nabla \times E = -\frac{\partial B}{\partial t}, \tag{2.45}$$

We derive the magnetic induction equation:

$$\frac{\partial B}{\partial t} = \nabla \times (V \times B). \tag{2.46}$$

The current density **j** can be related to the magnetic field through Ampère's law:

$$\nabla \times B = \mu_0 j + \frac{1}{c^2}\frac{\partial E}{\partial t}. \tag{2.47}$$

From Ohm's law, we had $E = V \times B$. Consequently, we can estimate the electric field as $E \sim V_0 B$, where V_0 is a characteristic speed of the process. Neglecting $\frac{\partial E}{\partial t}$ term in Eq. (2.47):

$$\nabla \times B = \mu_0 j, \tag{2.48}$$

or

$$j = \frac{1}{\mu_0}(\nabla \times B). \tag{2.49}$$

In addition, the magnetic field B must satisfy the condition $\nabla . B$. Thus, the closed set of MHD equations is as follows.

$$\frac{\partial B}{\partial t} = \nabla \times (V \times B)\,, \tag{2.50}$$

is the equation for magnetic induction. Finally, in the momentum equation, electromagnetic force F is expressed as follows.

$$F = J \times B = \sigma(E \times B) \times B \tag{2.51}$$

In the scope of this dissertation, MHD is crucial to analyze nanofluid flows over stretching sheets under the influence of strong magnetic fields. Hall current and ion slip, which become significant at low densities or high magnetic field intensities, modify the classical Ohm's law and introduce cross-flow currents. These additional currents influence the secondary velocity field. The extended MHD model used in these analyses incorporates modified expressions for current density and additional terms in the momentum and energy equations to fully capture the impact of electromagnetic interactions on heat and mass transfer behaviors in non-Newtonian nanofluids.

2.2 Heat and Mass Transfer

In many real-world engineering and industrial processes, there are often substantial temperature and concentration gradients between the surface of a heated body and the surrounding fluid stream [128]. The phenomena of heat and mass transfer resulting from these gradients are essential to the design and operation of many thermal systems. Consequently, the study of heat and mass transport has become crucial for numerous engineering applications, including thermal management of electronic components, heat exchangers, solar energy collectors, and nuclear reactor cooling systems. Moreover, electrically conducting fluids under the influence of convective forces and chemical reactions and interaction between heat and mass transfer in non-Newtonian fluids have also been the focus of numerous studies. These flows are of particular importance in applications such as plasma engineering, liquid metal cooling in nuclear systems, and other processes involving electromagnetic fields [129, 130].

2.2.1 Heat Transfer

In thermodynamics, heat transfer refers to the transmission of thermal energy from a region of higher temperature to a region of lower temperature [131]. This process occurs naturally when an object or fluid is at a different temperature than its surroundings or another body. Heat continues to flow until thermal equilibrium is achieved, that is, when both bodies reach the same temperature. According to the second law of thermodynamics, "heat transfer cannot be completely stopped when a temperature difference exists; it can only be reduced." This principle emphasizes that heat, or the movement of energy caused by a temperature difference, always happens spontaneously from hot to cold. The study of heat transfer involves understanding the rate at which this energy exchange occurs, which is fundamental to the design of thermal systems in mechanical, chemical, and environmental engineering.

There are three modes of heat transfer: conduction, convection, and radiation. All three modes require a temperature difference and involve the movement of thermal energy from a higher to a lower temperature region. However, each mode is governed by distinct physical mechanisms and laws.

2.2.1.1 Conduction

Conduction is the transfer of heat through a solid or stationary fluid as a result of a temperature gradient. According to Fourier's law, the rate of heat transfer q_y through a material is proportional to the negative temperature gradient and the thermal conductivity k of the material [132].

$$q_y = -kA\frac{\partial T}{\partial y}, \tag{2.52}$$

where q_y is the heat-transfer rate and $\frac{\partial T}{\partial y}$ is the temperature gradient in the direction of heat flow. The constant k is the thermal conductivity of the material, and the negative sign ensures that the heat flows from higher to lower temperatures. Thus, the local heat flux per unit area, q'', is given by:

$$q'' = -k\frac{\partial T}{\partial y}\bigg]_{\text{wall}}. \tag{2.53}$$

Conduction examples include heat transferred from a hot iron to clothes during ironing, melting of an ice cube in one's hand due to body heat, and the sensation of hot sand on beaches due to heat conducted from the surface.

Thermal diffusivity is another important property in heat conduction analysis, defined as follows.

$$\alpha = \frac{k}{\rho C_p} \tag{2.54}$$

where k represents thermal conductivity, ρ is density, and C_p is the is specific heat capacity. Thermal diffusivity quantifies the speed with which heat diffuses through a material. A high thermal diffusivity indicates rapid heat propagation, whereas a low value suggests that heat is primarily absorbed rather than conducted.

2.2.1.2 Convection

Convection involves the transfer of heat between a solid surface and a moving fluid or within the fluids themselves. It includes both forced convection, where external forces like fans or pumps move the fluid, and natural convection, driven by density differences due to temperature gradients [133]. The rate of convective heat transfer is described by Newton's law of cooling [134].

$$q'' = h(T_w - T_\infty), \tag{2.55}$$

where q is the heat-transfer rate, h is the convection heat-transfer coefficient and T_w and T_∞ are the wall and fluid temperatures respectively. Examples of convection include the boiling of water, where warmer, less dense molecules rise and cooler ones sink, creating a circular motion; ocean currents moving warm water from the equator to the poles; and blood circulation in warm-blooded animals that helps regulate body temperature.

2.2.1.3 Radiation

Unlike conduction and convection, radiation does not require a medium for energy transfer. Radiation is the energy emitted by matter in the form of electromagnetic waves due to changes in the electronic configurations of atoms or molecules. All matter above absolute zero emits thermal radiation in the form of electromagnetic waves owing to molecular and atomic activity. The Stefan-Boltzmann law quantifies the power radiated by a blackbody. Thus, the radiative heat flux is given by [135, 136]

$$q_r = -\frac{4\sigma^*}{3k^*}\frac{\partial T^4}{\partial y}, \tag{2.56}$$

where σ^* is the Stefan-Boltzmann constant and k^* is mean absorption coefficient. This relationship underscores the unique nature of radiation as a mode of heat transfer, independent of physical contact.

If the difference between the fluid temperature T and the ambient temperature T_∞ is very small, then the term T^4 in Eq. (2.56) can be linearized using a Taylor series expansion about T_∞ by neglecting the third and higher-order terms as follows.

$$\begin{aligned} T^4 &= T_\infty^4 + \frac{4T_\infty^3}{1!}(T - T_\infty) + \frac{12T_\infty^2}{2!}(T - T_\infty)^2 + \frac{24T_\infty}{3!}(T - T_\infty)^3 + \frac{24}{4!}(T - T_\infty)^4 + \cdots \\ &\approx T_\infty^4 + 4T_\infty^3(T - T_\infty) = 4T_\infty^3 T - 3T_\infty^4 \end{aligned} \tag{2.57}$$

and becomes:

$$\frac{\partial T^4}{\partial y} = \frac{\partial}{\partial y}\left(4T_\infty^3 T - 3T_\infty^4\right) = 4T_\infty^3 \frac{\partial T}{\partial y}. \tag{2.58}$$

Numerous studies have been conducted to explore the impact of thermal radiation by utilizing the linearized form of the Rosseland flow. However, it is important to note that the linearized version of the Rosseland assumption is only suitable for cases involving small temperature differences [136]. Consequently, when dealing with higher temperature differences, the linear radiation approach becomes inadequate. In such instances, it is more appropriate to employ nonlinear Rosseland diffusion, which remains valid for both small and significant temperature disparities between the surface and the surrounding fluid. Using the nonlinear Rosseland diffusion approximation, the radiative heat flux q_r can be written as follows [2].

$$q_r = -\frac{4\sigma^*}{3k^*}\frac{\partial T^4}{\partial y} = -\frac{16\sigma^*}{3k^*}T^3\frac{\partial T}{\partial y}, \tag{2.59}$$

This dissertation considers the effects of nonlinear thermal radiation throughout all of the investigations.

2.2.2 Mass Transfer

Mass transfer refers to the movement of particles from one region to another because of a concentration gradient within a system comprising one or more components. This transport arises naturally, driven by the tendency of molecules to move from areas of higher concentration to those of lower concentration in an effort to achieve equilibrium [137]. As long as a concentration difference exists in a system, mass transfer will continue to occur. It is a fundamental phenomenon in various engineering and natural processes. Examples of industrially important mass transfer processes include liquid ammonia evaporation in hydrogen-filled Electrolux refrigerators, air humidification in cooling towers, and the removal of environmental pollutants through absorption. Other notable instances are the diffusion of neutrons in nuclear reactors, carburizing processes in steel treatment, and evaporation in internal combustion engine carburetors.

In daily life, mass transfer is equally prevalent and observable [138]. Common examples include the dissolution of sugar added to a cup of coffee, the diffusion of smoke through tall chimneys, and the evaporation of water or other liquids into the surrounding air. Perfumes diffusing into the ambient space to create a pleasant fragrance and the separation of components in mixtures via distillation or absorption are also mass transfer-driven processes. These examples reinforce the omnipresence and significance of mass transfer in both engineered and natural systems. Understanding its mechanisms is essential for designing efficient systems for chemical, environmental, and mechanical engineering applications.

The mechanism of mass transfer is influenced by the dynamics of the system and can occur in three primary modes: diffusion, convection, and phase change [139, 140]. In mass transfer by diffusion, particles move on a microscopic scale from high to low concentration within a stagnant fluid medium. This can occur due to gradients in concentration, pressure, or temperature. In gases, molecular diffusion results from random molecular motion. When the fluid is turbulent, eddy diffusion dominates, enhancing the rate of mass transfer, as observed in the rapid dissipation of smoke from chimneys. Convective mass transfer, on the other hand, occurs between moving fluids and surfaces or between two immiscible moving fluids. This type depends heavily on the fluid flow characteristics (laminar or turbulent) and is evident in the evaporation of volatile substances like ether [128]. Lastly, mass transfer by change of phase involves phase transitions, such as the transition from liquid to vapor, and is governed by both diffusion and convection. Classic examples include boiling, evaporation from water bodies, and the rise of hot gases that diffuse into the atmosphere.

The theoretical framework for understanding diffusion processes is provided by Fick's Law of Diffusion. When the composition of a mixture varies spatially, a concentration gradient is established that drives diffusion. Fick's first law relates the diffusional mass flux of a species to the gradient of its concentration. It is mathematically expressed as:

$$\vec{j_i} = -\rho D_{im} \nabla m_i, \tag{2.60}$$

where $\vec{j_i}$ is the mass flux, ρ is the fluid density, D_{im} is the diffusion coefficient, and ∇m_i is the gradient of the mass fraction. In one-dimensional flow, this simplifies to:

$$J_A = -D_{AB}\frac{dC_A}{dz}, \tag{2.61}$$

where D_{AB} is the diffusivity of species A in species B, and $\frac{dC_A}{dz}$ is the concentration gradient in the z-direction. This law is analogous to Fourier's law in heat transfer and is essential in predicting diffusion rates in both simple and complex systems.

2.2.3 Coupled Heat and Mass Transfer

In scientific research and diverse engineering domains, such as condensation, evaporation, and chemical processing, transport mechanisms are frequently influenced by the combined effects of buoyancy forces resulting from both thermal and mass diffusion. The coupled behavior of heat and mass transfer has been widely studied due to its vital role in various applications, including chemical processing equipment, ocean circulation, emergency cooling systems in advanced nuclear reactors, plastic sheet cooling, fog formation and dissipation, food processing and dehydration, temperature and moisture control in agricultural fields, and polymer production [141]. In many fluid flow problems, especially in the study of nanofluids and non-Newtonian fluids, heat and mass transfer processes are inherently coupled [142]. This coupling refers to the simultaneous transfer of heat and mass in a system, where the movement of fluid due to thermal gradients influences the concentration distribution and vice versa. In such systems, heat transfer and mass transfer mechanisms cannot be considered independently, as velocity profiles, temperature, and concentration fields all interact and affect one another. The coupling becomes particularly significant in MHD flows, where external magnetic fields further complicate the interaction between these phenomena.

For example, when nanoparticles are suspended in a base fluid, their thermal conductivity generally enhances heat transfer. However, the concentration of these nanoparticles in the fluid also influences mass transfer, as they may adsorb or react with chemical species in the fluid. Furthermore, in the presence of external forces, such as the Lorentz force, which is induced by an external magnetic field, both temperature and concentration gradients are modified, thereby affecting the overall heat and mass transfer characteristics. In MHD flows, this interplay is further influenced by ion slip effects, Hall currents, and other physical phenomena, which can either enhance or suppress the transfer processes depending on the specific parameters of the system.

Mathematically, coupled heat and mass transfer is described by a set of partial differential equations that govern the temperature and concentration fields, which are typically solved simultaneously. The energy equation governs heat transfer, while the concentration equation governs mass transfer. In the presence of a magnetic field, these equations also account for the effects of the electromagnetic field, which modifies both the temperature and concentration profiles. Coupled heat and mass transfer also plays a vital role in various engineering applications, including heat exchangers, cooling systems, and chemical reactors. In these systems, efficient heat and mass transfer is crucial to ensuring optimal performance. The understanding of how these processes are coupled, especially in non-Newtonian fluids and nanofluid systems, is essential for designing systems that maximize heat and mass transfer while minimizing energy losses. The study of these coupled effects also helps in the development of advanced materials and fluid systems with enhanced thermal and mass transport properties, making it an important area of research in both fundamental and applied fluid dynamics.

2.2.4 Brownian Diffusion and Thermophoresis

In the study of nanofluids, the inclusion of nanoparticles significantly alters the behavior of heat and mass transport within the fluid medium. Among the various mechanisms responsible for this altered behavior, Brownian diffusion and thermophoresis are considered to be particularly influential. These mechanisms are essential in understanding the enhanced mass and heat transfer characteristics of nanofluids, particularly in the context of magnetohydrodynamic (MHD) non-Newtonian flows over stretching surfaces. One of the most prominent contributions in this area came from Buongiorno [43] in 2006, who proposed a comprehensive slip model identifying seven critical slip mechanisms: inertia, Brownian diffusion, thermophoresis, diffusiophoresis, the Magnus effect, fluid drainage, and gravity settling. After rigorous examination, it was concluded that Brownian motion and thermophoretic diffusion are the dominant phenomena responsible for the abnormal increase in thermal dispersion and convective heat transfer in nanofluids. These mechanisms originate from the relative slip between the nanoparticles and the base fluid, resulting in increased thermal conductivity and altered mass transport dynamics.

Brownian diffusion is the random, thermally induced movement of nanoparticles suspended in a fluid, driven by collisions with surrounding molecules. This movement facilitates the transport of nanoparticles from regions of higher concentration to regions of lower concentration, promoting uniform particle distribution. The extent of Brownian diffusion is quantified using the dimensionless Brownian motion parameter N_b, defined as follows.

$$N_b = \frac{\Lambda D_B (C_w - C_\infty)}{\upsilon}, \tag{2.62}$$

where $\Lambda = \frac{(\rho C_p)_p}{(\rho C_p)_f}$ is the ratio of effective heat capacities of the nanoparticle to the base fluid, D_B is the Brownian diffusion coefficient, C_w is the nanoparticle concentration near the surface, C_∞ is the ambient concentration, and υ is the kinematic viscosity of the nanofluid. A higher value of the Brownian motion parameter N_b intensifies the chaotic motion of nanoparticles, which improves their kinetic energy and leads to reduced viscosity in the flow region. Numerous theoretical and experimental investigations have demonstrated that increasing N_b promotes nanoparticle dispersion, thereby affecting both mass and thermal transport processes.

Thermophoresis is a phenomenon in which nanoparticles are transported from regions of higher temperature to lower temperature. This movement is driven by the thermophoretic force, which acts opposite to the temperature gradient, causing the particles to be repelled from the hot surface and attracted toward cooler regions. This mechanism is particularly relevant in applications involving aerosol technology, silicon thin film deposition, and nuclear reactor safety simulations. The thermophoresis parameter N_t, characterizes this effect and is given by the following mathematical formula.

$$N_t = \frac{\tau D_T (T_w - T_\infty)}{\upsilon T_\infty}, \tag{2.63}$$

where D_T is the thermophoretic diffusion coefficient, T_w is the surface temperature, and T_∞ denotes the ambient fluid temperature. An increased value of the thermophoresis parameter N_t implies stronger thermophoretic forces, leading to greater displacement of nanoparticles from the hot surface to the colder ambient environment.

The combined effects of Brownian diffusion and thermophoresis have significant implications in the mass transfer behavior of nanofluids. While Brownian motion aids in enhancing mixing and reducing concentration gradients, thermophoresis modifies the distribution of nanoparticles in response to thermal gradients, often resulting in enhanced temperature and concentration profiles near boundary layers. In particular, an increase in N_t may also impose resistance to the natural diffusion of mass, indicating a complex interplay between the mechanisms of heat and mass transport. Sheremet et al. [143] have simulated the transport of nanofluids inside the cavity using the two-phase nanofluid model, which incorporates Brownian diffusion and thermophoresis effects. Ullah et al. [144] examined how thermophoresis and Brownian diffusion affect the electrically conducting mixed convection flow of the Casson fluid caused by a moving wedge. Khan et al. [145] found that the temperature field increases with higher values of thermophoresis and Brownian motion parameters, while the mass concentration rises with increasing thermophoresis parameter but decreases with a larger Brownian motion parameter. By combining Brownian motion and thermophoretic diffusion, Waqas et al. [146] examined the behavior of nanofluids and found that a higher Brownian motion parameter improves the temperature profile while decreasing the volumetric concentration profile. Numerous researchers [147–149] investigated Brownian motion and thermophoresis in different scenarios.

In boundary layer studies involving nanofluid flows, such as those presented in the current dissertation, the roles of the inclusion of N_b and N_t in the governing equations ensure a more accurate representation of the physical processes and offer a deeper insight into the behavior of non-Newtonian nanofluids under MHD effects with Hall and ion slip phenomena.

2.3 Boundary Layer Flow and Some Prominent Dimensionless Prameters

2.3.1 The Concept of Boundary Layer Theory

The boundary layer theory was first introduced by Ludwig Prandtl in 1904, revolutionizing the analysis of viscous flows by demonstrating that the effects of viscosity are significant only within a thin layer adjacent to the surface, whereas their influence diminishes far from the surface. This thin layer is known as the boundary layer. Within this boundary layer, three distinct regions are recognized: the momentum (hydrodynamic) boundary layer, the thermal boundary layer, and the concentration (species) boundary layer.

The momentum boundary layer deals with the variation of the fluid velocity from zero at the surface (due to the no-slip condition) to the free-stream velocity away from the wall. The wall shear stress, denoted by τ_w, quantifies the tangential force exerted by the fluid on the surface. The thickness of the momentum boundary layer is determined by the balance between inertial forces and viscous forces in the fluid. In typical scenarios, the boundary layer is very thin near the surface and thickens as the distance from the leading edge of the surface increases. A sharp velocity gradient exists near the wall and the nature of this gradient, laminar or turbulent, significantly affects heat and mass transfer characteristics. Boundary layers can be either laminar, exhibiting smooth, orderly flow with momentum exchange occurring only at a microscopic level (governed by molecular viscosity μ) at low Reynolds numbers, or turbulent, marked by chaotic eddies and large-scale mixing of mass, momentum, and energy at higher Reynolds numbers, where molecular viscosity alone cannot account for the flow dynamics.

The thermal boundary layer represents the region of the fluid adjacent to the surface where the temperature gradient is most pronounced. Within this layer, heat transfer occurs due to the interaction between the surface and the fluid, influenced by the thermal conductivity and the heat transfer mechanisms within the fluid. As the fluid moves away from the surface, the temperature gradually approaches the free-stream temperature. The thickness of the thermal boundary layer depends on various factors, including thermal conductivity of the fluid, flow conditions, and any external influences, such as temperature gradients, magnetic fields, and heat generation or absorption.

Similarly, the concentration boundary layer refers to the thin region near a surface where the concentration of a specific species, such as nanoparticles, solutes, or chemicals, changes significantly from zero (or a reference concentration) at the surface to the ambient concentration in the freestream. This layer is critical in processes involving mass transfer, such as chemical reactions, diffusion, and biological transport. In the concentration boundary layer, the rate of mass transfer is influenced by various factors, including molecular diffusion, convection, and the presence of external forces such as magnetic fields or chemical reactions.

The simultaneous occurrence of velocity, temperature, and concentration gradients near the surface requires an analysis that accounts for the coupling of momentum, heat, and mass transfer. The interrelated nature of these transfers is more effectively understood through the use of dimensionless numbers. The Prandtl number (Pr), Schmidt number (Sc), and Lewis number (Le) are dimensionless numbers that characterize the relative importance of momentum, heat and mass transfer in a fluid flow. These numbers play a significant role in the analysis of boundary layer flows, particularly in the study of heat and mass transfer in both Newtonian and non-Newtonian fluids.

The Prandtl number (Pr) is defined as the ratio of momentum diffusivity (kinematic viscosity) to thermal diffusivity, expressed as:

$$\mathrm{Pr} = \frac{\nu}{\alpha} = \frac{\text{momentum diffusivity}}{\text{thermal diffusivity}}, \tag{2.64}$$

where ν is the kinematic viscosity and α is the thermal diffusivity. The Prandtl number helps to describe the relative thickness of the velocity boundary layer to the thermal boundary layer. For example, in fluids with a low Prandtl number ($Pr < 1$), such as liquid metals, heat diffuses faster than momentum, leading to a thicker thermal boundary layer. Conversely, for fluids with a high Prandtl number ($Pr > 1$), such as oils, the momentum boundary layer is thicker than the thermal boundary layer.

The Schmidt number (Sc) represents the ratio of momentum diffusivity to mass diffusivity and is given by:

$$\mathrm{Sc} = \frac{\nu}{D}, \tag{2.65}$$

where D is the mass diffusivity. The Schmidt number indicates the relative thickness of the momentum boundary layer compared to the concentration boundary layer. For fluids with a low Schmidt number ($Sc < 1$), mass diffusion dominates, resulting in a thicker concentration boundary layer. In contrast, a higher Schmidt number ($Sc > 1$) indicates that momentum diffusion is more dominant, leading to a thinner concentration boundary layer.

The Lewis number (Le) is a dimensionless number that is the ratio of thermal diffusivity to mass diffusivity.

$$\text{Le} = \frac{\alpha}{D}. \tag{2.66}$$

The Lewis number provides insights into the relationship between heat and mass transfer in a fluid. If the Lewis number is greater than unity ($Le > 1$), it suggests that thermal diffusion is slower than mass diffusion, resulting in a greater thickness of the thermal boundary layer relative to the concentration boundary layer. Conversely, a Lewis number less than unity ($Le < 1$) implies that mass diffusion dominates over thermal diffusion, leading to a thinner thermal boundary layer compared to the concentration boundary layer.

Understanding the influence of these dimensionless numbers is essential for designing systems involving heat and mass transfer, particularly in nanofluids and non-Newtonian fluid flow, where these parameters impact the efficiency of heat exchangers, chemical reactors, and other applications.

2.3.2 Skin Friction Coefficients

The skin friction coefficient is a fundamental parameter in fluid dynamics that quantifies the resistance exerted by a fluid flow against a solid surface due to viscous forces. It plays a crucial role in the study of boundary layer flows, especially in applications involving heat and mass transfer, as well as the movement of non-Newtonian fluids, including nanofluids. Mathematically, the skin friction coefficient (C_f) is expressed as the dimensionless ratio of the shear stress at the surface to the dynamic pressure of the fluid flow.

$$C_f = \frac{\tau_w}{\frac{1}{2}\rho U_w^2}, \tag{2.67}$$

where τ_w is the wall shear stress, ρ is the fluid density, and U_w is the velocity of the stretching surface. The wall shear stress itself is related to the velocity gradient at the surface, and in the case of non-Newtonian fluids, this relationship depends on the specific constitutive model used to describe the fluid's behavior.

Understanding and calculating the skin friction coefficient is essential for the design of systems such as heat exchangers, pumps, and turbines, where reducing drag is crucial for improving efficiency. It is also a key parameter in the analysis of lubrication systems and the study of fluid-structure interactions in biomedical applications, where the flow resistance at surfaces has direct implications for device performance and fluid dynamics.

2.3.3 Nusselt Number

The Nusselt number (Nu) is a fundamental dimensionless parameter in heat transfer that quantifies the enhancement of heat transfer through a fluid as a result of convection relative to conduction. It serves as a measure of the efficiency of convective heat transfer occurring at a surface in contact with a flowing fluid. In the context of boundary layer theory and magnetohydrodynamic (MHD) non-Newtonian nanofluid flows, the Nusselt number plays a vital role in characterizing the thermal behavior of the system and is crucial for analyzing how effectively heat is transported from a surface into the surrounding fluid.

The Nusselt number is defined as:

$$Nu_x = \frac{xq_w}{k(T_w - T_\infty)}, \tag{2.68}$$

where $q_w = -(k + q_r)\left[\frac{\partial T}{\partial y}\right]_{y=0}$ is the local convective heat transfer coefficient, x is the characteristic length, k is the thermal conductivity of the fluid, T_w is the wall temperature and T_∞ is the ambient temperature.

Accurate estimation of the Nusselt number is critical for engineering systems that rely on efficient thermal management, including electronics cooling, energy systems, and industrial processes. In research involving nanofluid and MHD flows, the Nusselt number provides a key metric for validating computational models and comparing different flow configurations and parameter effects.

2.3.4 Sherwood Number

The Sherwood number (Sh) is the mass transfer analog of the Nusselt number and represents the ratio of convective mass transfer to diffusive mass transport at a surface. In the study of boundary layer flows involving nanofluids and non-Newtonian fluids, particularly under the influence of magnetohydrodynamic (MHD) effects, the Sherwood number serves as a critical parameter for characterizing the efficiency of species (such as nanoparticles or solutes) being transferred from a surface into the surrounding fluid medium.

Mathematically, the Sherwood number is expressed as

$$Sh_x = \frac{xq_m}{D\,(C_w - C_\infty)}, \tag{2.69}$$

where $q_m = -\left[D_B\left(\frac{\partial C}{\partial y}\right)\right]_{y=0}$ is the convective mass transfer coefficient, D is the mass diffusivity, C_w and C_∞ are the wall and the ambient concentrations, respectively.

The Sherwood number is particularly important in engineering applications where mass transfer processes are vital, such as in chemical reactors, biomedical devices (e.g., drug delivery or dialysis), filtration systems, and environmental modeling (e.g., pollutant dispersion). Accurate prediction and control of the Sherwood number allow engineers and researchers to optimize system performance, enhance mixing and reaction rates, and ensure effective operation of devices involving complex fluid systems.

The study of boundary layer theory plays a crucial role in numerous engineering applications, including the design of airfoils, wings, wind tunnels, control surfaces, missiles, ships, submarines, automobiles, and civil structures such as buildings and bridges, making it indispensable for optimizing fluid flow behavior and improving aerodynamic and hydrodynamic performance. In the case of MHD flows, the dynamics of the boundary layer are significantly influenced by the presence of an external magnetic field. The Lorentz force, which arises from the interaction between the magnetic field and the electric current of the fluid, can modify the characteristics of the boundary layer. Additionally, the presence of nanoparticles in nanofluids adds complexity to the flow behavior because the interaction between the particles and the fluid influences the overall flow and heat transfer characteristics. Understanding these effects is vital for optimizing heat and mass transfer rates in MHD nanofluid applications, particularly in high-performance cooling systems.

2.4 Governing Equations and Conservation Laws

This section aims to introduce the basic governing equations that describe fluid flow and transport processes, which are derived from fundamental conservation laws and essential thermophysical principles. The so-called governing equations are the mathematical expressions of these laws. These equations are presented in a Cartesian coordinate system using vector notation. These governing equations include the continuity equation, which is based on the conservation of mass; the Navier-Stokes equations, which originate from Newton's second law of motion and represent the conservation of momentum; the energy equation, derived from the first law of thermodynamics; and the concentration equation, which enforces the conservation of species within the flow.

2.4.1 Continuity Equation

The continuity equation is derived from conservation of mass for a system, stating that "the rate at which mass enters a control volume minus the rate at which mass leaves the control volume is equal to the rate of accumulation of mass within the control volume." The mathematical equation of the law of conservation of mass to a flow is written as

$$\frac{\partial \rho}{\partial t} + \nabla.(\rho \vec{V}) = 0 \tag{2.70}$$

where ρ is the density of the fluid and V is the velocity of the fluid. For an incompressible fluid, Eq. (2.70) could be reduced to:

$$\nabla.\vec{V} = 0 \tag{2.71}$$

2.4.2 Momentum Equation

The conservation of momentum is rooted in Newton's second law of motion, which states that the rate of change of momentum in a fluid element is equal to the sum of forces acting on it. For incompressible flows, this principle is expressed in the form of the Navier-Stokes equations. These equations represent the balance between inertial forces, pressure gradients, viscous forces, and any external body forces. The general form of the momentum equation for an incompressible fluid is given by the following.

$$\rho \frac{DV}{Dt} = \rho \left(\frac{\partial \mathbf{V}}{\partial t} + (\mathbf{V} \cdot \nabla)\mathbf{V} \right) = \nabla.\tau + \rho F_B. \tag{2.72}$$

The Cauchy stress tensor τ can be decoposed as follows.

$$\tau = -PI + \tau_{ij}, \tag{2.73}$$

where P is its normal component, usually called the pressure , τ_{ij} the deviatoric or viscous stress tensor, and $\mathbf{I}$ is the identity matrix or unit tensor. So, Eq. (2.72) can be written in the form

$$\rho \left(\frac{\partial \mathbf{V}}{\partial t} + (\mathbf{V} \cdot \nabla)\mathbf{V} \right) = -\nabla p + \nabla \cdot \tau_{ij} + \rho \mathbf{F_B}, \tag{2.74}$$

where $\mathbf{F_B}$ denotes the body force.

In the consideration of MHD nanofluid flow in a porous medium, these body forces typically may include , external magnetic force $\mathbf{B}$, resistance by the porous medium (Darcy resistance), and buoyancy force (buoyancy due to temperature and concentration gradients). This leads to an augmented form of the momentum equation:

$$\rho\left(\frac{\partial \mathbf{V}}{\partial t}+(\mathbf{V}\cdot\nabla)\mathbf{V}\right)=-\nabla P+\nabla\cdot\tau_{ij}+\mathbf{J}\times\mathbf{B}+\rho g\beta_T(T-T_\infty)+\rho g\beta_C(C-C_\infty)-\frac{\mu}{K}\mathbf{V} \quad (2.75)$$

where k is the permeability of the porous medium, $\frac{\mu}{k}\mathbf{V}$ is the Darcy resistance term, and $\mathbf{J}\times\mathbf{B}$ is the mechanical Lorentz force generated by the motion of the fluid interacting with the external magnetic field. $\mathbf{g}$ is the acceleration due to gravity, β_T and β_C are the thermal and concentration expansion coefficients, respectively.

In addition, if the fluid flow problem is considered in a rotating frame of reference, it is necessary to account for the forces generated by the frame's rigid body rotation. And then the two terms, the Coriolis force term, $2\Omega\times\mathbf{V}$ and the centrifugal acceleration term $\Omega\times(\Omega\times r)$ will be introduced to the momentum equation and it is modified to have the following form.

$$\begin{aligned}&\rho\left[\frac{\partial \mathbf{V}}{\partial t}+(\mathbf{V}\cdot\nabla)\mathbf{V}+(2\Omega\times\mathbf{v})+\Omega\times(\Omega\times r)\right]\\&=-\nabla P+\nabla\cdot\tau_{ij}+\mathbf{J}\times\mathbf{B}+\rho g\left[\beta_T(T-T_\infty)+\beta_C(C-C_\infty)\right]-\frac{\mu}{K}\mathbf{V}\end{aligned} \quad (2.76)$$

where Ω is the angular velocity of the rotating reference frame and $\mathbf{r}$ is position vector. Gravitational and centrifugal forces depend on position rather than velocity and can therefore be incorporated into a modified pressure term, allowing them to be disregarded as distinct forces unless specified in the boundary conditions; in contrast, Coriolis forces must be explicitly considered.

2.4.3 Energy Equation

The energy equation describes the conservation of thermal energy in a fluid and is derived from the first law of thermodynamics. It accounts for the changes in internal energy caused by conduction, convection, viscous dissipation, Ohmic heating, thermal radiation, and internal heat generation or absorption. For incompressible flow, the general form of the energy equation is given by

$$\begin{aligned}\left(\rho C_p\right)_f\left[\frac{\partial \mathbf{T}}{\partial t}+(\mathbf{V}\cdot\nabla)\,\mathbf{T}\right]&=\kappa\nabla^2\mathbf{T}+\left(\tau_{ij}:\nabla\right)\mathbf{V}\\&+\left(\rho C_p\right)_p\left[D_B\nabla C\cdot\nabla T+\frac{D_T}{T_\infty}(\nabla T\cdot\nabla T)\right]\\&+\frac{1}{\sigma}(\mathbf{J}\cdot\mathbf{J})-\nabla q_r+Q_0\,(T-T_\infty)\,,\end{aligned} \quad (2.77)$$

where $\left(\rho C_p\right)_f$ and $\left(\rho C_p\right)_p$ are specific heat capacities of the nanofluid and the nanoparticles, respectively, and T is the temperature. κ denotes the thermal conductivity of the fluid; D_B and D_T represent the diffusion coefficients for Brownian and thermophoresis, respectively. T_∞ signifies the ambient temperature, q_r is the radiative heat flux, and the coefficient Q_0 stands for heat absorption ($Q_0 < 0$) and generation ($Q_0 > 0$).

2.4.4 Concentration Equation

It states that the total species concentration of the system under consideration is always constant. The concentration equation governs the distribution of species or nanoparticles within a fluid and is based on the law of conservation of mass for suspended particles. It accounts for various modes of mass transfer, including convection, Brownian motion, and thermophoresis (movement of particles due to temperature gradients). The general form of the concentration equation for an incompressible fluid, incorporating both Brownian diffusion and thermophoretic effects, is:

$$j = j_T + j_B = -\rho D_B \nabla C - \rho D_T \frac{\nabla T}{T_\infty}. \tag{2.78}$$

The equation for mass transfer in the absence of chemical reaction is generally presented as follows.

$$\frac{dC}{dt} = -\frac{1}{\rho}\nabla . j. \tag{2.79}$$

The conservation of nanoparticle concentration equation for a homogeneous chemical reaction is

$$\frac{\partial \mathbf{C}}{\partial t} + \left(\vec{\mathbf{V}} \cdot \nabla\right)\mathbf{C} = D_B \nabla^2 C + \frac{D_T}{T_\infty}\nabla^2 T - K_r\left(C - C_\infty\right), \tag{2.80}$$

where C is the nanoparticle concentration near the surface, C_∞ is the ambient concentration, and K_r denotes the chemical reaction constant.

Chapter 3

Research Methodology

3.1 Introduction

This chapter outlines the methodology employed to solve the coupled continuity, momentum, energy, and concentration equations for four distinct non-Newtonian fluids, namely Williamson, Casson, Tangent Hyperbolic, and Jeffrey nanofluids, under various physical constraints. The highly non-linear nature of the governing partial differential equations (PDEs), which arise from conservation laws of mass, momentum, energy, and nanoparticle concentration, necessitates the application of numerical techniques for their solution. By applying appropriate similarity transformations, the PDEs are reduced to a system of nonlinear ordinary differential equations (ODEs). These ODEs are solved numerically using the shooting technique in conjunction with higher-order Runge-Kutta methods (fifth- and sixth-order), implemented via Python programming.

3.2 Review of Related Numerical Methods

The solution of non-linear differential equations that govern fluid flow, heat transfer, and mass transfer has been a subject of extensive research. Due to the strong non-linearity of the governing equations, obtaining closed-form analytical solutions is challenging. Various methodologies of analytical, semi-analytical, and numerical methods have been developed to solve boundary layer problems involving non-Newtonian fluids, each with its own strengths and limitations.

Perturbation methods, for instance, are effective for weakly nonlinear problems.

Thamaraikannan et al. [150] applied the perturbation technique to solve the governing flow equations of the magnetohydrodynamic Casson nanofluid flow through a porous channel with periodic body acceleration. The tangent hyperbolic nanofluid for the tapered asymmetric channel was investigated by Kothandapani and Prakash [151] and they solved the problem analytically using the regular perturbation method. Hussain et al. [152] have also implemented the regular perturbation method during their investigation on the Couette flow of Casson nanofluid with variable viscosity and porous medium inside a vertical channel. There are also other researchers who have used perturbation methods. However, perturbation theory encompasses a range of techniques used to find approximate solutions to problems involving a small parameter. These methods are especially useful when the problem includes a term that is small in magnitude or when one physical effect is much less significant than another dominant one. Although widely implemented using software such as MATLAB, these methods are limited to small parameter values and yield approximate solutions valid only in restricted regimes.

The Homotopy Analysis Method (HAM), developed by Shijun Liao in 1992, is a powerful semi-analytical approach designed to solve nonlinear ordinary and partial differential equations, and it has been used extensively with symbolic computing platforms like Mathematica. Unlike many traditional perturbation techniques, HAM does not rely on small or large physical parameters, making it applicable to a wide range of nonlinear problems. Over the years, numerous researchers have applied HAM to various problems in applied mathematics and engineering, and it has proven to be highly effective in producing approximate analytic solutions for nonlinear systems. For example, Kohilavani et al. [153] used the homotopy analysis method (HAM) with an evolutionary algorithm to solve the ODE transformed from the governing equations of a non-Newtonian Casson base fluid flowing over a linearly stretchable surface problem. Walelign et al. [81] also conducted an analytical study on heat and mass transfer in unsteady MHD radiant flow of Williamson nanofluid over a stretching sheet using the homotopy analysis method. Using this method, Prajapati and Meher [154] explored the MHD tangent hyperbolic hybrid nanofluid flow over a porous stretched sheet with various base fluids. Liao [155] modified it and presented the optimal homotopy analysis method (OHAM), which is a more effective technique. Numerous research scholars have implemented the modified OHAM. The study on thermal and mass transport in the Williamson model flow through the optimal homotopic method conducted by Akbar et al. [156] is one of them. One of the unique features of HAM is the inclusion of a convergence control parameter (CCP), which allows the user to regulate the convergence behavior of the solution series. However, it is computationally intensive and requires careful selection of the CCP to ensure accurate results.

Numerical methods such as finite element methods (as evidenced by much literature [157–161]) and finite difference methods are also widely used to investigate fluid flow problems, but they require mesh generation, and their setup is computationally expensive. A finite difference scheme, the Keller Box Method, developed by Herbert B. Keller in the 1970s [162], is a highly stable and efficient numerical technique for solving two-point boundary value problems (BVPs), particularly those involving nonlinear ordinary differential equations (ODEs). As an implicit finite-difference scheme, it reduces higher-order ODEs to first-order systems, employs central difference approximations at midpoints (the "box" concept), and linearizes the system using Newton's method. The resulting equations are solved via a block tridiagonal matrix algorithm, ensuring both computational efficiency and accuracy. This method is especially effective for stiff, nonlinear systems and boundary layer problems, making it indispensable for modeling complex phenomena like MHD flows, non-Newtonian fluids, and coupled heat and mass transfer processes. Its adaptability extends to time-dependent and multidimensional problems, cementing its utility in computational fluid dynamics and applied mathematical modeling [163–165].

As a simpler alternative, the shooting method combined with Runge-Kutta integration provides an effective approach to solving boundary value problems in fluid dynamics. Although it may not match the stability of the Keller Box method for stiff systems, it remains widely used due to its conceptual simplicity and ease of implementation. This approach has been successfully applied to a range of complex phenomena, including MHD flows and nanofluid systems, making it a practical choice when computational efficiency and straightforward coding are prioritized.

3.3 Shooting Technique

The shooting technique is a numerical method to solve BVPs by transforming them into IVPs. This approach is particularly advantageous for systems of ODEs derived from similarity transformations of PDEs, as encountered in boundary layer flows. The core idea involves guessing missing initial conditions, solving the resulting IVP, and iteratively adjusting the guesses until the boundary conditions are satisfied. The first step in applying the shooting method is to reduce the governing PDEs to a system of ODEs using appropriate similarity variables. For instance, in the case of MHD nanofluid flow over a stretching sheet, the continuity, momentum, energy, and concentration equations are transformed into a set of coupled nonlinear ODEs. These

ODEs are then expressed as a system of first-order equations to facilitate numerical integration. The computed solution at the far-field boundary is compared with the prescribed boundary conditions. If the discrepancy exceeds a predefined tolerance, the initial guesses are adjusted using the Newton-Raphson method. This iterative process continues until the boundary conditions are satisfied within an acceptable error margin. Despite its advantages, the shooting method has limitations. It may struggle with problems exhibiting multiple solutions or extreme sensitivity to initial conditions. However, for the class of problems considered in this study, the method has proven stable and reliable, especially when combined with the higher-order Runge-Kutta integration [166–172].

3.4 Higher Order Runge-Kutta Method

Runge-Kutta (RK) methods are a family of iterative techniques used to solve ordinary differential equations (ODEs), known for their accuracy and stability. Higher-order RK methods, such as the fifth- and sixth-order variants, are particularly effective for stiff systems where lower-order methods may fail or require excessively small step sizes. The general form of an RK method involves evaluating the derivative at several points within each time step and combining these evaluations to approximate the solution. The number of function evaluations (stages) and the weighting coefficients determine the method's order, which reflects its truncation error. Higher-order methods achieve greater accuracy per step but incur a higher computational cost per evaluation. In this study, fifth- and sixth-order RK methods were employed to balance accuracy and computational efficiency. The fifth-order method provides a good compromise between precision and cost. It uses six function evaluations per step and includes embedded error estimation for adaptive step-size control. The sixth-order RK method offers even higher accuracy by employing seven stages per step. The additional stages allow for better resolution of solution features, reducing the need for excessively fine discretization. A critical aspect of RK methods is their stability, which determines how errors propagate over successive steps. Higher-order methods generally exhibit better stability properties, allowing for larger step sizes without compromising accuracy. This is particularly important in boundary layer problems, where resolving thin layers near the wall requires careful selection of step-sizes.

3.4.1 Fifth Order Runge-Kutta Method

The fifth-order Runge-Kutta (RK5) method is a widely used numerical technique to solve ODEs with high accuracy [173]. The RK5 method typically involves six function evaluations per step, with carefully chosen weighting coefficients to minimize truncation error. One of the key advantages of RK5 is its computational efficiency. For problems where the behavior of the solution is well-behaved and moderately nonlinear, RK5 provides a sweet spot between accuracy and cost [174]. This was evident in Williamson fluid simulations, where RK5 delivered reliable results without excessive computational overhead.

The formula for RK5 to solve the system of ODEs [174] of the form

$$y'(x) = f(x, y), \qquad y(x_0) = y_0, \tag{3.1}$$

is given by

$$y_{i+1} = y_i + \frac{7k_1 + 32k_3 + 12k_4 + 32k_5 + 7k_6}{90} \tag{3.2}$$

where y_i and y_{i+1} represent the computed values of y corresponding to the mesh points x_i and x_{i+1}, respectively. h denotes the uniform step size of the grid, and

$$k_1 = hf(x_i, y_i), \tag{3.3}$$

$$k_2 = hf\left(x_i + \frac{h}{2}, y_i + \frac{k_1}{2}\right), \tag{3.4}$$

$$k_3 = hf\left(x_i + \frac{h}{4}, y_i + \frac{3k_1 + k_2}{16}\right), \tag{3.5}$$

$$k_4 = hf\left(x_i + \frac{h}{2}, y_i + \frac{k_3}{2}\right), \tag{3.6}$$

$$k_5 = hf\left(x_i + \frac{3h}{4}, y_i + \frac{-3k_2 + 6k_3 + 9k_4}{16}\right), \tag{3.7}$$

$$k_6 = hf\left(x_i + h, y_i + \frac{k_1 + 4k_2 + 6k_3 - 12k_4 + 8k_5}{7}\right) \tag{3.8}$$

3.4.2 Sixth Order Runge-Kutta Method

The sixth-order Runge-Kutta method (RK6) represents a higher level of numerical precision, employing seven function evaluations per step to achieve superior accuracy [175]. This method is particularly advantageous for solving stiff and highly non-linear ODEs, where lower-order methods require prohibitively small step sizes. The applied RK6 method is a version developed by Butcher, characterized by its seven-stage evaluation and carefully optimized coefficients. The detailed derivation is discussed by Trikkaliotis and Gousidou-Koutita [175]. The high order of this method ensures that truncation errors are minimized, enabling accurate integration even over large intervals. One of the notable benefits of RK6 is its stability, which allows larger step sizes compared to lower-order methods while retaining accuracy. This property is especially valuable in parametric studies, where multiple simulations are required to explore the influence of various physical parameters.

The implemented formula for RK6 to solve the initial value problem:

$$\frac{dy}{dx} = f(x, y), \qquad y(x_0) = y_0 \tag{3.9}$$

is written as

$$y_{i+1} = y_i + \frac{1}{90}(7k_1 + 32k_3 + 12k_4 + 16k_5 + 16k_6 + 7k_7) \tag{3.10}$$

where the step size be $h = \frac{x_n - x_0}{n}$ and define discrete points $x_i = x_0 + ih$ for $i = 0, 1, \ldots, n$. The intermediate stage values are computed as follows:

$$k_1 = h\,f(x_i,\, y_i) \tag{3.11}$$

$$k_2 = h\,f\Big(x_i + \tfrac{1}{4}h,\, y_i + \tfrac{1}{4}k_1\Big) \tag{3.12}$$

$$k_3 = h\,f\Big(x_i + \tfrac{1}{4}h,\, y_i + \tfrac{1}{8}(k_1 + k_2)\Big) \tag{3.13}$$

$$k_4 = h\,f\Big(x_i + \tfrac{1}{2}h,\, y_i - \tfrac{5}{6}k_2 + \tfrac{4}{3}k_3\Big) \tag{3.14}$$

$$k_5 = h\,f\Big(x_i + \tfrac{3}{4}h,\, y_i + \tfrac{1}{8}k_1 + \tfrac{1}{8}k_2 + \tfrac{1}{2}k_4\Big) \tag{3.15}$$

$$k_6 = h\,f\Big(x_i + \tfrac{3}{4}h,\, y_i + \tfrac{3}{8}k_2 + \tfrac{1}{4}k_3 - \tfrac{1}{8}k_4 + \tfrac{1}{4}k_5\Big) \tag{3.16}$$

$$k_7 = h\,f\Big(x_i + h,\, y_i + \tfrac{1}{7}k_1 - \tfrac{2}{7}k_2 + \tfrac{4}{7}k_3 + \tfrac{4}{7}k_6\Big) \tag{3.17}$$

3.5 Numerical Simulation

The numerical simulations are based on solving the reduced system of ODEs using the shooting method and higher-order Runge-Kutta solvers. The procedure is as follows:

1. Apply similarity transformations to reduce the governing PDEs to a system of nonlinear ODEs.
2. Transform the higher-order ODEs into a first-order system.
3. Guess the unknown initial conditions and solve the initial value problem using the Runge-Kutta method.

4. Use an iterative algorithm to adjust the guesses until the boundary conditions are satisfied to a predefined tolerance.

5. Plot the resulting profiles (velocity, temperature, concentration) and compute physical quantities such as skin friction coefficient, Nusselt number, and Sherwood number.

Each model in the dissertation is validated by comparing the results obtained with those of the existing literature. The accuracy and convergence of the methods were confirmed through such comparisons.

3.6 Implementation

All simulations are performed using Python, taking advantage of its numerical and visualization capabilities. The code is modularly structured, allowing reuse and modification across different models and parameter ranges. The core modules are included as follows.

- Definition of governing equations and similarity transformations.
- Conversion to first-order systems.
- Implementation of the shooting algorithm and iterative correction.
- Execution of fifth- and sixth-order Runge-Kutta solvers.
- Graphical analysis of the results using Python's plotting libraries.

The output consists of plots showing the variation of velocity, temperature, and nanoparticle concentration with respect to key dimensionless parameters, as well as tables summarizing critical values of skin friction, the Nusselt number, and the Sherwood number.

3.7 Used Software

The choice of software tools played a pivotal role in the success of this dissertation. Python emerged as the platform of choice because of its open source nature and extensive scientific libraries. The Python ecosystem provided all necessary tools for numerical computation, visualization, and data analysis. NumPy served as the foundation for numerical operations and offers efficient array manipulations [176]. SciPy built upon this with advanced functionality for integration, optimization, and sparse matrix operations [177]. For ODE solving, ‘fsolve‘ is the workhorse, providing robust implementations. When higher-order methods are needed, custom solvers are developed using NumPy for the core computations. These solvers are carefully optimized to balance accuracy and performance. Matplotlib is used for visualization, making it possible to generate professional quality plots [178]. Its object-oriented approach provided detailed control over all elements of the figures, including axis labels and color schemes. For interactive exploration of results, Jupyter notebooks are employed, combining code execution with rich text documentation.

3.8 Validation

Validation is an integral part of the simulation process. The numerical results are compared with the previously published literature to ensure consistency. Excellent agreement is observed in all cases, affirming the reliability of the numerical framework developed in this study. The methodology is then applied to investigate the effects of various physical parameters on velocity, temperature, and concentration profiles, as well as on key engineering quantities such as skin friction, the Nusselt number, and the Sherwood number. Physically realistic results offer additional support for the validity of the selected approach.

A comprehensive mesh independence study was carried out to ensure that all numerical solutions reported in this dissertation are independent of discretization parameters. Following established computational fluid dynamics practices, the step size $\Delta\eta$ was systematically varied across three levels of refinement, and the corresponding effects on key physical quantities were carefully examined. The complete mesh independence analysis, including detailed numerical tables and convergence plots, is provided in Appendix A.

The governing equations are defined over a semi-infinite physical domain, $\eta \in [0, \infty)$, which necessitates appropriate truncation for numerical implementation. The suitability of the truncated computational domain was rigorously assessed by comparing solutions obtained with $\eta_{\text{max}} = 5, 7, 10$. A detailed account of the domain truncation validation is presented in Appendix B.

3.9 Numerical Solution Procedure

The overall numerical modeling procedure is represented by the following flow chart.

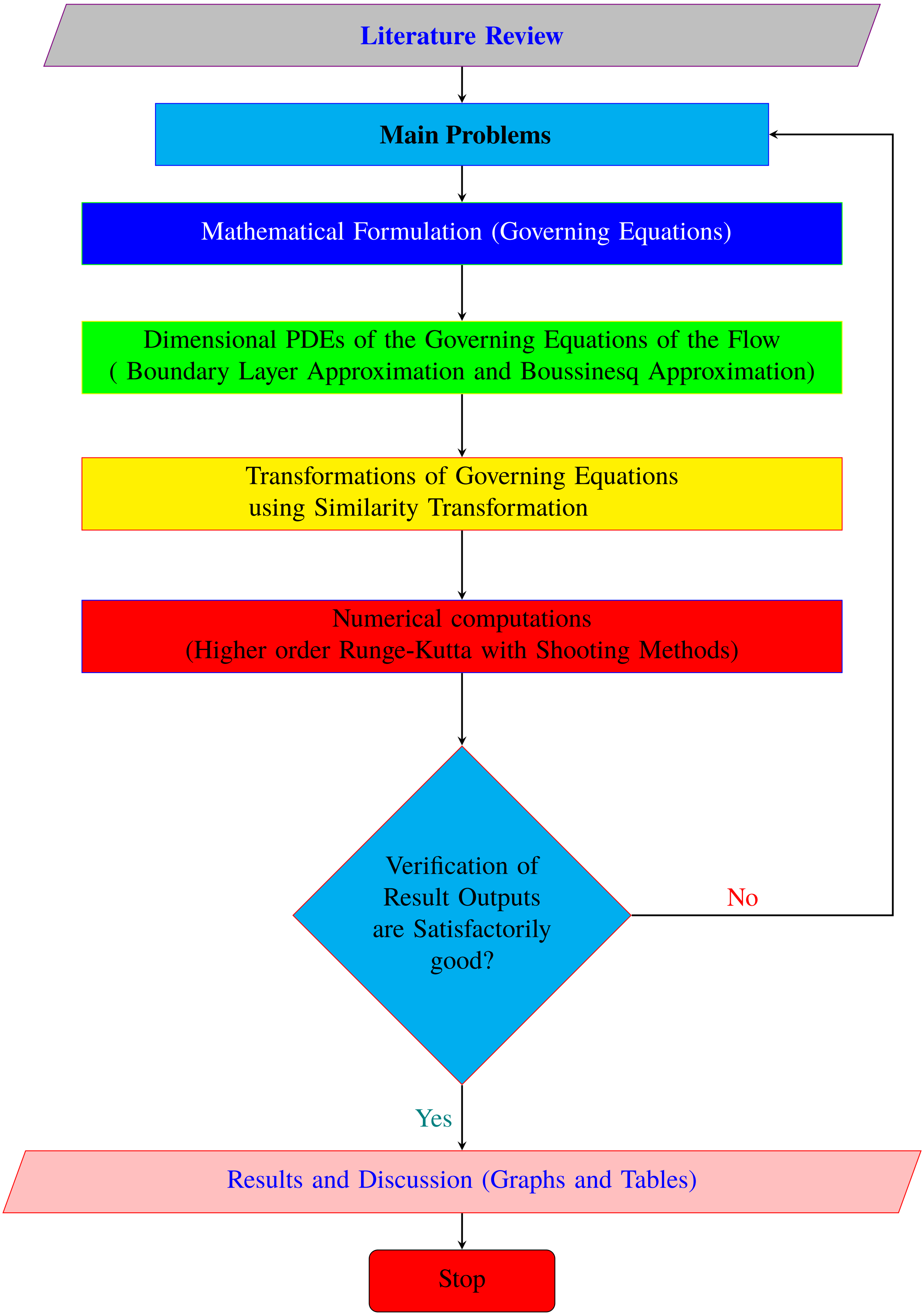

Figure 3.1: Research framework

Chapter 4

Effects of Hall, Ion Slip, Viscous Dissipation and Nonlinear Thermal Radiation on MHD Williamson Nanofluid Flow Past a Stretching Sheet

4.1 Introduction

One of the non-Newtonian fluids that has gained prominence in the study of fluid dynamics is the Williamson fluid, which was discovered by Williamson in 1929. The Williamson fluid model is widely utilized to capture the shear-thinning behavior observed in many practical systems. It describes the relationship between shear stress and the shear rate in these fluids, which is responsible for the reduction in viscosity as the shear rate increases. The two-dimensional flow of the Williamson fluid model over a stretching sheet has been studied by Nadeem et al. [59]. Vajravelu et al. [179] analyzed the peristaltic flow of a Williamson fluid in asymmetric channels with permeable walls. The flow of Williamson fluid with pressure-dependent viscosity in an inclined channel was considered by Zehra et al. [180].

The current study aims to comprehensively analyze the effects of Hall, ion slip, viscous dissipation, and nonlinear thermal radiation on the MHD Williamson nanofluid flow past a stretching sheet. By combining these factors, the study addresses a research gap and provides a novel investigation of the combined effects. To solve the governing equations involved in studying the combined effects of these phenomena, numerical methods are employed. Using appropriate similarity transformation equations, the highly non-linear partial differential equations are reduced to a system of ODE's and solved numerically. The fifth-order Runge-Kutta (RK5) scheme combined with the shooting technique allows for the determination of solutions to the governing equations. Using graphs and tables, the findings are discussed for a few relevant and interesting parameters. Furthermore, the validity of the method was verified by comparing the numerical findings with published works, and the results indicate a wonderful agreement.

4.2 Mathematical Formulation

4.2.1 Model Assumptions

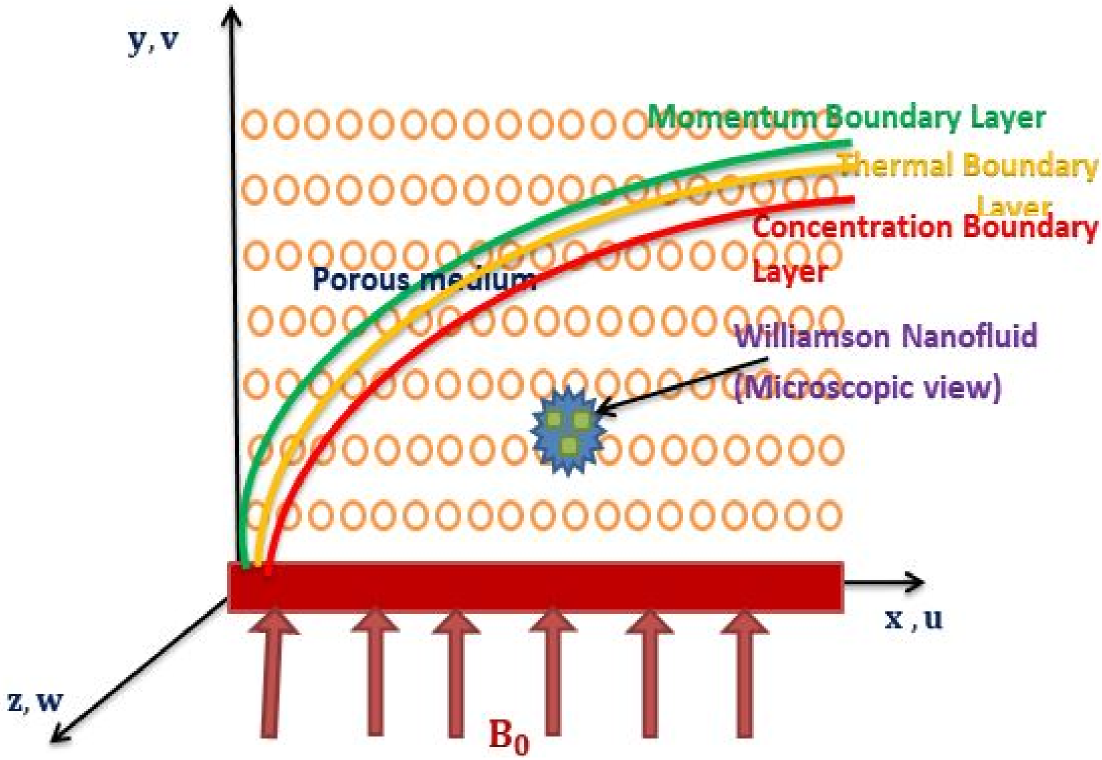

Figure 4.1: A schematic of the physical model

A steady, laminar, viscous, incompressible, electrically conducting MHD Williamson nanofluid flow over a porous medium with no slip effect stretching linearly with velocity $U_w(x) = bx$, where b is the stretching rate, along the x-axis with the additional effects of viscous dissipation has been considered. A strong constant magnetic field of intensity B_0 is supplied in the direction along the y-axis. Due to this strong magnetic field strength, the electrically conducting fluid has the Hall and ion-slip effects, which give rise to a force on the fluid in the z-direction, and hence the flow becomes three dimensional. The flow in the region $y \geq 0$ is taken into account, as indicated in Fig.

4.1. In addition, the effects of Joule (ohmic) heating, heat generation/absorption, nonlinear thermal radiation, and (homogeneous) chemical reaction are considered.

4.2.2 Conservation Equations

The balance of mass, momentum, energy, and nanoparticles concentration are given by the conservation equations in vector form as follows:

4.2.2.1 Continuity Equation

The continuity equation for conservation of mass becomes

$$\nabla \cdot V = 0, \tag{4.1}$$

where ∇ and $\vec{V}$ denote the Del (nabla) operator and the flow velocity vector, respectively. In three-dimensional Cartesian coordinates (x, y, z), the corresponding velocity field is $\mathbf{V}(u, v, w)$ and the continuity equation Eq. (4.1) is also written as follows.

$$\frac{\partial u}{\partial x} + \frac{\partial v}{\partial y} + \frac{\partial w}{\partial z} = 0, \tag{4.2}$$

4.2.2.2 Conservation of Momentum Equation

The balance of linear momentum is given by

$$\rho_f \left[\frac{\partial V}{\partial t} + (V \cdot \nabla) V \right] = -\nabla P + \nabla \cdot \tau_{ij} + (\mathbf{J} \times \mathbf{B}) - \frac{\mu}{K} V, \tag{4.3}$$

where ρ_f is the density of the nanofluid, t is the time variable, P is the fluid pressure, τ_{ij} is the Cauchy stress tensor, B is external magnetic field, $J = (J_x, J_y, J_z)$ is current density, E represents the electric field and μ is coefficient of dynamic viscosity, $(\mathbf{J} \times \mathbf{B})$ is the mechanical Lorentz force generated by the motion of the fluid interacted with the external magnetic field and K is the porosity of the medium.

In this formulation, the pressure field is assumed to be isotropic, i.e. it acts uniformly in all directions and does not contribute any streamwise variation within the boundary-layer region under consideration. Physically, this corresponds to neglecting any externally imposed pressure gradient and assuming that the pressure inside the thin fluid layer equals the ambient free-stream pressure, which remains constant. Under this assumption, the pressure term in the momentum equations, $-\nabla p$, reduces to a uniform isotropic contribution that can be absorbed into the thermodynamic pressure. Consequently, no explicit pressure-gradient term appears in the reduced governing equations. The resulting momentum equation then balances the inertial and convective accelerations with the non-Newtonian viscous stresses, Lorentz force due to the applied magnetic field, and the resistance by the porosity of the medium.

Now, the three-dimensional momentum equations in terms of the stress tensor become

$$\rho_f\left(u\frac{\partial u}{\partial x}+v\frac{\partial u}{\partial y}+w\frac{\partial u}{\partial z}\right)=\frac{\partial \tau_{xx}}{\partial x}+\frac{\partial \tau_{xy}}{\partial y}+\frac{\partial \tau_{xz}}{\partial z}+FB_x, \tag{4.4}$$

$$\rho_f\left(u\frac{\partial v}{\partial x}+v\frac{\partial v}{\partial y}+w\frac{\partial v}{\partial z}\right)=\frac{\partial \tau_{yx}}{\partial x}+\frac{\partial \tau_{yy}}{\partial y}+\frac{\partial \tau_{yz}}{\partial z}+FB_y, \tag{4.5}$$

$$\rho_f\left(u\frac{\partial w}{\partial x}+v\frac{\partial w}{\partial y}+w\frac{\partial w}{\partial z}\right)=\frac{\partial \tau_{zx}}{\partial x}+\frac{\partial \tau_{zy}}{\partial y}+\frac{\partial \tau_{zz}}{\partial z}+FB_z, \tag{4.6}$$

where $FB=(FB_x, FB_y, FB_z)$ represents the two considered body forces of the Lorentz force due to the applied magnetic field and the resistance by the porosity of the medium.

Substituting the stress components from Eq. (2.13) into Eqs. (4.4)–(4.6) and computing the partial derivatives of the components of the stress tensor, we apply the boundary layer approximations. This process yields the following simplified momentum equations:

$$\rho_f\left(u\frac{\partial u}{\partial x}+v\frac{\partial u}{\partial y}+w\frac{\partial u}{\partial z}\right)=\mu_0\left(1+\sqrt{2}\Gamma\frac{\partial u}{\partial y}\right)\frac{\partial^2 u}{\partial y^2}+FB_x, \tag{4.7}$$

$$\rho_f\left(u\frac{\partial w}{\partial x}+v\frac{\partial w}{\partial y}+w\frac{\partial w}{\partial z}\right)=\mu_0\left(1+\sqrt{2}\Gamma\frac{\partial w}{\partial y}\right)\frac{\partial^2 w}{\partial y^2}+FB_z, \tag{4.8}$$

where μ_0 is limiting viscosity at zero shear rate and $\Gamma > 0$ is a time constant.

For a strong constant magnetic field of intensity B_0 supplied in the direction along the y-axis, the Lorentz force $\vec{J}\times\vec{B}$ can be decomposed as follows.

$$J\times B=\begin{vmatrix}\mathbf{i} & \mathbf{j} & \mathbf{k}\\ J_x & J_y & J_z\\ 0 & B_0 & 0\end{vmatrix}=-B_0J_z\hat{\mathbf{i}}+B_0J_x\hat{\mathbf{k}}. \tag{4.9}$$

Hall and ion slip currents cannot be disregarded because it is assumed that the electron-atom collision frequency is quite high. As a result, the z-direction velocity is produced by the Hall and ion slip currents. The modified generalized Ohm's law formula, which considers the Hall and ion slip effects at very large magnetic field strengths, is shown in [181].

$$\begin{aligned} J =&\sigma(E+(V\times B))-\frac{\overline{\omega}_e\tau_e}{B_0}(J\times B)+\frac{\overline{\omega}_e\tau_e\beta_i}{B_0^2}((J\times B)\times B)\\ =&\ \sigma(E+(V\times B))-\frac{\beta_e}{B_0}(J\times B)+\frac{\beta_e\beta_i}{B_0^2}((J\times B)\times B),\end{aligned} \tag{4.10}$$

where σ denoting the electric conductivity of the fluid, $\beta_e = \overline{\omega}_e \tau_e$ is Hall parameter and $\beta_i = \overline{\omega}_i \tau_i$ represents the ion slip parameter. The thermoelectric effects and the gradient of electron pressure are disregarded, and this results in the electric field $E = 0$ [181]. Following these assumptions, Eq. (4.10) can be simplified as follows.

$$\sigma(E + (V \times B)) = \sigma(V \times B) = \sigma \begin{vmatrix} \mathbf{i} & \mathbf{j} & \mathbf{k} \\ u & v & w \\ 0 & B_0 & 0 \end{vmatrix} = \sigma(-B_0 w \hat{\mathbf{i}} + B_0 u \hat{\mathbf{k}}), \tag{4.11}$$

and

$$(J \times B) \times B = \begin{vmatrix} \mathbf{i} & \mathbf{j} & \mathbf{k} \\ -B_0 J_z & 0 & B_0 J_x \\ 0 & B_0 & 0 \end{vmatrix} = -B_0^2 J_x \hat{\mathbf{i}} - B_0^2 J_z \hat{\mathbf{k}} = -B_0^2 (J_x \hat{\mathbf{i}} + J_z \hat{\mathbf{k}}). \tag{4.12}$$

Consequently, Eq. (4.10) is reduced to

$$J = (J_x, J_y, J_z) = \sigma(-B_0 w \hat{\mathbf{i}} + B_0 u \hat{\mathbf{k}}) - \beta_e(-B_0 J_z \hat{\mathbf{i}} + B_0 J_x \hat{\mathbf{k}}) - \beta_e \beta_i (J_x \hat{\mathbf{i}} + J_z \hat{\mathbf{k}}). \tag{4.13}$$

Additionally, Eq. (4.13) can also be written as the system of equations as follows.

$$\begin{cases} J_x = -\sigma B_0 w + \beta_e J_z - \beta_e \beta_i J_x \\ J_z = \sigma B_0 u - \beta_e J_x - \beta_e \beta_i J_z \end{cases} \tag{4.14}$$

or

$$\begin{cases} (1 + \beta_e \beta_i) J_x - \beta_e J_z = -\sigma B_0 w \\ (1 + \beta_e \beta_i) J_z + \beta_e J_x = \sigma B_0 u \end{cases} \tag{4.15}$$

Solving this system of equations Eq. (4.15) simultaneously, we obtain J_x and J_z as:

$$J_x = \frac{\sigma B_0 \left(\beta_e u - (1 + \beta_e \beta_i) w\right)}{(1 + \beta_e \beta_i)^2 + \beta_e^2}, \tag{4.16}$$

$$J_z = \frac{\sigma B_0 \left((1 + \beta_e \beta_i) u + \beta_e w\right)}{(1 + \beta_e \beta_i)^2 + \beta_e^2}. \tag{4.17}$$

Finally, using Eqns. (4.9), (4.16), and (4.17) the reduced form the Lorentz force, in this particular study, is

$$\begin{aligned} J \times B &= -B_0 J_z \hat{\mathbf{i}} + B_0 J_x \hat{\mathbf{k}} \\ &= -\frac{\sigma B_0^2 \left((1 + \beta_e \beta_i) u + \beta_e w\right)}{(1 + \beta_e \beta_i)^2 + \beta_e^2} \hat{\mathbf{i}} + \frac{\sigma B_0^2 \left(\beta_e u - (1 + \beta_e \beta_i) w\right)}{(1 + \beta_e \beta_i)^2 + \beta_e^2} \hat{\mathbf{k}}. \end{aligned} \tag{4.18}$$

4.2.2.3 Conservation of Energy equation

The conservation of thermal energy is given by

$$\begin{aligned}\left(\rho C_p\right)_f\left[\frac{\partial \mathbf{T}}{\partial t}+(\mathbf{V}\cdot\nabla)\,\mathbf{T}\right] &= \kappa\nabla^2\mathbf{T}+\left(\tau_{ij}:\nabla\right)\mathbf{V}\\ &\quad+\left(\rho C_p\right)_p\left[D_B\nabla C\cdot\nabla T+\frac{D_T}{T_\infty}\left(\nabla T\cdot\nabla T\right)\right]\\ &\quad+\frac{1}{\sigma}\left(\mathbf{J}\cdot\mathbf{J}\right)-\nabla q_r+Q_0\left(T-T_\infty\right),\end{aligned}\tag{4.19}$$

where $\left(\rho C_p\right)_f$ and $\left(\rho C_p\right)_p$ are specific heat capacities of the nanofluid and the nanoparticles, respectively, and T is the temperature. κ denotes the thermal conductivity of the fluid; D_B and D_T represent the diffusion coefficients for Brownian and thermophoresis, respectively. T_∞ signifies the ambient temperature, q_r is the radiative heat flux, and the coefficient Q_0 represents heat absorption ($Q_0 < 0$) and generation ($Q_0 > 0$).

Using the expression for current density from Eqs. (4.10), (4.16) and (4.17), the ohmic (Joule) heating term ($\frac{1}{\sigma}\left(\mathbf{J}\cdot\mathbf{J}\right)$) can now be expressed as follows.

$$\begin{aligned}\frac{1}{\sigma}\left(\mathbf{J}\cdot\mathbf{J}\right) &= \frac{1}{\sigma}\left[\left(J_x,0,J_z\right)\cdot\left(J_x,0,J_z\right)\right]\\ &= \frac{1}{\sigma}\left[\frac{\sigma^2B_0^2\left(u^2+w^2\right)}{\left(1+\beta_e\beta_i\right)^2+\beta_e^2}\right]\\ &= \frac{\sigma B_0^2\left(u^2+w^2\right)}{\left(1+\beta_e\beta_i\right)^2+\beta_e^2}.\end{aligned}\tag{4.20}$$

By employing the non linear Rosseland diffusion approximation, the radiative heat flux q_r can be written as [2]:

$$q_r = -\frac{4\sigma^*}{3k^*}\frac{\partial T^4}{\partial y} = -\frac{16\sigma^*}{3k^*}T^3\frac{\partial T}{\partial y},\tag{4.21}$$

and therefore;

$$\begin{aligned}\frac{1}{\rho C_p}\frac{\partial}{\partial y}\left(q_r\right) &= \frac{1}{\rho C_p}\frac{\partial}{\partial y}\left(-\frac{4\sigma^*}{3k^*}\frac{\partial T^4}{\partial y}\right)\\ &= -\frac{16\sigma^*}{3k^*\rho C_p}\frac{\partial}{\partial y}\left(T^3\frac{\partial T}{\partial y}\right),\end{aligned}\tag{4.22}$$

where σ^* is the Stefan-Boltzmann constant and k^* is the mean absorption coefficient.

From Eq. (4.19), the term $Q_0\left(T-T_\infty\right)$ is the heat source term. In addition, using the boundary layer approximation in three-dimensional Cartesian coordinates, the viscous dissipation term can also be obtained from $\left(\vec{\tau_{ij}} : \nabla\right)\vec{\mathbf{V}}$, and after simplification it becomes:

$$\Phi = \frac{\upsilon}{C_p}\left[1 + \frac{\Gamma}{\sqrt{2}}\sqrt{\left(\frac{\partial u}{\partial y}\right)^2 + \left(\frac{\partial w}{\partial y}\right)^2}\right]\left[\left(\frac{\partial u}{\partial y}\right)^2 + \left(\frac{\partial w}{\partial y}\right)^2\right]. \tag{4.23}$$

4.2.2.4 Conservation of Nanoparticle Concentration Equation

Conservation of nanoparticle concentration equation for a homogeneous chemical reaction is

$$\frac{\partial \mathbf{C}}{\partial t} + (\mathbf{V}\cdot\nabla)\,\mathbf{C} = D_B\nabla^2 C + \frac{D_T}{T_\infty}\nabla^2 T - R_0\,(C - C_\infty)\,, \tag{4.24}$$

where C is the nanoparticle concentration near the surface, C_∞ is the ambient concentration and R_0 denotes chemical reaction constant.

4.2.3 Coupled Governing Equations and Boundary Conditions

By incorporating the simplified equations above and using the boundary layer approximation in Cartesian coordinates, we rewrite the governing equations for the flow as follows [2]:

$$\frac{\partial u}{\partial x} + \frac{\partial v}{\partial y} + \frac{\partial w}{\partial z} = 0, \tag{4.25}$$

$$u\frac{\partial u}{\partial x} + v\frac{\partial u}{\partial y} + w\frac{\partial u}{\partial z} = \upsilon\left(1 + \sqrt{2}\Gamma\frac{\partial u}{\partial y}\right)\frac{\partial^2 u}{\partial y^2} - \frac{\sigma B_0^2\left[(1+\beta_e\beta_i)u + \beta_e w\right]}{\rho\left[(1+\beta_e\beta_i)^2 + \beta_e^2\right]} - \frac{\upsilon}{K}u, \tag{4.26}$$

$$u\frac{\partial w}{\partial x} + v\frac{\partial w}{\partial y} + w\frac{\partial w}{\partial z} = \upsilon\left(1 + \sqrt{2}\Gamma\frac{\partial w}{\partial y}\right)\frac{\partial^2 w}{\partial y^2} + \frac{\sigma B_0^2\left[\beta_e u - (1+\beta_e\beta_i)w\right]}{\rho\left[(1+\beta_e\beta_i)^2 + \beta_e^2\right]} - \frac{\upsilon}{K}w, \tag{4.27}$$

$$\begin{aligned} u\frac{\partial T}{\partial x} + v\frac{\partial T}{\partial y} + w\frac{\partial T}{\partial z} &= \alpha\frac{\partial^2 T}{\partial y^2} + \Lambda\left[D_B\frac{\partial C}{\partial y}\frac{\partial T}{\partial y} + \frac{D_T}{T_\infty}\left(\frac{\partial T}{\partial y}\right)^2\right] + \frac{16\sigma^*}{3k^*\left(\rho C_p\right)_f}\frac{\partial}{\partial y}\left(T^3\frac{\partial T}{\partial y}\right) \\ &+ \frac{\upsilon}{C_p}\left[1 + \frac{\Gamma}{\sqrt{2}}\sqrt{\left(\frac{\partial u}{\partial y}\right)^2 + \left(\frac{\partial w}{\partial y}\right)^2}\right]\left[\left(\frac{\partial u}{\partial y}\right)^2 + \left(\frac{\partial w}{\partial y}\right)^2\right] \\ &+ \frac{\sigma B_0^2\left[u^2 + w^2\right]}{\left(\rho C_p\right)_f\left[(1+\beta_e\beta_i)^2 + \beta_e^2\right]} + \frac{Q_0}{\left(\rho C_p\right)_f}(T - T_\infty)\,, \end{aligned} \tag{4.28}$$

$$u\frac{\partial C}{\partial x} + v\frac{\partial C}{\partial y} + w\frac{\partial C}{\partial z} = D_B\frac{\partial^2 C}{\partial y^2} + \frac{D_T}{T_\infty}\frac{\partial^2 T}{\partial y^2} - R_0\,(C - C_\infty)\,, \tag{4.29}$$

where $\upsilon = \dfrac{\mu}{\rho}$ represents the momentum diffusivity, $\alpha = \dfrac{\kappa}{\left(\rho C_p\right)_f}$ represents the thermal diffusivity and $\Lambda = \dfrac{\left(\rho C_p\right)_p}{\left(\rho C_p\right)_f}$ is the effective heat capacity ratio of the nanoparticle material to the effective heat capacity of the fluid.

The boundary conditions for the problem are given by

$$\begin{cases} u = U_w(x) = bx, \quad v = 0, \quad w = 0, \quad T = T_w, \quad D_B \dfrac{\partial C}{\partial y} + \dfrac{D_T}{T_\infty}\dfrac{\partial T}{\partial y} = 0, \quad at \quad y = 0, \\ u \to 0, \quad w \to 0, \quad T \to T_\infty, \quad C \to C_\infty, \quad as \quad y \to \infty, \end{cases} \tag{4.30}$$

where $U_w(x) = bx$ represents the stretching surface velocity in which $b > 0$ is the stretching rate.

4.2.4 Similarity Transformation

We consider coupled non-linear PDEs (4.25)- (4.29), whose closed-form solutions are challenging to find. Hence, the following transformation equations are introduced to simplify the analysis by reducing the governing equations into a system of ODEs.

$$\begin{aligned} &\eta = \sqrt{\frac{b}{\upsilon}}y, \quad \psi = \sqrt{b\upsilon}xf(\eta), \quad w = U_w(x)h(\eta) = bxh(\eta), \\ &\theta(\eta) = \frac{T - T_\infty}{T_w - T_\infty}, \quad \phi(\eta) = \frac{C - C_\infty}{C_w - C_\infty}, \end{aligned} \tag{4.31}$$

where η is the new similitude variable, $f(\eta)$ is the dimensionless stream function, $h(\eta)$ is the dimensionless cross flow velocity, $\theta(\eta)$ is dimensionless temperature distribution, $\phi(\eta)$ is the nondimensional nanoparticles concentration and ψ is the flow function defined by $u = \dfrac{\partial \psi}{\partial y} \quad and \quad v = -\dfrac{\partial \psi}{\partial x}$.

Based on the assumption, the flow is considered in the $x-$ and $z-$ directions only. So, we need to compute the necessary partial derivatives of u and w using the above similarity transformations.

$$\begin{cases} \dfrac{\partial u}{\partial x} = bf', \\ \dfrac{\partial u}{\partial y} = bxf'' \cdot \sqrt{\dfrac{b}{\upsilon}}, \quad \dfrac{\partial u}{\partial z} = 0, \\ \dfrac{\partial^2 u}{\partial y^2} = bxf''' \cdot \dfrac{b}{\upsilon}, \end{cases} \tag{4.32}$$

$$\begin{cases} \dfrac{\partial w}{\partial x} = bh, \\ \dfrac{\partial w}{\partial y} = bxh'\sqrt{\dfrac{b}{\upsilon}}, \quad \dfrac{\partial w}{\partial z} = 0, \\ \dfrac{\partial^2 w}{\partial y^2} = bxh'' \cdot \dfrac{b}{\upsilon} \end{cases} \tag{4.33}$$

The continuity equation (4.25) is identically satisfied when the aforementioned similarity transformations are used. Now the remaining Eqs. (4.26)–(4.29) can also be transformed into their dimensionless ODE through applications of the similarity transformations.

Substituting Eq. (4.32) on the left-hand side (LHS) of Eq. (4.26), we have

$$u\frac{\partial u}{\partial x} + v\frac{\partial u}{\partial y} + w\frac{\partial u}{\partial z} = bxf' \cdot bf' - \sqrt{b\upsilon}f \cdot bxf''\sqrt{\frac{b}{\upsilon}} + 0 = b^2xf'^2 - b^2xff''. \tag{4.34}$$

Similarly, the right-hand side (RHS) of Eq. (4.26) becomes

$$\begin{aligned} &\upsilon\left(1 + \sqrt{2}\Gamma\frac{\partial u}{\partial y}\right)\frac{\partial^2 u}{\partial y^2} - \frac{\sigma B_0^2\left[(1+\beta_e\beta_i)u + \beta_e w\right]}{\rho\left[(1+\beta_e\beta_i)^2 + \beta_e^2\right]} - \frac{\upsilon}{K}u \\ &= \upsilon\left[\left(1 + \sqrt{2}\Gamma bxf'' \cdot \sqrt{\frac{b}{\upsilon}}\right)bxf''' \cdot \frac{b}{\upsilon}\right] - \frac{\sigma B_0^2 bx\left[(1+\beta_e\beta_i)f' + \beta_e h\right]}{\rho\left[(1+\beta_e\beta_i)^2 + \beta_e^2\right]} - \frac{\upsilon bx}{K}f' \\ &= b^2x\left[\left(f''' + \sqrt{2}\Gamma bx \cdot \sqrt{\frac{b}{\upsilon}}f''f'''\right) - \frac{\sigma B_0^2\left[(1+\beta_e\beta_i)f' + \beta_e h\right]}{\rho b\left[(1+\beta_e\beta_i)^2 + \beta_e^2\right]} - \frac{\upsilon}{bK}f'\right]. \end{aligned} \tag{4.35}$$

Dividing the entire equation by b^2x, we obtain the dimensionless ODE form of $x-$ momentum Eq. (4.26) as:

$$f''' - f'^2 + ff'' + \sqrt{2}\Gamma bx \cdot \sqrt{\frac{b}{\upsilon}}f''f''' - \frac{\sigma B_0^2\left[(1+\beta_e\beta_i)f' + \beta_e h\right]}{\rho b\left[(1+\beta_e\beta_i)^2 + \beta_e^2\right]} - \frac{\upsilon}{bK}f' = 0. \tag{4.36}$$

We now extend the similarity transformations to the z-momentum equation. Substituting Eq. (4.33) into the left-hand side (LHS) of Eq. (4.27) yields:

$$u\frac{\partial w}{\partial x} + v\frac{\partial w}{\partial y} + w\frac{\partial w}{\partial z} = bxf' \cdot bh - \sqrt{b\upsilon}f \cdot bxh'\sqrt{\frac{b}{\upsilon}} + 0 = b^2xf'h - b^2xfh' \tag{4.37}$$

And the right-hand side (RHS) of Eq.(4.27) can also be transformed as follows.

$$
\begin{aligned}
&\upsilon\left(1+\sqrt{2}\Gamma\frac{\partial w}{\partial y}\right)\frac{\partial^2 w}{\partial y^2}+\frac{\sigma B_0^2\left[\beta_e u-(1+\beta_e\beta_i)w\right]}{\rho\left[(1+\beta_e\beta_i)^2+\beta_e^2\right]}-\frac{\upsilon}{K}w\\
=&\upsilon\left(1+\sqrt{2}\Gamma bxh'\sqrt{\frac{b}{\upsilon}}\right)bxh''\cdot\frac{b}{\upsilon}+\frac{\sigma B_0^2 bx\left[\beta_e f'-(1+\beta_e\beta_i)h\right]}{\rho\left[(1+\beta_e\beta_i)^2+\beta_e^2\right]}-\frac{\upsilon}{K}bxh\\
=&b^2x\left[\left(h''+\sqrt{2}\Gamma bx\sqrt{\frac{b}{\upsilon}}h'h''\right)+\frac{\sigma B_0^2\left[\beta_e f'-(1+\beta_e\beta_i)h\right]}{\rho b\left[(1+\beta_e\beta_i)^2+\beta_e^2\right]}-\frac{\upsilon}{bK}h\right].
\end{aligned}
\tag{4.38}
$$

Dividing by b^2x, the dimensionless ODE form of the z-momentum equation Eq. (4.27) becomes:

$$
h''-f'h+fh'+\sqrt{2}\Gamma bx\sqrt{\frac{b}{\upsilon}}h'h''+\frac{\sigma B_0^2\left[\beta_e f'-(1+\beta_e\beta_i)h\right]}{\rho b\left[(1+\beta_e\beta_i)^2+\beta_e^2\right]}-\frac{\upsilon}{bK}h=0. \tag{4.39}
$$

To transform the energy equation to its dimensionless form using the similarity transformations (4.31), we compute the following necessary partial derivatives in addition to Eq (4.32) and (4.33).

$$
\begin{cases}
\dfrac{\partial T}{\partial x}=0, \quad \dfrac{\partial T}{\partial y}=(T_w-T_\infty)\theta'\sqrt{\dfrac{b}{\upsilon}}, \quad \dfrac{\partial T}{\partial z}=0,\\
\dfrac{\partial^2 T}{\partial y^2}=(T_w-T_\infty)\theta''\dfrac{b}{\upsilon},\\
\dfrac{\partial C}{\partial y}=(C_w-C_\infty)\phi'\sqrt{\dfrac{b}{\upsilon}}
\end{cases}
\tag{4.40}
$$

The transformation of each term in the energy equation is now carried out as follows. To transform LHS (convection term) of Eq. (4.28), we have

$$
u\frac{\partial T}{\partial x}+v\frac{\partial T}{\partial y}+w\frac{\partial T}{\partial z}=0+(-\sqrt{b\upsilon}f)(T_w-T_\infty)\theta'\sqrt{\frac{b}{\upsilon}}+0=-b(T_w-T_\infty)f\theta'. \tag{4.41}
$$

The dimensionless form of the thermal diffusion term can be expressed as follows.

$$
\alpha\frac{\partial^2 T}{\partial y^2}=\alpha(T_w-T_\infty)\theta''\frac{b}{\upsilon}. \tag{4.42}
$$

The dimensionless form of Nanoparticle diffusion (Brownian and thermophoresis diffusion) can also be transformed as follows.

$$
\Lambda\left(D_B\frac{\partial T}{\partial y}\frac{\partial C}{\partial y}+\frac{D_T}{T_\infty}\left(\frac{\partial T}{\partial y}\right)^2\right)=\frac{\Lambda b}{\upsilon}\left[D_B(T_w-T_\infty)(C_w-C_\infty)\theta'\phi'+\frac{D_T(T_w-T_\infty)^2}{T_\infty}\theta'^2\right]. \tag{4.43}
$$

To transform the nonlinear thermal radiation term $\frac{16\sigma^*}{3k^*(\rho C_p)_f}\frac{\partial}{\partial y}\left(T^3\frac{\partial T}{\partial y}\right)$, define the temperature ratio parameter:

$$\theta_r = \frac{T_w}{T_\infty} \quad \Rightarrow \quad T = T_\infty\left[(\theta_r - 1)\theta + 1\right]. \tag{4.44}$$

Consequently,

$$\begin{aligned} T^3\frac{\partial T}{\partial y} &= T^3\left(\frac{dT}{d\eta}\cdot\frac{d\eta}{dy}\right) = \left(T_\infty^3\left((\theta_r-1)\theta+1\right)^3\right)\left(T_\infty(\theta_r-1)\theta'\sqrt{\frac{b}{\upsilon}}\right) \\ &= T_\infty^4(\theta_r-1)\left((\theta_r-1)\theta+1\right)^3\theta'\sqrt{\frac{b}{\upsilon}}, \end{aligned} \tag{4.45}$$

and differentiating w.r.t. y

$$\begin{aligned} \frac{\partial}{\partial y}\left(T^3\frac{\partial T}{\partial y}\right) &= \frac{d}{d\eta}\left(T^3\frac{\partial T}{\partial y}\right)\cdot\frac{d\eta}{dy} \\ &= T_\infty^4(\theta_r-1)\cdot\frac{b}{\upsilon}\cdot\Big[3\left((\theta_r-1)\theta+1\right)^2(\theta_r-1)\theta'^2 \\ &\quad + \left((\theta_r-1)\theta+1\right)^3\theta''\Big] \\ &= T_\infty^3(T_w-T_\infty)\frac{b}{\upsilon}\Big[3\left((\theta_r-1)\theta+1\right)^2(\theta_r-1)\theta'^2 \\ &\quad + \left((\theta_r-1)\theta+1\right)^3\theta''\Big]. \end{aligned} \tag{4.46}$$

So, substituting Eq.(4.46) into the radiation term, we obtain:

$$\begin{aligned} \frac{16\sigma^*}{3k^*(\rho C_p)_f}\frac{\partial}{\partial y}\left(T^3\frac{\partial T}{\partial y}\right) = &\frac{16\sigma^* T_\infty^3(T_w-T_\infty)}{3k^*(\rho C_p)_f}\frac{b}{\upsilon}\Big[3\left((\theta_r-1)\theta+1\right)^2(\theta_r-1)\theta'^2 \\ &+ \left((\theta_r-1)\theta+1\right)^3\theta''\Big]. \end{aligned} \tag{4.47}$$

Transforming the heat source term using the similarity transformation, we have:

$$\frac{Q_0(T-T_\infty)}{(\rho C_p)_f} = \frac{Q_0}{(\rho C_p)_f}(T_w-T_\infty)\theta. \tag{4.48}$$

The dimensionless form of the Joule heating (magnetic dissipation) term can also be derived as follows.

$$\frac{\sigma B_0^2(u^2+w^2)}{(\rho C_p)_f\left[(1+\beta_e\beta_i)^2+\beta_e^2\right]} = \frac{\sigma B_0^2(bx)^2\left[f'^2+h^2\right]}{(\rho C_p)_f\left[(1+\beta_e\beta_i)^2+\beta_e^2\right]}. \tag{4.49}$$

The dimensionless form of the viscous dissipation term is transformed using the given similarity transformations as follows.

$$\begin{aligned}
&\frac{\upsilon}{C_p}\left[1+\frac{\Gamma}{\sqrt{2}}\sqrt{\left(\frac{\partial u}{\partial y}\right)^2+\left(\frac{\partial w}{\partial y}\right)^2}\right]\left[\left(\frac{\partial u}{\partial y}\right)^2+\left(\frac{\partial w}{\partial y}\right)^2\right]\\
&=\frac{\upsilon}{C_p}\left[1+\frac{\Gamma}{\sqrt{2}}\sqrt{\left(bxf''\sqrt{\frac{b}{\upsilon}}\right)^2+\left(bxh'\sqrt{\frac{b}{\upsilon}}\right)^2}\right]\left[\left(bxf''\sqrt{\frac{b}{\upsilon}}\right)^2+\left(bxh'\sqrt{\frac{b}{\upsilon}}\right)^2\right]\\
&=\frac{b^3x^2}{C_p}\left[1+\frac{\Gamma}{\sqrt{2}}bx\sqrt{\frac{b}{\upsilon}}\sqrt{(f'')^2+(h')^2}\right]\left[(f'')^2+(h')^2\right].
\end{aligned} \tag{4.50}$$

By combining Eqs. (4.41)–(4.43), (4.47)–(4.50), and then dividing the result by $\alpha(T_w-T_\infty)\frac{b}{\upsilon}$, the energy equation in its non-dimensional form becomes:

$$\begin{aligned}
&\frac{\upsilon}{\alpha}f\theta'+\theta''+\frac{\Lambda D_B(C_w-C_\infty)}{\alpha}\theta'\phi'+\frac{\Lambda D_T(T_w-T_\infty)}{\alpha T_\infty}\theta'^2\\
&+\frac{16\sigma^*T_\infty^3}{3k^*(\rho C_p)_f\alpha}\left[3\left((\theta_r-1)\theta+1\right)^2(\theta_r-1)\theta'^2+\left((\theta_r-1)\theta+1\right)^3\theta''\right]\\
&+\frac{Q_0\upsilon}{(\rho C_p)_f\alpha b}\theta+\frac{\sigma B_0^2bx^2\nu\left[f'^2+h^2\right]}{(\rho C_p)_f\alpha(T_w-T_\infty)\left[(1+\beta_e\beta_i)^2+\beta_e^2\right]}\\
&+\frac{b^2x^2\upsilon}{C_p\alpha(T_w-T_\infty)}\left[1+\frac{\Gamma}{\sqrt{2}}bx\sqrt{\frac{b}{\upsilon}}\sqrt{(f'')^2+(h')^2}\right]\left[(f'')^2+(h')^2\right]=0.
\end{aligned} \tag{4.51}$$

The non-dimensionalization of the nanoparticle concentration equation using the similarity transformations in Eq. (4.31) requires applying the following partial derivatives.

$$\begin{cases}
\dfrac{\partial C}{\partial x}=\dfrac{\partial C}{\partial\phi}\dfrac{\partial\phi}{\partial x}=(C_w-C_\infty)\dfrac{\partial\phi}{\partial x}=0 \quad (\text{since } \phi=\phi(\eta), \eta \text{ is independent of } x)\\
\dfrac{\partial C}{\partial z}=(C_w-C_\infty)\dfrac{\partial\phi}{\partial z}=0,\\
\dfrac{\partial^2 C}{\partial y^2}=(C_w-C_\infty)\phi''\dfrac{b}{\upsilon}.
\end{cases} \tag{4.52}$$

By substituting the partial derivatives from Eqs. (4.32), (4.33), (4.40), and (4.52) into Eq. (4.29), the left-hand side transforms as follows.

$$u\frac{\partial C}{\partial x}+v\frac{\partial C}{\partial y}+w\frac{\partial C}{\partial z}=0-\sqrt{b\upsilon}f(C_w-C_\infty)\phi'\sqrt{\frac{b}{\upsilon}}+0=-b(C_w-C_\infty)f\phi', \tag{4.53}$$

while the right-hand side becomes:

$$\begin{aligned} D_B\frac{\partial^2 C}{\partial y^2}+\frac{D_T}{T_\infty}\frac{\partial^2 T}{\partial y^2}-R_0(C-C_\infty) = D_B(C_w-C_\infty)\phi''\frac{b}{\upsilon} \\ +\frac{D_T}{T_\infty}(T_w-T_\infty)\theta''\frac{b}{\upsilon} \\ -R_0(C_w-C_\infty)\phi. \end{aligned} \tag{4.54}$$

Combining Eqs. (4.53) and (4.54) and then dividing by $\frac{bD_B(C_w-C_\infty)}{\upsilon}$, the dimensionless ODE form of the nanoparticle concentration becomes

$$\phi'' = -\frac{\upsilon}{D_B}f\phi' - \frac{D_T(T_w-T_\infty)}{D_B T_\infty(C_w-C_\infty)}\theta'' + \frac{R_0\upsilon}{bD_B}\phi. \tag{4.55}$$

The boundary conditions can be simplified using the previously introduced similarity transformations. From the definition of the similarity variable in Eq. (4.31), $\eta = y\sqrt{\frac{b}{\upsilon}}$, it follows that $\eta = 0$ when $y = 0$, and $\eta \to \infty$ as $y \to \infty$. This relationship allows the boundary conditions to be expressed in terms of the dimensionless variable η, thereby facilitating the conversion of the governing PDEs into ODEs.

At $y = 0$ we have $\eta = 0$ and transformations for the boundary conditions (velocity, temperature, concentration) are summarized below.

$$\begin{cases} u = bxf'(\eta) \Rightarrow u(0) = bxf'(0) = bx \Rightarrow f'(0) = 1, \\ v = -\sqrt{b\upsilon}f(\eta) \Rightarrow v(0) = 0 = -\sqrt{b\upsilon}f(0) \Rightarrow f(0) = 0, \\ w = bxh(\eta) \Rightarrow h(0) = 0, \\ \theta(0) = \dfrac{T(0)-T_\infty}{T_w-T_\infty} = \dfrac{T_w-T_\infty}{T_w-T_\infty} = 1, \\ D_B\dfrac{\partial C}{\partial y}+\dfrac{D_T}{T_\infty}\dfrac{\partial T}{\partial y} = 0 \Rightarrow N_b\phi'(0)+N_t\theta'(0) = 0. \end{cases} \tag{4.56}$$

Also, as $y \to \infty$, $\eta \to \infty$ and consequently we have the following transformations.

$$\begin{cases} u \to 0 \Rightarrow f'(\eta) \to 0, \\ w \to 0 \Rightarrow h(\eta) = 0, \\ \theta(\eta) \to \dfrac{T_\infty-T_\infty}{T_w-T_\infty} = 0, \\ \phi(\eta) \to \dfrac{C_\infty-C_\infty}{C_w-C_\infty} = 0. \end{cases} \tag{4.57}$$

The transformed dimensionless governing equations for momentum Eqs. (4.36) and (4.39), energy Eq. (4.51), and nanoparticle concentration Eq. (4.55) are simplified using the introduced non-dimensional parameters in Table 4.1.

This yields the following system of coupled nonlinear ordinary differential equations:

$$f''' - f'^2 + ff'' + Wef''f''' - \frac{M\left[(1+\beta_e\beta_i)f' + \beta_e h\right]}{(1+\beta_e\beta_i)^2 + \beta_e^2} - Daf' = 0, \tag{4.58}$$

$$h'' + Weh'h'' + fh' - f'h + \frac{M\left[\beta_e f' - (1+\beta_e\beta_i)h\right]}{(1+\beta_e\beta_i)^2 + \beta_e^2} - Dah = 0, \tag{4.59}$$

$$\begin{aligned}\theta'' + Pr\Big[Q_h\theta + \theta' f + \frac{MEc\left(f'^2 + h^2\right)}{(1+\beta_e\beta_i)^2 + \beta_e^2} + Ec\left(1 + \frac{1}{2}We\left(f''^2 + h'^2\right)^{\frac{1}{2}}\right)\left(f''^2 + h'^2\right) \\ + N_b\theta'\phi' + N_t\left(\theta'\right)^2\Big] + R_n\left[\theta''\left(1 + (\theta_r - 1)\theta\right)^3 + 3(\theta_r - 1)\left(1 + (\theta_r - 1)\theta\right)^2\theta'^2\right] = 0,\end{aligned} \tag{4.60}$$

$$\phi'' + Scf\phi' + \frac{N_t}{N_b}\theta'' - ScC_r\phi = 0. \tag{4.61}$$

Rearranging equations (4.58)–(4.61), we have

$$f''' = \frac{\left[f'^2 - ff'' + \dfrac{M}{(1+\beta_e\beta_i)^2 + \beta_e^2}\left[(1+\beta_e\beta_i)f' + \beta_e h\right] + Daf'\right]}{\left[1 + Wef''\right]}, \tag{4.62}$$

$$h'' = \frac{\left[-fh' + f'h - \dfrac{M}{(1+\beta_e\beta_i)^2 + \beta_e^2}\left[\beta_e f' - (1+\beta_e\beta_i)h\right] + Dah\right]}{\left[1 + Weh'\right]}, \tag{4.63}$$

$$\begin{aligned}\theta'' =& \frac{-1}{\left[1 + R_n\left(1 + (\theta_r - 1)\theta\right)^3\right]}\Bigg[Pr\Big(Q_h\theta + \theta' f + \frac{MEc\left(f'^2 + h^2\right)}{(1+\beta_e\beta_i)^2 + \beta_e^2} \\ &+ Ec\left(1 + \frac{1}{2}We\left(f''^2 + h'^2\right)^{\frac{1}{2}}\right)\left(f''^2 + h'^2\right) + N_b\theta'\phi' + N_t\left(\theta'\right)^2\Big) \\ &+ R\left[3(\theta_r - 1)\left(1 + (\theta_r - 1)\theta\right)^2\theta'^2\right]\Bigg],\end{aligned} \tag{4.64}$$

$$\phi'' = -Scf\phi' + ScC_r\phi - \frac{N_t}{N_b}\theta''. \tag{4.65}$$

The transformed boundary conditions are

$$\begin{cases} f'(0) = 1, \quad f(0) = 0, \quad h(0) = 0, \quad \theta(0) = 1, \quad N_b\phi'(0) + N_t\theta'(0) = 0, at \;\; \eta = 0, \\ f' \to 0, \quad h \to 0, \quad \theta \to 0, \quad \phi \to 0 \quad as \;\; \eta \to \infty. \end{cases} \tag{4.66}$$

The dimensionless parameters existing in Equations (4.58)– (4.61) can be described as follows.

Table 4.1: Dimensionless parameters and their definitions

Symbol & Formula	Description
$M = \dfrac{\sigma B_0^2}{\rho b}$	Magnetic field parameter
$We = \sqrt{2}\Gamma bx\sqrt{\dfrac{b}{\upsilon}}$	Williamson fluid parameter
$R_n = \dfrac{16\sigma^* T_\infty^3}{3\kappa k^*}$	Nonlinear thermal radiation parameter
$\theta_r = \dfrac{T_w}{T_\infty}$	Ratio temperature parameter
$Pr = \dfrac{\upsilon}{\alpha}$	Prandtl number
$Sc = \dfrac{\upsilon}{D_B}$	Schmidt number
$C_r = \dfrac{R_0}{b}$	Scaled chemical reaction parameter
$Q_h = \dfrac{Q_0}{\left(\rho C_p\right)_f b}$	Heat generation ($Q_h > 0$) or absorption parameter ($Q_h < 0$)
$Ec = \dfrac{U_w^2(x)}{C_p\left(T_w - T_\infty\right)}$	Eckert number
$Da = \dfrac{\upsilon}{bK}$	Darcy number
$N_b = \dfrac{\Lambda D_B(C_w - C_\infty)}{\upsilon}$	Brownian motion parameter $\left(\Lambda = \dfrac{\left(\rho C_p\right)_p}{\left(\rho C_p\right)_f}\right)$
$N_t = \dfrac{\Lambda D_T\left(T_w - T_\infty\right)}{\upsilon T_\infty}$	Thermophoretic parameter

4.2.5 Engineering Relevant Quantities in Boundary Layer

In the study of boundary layer flows, particularly in the context of the non-Newtonian Williamson fluid, certain physical quantities are of prime practical importance. These include the local skin friction coefficient (C_f), the local Nusselt number (Nu_x), and the local Sherwood number (Sh_x). These quantities respectively measure the momentum transfer, heat transfer, and mass transfer at the fluid–solid interface, and are essential in characterizing the efficiency of thermal and solutal transport in engineering systems.

4.2.5.1 Skin Friction Coefficients

The local skin friction coefficient quantifies the tangential shear force exerted by the fluid on the surface per unit dynamic pressure. Because of the three-dimensional nature of the flow, the surface drag is described by two distinct components of skin friction.

$$C_{fx} = \frac{\tau_{wx}}{\rho U_w^2}, \quad C_{fz} = \frac{\tau_{wz}}{\rho U_w^2}, \tag{4.67}$$

where τ_{wx} and τ_{wz} represent the wall shear stresses in the $x-$ and $z-$ directions, respectively. For the Williamson fluid model, these incorporate shear-thinning effects via the relaxation time Γ and shear rate $\dot{\gamma}$.

From the constitutive equation Eq. (2.7) and (2.13), the deviatoric stress tensor components at the wall ($y = 0$) are:

$$\tau_{yx} = \mu_0 (1 + \Gamma\dot{\gamma})\left(\frac{\partial u}{\partial y} + \frac{\partial v}{\partial x}\right), \quad \tau_{yz} = \mu_0 (1 + \Gamma\dot{\gamma})\left(\frac{\partial v}{\partial z} + \frac{\partial w}{\partial y}\right), \tag{4.68}$$

where μ_0 is the reference dynamic viscosity of the fluid and Γ is the Williamson fluid parameter (related to the time constant of the fluid).

Under boundary layer assumptions ($v = 0$ at $y = 0$, $\partial v/\partial x \approx 0$, $\partial v/\partial z \approx 0$), and using the shear rate definition Eq. (2.12), $\dot{\gamma}$ simplifies to:

$$\dot{\gamma} \approx \frac{1}{\sqrt{2}}\left|\frac{\partial u}{\partial y}\right| \quad (\text{for } \tau_{wx}), \quad \dot{\gamma} \approx \frac{1}{\sqrt{2}}\left|\frac{\partial w}{\partial y}\right| \quad (\text{for } \tau_{wz}). \tag{4.69}$$

Thus, the wall shear stresses reduce to:

$$\tau_{wx} = \mu_0 \left[\frac{\partial u}{\partial y} + \frac{\Gamma}{\sqrt{2}}\left(\frac{\partial u}{\partial y}\right)^2\right]_{y=0}, \quad \tau_{wz} = \mu_0 \left[\frac{\partial w}{\partial y} + \frac{\Gamma}{\sqrt{2}}\left(\frac{\partial w}{\partial y}\right)^2\right]_{y=0}. \tag{4.70}$$

Using similarity transformations Eq. (4.31):

$$\eta = y\sqrt{\frac{b}{\upsilon}}, \quad u = bxf'(\eta), \quad w = bxh(\eta), \tag{4.71}$$

the velocity gradients at $y = 0$ ($\eta = 0$) are as follows.

$$\begin{cases} \left.\dfrac{\partial u}{\partial y}\right|_{y=0} = bxf''(0)\sqrt{\dfrac{b}{\upsilon}}, \\ \left.\dfrac{\partial w}{\partial y}\right|_{y=0} = bxh'(0)\sqrt{\dfrac{b}{\upsilon}}. \end{cases} \tag{4.72}$$

Substituting Eq. (4.72) into Eq. (4.70):

$$\tau_{wx} = \mu_0\left[bxf''(0)\sqrt{\frac{b}{\upsilon}} + \frac{\Gamma}{\sqrt{2}}\left(bxf''(0)\sqrt{\frac{b}{\upsilon}}\right)^2\right] = \mu_0 bx\sqrt{\frac{b}{\upsilon}}\left[f''(0) + \frac{\Gamma}{\sqrt{2}}bx\sqrt{\frac{b}{\upsilon}}f''(0)^2\right],$$
$$\tau_{wz} = \mu_0\left[bxh'(0)\sqrt{\frac{b}{\upsilon}} + \frac{\Gamma}{\sqrt{2}}\left(bxh'(0)\sqrt{\frac{b}{\upsilon}}\right)^2\right] = \mu_0 bx\sqrt{\frac{b}{\upsilon}}\left[h'(0) + \frac{\Gamma}{\sqrt{2}}bx\sqrt{\frac{b}{\upsilon}}h'(0)^2\right]. \tag{4.73}$$

Consequently, the skin friction coefficients Eq. (4.67) can be non-dimentionalized as follows.

$$\begin{aligned} C_{fx}\sqrt{\mathrm{Re}_x} &= \frac{\sqrt{\mathrm{Re}x}}{\rho(bx)^2}\cdot\mu_0 bx\sqrt{\frac{b}{\upsilon}}\left[f''(0) + \frac{\Gamma}{\sqrt{2}}bx\sqrt{\frac{b}{\upsilon}}f''(0)^2\right] \\ &= f''(0) + \frac{\Gamma}{\sqrt{2}}bx\sqrt{\frac{b}{\upsilon}}f''(0)^2, \\ C_{fz}\sqrt{\mathrm{Re}_x} &= \frac{\sqrt{\mathrm{Re}x}}{\rho(bx)^2}\cdot\mu_0 bx\sqrt{\frac{b}{\upsilon}}\left[h'(0) + \frac{\Gamma}{\sqrt{2}}bx\sqrt{\frac{b}{\upsilon}}h'(0)^2\right] \\ &= h'(0) + \frac{\Gamma}{\sqrt{2}}bx\sqrt{\frac{b}{\upsilon}}h'(0)^2, \end{aligned} \tag{4.74}$$

where $\mathrm{Re}x = \dfrac{xU_w}{\upsilon} = \frac{bx^2}{\upsilon}$ is local Reynolds number and U_w is the wall stretching velocity. Defining the Weissenberg number (Williamson parameter) $We = \sqrt{2}\Gamma bx\sqrt{\frac{b}{\upsilon}}$, Eq. (4.74) simplifies to:

$$\begin{aligned} C_{fx}\sqrt{\mathrm{Re}x} &= f''(0) + \frac{We}{2}\left(f''(0)\right)^2, \\ C_{fz}\sqrt{\mathrm{Re}_x} &= h'(0) + \frac{We}{2}\left(h'(0)\right)^2. \end{aligned} \tag{4.75}$$

4.2.5.2 Local Nusselt Number

The local Nusselt number is a dimensionless measure of convective heat transfer relative to conductive heat transfer across the thermal boundary layer. It is defined by:

$$Nu_x = \frac{xq_w}{\kappa(T_w - T_\infty)} \tag{4.76}$$

where q_w is the local surface heat flux and κ is the thermal conductivity of the fluid. For the radiation-enhanced heat transfer case, the total heat flux at the wall incorporates both conduction and radiation effects, and is given by:

$$q_w = -\left(k + \frac{16\sigma^*}{3k^*}T^3\right)\left.\frac{\partial T}{\partial y}\right|_{y=0} \tag{4.77}$$

Substituting Eq. (4.77) into Eq. (4.76):

$$Nu_x = \frac{-x}{T_w - T_\infty}\left(1 + \frac{16\sigma^* T_w^3}{3\kappa k^*}\right)\frac{\partial T}{\partial y}\bigg|_{y=0}. \tag{4.78}$$

Using the similarity transformation of Eq. (4.31) for temperature:

$$\theta(\eta) = \frac{T - T_\infty}{T_w - T_\infty}, \quad \frac{\partial T}{\partial y}\bigg|_{y=0} = (T_w - T\infty)\sqrt{\frac{b}{\upsilon}}\theta'(0), \tag{4.79}$$

Eq. (4.78) becomes:

$$Nu_x = -\frac{x}{T_w - T_\infty}\left(1 + \frac{16\sigma^* T_w^3}{3\kappa k^*}\right)(T_w - T_\infty)\sqrt{\frac{b}{\upsilon}}\theta'(0) = -x\sqrt{\frac{b}{\upsilon}}\left(1 + \frac{16\sigma^* T_w^3}{3kk^*}\right)\theta'(0). \tag{4.80}$$

With the temperature ratio $\theta_r = \dfrac{T_w}{T_\infty}$ and radiation parameter $R_n = \dfrac{16\sigma^* T_\infty^3}{3\kappa k^*}$, we obtain:

$$T_w^3 = \theta_r^3 T_\infty^3, \quad \frac{16\sigma^* T_w^3}{3kk^*} = R_n\theta_r^3. \tag{4.81}$$

Thus,

$$Nu_x = -x\sqrt{\frac{b}{\upsilon}}\left(1 + R_n\theta_r^3\right)\theta'(0). \tag{4.82}$$

Finally, the dimensionless form the Nusselt number is:

$$\frac{Nu_x}{\sqrt{\mathrm{Re}_x}} = -\left(1 + R_n\theta_r^3\right)\theta'(0). \tag{4.83}$$

4.2.5.3 Local Sherwood Number

The local Sherwood number represents the dimensionless mass transfer rate at the wall and is defined as:

$$Sh_x = \frac{xq_m}{D_B(C_w - C_\infty)} \tag{4.84}$$

where q_m is the mass flux at the surface.

The wall mass flux follows Fick's law:

$$q_m = -D_B\frac{\partial C}{\partial y}\bigg|_{y=0}. \tag{4.85}$$

Substituting Eq. (4.85) into Eq. (4.84), we obtain:

$$Sh_x = \frac{-x}{C_w - C_\infty}\frac{\partial C}{\partial y}\bigg|_{y=0}. \tag{4.86}$$

Using the similarity transformation for concentration:

$$\phi(\eta) = \frac{C - C_\infty}{C_w - C_\infty}, \quad \left.\frac{\partial C}{\partial y}\right|_{y=0} = (C_w - C\infty)\sqrt{\frac{a_1}{\nu}}\phi'(0), \tag{4.87}$$

Eq. (4.86) simplifies to:

$$Sh_x = -\frac{x}{C_w - C_\infty} \cdot (C_w - C_\infty)\sqrt{\frac{b}{\upsilon}}\phi'(0) = -x\sqrt{\frac{b}{\upsilon}}\phi'(0). \tag{4.88}$$

The dimensionless form of the Sherwood number is:

$$\frac{Sh_x}{\sqrt{\mathrm{Re}_x}} = -\phi'(0). \tag{4.89}$$

4.3 Method of Solution

In this study, the shooting technique in conjunction with the fifth-order Runge-Kutta (RK5) method is utilized to solve the governing equations of the MHD Williamson nanofluid flow over a stretching sheet by considering the effects of pertinent physical parameters. The numerical computations are performed using an open-access Python programming tool. The higher-order differential equations are converted into a system of first-order ordinary differential equations (ODEs) using auxiliary variables. The initial values and boundary conditions are specified, and the RK5 method is employed to integrate the ODEs numerically. We adjust the initial guess for the unknown boundary conditions iteratively based on the residual. Once the desired accuracy is achieved, we obtain the final solution by determining the values of the variables throughout the domain. The numerical solutions are found with a step size of 0.1 and an error tolerance of 10^{-7}. The Python programming tool facilitates the implementation and analysis of the numerical method, allowing for efficient computation and visualization of the results.

Accordingly, in order to apply the shooting technique, the system of non-linear ODEs expressed in equations (4.62)-(4.65) subject to the boundary conditions (4.66) are reduced into a system of first order through substituting $(y_1, y_2, y_3, y_4, y_5, y_6, y_7, y_8, y_9) = (f, f', f'', h, h', \theta, \theta', \phi, \phi')$, which is written as the following system of ODE's

$$\begin{cases} y_1' = y_2 \\ y_2' = y_3 \\ y_3' = \dfrac{\left[y_2^2 - y_1 y_3 + \dfrac{M}{(1+\beta_e\beta_i)^2 + \beta_e^2}\left[(1+\beta_e\beta_i)y_2 + \beta_e y_4\right] + Da y_2\right]}{[1 + We y_3]} \\ y_4' = y_5 \\ y_5' = \dfrac{\left[-y_1 y_5 + y_2 y_4 - \dfrac{M}{(1+\beta_e\beta_i)^2 + \beta_e^2}\left[\beta_e y_2 - (1+\beta_e\beta_i)y_4\right] + Da y_4\right]}{[1 + We y_5]} \\ y_6' = y_7 \\ y_7' = \dfrac{-1}{\left[1 + R_n\left(1 + (\theta_r - 1)y_6\right)^3\right]}\Bigg[Pr\Bigg(Q_h y_6 + y_7 y_1 + \dfrac{MEc}{(1+\beta_e\beta_i)^2 + \beta_e^2}\left(y_2^2 + y_4^2\right) \\ \qquad + Ec\left(1 + \dfrac{1}{2}We\left(y_3^2 + y_5^2\right)^{\frac{1}{2}}\right)\left(y_3^2 + y_5^2\right) + N_b y_7 y_9 \\ \qquad + N_t y_7^2\Bigg) + R_n\left[3(\theta_r - 1)\left(1 + (\theta_r - 1)y_6\right)^2 y_7^2\right]\Bigg] \\ y_8' = y_9 \\ y_9' = -Sc y_1 y_9 + Sc C_r y_8 - \dfrac{N_t}{N_b} y_7' \end{cases} \tag{4.90}$$

with corresponding initial conditions

$$\begin{cases} y_1(0) = 0, \\ y_2(0) = 1, \\ y_3(0) = \xi_1, \\ y_4(0) = 0, \\ y_5(0) = \xi_2, \\ y_6(0) = 1, \\ y_7(0) = \xi_3, \\ y_8(0) = \xi_4, \\ N_b y_9(0) + N_t y_7(0) = 0, \end{cases} \tag{4.91}$$

in which ξ_1, ξ_2, ξ_3 and ξ_4 are the missing initial conditions.

4.4 Results and Discussion

In this section, we present the numerical results obtained for the problem considering various physical effects. The governing equations, given by Eqs. (4.58)-(4.61), along with the corresponding boundary conditions (4.66), were solved numerically using the

Runge-Kutta (RK) method with Shooting technique.

We conducted a comprehensive investigation by varying the physical parameters involved in the problem. Numerical computations were carried out to determine the values of various physical quantities of interest, including velocity, temperature, nanoparticle concentration, skin friction coefficient, Nusselt number, and Sherwood number. These quantities were evaluated over a wide range of parameter values, enabling a detailed examination of the influence of each parameter on the flow, heat transfer, and mass transfer characteristics. The obtained results are presented graphically in the form of figures, with each figure illustrating the variation of a specific physical quantity with respect to the corresponding parameter. These graphical representations provide valuable insights into the behavior of the system under consideration and clearly demonstrate the effects of different parameters on the velocity and temperature profiles, as well as on the distribution of nanoparticle concentration.

4.4.1 Validation of the Numerical Method

We conducted a comparative analysis between our numerical findings and the results reported in previous studies. The purpose of this comparison was to validate the accuracy of our numerical solution and assess the agreement with existing literature. Tables 4.2 summarizes the comparison between our results and those obtained from previous investigations. The results of the comparison indicate a generally excellent agreement between our findings and the results reported in earlier studies. The minimal discrepancies observed can be attributed to differences in numerical methods, discretization schemes, and boundary conditions employed in the various investigations. Overall, the close agreement between our numerical results and the existing literature validates the accuracy and reliability of our computational approach.

Table 4.2: Comparison of $-\theta'(0)$ values with Khan and Pop [1], Bouslimi et al. [2] and the current investigation for $Pr = Sc = 10$, and in the absence of M, Da, Ec, C_r, Q_h, R_n, θ_r, We, β_i, and β_e.

N_t	$N_b = 0.1$			$N_b = 0.2$		
	Khan and Pop [1]	Bouslimi et al. [2]	Present Study	Khan and Pop [1]	Bouslimi et al. [2]	Present Study
0.1	0.9524	0.9501	0.952181	0.5056	0.5065	0.505906
0.2	0.6932	0.6910	0.693212	0.3654	0.3646	0.365712
0.3	0.5201	0.5237	0.520229	0.2731	0.2735	0.273434
0.4	0.4026	0.4083	0.402775	0.2110	0.2124	0.211289
0.5	0.3211	0.3270	0.328232	0.1681	0.1710	0.171994

4.4.2 Profiles of Velocity, Temperature and Nanoparticle concentration with Prominent Flow Parameters

The influence of Hall currents (β_e), ion slip (β_i), Williamson parameter (We), non-linear thermal radiation parameter (R_n), and Eckert number (Ec) on the non-dimensional velocities f' and h, temperature (θ), and concentration (ϕ) are shown graphically in Figs. 4.2-4.18. The remaining physical parameters are kept constant throughout the study, with the following corresponding values: $Sc = 2$, $Pr = 5$, $C_r = 0.6$, $N_b = N_t = Da = M = 0.5$, $R_n = 1.2$, $Ec = 0.4$, $\theta_r = 1.2$, $We = 0.2$, $Q_h = -0.1$, $\beta_e = 2$ and $\beta_i = 1$, unless otherwise specified in the plots. The ranges of parameters used in the study are as follows: $2 \leq \beta_e \leq 10$, $1 \leq \beta_i \leq 2$, $0.1 \leq R_n \leq 2$, $0.1 \leq We \leq 0.5$, $0.1 \leq Ec \leq 1.5$, $1 \leq C_r \leq 5$, $0 \leq M \leq 2$, $0.1 \leq \theta_r \leq 1.5$, and $0 \leq Da \leq 2$.

Figs. 4.2–4.5 display that as the Hall parameter increases, the secondary velocity, temperature and concentration profiles decrease, while the principal velocity of the MHD Williamson nanofluid flow increase. Physically, this can be attributed to the Lorentz force induced by the magnetic field, which acts perpendicular to the flow direction. The Lorentz force restrains the fluid motion, resulting in a reduction in the principal velocity. But this resistive force is decreased when the Hall parameter is included since it lowers effective conductivity. Consequently, increasing the Hall parameter facilitates the fluid flow and also limits the rise in temperature and concentration profiles within the nanofluid.

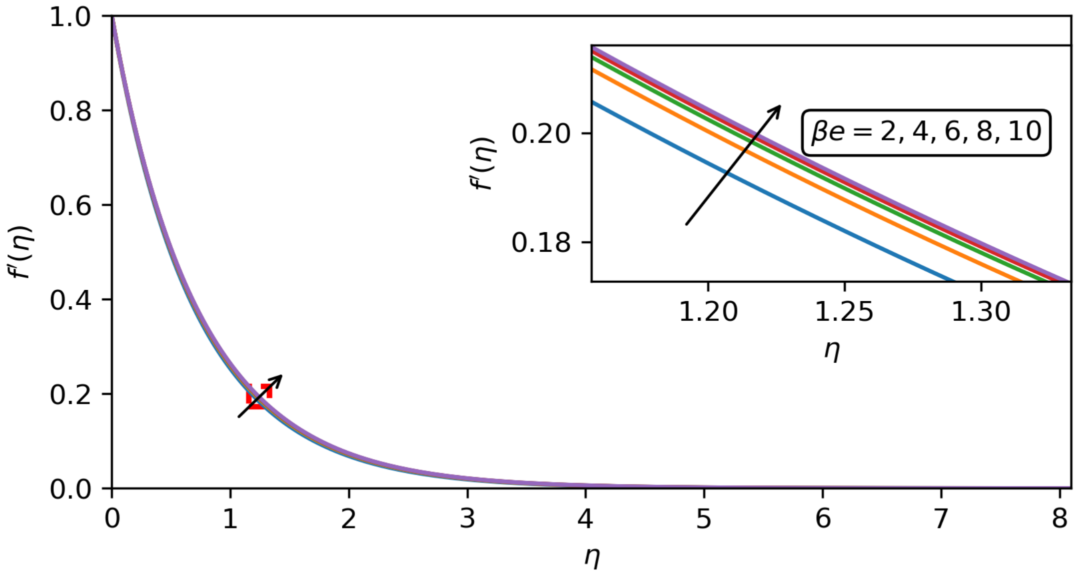

Figure 4.2: The principal velocity profile $f'(\eta)$ with Hall parameter β_e.

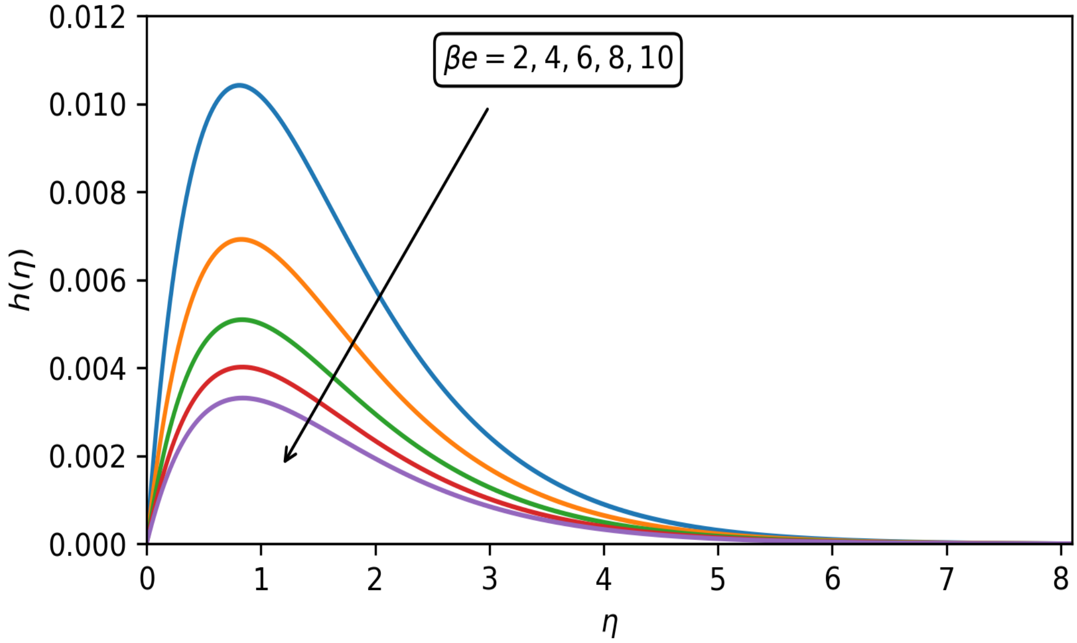

Figure 4.3: The secondary velocity profile $h(\eta)$ with Hall parameter β_e.

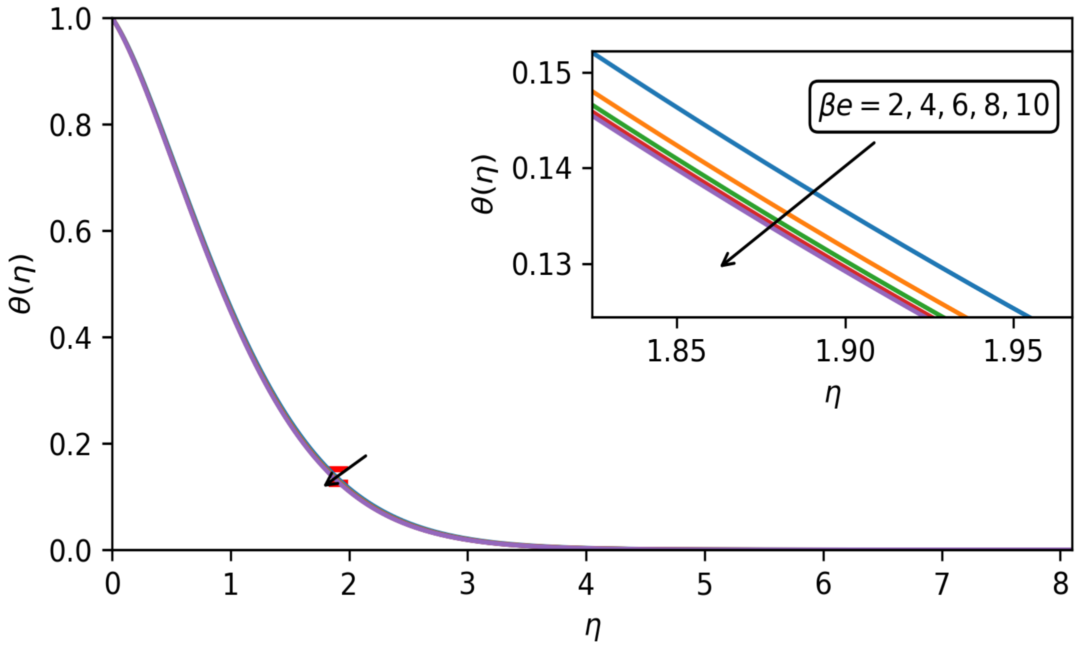

Figure 4.4: Temperature profile $\theta(\eta)$ with Hall parameter β_e.

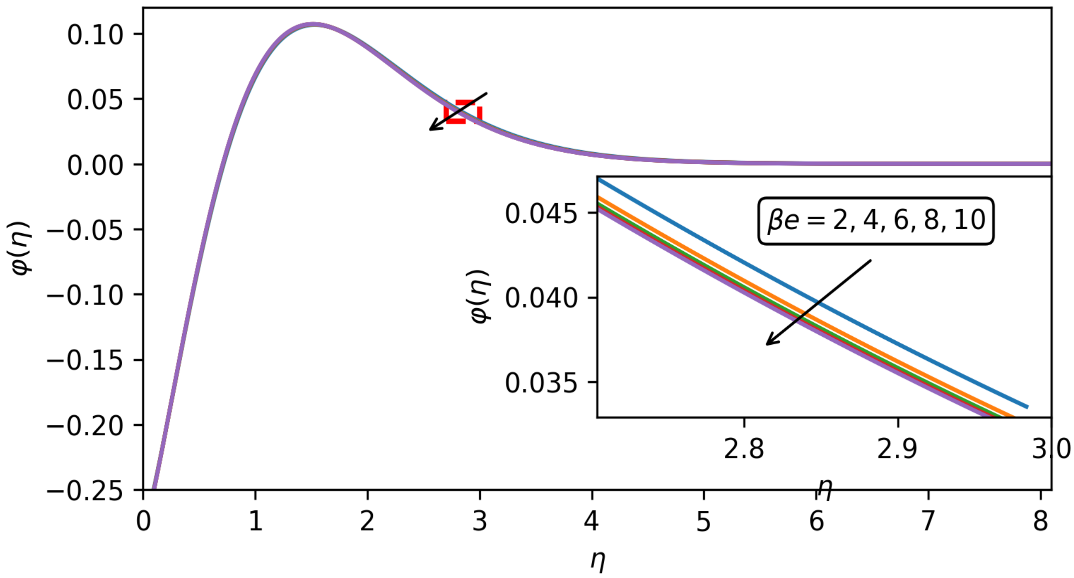

Figure 4.5: Concentration profile $\phi(\eta)$ with Hall parameter β_e.

The ion slip effect produces similar results to the Hall parameter as presented in Figs 4.6–4.9, with increasing principal velocity profile and decreasing secondary velocity, temperature and concentration profiles. Physically, the ion slip effect refers to the relative motion between ions and the fluid in an electrically conducting flow. The ion slip effect influences the flow dynamics by altering the velocity distribution and reducing the transport of heat and particles in the nanofluid, causing a decrease in the temperature and concentration profiles.

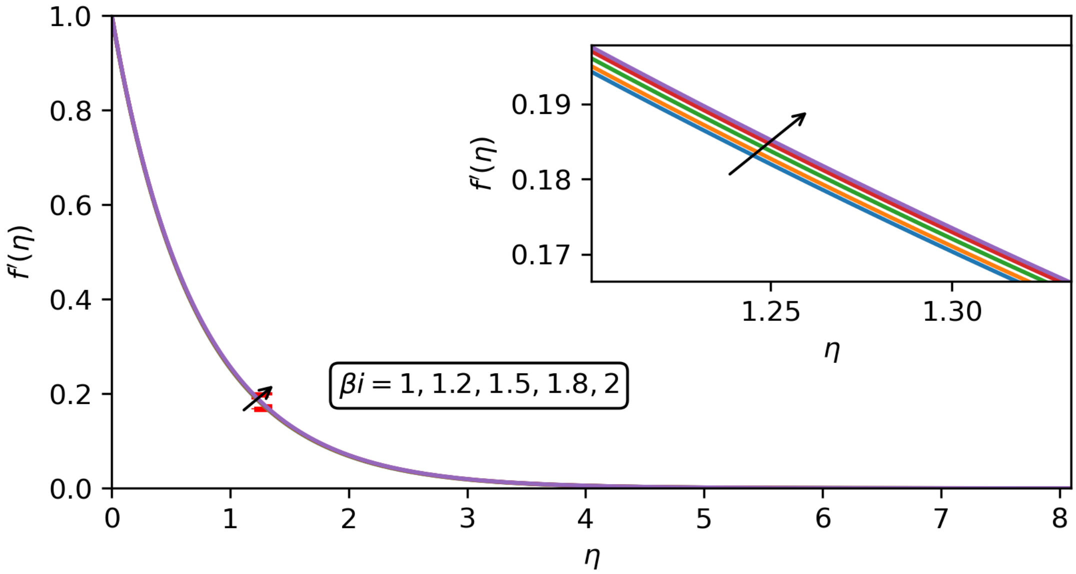

Figure 4.6: The principal velocity profile $f'(\eta)$ with ion slip parameter β_i.

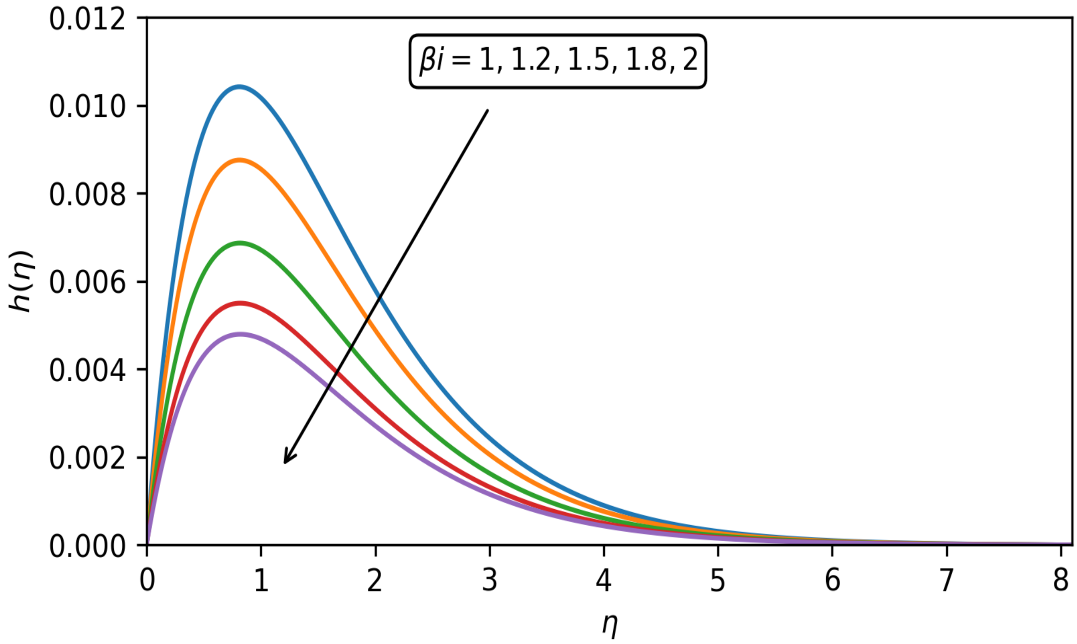

Figure 4.7: The secondary velocity profile $h(\eta)$ with ion slip parameter β_i.

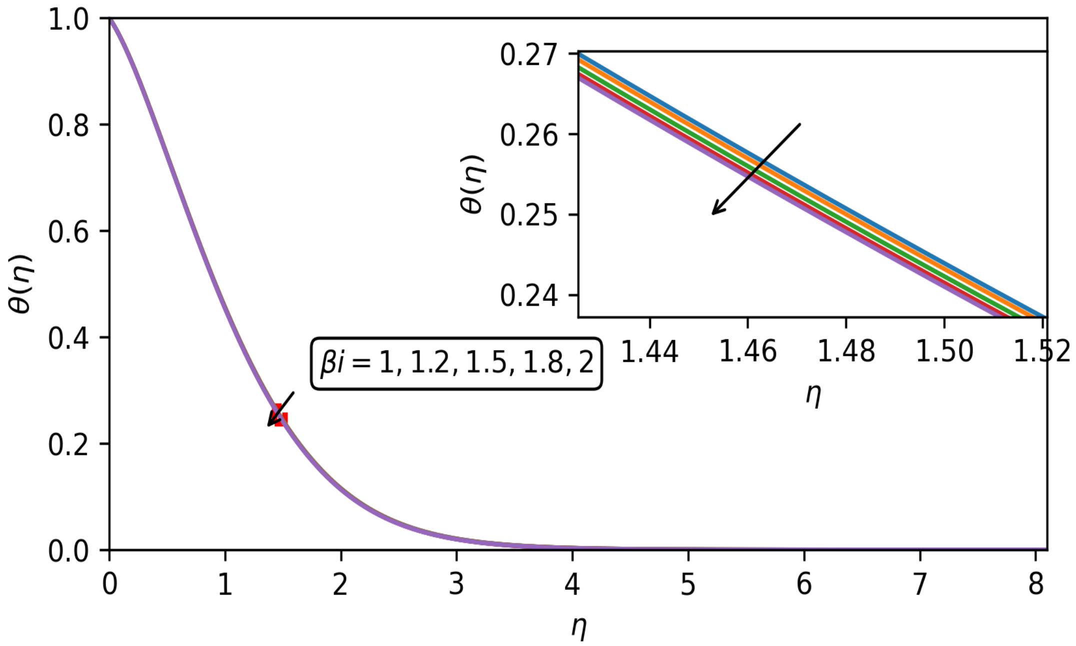

Figure 4.8: Temperature profile $\theta(\eta)$ with ion slip parameter β_i.

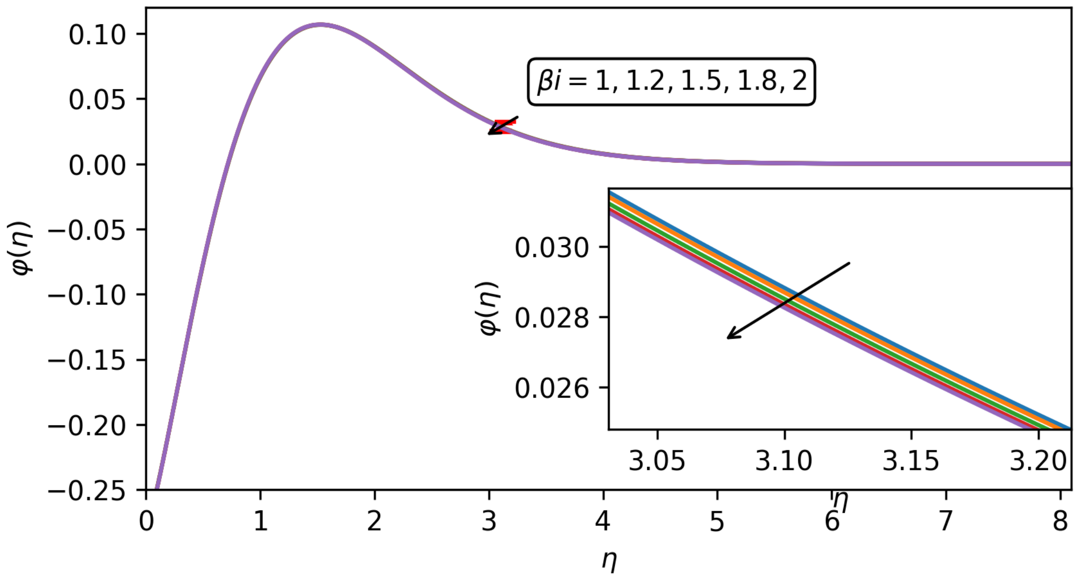

Figure 4.9: Concentration profile $\phi(\eta)$ with ion slip parameter β_i.

As depicted in Figs.4.10 and 4.11, with an increase in nonlinear thermal radiation parameter, the temperature and concentration profiles are enhanced. This is due to the fact that, as the nonlinear thermal radiation effect increases, more energy is transferred through radiation, leading to enhanced temperature and concentration profiles. This is because the thermal radiation provides an additional heat source, resulting in higher local temperatures and increased concentration gradients as well as the boundary layer's thickness.

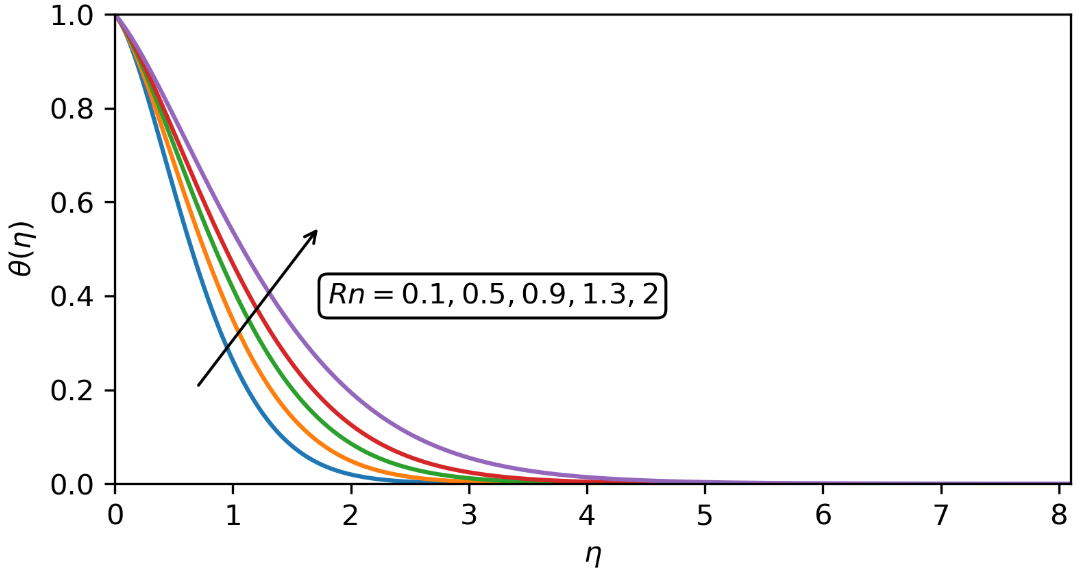

Figure 4.10: Temperature profile $\theta(\eta)$ with nonlinear thermal radiation parameter R_n.

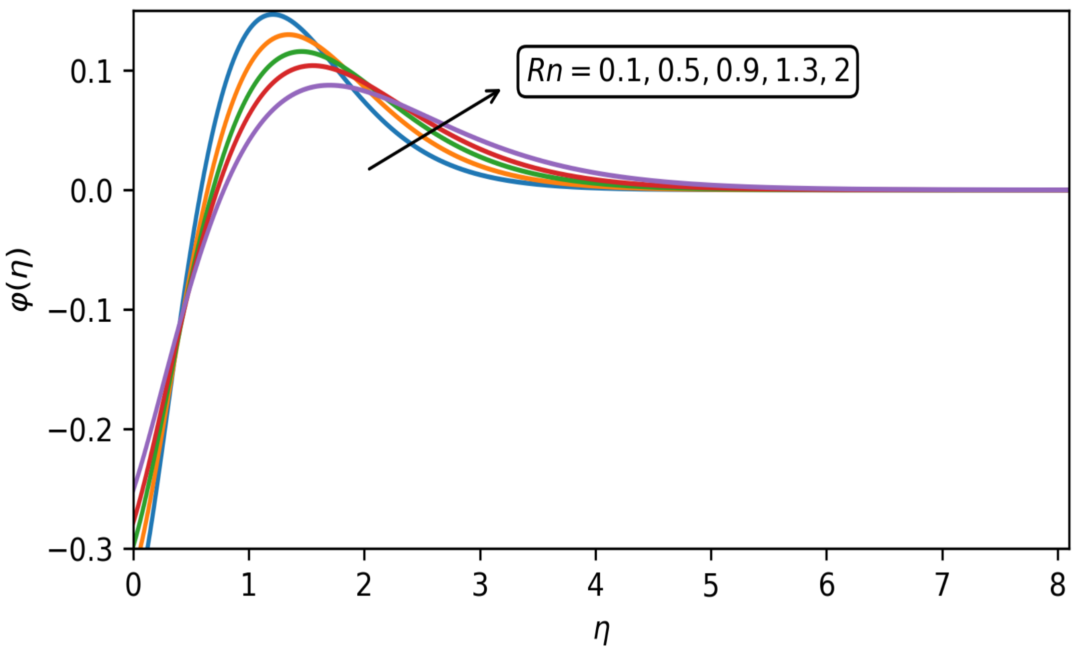

Figure 4.11: Concentration profile $\phi(\eta)$ with nonlinear thermal radiation parameter R_n.

As illustrated in Figs.4.12–4.15, increasing the Williamson parameter, characterized by the Weissenberg number (We), leads to a decrease in the velocity profiles, while the temperature and concentration profiles increase. The Williamson parameter represents the viscoelastic behavior of the fluid flow. When the Williamson parameter (We) increases, it indicates a higher degree of elasticity and viscoelastic effects in the flow. As a consequence, the flow experiences stronger resistance to deformation and exhibits more pronounced viscoelastic behavior. The viscoelastic effects cause the fluid to exhibit more elasticity, leading to a reduction in the fluid's ability to deform under the influence of external forces. Consequently, the flow velocity decreases. On the other hand, the viscoelastic effects introduce additional mechanisms for heat and mass transport, such as elongational flow and stretching of fluid elements, which promote higher temperature and concentration gradients within the flow field.

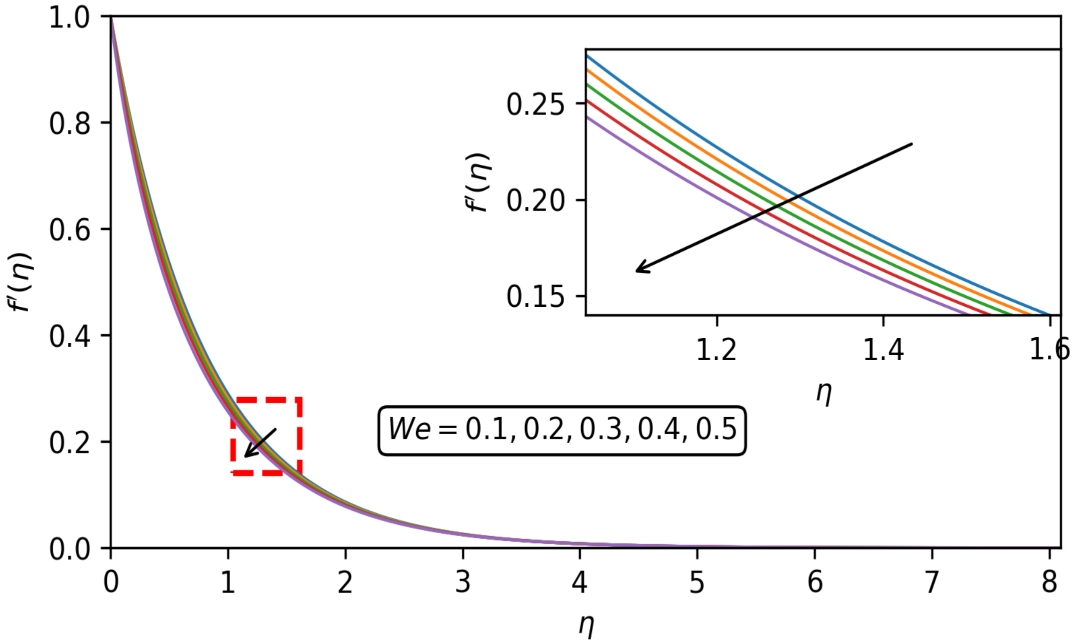

Figure 4.12: The principal velocity profile $f'(\eta)$ with Williamson parameter We.

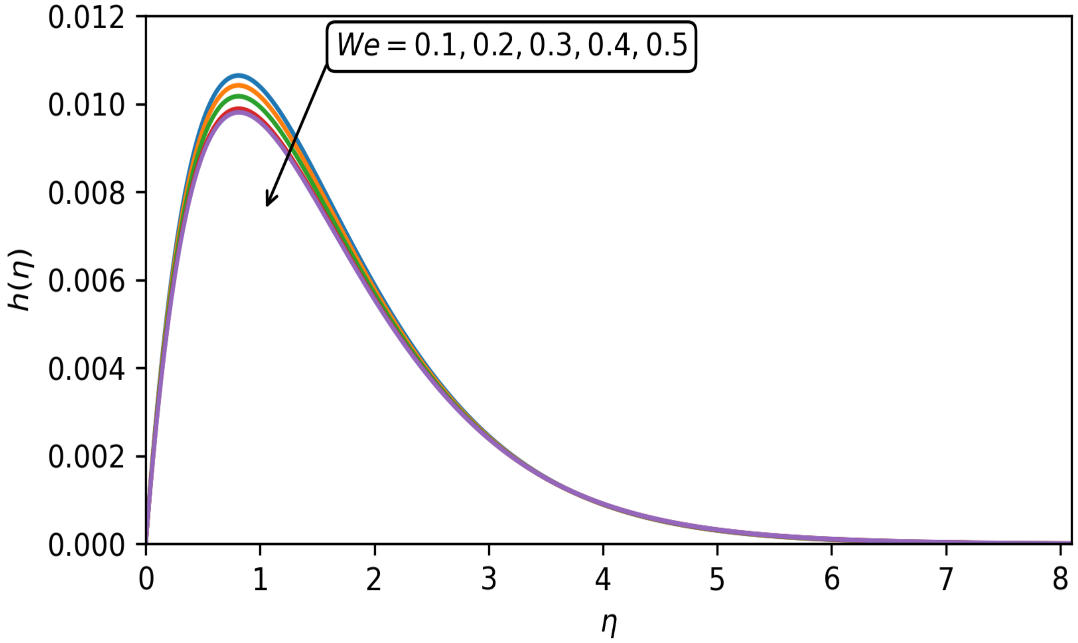

Figure 4.13: The secodary velocity profile $h(\eta)$ with Williamson parameter We.

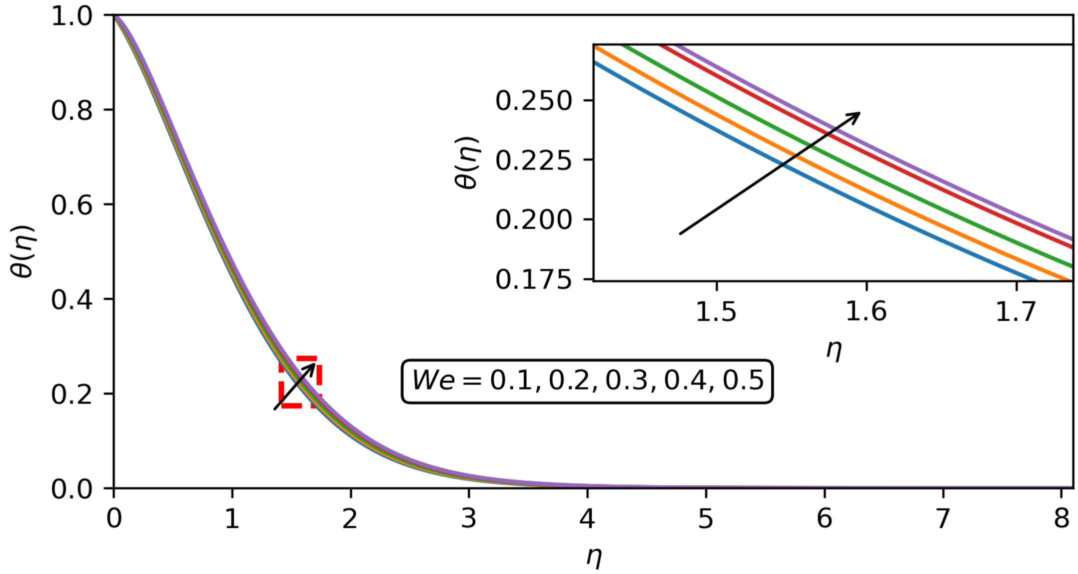

Figure 4.14: Temperature profile $\theta(\eta)$ with Williamson parameter We.

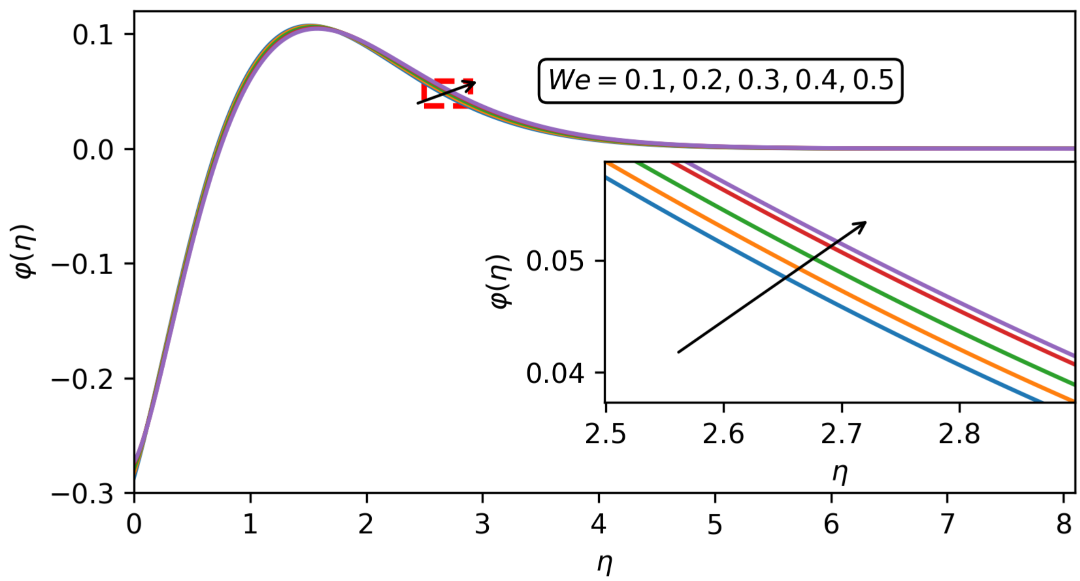

Figure 4.15: Concentration profile $\phi(\eta)$ with Williamson parameter We.

Figs.4.16 and 4.17 show that as the Eckert number increases, the temperature and concentration profiles increase due to enhanced viscous dissipation effects. Viscous dissipation refers to the energy conversion that occurs due to the internal friction within the fluid. As the Eckert number increases, the flow experiences higher kinetic energy, leading to stronger fluid friction and subsequent energy dissipation. This dissipated energy contributes to an increase in temperature within the flow field. Additionally, the concentration of nanoparticles also increases, indicating a higher deposition of nanoparticles near the surface. It is important to note that the impact of the Eckert number on temperature and concentration profiles is primarily driven by viscous dissipation effects in this context.

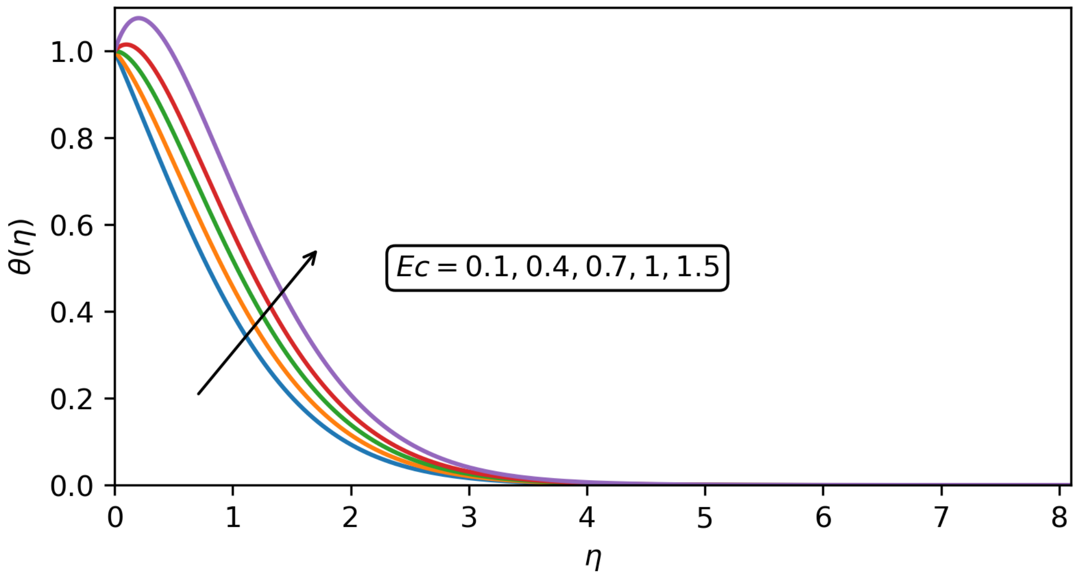

Figure 4.16: Temperature profile $\theta(\eta)$ with Eckert number, Ec.

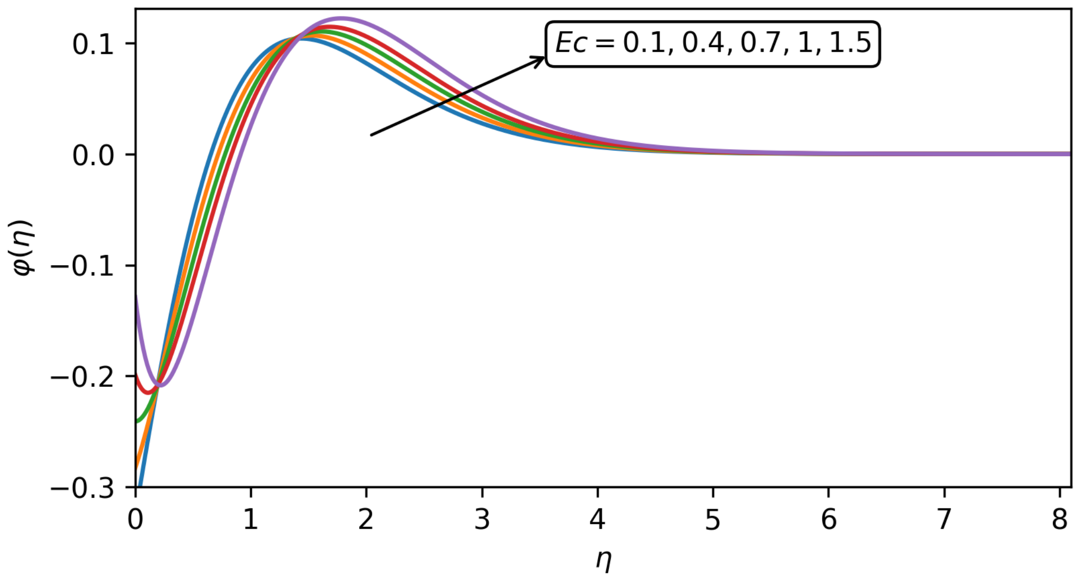

Figure 4.17: Concentration profile $\phi(\eta)$ with Eckert number, Ec.

As depicted in Fig. 4.18, the chemical reaction parameter, C_r, has negative influence on concentration distribution. The chemical reaction parameter represents the presence of chemical reactions in the fluid. When this parameter increases, it indicates a higher reaction rate. The negative influence on concentration distribution suggests that the chemical reactions tend to reduce the concentration of nanoparticles near the surface.

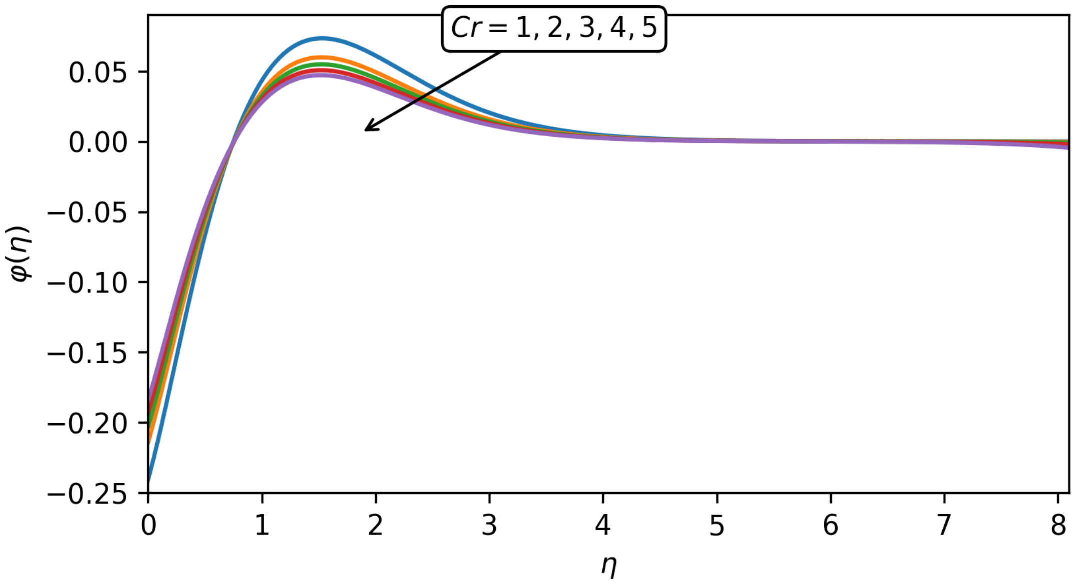

Figure 4.18: Impact of the chemical reaction parameter, C_r, on the distribution of concentration (nanoparticles volume fraction), $\phi(\eta)$

4.4.3 Effects of Pertinent Flow Parameters on Skin Friction Coefficients, Nusselt Number and Sherwood Number

The investigation of the combined effects of the Hall current and the ion slip parameter on the primary and secondary skin friction coefficients, Nusselt number, and Sherwood number reveals important flow characteristics. As depicted in Figs. 4.19–4.22, an increase in both the Hall and the ion slip parameter leads to an increase in the Nusselt number. This behavior can be attributed to the augmented heat transfer rate near the stretching surface due to the presence of Hall and ion slip effects. However, these effects cause a decrease in the skin friction coefficients and Sherwood number. The reduction in the skin friction coefficients can be explained by the alteration of the flow structure and boundary layer development resulting from the combined action of Hall and ion slip effects. Similarly, the decrease in the Sherwood number can be attributed to the reduced rate of mass transfer near the surface due to the Hall and ion slip effects.

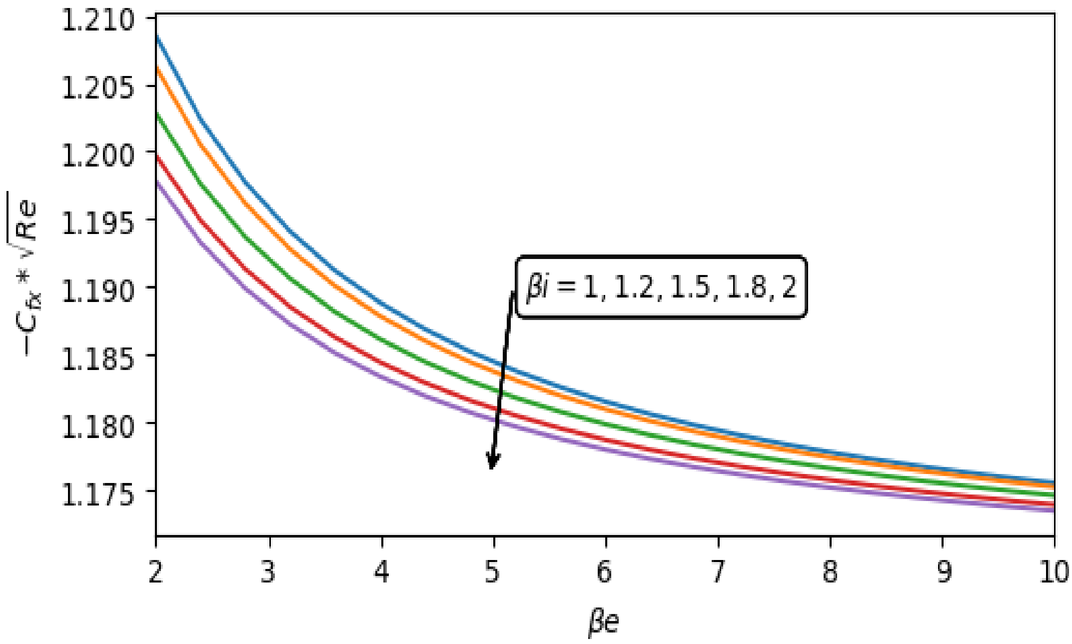

Figure 4.19: Influences of β_e and β_i on $-\left(f''(0) + \frac{We}{2} f''^2(0)\right)$

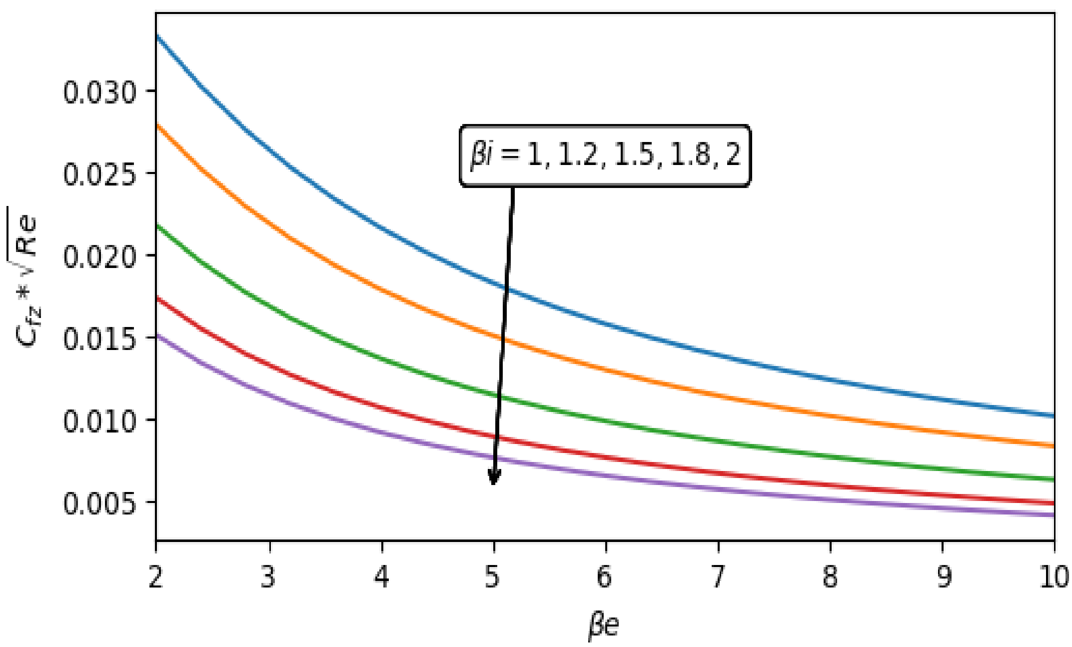

Figure 4.20: Influences of β_e and β_i on $h'(0) + \frac{We}{2} h'^2(0)$

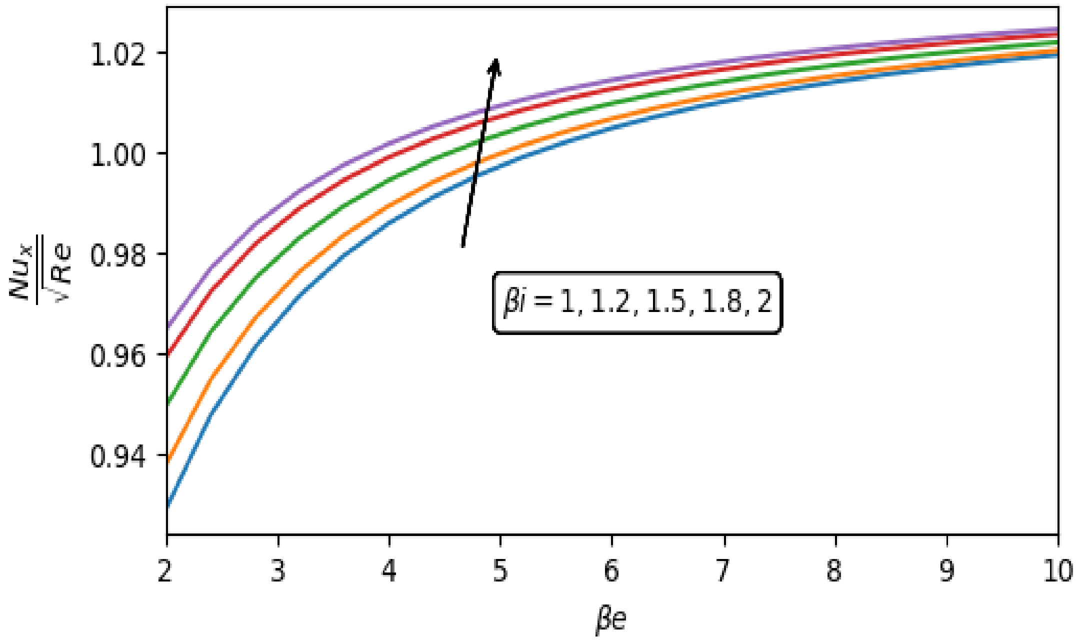

Figure 4.21: Influences of β_e and β_i on $-\left(1 + R\theta_w^3\right)\theta'(0)$

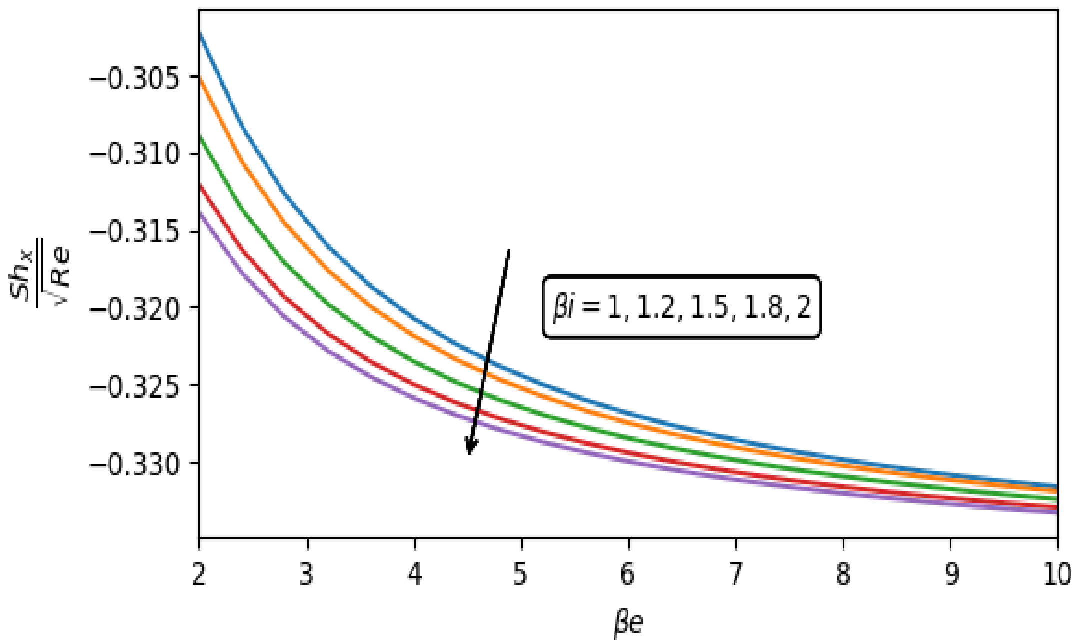

Figure 4.22: Influences of β_e and β_i on $-\phi'(0)$

Furthermore, the simultaneous influence of the Eckert number and the nonlinear thermal radiation parameter on the Nusselt number and Sherwood number are illustrated in Figs. 4.23–4.24. The increase in the Eckert number leads to a decrease in the Nusselt number, indicating a reduction in convective heat transfer near the surface. On the other hand, an increase in the nonlinear thermal radiation parameter results in a decrease in the Sherwood number, suggesting a reduction in the rate of mass transfer near the stretching sheet. These findings emphasize the significant role of non linear thermal radiation and the Eckert number in the heat and mass transfer characteristics of the nanofluid flow.

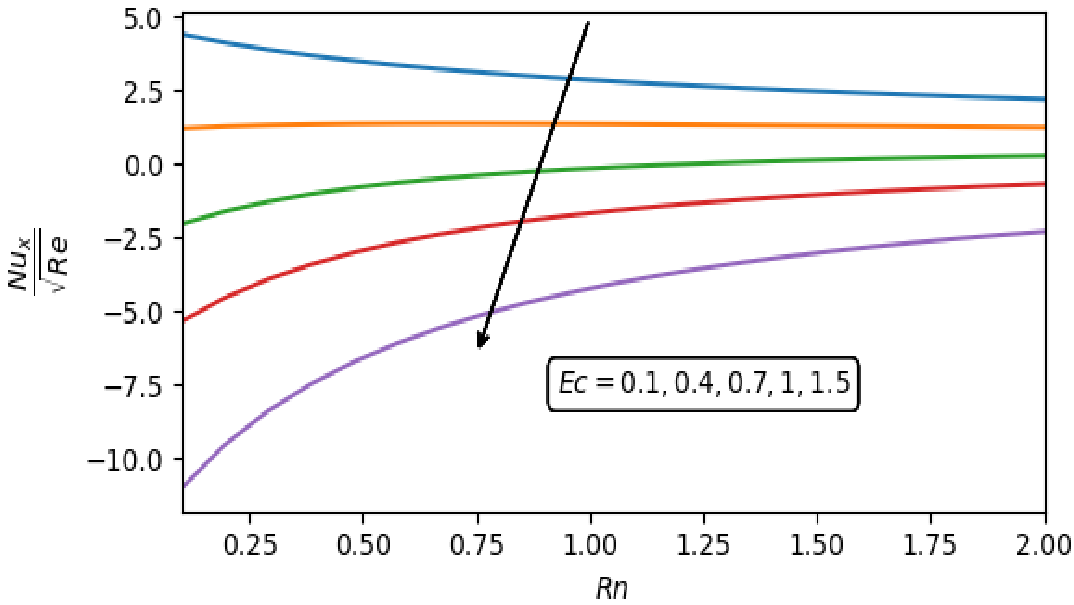

Figure 4.23: Influences of R_n and Ec on $-\left(1 + R_n\theta_r^3\right)\theta'(0)$

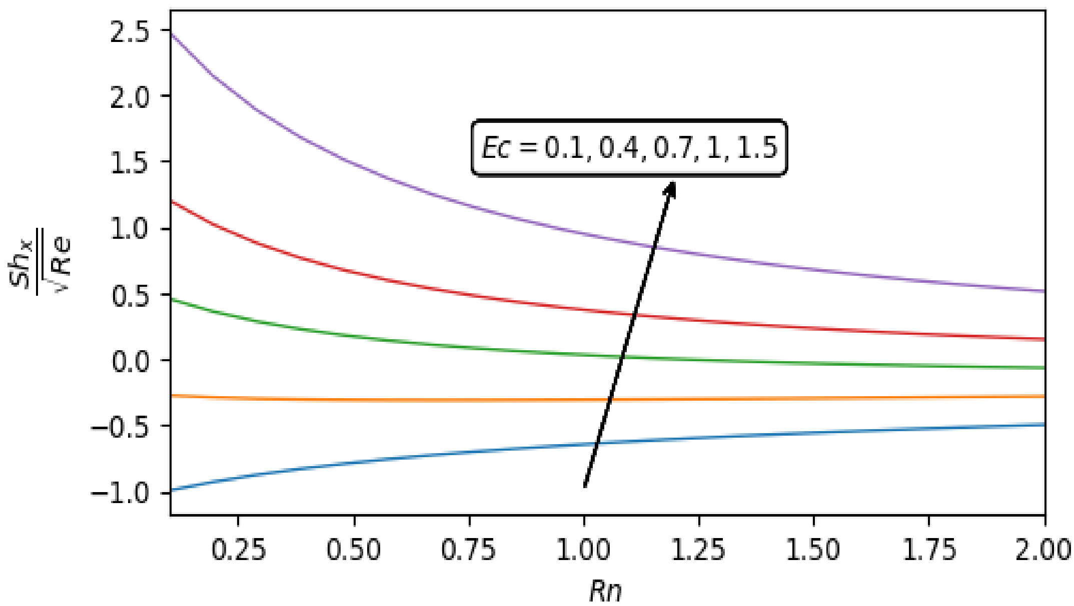

Figure 4.24: Influences of R_n and Ec on $-\phi'(0)$

Table 4.3 presents the numerical values of the primary skin friction coefficient ($-C_{fx}\sqrt{Re}$, the secondary skin friction coefficient ($C_{hz}\sqrt{Re}$), the reduced Nusselt number $\left(\frac{Nu_x}{\sqrt{Re_x}}\right)$ and Sherwood number $\left(\frac{Sh_x}{\sqrt{Re_x}}\right)$ for specific parameter values. The primary skin friction coefficient increases with an increase in the Williamson parameter, magnetic parameter, and Darcy number. Conversely, it decreases with an increase in the Hall and ion slip parameters. These observations indicate that the flow resistance near the stretching sheet is influenced by these parameters. In contrast, the secondary skin friction coefficient decreases for all the considered parameters, suggesting a decrease in the flow resistance in the secondary flow direction. These findings highlight the significance of these parameters in determining the skin friction characteristics of the nanofluid flow.

The Nusselt number, which represents the rate of heat transfer near the surface, exhibits a decreasing trend with an increase in the magnetic field parameter, Williamson parameter, Eckert number, chemical reaction parameter, and Darcy number. Conversely, it shows an increasing trend with an increase in the Hall parameter, ion slip parameter, nonlinear thermal radiation parameter and the ratio temperature parameter. These results indicate that the rate of heat transfer near the surface is significantly influenced by magnetic forces, ion slip effects, thermal radiation, and other flow parameters.

To provide a physical explanation for these observations, we consider the combined effects of these parameters on the flow behavior. The Hall parameter and ion slip parameter, for instance, introduce a resistance to the additional electromagnetic forces, which disrupt the flow and reduce the rate of heat transfer near the surface. Consequently, the rate of heat transfer will be enhanced by the Hall and ion slip parameters. Similarly, an increase in the Williamson parameter, magnetic field parameter, Eckert number, chemical reaction parameter, and Darcy number leads to increased thermal resistance and reduced heat transfer efficiency. On the other hand, an increase in the nonlinear thermal radiation parameter and the ratio temperature parameter intensify the temperature gradient, promoting heat transfer rate from the surface.

In contrast to the Nusselt number, the Sherwood number, which represents rate of mass transfer, exhibits an opposite trend for all the considered parameters. It increases with an increase in the magnetic field parameter, Williamson parameter, Eckert number, chemical reaction parameter, and Darcy number, while decreasing with an increase in the Hall parameter, ion slip parameter, nonlinear thermal radiation parameter and the ratio temperature parameter.

The results obtained provide valuable insights into the complex behavior of the MHD Williamson nanofluid flow through a stretching sheet. The observed trends and variations in the skin friction coefficients, Nusselt number, and Sherwood number can be attributed to the interplay between different physical phenomena. These findings improve our understanding of the heat and mass transfer characteristics in such systems.

Table 4.3: Numerical values of the skin friction coefficients, Nusselt number and Sherwood number of some values of parameters for $Pr = 5$, $C_r = 0.6$, $N_b = N_t = Da = 0.5$, $Sc = 2$, $R_n = \theta_r = 1.2$, $Ec = 0.4$, $We = 0.2$, $Q_h = -0.1$, $\beta_i = 0.2, \beta_e = 1$

β_e	β_i	We	M	R_n	Ec	θ_r	C_r	Da	$-C_{fx}\sqrt{Re}$	$C_{hz}\sqrt{Re}$	$\frac{Nu_x}{\sqrt{Re_x}}$	$\frac{Sh_x}{\sqrt{Re_x}}$
2									1.2085590	0.0333222	0.9290173	-0.3022571
4									1.1888279	0.0216316	0.9857799	-0.3207248
6									1.1815557	0.0157889	1.0046618	-0.3268681
	1								1.2085590	0.0333222	0.9290173	-0.3022571
	1.2								1.2062538	0.0279136	0.9379111	-0.3051507
	1.5								1.2028406	0.0218028	0.9495227	-0.3089285
		0.1							1.0647266	0.0339215	1.0508967	-0.3419111
		0.2							1.1096698	0.0333773	0.9290173	-0.3022571
		0.3							1.1707887	0.0327505	0.7779836	-0.2531180
			0						1.1663426	9.29e195	1.0393836	-0.3381649
			0.5						1.2085590	0.0333222	0.9290173	-0.3022571
			1						1.2497520	0.0635891	0.8190082	-0.2664654
				0.1					1.2085590	0.0333222	0.6975202	-0.2729807
				0.5					1.2085590	0.0333222	0.7865141	-0.3078092
				0.9					1.2085590	0.0333222	0.7874484	-0.3081748
					0.1				1.2085590	0.0333222	1.8579145	-0.6044750
					0.4				1.2085590	0.0333222	0.9290173	-0.3022571
					0.7				1.2085590	0.0333222	0.0061376	-0.0019969
						0.1			1.2085590	0.0333222	0.4219929	-0.3351277
						0.3			1.2085590	0.0333222	0.4606319	-0.3658132
						0.6			1.2085590	0.0333222	0.4909955	-0.3899266
							1		1.2085590	0.0333222	0.8878232	-0.2888545
							2		1.2085590	0.0333222	0.8228791	-0.2677248
							3		1.2085590	0.0333222	0.8019688	-0.2609217
								0	1.0132588	0.0436357	1.3117381	-0.4267758
								0.5	1.2085590	0.0333222	0.9290173	-0.3022571
								1	1.3721544	0.0279613	0.5888488	-0.1915828

4.5 Conclusion

In this study, the effects of the Hall and ion slip, viscous dissipation, and nonlinear thermal radiation of MHD Williamson nanofluid flow over a stretching sheet is investigated, taking into account Joule (ohmic) heating, heat generation/absorption, and chemical reaction effects by incorporating the magnetic field parameter (M), the Williamson fluid parameter (We), the nonlinear thermal radiation parameter (R_n), the Prandtl number (Pr), the Schmidt number (Sc), the chemical reaction parameter (C_r), the heat generation ($Q_h > 0$) or absorption parameter ($Q_h < 0$), the Eckert number (Ec), the Darcy number (Da), the Brownian motion parameter (N_b) and the thermophoretic parameter (N_t). By numerically solving the governing equations using the fifth order Runge-Kutta method with shooting, we obtained valuable insights into the flow, heat and mass transfer characteristics of the system.

The numerical results provided a comprehensive understanding of the influence of various physical parameters on the velocity, temperature, nanoparticle concentration, skin friction coefficient, Nusselt number and Sherwood number. The graphical representations of these results allowed us to observe the trends and variations of these quantities with respect to the relevant parameters. The obtained data serves as a valuable resource for researchers and engineers working on similar problems.

The comprehensive analysis conducted in this study improves our understanding of the flow, heat and mass transfer phenomena occurring in MHD Williamson nanofluid flow over a stretching sheet. The consideration of multiple physical effects and the inclusion of Hall and ion slip effects provide a more realistic representation of the system's behavior. The results obtained can help in the design and optimization of various engineering processes involving nanofluid flow, heat and mass transfer.

As a result, the following findings were reached:

- When the Hall parameter increases, the principal velocity profile rise but the secondary velocity, temperature and concentration profiles decline.
- The ion slip effect produce similar results to the Hall parameter with increasing principal velocity profile and decreasing secondary velocity, temperature and concentration profiles.
- The temperature and concentration profiles also rise with the enhancement of nonlinear thermal radiation parameter and Eckert number.
- Furthermore, it was illustrated that elevated values of the Williamson fluid parameter correspond to a progressive advancement in the distribution of

temperature and concentration, accompanied by a concomitant decrease in velocity profiles.

- The primary skin friction coefficient is accelerated by raising the magnetic field parameter, Williamson parameter, or Darcy number but decelerated with increment of Hall and ion slip parameters.

- The secondary skin friction coefficient declines under Hall parameter, ion slip, Williamson parameter, or Darcy number, in contrast it is enhanced with an increase in magnetic field parameter.

- The local Nusselt number was reduced under the effects of magnetic field parameter, Williamson parameter, Eckert number, chemical reaction parameter and Darcy number but it increases with an increase in the Hall parameter, ion slip parameter, non linear thermal radiation, and the ratio temperature parameter.

- There appears to be an inverse relationship between mass transfer and heat transfer characteristics, since the Sherwood number shows a tendency opposite to the Nusselt number for all the factors taken into consideration.

In conclusion, this study contributes to existing knowledge by providing a detailed numerical investigation of the Hall and ion slip effects of the MHD Williamson nanofluid flow over a stretching sheet. The results obtained, along with comparison with previous studies, confirm the validity of our numerical approach and offer valuable information on the momentum, heat, and mass transfer characteristics of the system.

Chapter 5

Mixed Convection Flow of MHD Casson Nanofluid over a Vertically Extending Sheet with Effects of Hall, Ion Slip and Nonlinear Thermal Radiation

5.1 Introduction

Mixed convection flow, which arises due to the combined influence of buoyancy-driven and externally induced flow, is encountered in numerous practical situations, including cooling systems, heat exchangers, and chemical processes. While dealing with mixed convection flow, the vertical flow has to be considered. "Flow over a vertically stretching sheet is of practical interest in manufacturing processes like hot rolling, drawing of wire, continuous casting, production of glass fiber, and fabrication of paper, where the quality of the final products depends on the flow and heat transfer characteristics" Ali and Al-Yousef [182]. When the buoyancy forces either assist or impede the flow, Ali and Al-Yousef [182] investigated the boundary layer flow over a vertically moving surface with either suction or injection. The effect of temperature-reliant viscosity on the laminar mixed convection boundary layer flow over a continuously vertically moving surface was investigated by the work of Ali [183]. The mixed convection boundary layer flow in various scenarios was also examined by researchers [184–187]. Therefore, mixed convection flows involve the simultaneous occurrence of forced convection and natural convection (buoyancy-driven) effects in a fluid flow. These flows are encountered in various practical applications, including industrial processes and engineering systems. In particular, in the case of the natural convection flow, thermal expansions and / or density differences are the main causes of vertical flow.

Casson fluid model, introduced by Casson in 1959 [188], is commonly used to describe the flow behavior of various fluids, such as suspensions, emulsions, and biological fluids (the flow of human blood). It has found widespread applications across a diverse range of industries, such as food processing, pharmaceuticals, cosmetics, and oil drilling. And it is also helpful when predicting the flow of human blood in small blood vessels with low shear rates. Researchers focus on the analysis of Casson fluid in various flow scenarios; a few of these studies are included as follows. Mukhopadhyay et al. [189] employed the Casson fluid model to investigate the unsteady, two-dimensional flow of a non-Newtonian fluid over a stretching surface with a specific surface temperature. Whereas, Nandeppanavar et al. [190] investigated the steady, two-dimensional flow of Casson nanofluid over an exponential stretching sheet. They also found that the fluid's velocity drops with an increasing Casson parameter. The effects of mass transfer and heat on the MHD flow of Casson fluid through a porous medium with a shrinking wall were examined by Awais et al. [191]. Additional research on the phenomenon of Casson nanofluid flow is provided in [81, 192–195].

To the best of our knowledge, the use of the shooting technique integrated with the 6th-order Runge-Kutta method, implemented in Python, and a comprehensive investigation on the mixed convection flow of a magnetohydrodynamic (MHD) Casson nanofluid over a vertically stretching sheet within a porous medium, considering the combined effects of nonlinear thermal radiation, viscous dissipation, Ohmic heating, Hall, ion slip, heat generation/absorption, and chemical reaction, represents a novel contribution to the field. Utilizing an open-source Python tool, this numerical approach discretizes the governing equations and solves them iteratively to produce accurate solutions. The objectives of this study are to analyze the effects of the aforementioned pertinent physical parameters on the concentration, temperature, and velocity profiles and also to investigate the rates of mass, heat, and momentum transfer near the surface under varying parameter influences. Thus, this study aims to fill a gap in the existing literature and provide valuable insights for the design and optimization of advanced flow scenarios.

5.2 Mathematical Formulation

5.2.1 Model Assumptions

The study examines a three-dimensional steady, laminar, viscous, homogeneous, incompressible, and mixed convection flow of MHD Casson nanofluid within a porous medium without any slip effect. The sheet stretches vertically along the x-axis with a velocity $U_w(x) = ax$, where $a > 0$ denotes the stretching rate. Figure 5.1 demonstrates how the flow in the region $y \geq 0$ is utilized and taken into account, with the $y - axis$ being normal to the sheet. In the event of buoyancy force, the Boussinesq approximation is considered. It is assumed that the nanoparticle and the base fluid are in thermal equilibrium. The investigation also looks at the impacts of Joule heating, viscous dissipation, and nonlinear thermal radiation. The impacts of heat generation and chemical reactions are also considered. The y-axis is subjected to an intense B_0 strong constant magnetic field. This massive magnetic field intensity induces the Hall and ion-slip phenomena in the electrically conducting fluid, which exert force on the fluid in the z-direction and make the flow 3-D.

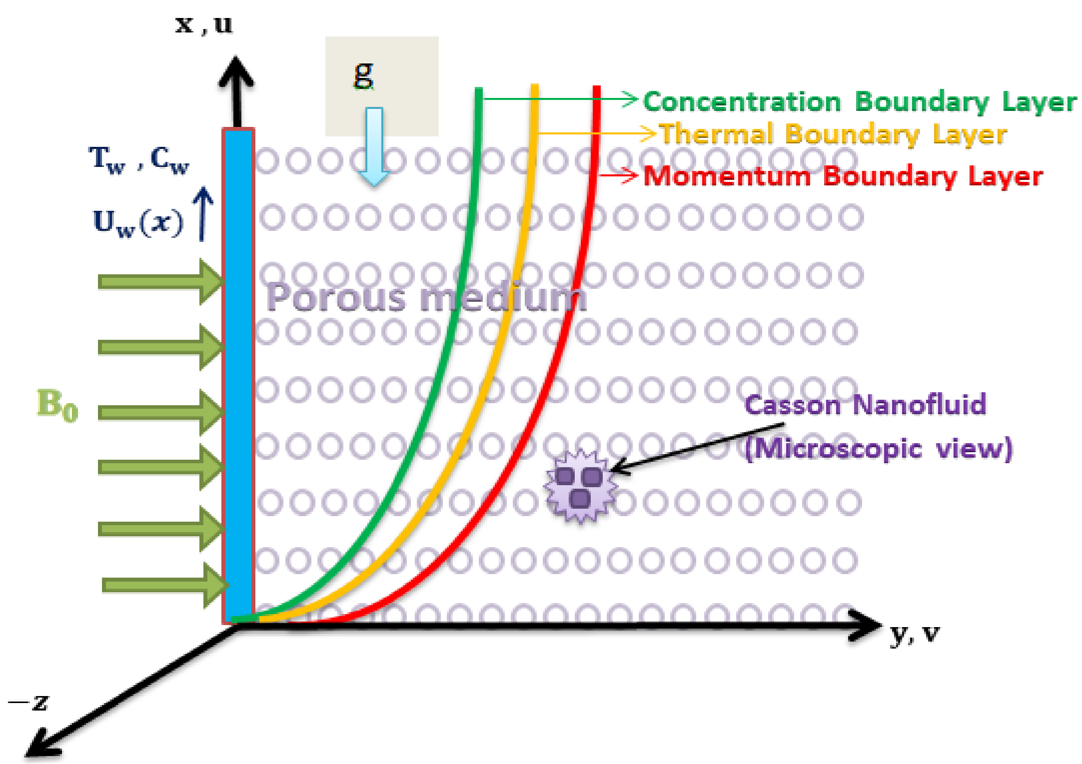

Figure 5.1: Physical model

5.2.2 Conservation Equations

5.2.2.1 Conservation of Mass

The equation for conservation of mass of incompressible flow is given by

$$\nabla \cdot V = 0, \tag{5.1}$$

where ∇ and $\vec{V}$ denote the Del (nabla) operator and the flow velocity vector, respectively. In three-dimensional Cartesian coordinates (x, y, z), the corresponding velocity field is $\mathbf{V}(u, v, w)$ and the equation for conservation of mass Eq. (5.1) is written as follows.

$$\frac{\partial u}{\partial x} + \frac{\partial v}{\partial y} + \frac{\partial w}{\partial z} = 0, \tag{5.2}$$

5.2.2.2 Conservation of Momentum Equation

By employing the Boussinesq approximation, the governing momentum equation for the considered flow problem can be expressed as

$$\begin{aligned} \rho_f \left[\frac{\partial V}{\partial t} + (V \cdot \nabla) V \right] = & -\nabla P + \nabla \cdot \tau_{ij} + (\mathbf{J} \times \mathbf{B}) - \frac{\mu}{K} V \\ & + \rho g \left[\beta_T (T - T_\infty) + \beta_C (C - C_\infty) \right], \end{aligned} \tag{5.3}$$

where t is the time variable, P is the fluid pressure, τ_{ij} is the Cauchy stress tensor, $B = (0, B_0, 0)$ is external magnetic field, $J = (J_x, J_y, J_z)$ is current density, and μ is coefficient of dynamic viscosity, $(\mathbf{J} \times \mathbf{B})$ is the mechanical Lorentz force generated by the motion of the fluid interacted with the external magnetic field. The constants B_0, ρ_f, β_T, β_C, K, g, T, T_∞, C, and C_∞ represent the external magnetic field, nanofluid density, coefficient of the thermal expansion, coefficient of concentration expansion, porosity of the medium, acceleration due to gravity, temperature, ambient temperature, nanoparticle concentration and ambient concentration.

The three-dimensional momentum equations for steady-state flow without a pressure gradient, expressed in terms of the stress tensor, are given by

$$\rho_f \left(u\frac{\partial u}{\partial x} + v\frac{\partial u}{\partial y} + w\frac{\partial u}{\partial z} \right) = \frac{\partial \tau_{xx}}{\partial x} + \frac{\partial \tau_{xy}}{\partial y} + \frac{\partial \tau_{xz}}{\partial z} + FB_x, \tag{5.4}$$

$$\rho_f \left(u\frac{\partial v}{\partial x} + v\frac{\partial v}{\partial y} + w\frac{\partial v}{\partial z} \right) = \frac{\partial \tau_{yx}}{\partial x} + \frac{\partial \tau_{yy}}{\partial y} + \frac{\partial \tau_{yz}}{\partial z} + FB_y, \tag{5.5}$$

$$\rho_f \left(u\frac{\partial w}{\partial x} + v\frac{\partial w}{\partial y} + w\frac{\partial w}{\partial z} \right) = \frac{\partial \tau_{zx}}{\partial x} + \frac{\partial \tau_{zy}}{\partial y} + \frac{\partial \tau_{zz}}{\partial z} + FB_z, \tag{5.6}$$

where FB_x, FB_y, FB_z are the body force components in the x, y, and z directions, respectively, which include the Lorentz force, the resistance due to porosity, and buoyancy forces.

The application of boundary layer approximations to the momentum equations, after substituting the stress components from Eq. (2.25) and computing the stress gradients, leads to the following simplified forms:

$$\rho_f \left(u \frac{\partial u}{\partial x} + v \frac{\partial u}{\partial y} + w \frac{\partial u}{\partial z} \right) = \mu_B \left(1 + \frac{1}{\beta} \right) \frac{\partial^2 u}{\partial y^2} + F B_x, \tag{5.7}$$

$$\rho_f \left(u \frac{\partial w}{\partial x} + v \frac{\partial w}{\partial y} + w \frac{\partial w}{\partial z} \right) = \mu_B \left(1 + \frac{1}{\beta} \right) \frac{\partial^2 w}{\partial y^2} + F B_z, \tag{5.8}$$

where μ_B denotes the plastic dynamic viscosity of the fluid.

Following [196], the modified generalized formula for Ohm's law is given, which takes into consideration the influences of Hall and ion slip at very high magnetic field strengths:

$$J = \sigma(E + (V \times B)) - \frac{\omega_e \tau_e}{B_0}(J \times B) + \frac{\omega_e \tau_e \beta_i}{B_0^2}((J \times B) \times B), \tag{5.9}$$

where σ is the electric conductivity of the fluid, E represents the electric field, ω_e represents the cyclotron frequency, and τ_e represents the electrical collision time. By applying simplifications as from Eqs. (4.9) to (4.18), Eq. (5.9) is reduced to:

$$\begin{aligned} J_x &= \frac{\sigma B_0 \left(\beta_e u - (1 + \beta_e \beta_i) w\right)}{(1 + \beta_e \beta_i)^2 + \beta_e^2}, \\ J_z &= \frac{\sigma B_0 \left((1 + \beta_e \beta_i) u + \beta_e w\right)}{(1 + \beta_e \beta_i)^2 + \beta_e^2}, \end{aligned} \tag{5.10}$$

where, β_i, and $\beta_e = \omega_e \tau_e$ represent the ion slip and Hall parameters respectively. Finally, the reduced form of the Lorentz force is

$$\begin{aligned} J \times B &= -B_0 J_z \hat{\mathbf{i}} + B_0 J_x \hat{\mathbf{k}} \\ &= -\frac{\sigma B_0^2 \left((1 + \beta_e \beta_i) u + \beta_e w\right)}{(1 + \beta_e \beta_i)^2 + \beta_e^2} \hat{\mathbf{i}} + \frac{\sigma B_0^2 \left(\beta_e u - (1 + \beta_e \beta_i) w\right)}{(1 + \beta_e \beta_i)^2 + \beta_e^2} \hat{\mathbf{k}}. \end{aligned} \tag{5.11}$$

5.2.2.3 Conservation of Energy equation

The energy equation is given by

$$\begin{aligned} \left(\rho C_p\right)_f \left[\frac{\partial \mathbf{T}}{\partial t} + (\mathbf{V} \cdot \nabla) \mathbf{T} \right] &= \kappa \nabla^2 \mathbf{T} + \left(\tau_{ij} : \nabla\right) \mathbf{V} \\ &+ \left(\rho C_p\right)_p \left[D_B \nabla C \cdot \nabla T + \frac{D_T}{T_\infty} (\nabla T \cdot \nabla T) \right] \\ &+ \frac{1}{\sigma} (\mathbf{J} \cdot \mathbf{J}) - \nabla q_r + Q_0 (T - T_\infty), \end{aligned} \tag{5.12}$$

where $\left(\rho C_p\right)_f$ and $\left(\rho C_p\right)_p$ are specific heat capacities of the nanofluid and the nanoparticles, respectively, and T is the temperature. κ denotes the thermal conductivity of the fluid; D_B and D_T represent the diffusion coefficients for Brownian and thermophoresis, respectively. T_∞ signifies the ambient temperature, q_r is the radiative heat flux, and the coefficient Q_0 represents heat absorption ($Q_0 < 0$) and generation ($Q_0 > 0$).

Substituting the current density expressions from Eqs. (5.9) and (5.10), the ohmic (Joule) heating term $\left(\frac{1}{\sigma}, \mathbf{J} \cdot \mathbf{J}\right)$ can be reformulated as

$$\frac{1}{\sigma}(\mathbf{J} \cdot \mathbf{J}) = \frac{1}{\sigma}\left[(J_x, 0, J_z) \cdot (J_x, 0, J_z)\right] = \frac{\sigma B_0^2 \left(u^2 + w^2\right)}{(1 + \beta_e \beta_i)^2 + \beta_e^2}. \tag{5.13}$$

Assuming a sufficiently large temperature change, according to Shamshuddin et al. [96], the radiative heating flux q_r is computed and expressed as follows:

$$q_r = -\frac{4\sigma^*}{3k^*}\frac{\partial T^4}{\partial y} = -\frac{16\sigma^*}{3k^*} T^3 \frac{\partial T}{\partial y}, \tag{5.14}$$

where k^* and σ^* are the mean absorption coefficient and Stefan-Boltzmann constant respectively. And therefore, the thermal radiation term can be expressed as:

$$\frac{1}{\rho C_p}\frac{\partial}{\partial y}(q_r) = -\frac{16\sigma^*}{3k^* \rho C_p}\frac{\partial}{\partial y}\left(T^3 \frac{\partial T}{\partial y}\right), \tag{5.15}$$

From Eq. (5.12), the term $Q_0 (T - T_\infty)$ is the heat source term. Moreover, within the framework of the boundary layer approximation in three-dimensional Cartesian coordinates, the viscous dissipation term expressed as $\left(\vec{\tau_{ij}} : \nabla\right)\vec{\mathbf{V}}$ reduces to

$$\Phi = \frac{\upsilon}{C_p}\left(1 + \frac{1}{\beta}\right)\left[\left(\frac{\partial u}{\partial y}\right)^2 + \left(\frac{\partial w}{\partial y}\right)^2\right]. \tag{5.16}$$

5.2.2.4 Conservation of Nanoparticle Concentration Equation

Conservation of nanoparticle concentration for a homogeneous chemical reaction is

$$\frac{\partial \mathbf{C}}{\partial t} + (\mathbf{V} \cdot \nabla)\mathbf{C} = D_B \nabla^2 C + \frac{D_T}{T_\infty}\nabla^2 T - R_0 (C - C_\infty), \tag{5.17}$$

where C is the nanoparticle concentration near the surface, C_∞ is the ambient concentration and R_0 denotes chemical reaction constant. D_B and D_T represent the Brownian motion coefficient, thermophoresis coefficient respectively.

5.2.3 Coupled Governing Equations and Boundary Conditions

The governing equations, comprising continuity, momentum, energy, and concentration equations, are stated by combining previously reduced equations and applying the boundary layer approximation, as per the cited references [4, 197]:

$$\frac{\partial u}{\partial x} + \frac{\partial v}{\partial y} + \frac{\partial w}{\partial z} = 0, \tag{5.18}$$

$$\begin{aligned} u\frac{\partial u}{\partial x} + v\frac{\partial u}{\partial y} + w\frac{\partial u}{\partial z} = \upsilon\left(1 + \frac{1}{\beta}\right)\frac{\partial^2 u}{\partial y^2} - \frac{\sigma B_0^2\left[(1+\beta_e\beta_i)u + \beta_e w\right]}{\rho\left[(1+\beta_e\beta_i)^2 + \beta_e^2\right]} - \frac{\upsilon}{K}u \\ + g\beta_T\left(T - T_\infty\right) + g\beta_C\left(C - C_\infty\right), \end{aligned} \tag{5.19}$$

$$u\frac{\partial w}{\partial x} + v\frac{\partial w}{\partial y} + w\frac{\partial w}{\partial z} = \upsilon\left(1 + \frac{1}{\beta}\right)\frac{\partial^2 w}{\partial y^2} + \frac{\sigma B_0^2\left[\beta_e u - (1+\beta_e\beta_i)w\right]}{\rho\left[(1+\beta_e\beta_i)^2 + \beta_e^2\right]} - \frac{\upsilon}{K}w, \tag{5.20}$$

$$\begin{aligned} u\frac{\partial T}{\partial x} + v\frac{\partial T}{\partial y} + w\frac{\partial T}{\partial z} =& \alpha\frac{\partial^2 T}{\partial y^2} + \Lambda\left[D_B\frac{\partial C}{\partial y}\frac{\partial T}{\partial y} + \frac{D_T}{T_\infty}\left(\frac{\partial T}{\partial y}\right)^2\right] \\ &+ \frac{16\sigma^*}{3k^*\left(\rho C_p\right)_f}\frac{\partial}{\partial y}\left(T^3\frac{\partial T}{\partial y}\right) \\ &+ \frac{\sigma B_0^2\left[u^2 + w^2\right]}{\left(\rho C_p\right)_f\left[(1+\beta_e\beta_i)^2 + \beta_e^2\right]} + \frac{Q_0}{\left(\rho C_p\right)_f}\left(T - T_\infty\right) \\ &+ \frac{\upsilon}{C_p}\left(1 + \frac{1}{\beta}\right)\left[\left(\frac{\partial u}{\partial y}\right)^2 + \left(\frac{\partial w}{\partial y}\right)^2\right], \end{aligned} \tag{5.21}$$

$$u\frac{\partial C}{\partial x} + v\frac{\partial C}{\partial y} + w\frac{\partial C}{\partial z} = D_B\frac{\partial^2 C}{\partial y^2} + \frac{D_T}{T_\infty}\frac{\partial^2 T}{\partial y^2} - R_0\left(C - C_\infty\right), \tag{5.22}$$

where (u, v, w) denotes the fluid velocity components in the x, y, and z directions, respectively; $\upsilon = \frac{\mu}{\rho}$, $\alpha = \frac{\kappa}{\left(\rho C_p\right)_f}$, and $\Lambda = \frac{\left(\rho C_p\right)_p}{\left(\rho C_p\right)_f}$ represent the momentum diffusivity, the thermal diffusivity and the effective heat capacity ratio of the nanoparticle to the effective heat capacity of the nanofluid respectively.

The following are the problem's specified boundary conditions:

$$\begin{cases} u = U_w(x) = ax, \;\; v = 0 = w, \;\; T = T_w, \;\; C = C_w \;\; at \;\; y = 0, \\ u \to 0, \;\; w \to 0, \;\; T \to T_\infty, \;\; C \to C_\infty, \;\; as \;\; y \to \infty, \end{cases} \tag{5.23}$$

where T_w and C_w represent the fluid's constant surface temperature and the concentration of nanoparticles at the surface respectively.

5.2.4 Similarity Transformation

Recognizing the inherent challenges in obtaining exact analytical solutions for the system of coupled, nonlinear partial differential equations described by Eqs. (5.18)–(5.22), the researchers have adopted a pragmatic approach to simplify the analysis by transforming the governing equations into a more tractable system of ordinary differential equations (ODEs). This strategic reduction, facilitated through the application of the specified transformation equations, enables a more manageable and insightful investigation of the complex phenomena.

$$\begin{aligned}
&\eta = \sqrt{\frac{a}{\upsilon}}y, \quad \psi = \sqrt{a\upsilon}xf(\eta), \quad w = U_w(x)h(\eta) = axh(\eta),\\
&\theta(\eta) = \frac{T - T_\infty}{T_w - T_\infty}, \quad \phi(\eta) = \frac{C - C_\infty}{C_w - C_\infty},
\end{aligned} \tag{5.24}$$

where η is the new similitude variable, and define dimensionless variables including the stream function $f'(\eta)$, the cross flow velocity $h(\eta)$, the temperature distribution $\theta(\eta)$ and the nanoparticles concentration $\phi(\eta)$. The flow function ψ relates to the partial derivatives of the velocity components as $v = -\frac{\partial\psi}{\partial x}$ and $u = \frac{\partial\psi}{\partial y}$.

Considering the stated assumption, the flow is analyzed solely along the x– and z–axes, which necessitates computing the partial derivatives of u and w through the aforementioned similarity transformations.

$$\begin{cases}
\dfrac{\partial u}{\partial x} = af',\\
\dfrac{\partial u}{\partial y} = axf''\sqrt{\dfrac{a}{\upsilon}}, \quad \dfrac{\partial u}{\partial z} = 0,\\
\dfrac{\partial^2 u}{\partial y^2} = axf'''\dfrac{a}{\upsilon},
\end{cases} \tag{5.25}$$

$$\begin{cases}
\dfrac{\partial w}{\partial x} = ah,\\
\dfrac{\partial w}{\partial y} = axh'\sqrt{\dfrac{a}{\upsilon}}, \quad \dfrac{\partial w}{\partial z} = 0\\
,\dfrac{\partial^2 w}{\partial y^2} = axh''\dfrac{a}{\upsilon}
\end{cases} \tag{5.26}$$

The continuity equation (5.18) is automatically satisfied under the application of the prescribed similarity transformations. Consequently, the governing equations (5.19)–(5.22) can likewise be reduced to their corresponding dimensionless ODEs through the same transformations.

Substituting Eq. (5.25) into the left-hand side (LHS) of Eq. (5.19) yields:

$$u\frac{\partial u}{\partial x}+v\frac{\partial u}{\partial y}+w\frac{\partial u}{\partial z}=axf'\cdot af'-\sqrt{a\upsilon}f\cdot axf''\sqrt{\frac{a}{\upsilon}}+0=a^2xf'^2-a^2xff'' \\ =a^2x\left(f'^2-ff''\right). \tag{5.27}$$

Analogously, the right-hand side (RHS) of Eq. (5.19) can be expressed as:

$$\begin{aligned}
&\upsilon\left(1+\frac{1}{\beta}\right)\frac{\partial^2 u}{\partial y^2}-\frac{\sigma B_0^2\left[(1+\beta_e\beta_i)u+\beta_e w\right]}{\rho\left[(1+\beta_e\beta_i)^2+\beta_e^2\right]}-\frac{\upsilon}{K}u+g\beta_T\left(T-T_\infty\right)+g\beta_C\left(C-C_\infty\right)\\
&=\upsilon\left[\left(1+\frac{1}{\beta}\right)axf'''\cdot\frac{a}{\upsilon}\right]-\frac{\sigma B_0^2ax\left[(1+\beta_e\beta_i)f'+\beta_e h\right]}{\rho\left[(1+\beta_e\beta_i)^2+\beta_e^2\right]}-\frac{\upsilon ax}{K}f'\\
&\qquad+g\beta_T\theta\left(T_w-T_\infty\right)+g\beta_C\phi\left(C_w-C_\infty\right)\\
&=a^2x\left[\left(1+\frac{1}{\beta}\right)f'''-\frac{\sigma B_0^2\left[(1+\beta_e\beta_i)f'+\beta_e h\right]}{\rho b\left[(1+\beta_e\beta_i)^2+\beta_e^2\right]}-\frac{\nu}{bK}f'\right]\\
&\qquad+g\beta_T\theta\left(T_w-T_\infty\right)+g\beta_C\phi\left(C_w-C_\infty\right).
\end{aligned} \tag{5.28}$$

Combining Eq. (5.27) with Eq. (5.28) and dividing throughout by a^2x, the x–momentum equation (5.19) is transformed into its dimensionless ODE form:

$$\begin{aligned}
&\left(1+\frac{1}{\beta}\right)f'''-f'^2+ff''-\frac{\sigma B_0^2\left[(1+\beta_e\beta_i)f'+\beta_e h\right]}{\rho a\left[(1+\beta_e\beta_i)^2+\beta_e^2\right]}-\frac{\nu}{aK}f'\\
&\quad+\frac{g\beta_T\left(T_w-T_\infty\right)}{a^2x}\theta+\frac{g\beta_C\left(C_w-C_\infty\right)}{a^2x}\phi=0.
\end{aligned} \tag{5.29}$$

Applying the similarity transformations to the z–momentum equation, and substituting Eq. (5.26) into its left-hand side (LHS) of (5.20), we obtain:

$$u\frac{\partial w}{\partial x}+v\frac{\partial w}{\partial y}+w\frac{\partial w}{\partial z}=axf'ah-\sqrt{a\upsilon}faxh'\sqrt{\frac{a}{\upsilon}}+0=a^2xf'h-a^2xfh' \\ =a^2x\left(f'h-fh'\right). \tag{5.30}$$

And the right-hand side (RHS) can also be transformed as follows.

$$\begin{aligned}
&\upsilon\left(1+\frac{1}{\beta}\right)\frac{\partial^2 w}{\partial y^2}+\frac{\sigma B_0^2\left[\beta_e u-(1+\beta_e\beta_i)w\right]}{\rho\left[(1+\beta_e\beta_i)^2+\beta_e^2\right]}-\frac{\upsilon}{K}w\\
&=\upsilon\left(1+\frac{1}{\beta}\right)axh''\cdot\frac{a}{\upsilon}+\frac{\sigma B_0^2ax\left[\beta_e f'-(1+\beta_e\beta_i)h\right]}{\rho\left[(1+\beta_e\beta_i)^2+\beta_e^2\right]}-\frac{\upsilon}{K}axh\\
&=a^2x\left[\left(1+\frac{1}{\beta}\right)h''+\frac{\sigma B_0^2\left[\beta_e f'-(1+\beta_e\beta_i)h\right]}{\rho a\left[(1+\beta_e\beta_i)^2+\beta_e^2\right]}-\frac{\upsilon}{aK}h\right].
\end{aligned} \tag{5.31}$$

Dividing by a^2x, the dimensionless ODE form of the z-momentum equation Eq. (5.20) becomes

$$\left(1+\frac{1}{\beta}\right)h''-f'h+fh'+\frac{\sigma B_0^2\left[\beta_e f'-(1+\beta_e\beta_i)h\right]}{\rho a\left[(1+\beta_e\beta_i)^2+\beta_e^2\right]}-\frac{\upsilon}{aK}h=0. \tag{5.32}$$

For the transformation of the energy equation into its non-dimensional form via the similarity transformations (5.24), the following additional partial derivatives are evaluated alongside Eqs. (5.25) and (5.26).

$$\begin{cases}\dfrac{\partial T}{\partial x}=0, \quad \dfrac{\partial T}{\partial y}=(T_w-T_\infty)\theta'\sqrt{\dfrac{a}{\upsilon}}, \quad \dfrac{\partial T}{\partial z}=0,\\ \dfrac{\partial^2 T}{\partial y^2}=(T_w-T_\infty)\theta''\dfrac{a}{\upsilon},\\ \dfrac{\partial C}{\partial y}=(C_w-C_\infty)\phi'\sqrt{\dfrac{a}{\upsilon}}\end{cases} \tag{5.33}$$

The LHS of Eq. (5.21) can be transformed as follows.

$$u\frac{\partial T}{\partial x}+v\frac{\partial T}{\partial y}+w\frac{\partial T}{\partial z}=0+(-\sqrt{a\upsilon}f)(T_w-T_\infty)\theta'\sqrt{\frac{a}{\upsilon}}+0=-a(T_w-T_\infty)f\theta'. \tag{5.34}$$

To transform the thermal diffusion term, we have:

$$\alpha\frac{\partial^2 T}{\partial y^2}=\alpha(T_w-T_\infty)\theta''\frac{a}{\upsilon}. \tag{5.35}$$

The Brownian and thermophoresis diffusion can also be transformed as follows.

$$\begin{aligned}\Lambda\left(D_B\frac{\partial T}{\partial y}\frac{\partial C}{\partial y}+\frac{D_T}{T_\infty}\left(\frac{\partial T}{\partial y}\right)^2\right)=\frac{\Lambda a}{\upsilon}\Bigg[&D_B(T_w-T_\infty)(C_w-C_\infty)\theta'\phi'\\ &+\frac{D_T(T_w-T_\infty)^2}{T_\infty}\theta'^2\Bigg].\end{aligned} \tag{5.36}$$

Using Eq.(4.46), the thermal radiation term is converted to:

$$\begin{aligned}\frac{16\sigma^*}{3k^*(\rho C_p)_f}\frac{\partial}{\partial y}\left(T^3\frac{\partial T}{\partial y}\right)=\frac{16\sigma^*T_\infty^3(T_w-T_\infty)}{3k^*(\rho C_p)_f}\frac{a}{\upsilon}\Big[&3\left((\theta_r-1)\theta+1\right)^2(\theta_r-1)\theta'^2\\ &+\left((\theta_r-1)\theta+1\right)^3\theta''\Big].\end{aligned} \tag{5.37}$$

The heat source term can also be translated using the similarity transformation as follows.

$$\frac{Q_0(T-T_\infty)}{(\rho C_p)_f}=\frac{Q_0}{(\rho C_p)_f}(T_w-T_\infty)\theta. \tag{5.38}$$

The Joule (ohmic) heating term is derived as follows.

$$\frac{\sigma B_0^2(u^2+w^2)}{(\rho C_p)_f\left[(1+\beta_e\beta_i)^2+\beta_e^2\right]}=\frac{\sigma B_0^2(ax)^2\left[f'^2+h^2\right]}{(\rho C_p)_f\left[(1+\beta_e\beta_i)^2+\beta_e^2\right]}. \tag{5.39}$$

The viscous dissipation term is transformed using the given similarity transformations as follows.

$$\begin{aligned}\frac{\upsilon}{C_p}\left(1+\frac{1}{\beta}\right)\left[\left(\frac{\partial u}{\partial y}\right)^2+\left(\frac{\partial w}{\partial y}\right)^2\right]&=\frac{\upsilon}{C_p}\left(1+\frac{1}{\beta}\right)\left[\left(axf''\sqrt{\frac{a}{\upsilon}}\right)^2+\left(axh'\sqrt{\frac{a}{\upsilon}}\right)^2\right]\\&=\frac{b^3x^2}{C_p}\left(1+\frac{1}{\beta}\right)\left[(f'')^2+(h')^2\right].\end{aligned} \tag{5.40}$$

Combining Eqs. (5.34)–(5.36), (5.37)–(5.40), and dividing by $\alpha(T_w-T_\infty)\frac{a}{\upsilon}$, the energy equation in its non-dimensional form becomes:

$$\begin{aligned}\theta''=&-\frac{\upsilon}{\alpha}f\theta'-\frac{\Lambda D_B(C_w-C_\infty)}{\alpha}\theta'\phi'-\frac{\rho D_T(T_w-T_\infty)}{\alpha T_\infty}\theta'^2\\&-\frac{16\sigma^*T_\infty^3}{3k^*(\rho c)_f\alpha}\left[3\left((\theta_r-1)\theta+1\right)^2(\theta_r-1)\theta'^2+\left((\theta_r-1)\theta+1\right)^3\theta''\right]\\&-\frac{Q_0\upsilon}{(\rho C_p)_f\alpha a}\theta-\frac{\sigma B_0^2ax^2\nu\left[f'^2+h^2\right]}{(\rho C_p)_f\alpha(T_w-T_\infty)\left[(1+\beta_e\beta_i)^2+\beta_e^2\right]}\\&-\frac{a^2x^2\upsilon}{C_p\alpha(T_w-T_\infty)}\left(1+\frac{1}{\beta}\right)\left[(f'')^2+(h')^2\right].\end{aligned} \tag{5.41}$$

The transformation of the nanoparticle concentration equation Eq. (5.22) into its dimensionless form, using the similarity relations of Eq. (5.24), necessitates the computation of the following partial derivatives.

$$\begin{cases}\dfrac{\partial C}{\partial x}=\dfrac{\partial C}{\partial\phi}\cdot\dfrac{\partial\phi}{\partial x}=(C_w-C_\infty)\cdot\dfrac{\partial\phi}{\partial x}=0,\\[2mm]\dfrac{\partial C}{\partial z}=(C_w-C_\infty)\dfrac{\partial\phi}{\partial z}=0,\\[2mm]\dfrac{\partial^2C}{\partial y^2}=(C_w-C_\infty)\phi''\dfrac{b}{\upsilon}.\end{cases} \tag{5.42}$$

Applying Eqs. (5.25), (5.26), (5.33), and (5.42), Eq. (5.22) transforms as follows.

$$\begin{aligned}&0-\sqrt{a\upsilon}f(C_w-C_\infty)\phi'\sqrt{\frac{a}{\upsilon}}+0\\&=D_B(C_w-C_\infty)\phi''\cdot\frac{a}{\upsilon}+\frac{D_T}{T_\infty}(T_w-T_\infty)\theta''\cdot\frac{a}{\upsilon}-R_0(C_w-C_\infty)\phi.\end{aligned} \tag{5.43}$$

Dividing by $D_B(C_w - C_\infty)\dfrac{a}{\upsilon}$, the dimensionless ODE form of the nanoparticle concentration becomes

$$\phi'' = -\frac{\upsilon}{D_B} f\phi' - \frac{D_T(T_w - T_\infty)}{D_B T_\infty (C_w - C_\infty)}\theta'' + \frac{R_0 \upsilon}{a D_B}\phi. \tag{5.44}$$

The similarity transformations Eq. (5.24) are applied to non-dimensionalize the boundary conditions Eq. (5.23). Since $\eta = 0$ at the surface ($y = 0$) and $\eta \to \infty$ in the free stream ($y \to \infty$), allows the conditions to be stated exclusively in terms of η, thereby facilitating the reduction of the governing PDEs to ODEs.

At $y = 0$,

$$\begin{cases} u(0) = axf'(0) = ax \Rightarrow f'(0) = 1, \\ v(0) = -\sqrt{a\upsilon} f(0) = 0 \Rightarrow f(0) = 0, \\ w(0) = axh(0) \Rightarrow h(0) = 0, \\ \theta(0) = \dfrac{T(0) - T_\infty}{T_w - T_\infty} = \dfrac{T_w - T_\infty}{T_w - T_\infty} = 1, \\ \phi(0) = \dfrac{C(0) - C_\infty}{C_w - C_\infty} = \dfrac{C_w - C_\infty}{C_w - C_\infty} = 1. \end{cases} \tag{5.45}$$

As $y \to \infty$, we have the following transformations.

$$\begin{cases} u \to 0 \Rightarrow f'(\eta) \to 0, \\ w \to 0 \Rightarrow h(\eta) = 0, \\ \theta(\eta) \to \dfrac{T_\infty - T_\infty}{T_w - T_\infty} = 0, \\ \phi(\eta) \to \dfrac{C_\infty - C_\infty}{C_w - C_\infty} = 0. \end{cases} \tag{5.46}$$

Eqs. (5.19)-(5.22) are reduced to become the following system of coupled ODEs.

$$\left(1 + \frac{1}{\beta}\right) f''' - f'^2 + ff'' - Daf' - \frac{M\left[(1 + \beta_e\beta_i)f' + \beta_e h\right]}{(1 + \beta_e\beta_i)^2 + \beta_e^2} + \lambda_t\theta + \lambda_c\phi = 0, \tag{5.47}$$

$$\left(1 + \frac{1}{\beta}\right) h'' - f'h + fh' - Dah + \frac{M\left[\beta_e f' - (1 + \beta_e\beta_i)h\right]}{(1 + \beta_e\beta_i)^2 + \beta_e^2} = 0, \tag{5.48}$$

$$\begin{gathered} \theta'' + Pr\left[f\theta' + N_b\theta'\phi' + N_t(\theta')^2 + Ec\left(1 + \frac{1}{\beta}\right)\left(f''^2 + h'^2\right) + \frac{MEc\left(f'^2 + h^2\right)}{(1 + \beta_e\beta_i)^2 + \beta_e^2} + Q_h\theta\right] \\ + R_n\left[3(\theta_r - 1)\Big(\theta(\theta_r - 1) + 1\Big)^2\theta'^2 + \Big(\theta(\theta_r - 1) + 1\Big)^3\theta''\right] = 0, \end{gathered} \tag{5.49}$$

$$\phi'' + \frac{N_t}{N_b}\theta'' + Scf\phi' - ScC_r\phi = 0. \tag{5.50}$$

Consequently, the boundary conditions of the problem have been transformed as follows.

$$\begin{cases} f'(\eta) = 1, \quad f(\eta) = 0, \quad h(\eta) = 0, \quad \theta(\eta) = 1, \quad \phi(\eta) = 1, \; at \;\; \eta = 0, \\ f' \to 0, \quad h \to 0, \quad \theta \to 0, \quad \phi \to 0 \quad as \;\; \eta \to \infty. \end{cases} \tag{5.51}$$

Equations (5.47)–(5.50) can be rearranged to yield

$$f''' = \frac{\left[f'^2 - ff'' + Daf' + \dfrac{M\left[(1+\beta_e\beta_i)f' + \beta_e h\right]}{(1+\beta_e\beta_i)^2 + \beta_e^2} - \lambda_t\theta - \lambda_c\phi \right]}{\left(1 + \dfrac{1}{\beta}\right)}, \tag{5.52}$$

$$h'' = \frac{\left[f'h - fh' + Dah - \dfrac{M\left[\beta_e f' - (1+\beta_e\beta_i)h\right]}{(1+\beta_e\beta_i)^2 + \beta_e^2} \right]}{\left(1 + \dfrac{1}{\beta}\right)}, \tag{5.53}$$

$$\begin{aligned} \theta'' = \frac{-1}{\left(1 + R_n\left(1 + (\theta_r - 1)\theta\right)^3\right)} & \Bigg[Pr\Bigg(f\theta' + N_b\theta'\phi' + N_t\left(\theta'\right)^2 \\ & + Ec\left(1 + \frac{1}{\beta}\right)\left(f''^2 + h'^2\right) + Q_h\theta \\ & + \frac{MEc\left(f'^2 + h^2\right)}{(1+\beta_e\beta_i)^2 + \beta_e^2} \Bigg) \\ & + R_n\Big(3(\theta_r - 1)\left((\theta_r - 1)\theta + 1\right)^2 \theta'^2\Big) \Bigg], \end{aligned} \tag{5.54}$$

$$\phi'' = -Scf\phi' - \frac{N_t}{N_b}\theta'' + ScC_r\phi. \tag{5.55}$$

The relevant dimensionless parameters present in Equations (5.47)-(5.50) are described in detail as follows.

Table 5.1: Dimensionless parameters and their definitions

Symbol & Formula	Description
$Da = \frac{\upsilon}{aK}$	Darcy number,
$R_n = \frac{16\sigma^* T_\infty^3}{3\kappa k^*}$	nonlinear thermal radiation parameter,
$\theta_r = \frac{T_w}{T_\infty}$	ratio of temperature parameter,
$Pr = \frac{\upsilon}{\alpha}$	Prandtl number,
$Sc = \frac{\upsilon}{D_B}$	Schmidt number,
$N_b = \frac{\Lambda D_B (C_w - C_\infty)}{\upsilon}$	Brownian motion parameter $\left(\Lambda = \frac{\left(\rho C_p\right)_p}{\left(\rho C_p\right)_f}\right)$
$N_t = \frac{\Lambda D_T \left(T_w - T_\infty\right)}{\upsilon T_\infty}$	Thermophoretic parameter
$M = \frac{\sigma B_0^2}{\rho_f a}$	magnetic field parameter,
$Ec = \frac{a^2 x^2}{C_p \left(T_w - T_\infty\right)}$	Eckert number,
$Q_h = \frac{Q_0}{\left(\rho C_p\right)_f a}$	heat generation / absorption parameter,
$C_r = \frac{R_0}{a}$	scaled chemical reaction parameter,
$\lambda_t = \frac{Gr_t}{Re_x^2} = \frac{g\beta_T (T_w - T_\infty)}{a^2 x}$	mixed convection parameters (thermal expansion parameter),
$\lambda_c = \frac{Gr_m}{Re_x^2} = \frac{g\beta_C (C_w - C_\infty)}{a^2 x}$	modified mixed convection parameters (due to density difference)
$Gr_t = \frac{g\beta_T \left(T - T_\infty\right)}{\upsilon^2}$	Grashof number (thermal),
$Gr_m = \frac{\beta_C \left(C - C_\infty\right)}{\upsilon^2}$	Grashof number (mass) and
$Re_x = \frac{x U_w(x)}{\upsilon}$	local Reynolds number.

5.2.5 Engineering Relevant Quantities in Boundary Layer

Boundary layer theory provides critical tools for quantifying momentum, thermal, and nanoparticle transport rates in fluid systems. These transfer rates are characterized by three fundamental dimensionless parameters: the local skin friction coefficient for momentum transfer, the Nusselt number for heat transfer, and the Sherwood number for mass transfer. Their rigorous mathematical formulation is presented below.

5.2.5.1 Skin Friction Coefficients

The primary and secondary skin friction coefficients C_{fx} and C_{fz} in the x and z directions are defined as follows:

$$C_{fx} = \frac{\tau_{wx}}{\rho U_w^2}, \quad C_{fz} = \frac{\tau_{wz}}{\rho U_w^2}, \tag{5.56}$$

where τ_{wx} and τ_{wz} represent the wall shear stresses in the $x-$ and $z-$ directions, respectively.

From the constitutive equation of Casson fluid Eq. (2.25), the stress tensor components at the wall ($y = 0$) are:

$$\tau_{yx} = \mu_B\left(1 + \frac{1}{\beta}\right)\left(\frac{\partial u}{\partial y} + \frac{\partial v}{\partial x}\right), \quad \tau_{yz} = \mu_B\left(1 + \frac{1}{\beta}\right)\left(\frac{\partial v}{\partial z} + \frac{\partial w}{\partial y}\right). \tag{5.57}$$

where μ_B is the dynamic viscosity of the Casson fluid. Under boundary layer assumptions ($v = 0$ at $y = 0$, $\partial v/\partial x \approx 0$, $\partial v/\partial z \approx 0$), the wall shear stresses reduce to:

$$\tau_{wx} = \mu_B\left[\left(1 + \frac{1}{\beta}\right)\left(\frac{\partial u}{\partial y}\right)\right]_{y=0}, \quad \tau_{wz} = \mu_B\left[\left(1 + \frac{1}{\beta}\right)\left(\frac{\partial w}{\partial y}\right)\right]_{y=0}. \tag{5.58}$$

Using similarity transformations Eq. (5.24), the velocity gradients at $y = 0$ ($\eta = 0$) are:

$$\begin{cases} \left.\dfrac{\partial u}{\partial y}\right|_{y=0} = axf''(0)\sqrt{\dfrac{a}{\upsilon}}, \\ \left.\dfrac{\partial w}{\partial y}\right|_{y=0} = axh'(0)\sqrt{\dfrac{a}{\upsilon}}. \end{cases} \tag{5.59}$$

Substituting Eq. (5.59) into Eq. (5.58):

$$\begin{cases} \tau_{wx} = \mu_B\left[\left(1 + \dfrac{1}{\beta}\right)\left(axf''(0)\sqrt{\dfrac{a}{\upsilon}}\right)\right] = \mu_B ax\sqrt{\dfrac{a}{\upsilon}}\left[\left(1 + \dfrac{1}{\beta}\right)f''(0)\right], \\ \tau_{wz} = \mu_B\left[\left(1 + \dfrac{1}{\beta}\right)\left(axh'(0)\sqrt{\dfrac{a}{\upsilon}}\right)\right] = \mu_B ax\sqrt{\dfrac{a}{\upsilon}}\left[\left(1 + \dfrac{1}{\beta}\right)h'(0)\right]. \end{cases} \tag{5.60}$$

Thus, the dimensionless form of the skin friction coefficients of Eq. (5.56) are as follows.

$$C_{fx}\sqrt{\mathrm{Re}_x} = \frac{\sqrt{\mathrm{Re}x}}{\rho(ax)^2} \cdot \mu_B ax\sqrt{\frac{a}{\upsilon}}\left[\left(1 + \frac{1}{\beta}\right)f''(0)\right], \tag{5.61}$$

$$C_{fz}\sqrt{\mathrm{Re}_x} = \frac{\sqrt{\mathrm{Re}x}}{\rho(ax)^2} \cdot \mu_B ax\sqrt{\frac{a}{\upsilon}}\left[\left(1 + \frac{1}{\beta}\right)h'(0)\right], \tag{5.62}$$

where $\text{Re}x = \dfrac{xU_w}{\upsilon} = \frac{ax^2}{\upsilon}$ is local Reynolds number. Eqs. (5.61) and (5.62) can be simplified to

$$C_{fx}\sqrt{\text{Re}x} = \left(1 + \frac{1}{\beta}\right) f''(0), \tag{5.63}$$

$$C_{fz}\sqrt{\text{Re}_x} = \left(1 + \frac{1}{\beta}\right) h'(0). \tag{5.64}$$

5.2.5.2 Local Nusselt Number

The Nusselt number characterizes convective heat transfer efficiency relative to conduction and is defined by:

$$Nu_x = \frac{xq_w}{\kappa(T_w - T_\infty)}, \tag{5.65}$$

where q_w is the total wall heat flux, combining molecular conduction and radiative transfer:

$$q_w = -\left(k + \frac{16\sigma^*}{3k^*} T^3\right) \frac{\partial T}{\partial y}\bigg|_{y=0}. \tag{5.66}$$

Substituting Eq. (5.66) into Eq. (5.65):

$$Nu_x = \frac{-x}{T_w - T_\infty}\left(1 + \frac{16\sigma^* T_w^3}{3\kappa k^*}\right) \frac{\partial T}{\partial y}\bigg|_{y=0}. \tag{5.67}$$

Using the similarity transformation of Eq. (5.24) for temperature:

$$\theta(\eta) = \frac{T - T_\infty}{T_w - T_\infty}, \quad \frac{\partial T}{\partial y}\bigg|_{y=0} = (T_w - T\infty)\sqrt{\frac{a}{\upsilon}}\theta'(0), \tag{5.68}$$

Eq. (5.67) becomes:

$$\begin{aligned} Nu_x &= -\frac{x}{T_w - T_\infty}\left(1 + \frac{16\sigma^* T_w^3}{3\kappa k^*}\right)(T_w - T_\infty)\sqrt{\frac{a}{\upsilon}}\theta'(0) \\ &= -x\sqrt{\frac{a}{\upsilon}}\left(1 + \frac{16\sigma^* T_w^3}{3kk^*}\right)\theta'(0) \\ &= -x\sqrt{\frac{a}{\upsilon}}\left(1 + R_n\theta_r^3\right)\theta'(0). \end{aligned} \tag{5.69}$$

Finally, the dimensionless Nusselt number is:

$$\frac{Nu_x}{\sqrt{\text{Re}_x}} = -\left(1 + R_n\theta_r^3\right)\theta'(0). \tag{5.70}$$

5.2.5.3 Local Sherwood Number

The Sherwood number describes convective-diffusive mass transfer efficiency.

$$Sh_x = \frac{xq_m}{D_B(C_w - C_\infty)}, \tag{5.71}$$

with q_m defined by Fick's law for wall mass flux:

$$q_m = -D_B \frac{\partial C}{\partial y}\bigg|_{y=0}. \tag{5.72}$$

This reduces to the concentration gradient expression as follows.

$$Sh_x = \frac{-x}{C_w - C_\infty} \frac{\partial C}{\partial y}\bigg|_{y=0}. \tag{5.73}$$

Using the similarity transformation for concentration:

$$\phi(\eta) = \frac{C - C_\infty}{C_w - C_\infty}, \quad \frac{\partial C}{\partial y}\bigg|_{y=0} = (C_w - C\infty)\sqrt{\frac{a}{\upsilon}}\phi'(0), \tag{5.74}$$

Eq. (5.73) simplifies to:

$$Sh_x = -\frac{x}{C_w - C_\infty} \cdot (C_w - C_\infty)\sqrt{\frac{a}{\upsilon}}\phi'(0) = -x\sqrt{\frac{a}{\upsilon}}\phi'(0). \tag{5.75}$$

The dimensionless form of the Sherwood number is:

$$\frac{Sh_x}{\sqrt{\mathrm{Re}_x}} = -\phi'(0). \tag{5.76}$$

5.3 Method of Solutions

The present problem is numerically solved using the shooting technique with a sixth-order Runge-Kutta (RK6) procedure. For approximating solutions to ODEs, the Runge-Kutta method with high-order accuracy serves as an efficient tool. As a first step, Eqs. (5.52)–(5.55) in addition to the boundary conditions Eq. (5.51) are transformed into a system of first-order ODEs. This transformation is achieved by introducing the substitution ($f = f_1, \quad f' = f_2, \quad f'' = f_3, \quad h = f_4, \quad h' = f_5, \quad \theta = f_6, \quad \theta' = f_7, \quad \phi = f_8, \quad \phi' = f_9$), which simplifies the equations to the following initial value problems (IVPs).

$$\begin{cases} f_1' = f_2 & f_1(0) = 0, \\ f_2' = f_3 & f_2(0) = 1, \\ f_3' = \dfrac{\left[-f_1 f_3 + f_2^2 + Da f_2 + \dfrac{M\left((1+\beta_e\beta_i) f_2 + \beta_e f_4\right)}{(1+\beta_e\beta_i)^2 + \beta_e^2} - \lambda_t f_6 - \lambda_c f_8\right]}{\left(1 + \dfrac{1}{\beta}\right)} & f_3(0) = \delta_1, \\ f_4' = f_5 & f_4(0) = 0, \\ f_5' = \dfrac{\left[-f_1 f_5 + f_2 f_4 + Da f_4 - \dfrac{M\left(\beta_e f_2 - (1+\beta_e\beta_i) f_4\right)}{(1+\beta_e\beta_i)^2 + \beta_e^2}\right]}{\left(1 + \dfrac{1}{\beta}\right)} & f_5(0) = \delta_2, \\ f_6' = f_7 & f_6(0) = 1, \\ f_7' = \dfrac{-1}{\left(1 + R_n\left(1 + (\theta_r - 1) f_6\right)^3\right)} \Bigg[Pr\Bigg(Q_h f_6 + f_7 f_1 + N_b f_7 f_9 + N_t f_7^2 \\ \qquad + Ec\left(1 + \dfrac{1}{\beta}\right)\left(f_3^2 + f_5^2\right) & f_7(0) = \delta_3, \\ \qquad + \dfrac{MEc\left(f_2^2 + f_4^2\right)}{(1+\beta_e\beta_i)^2 + \beta_e^2}\Bigg) \\ \qquad + R_n\left[3(\theta_r - 1)\left(1 + (\theta_r - 1) f_6\right)^2 f_7^2\right]\Bigg] \\ f_8' = f_9 & f_8(0) = 1, \\ f_9' = -Sc f_1 f_9 - \dfrac{N_t}{N_b} f_7' + Sc C_r f_8 & f_9(0) = \delta_4, \end{cases} \tag{5.77}$$

where δ_1, δ_2, δ_3 and δ_4 are the missing initial conditions.

Eq. (5.77) is then computed numerically using RK6 method. This is accomplished by guessing appropriate initial values for the missing initial conditions, δ_1, δ_2, δ_3 and δ_4. The shooting technique helps in adjusting these initial guesses based on the convergence behavior of the computed solutions. This process of iteration persists until the targeted level of accuracy is attained. In order to guarantee precise and reliable outcomes, a step size of 0.1 and an error tolerance of 10^{-6} are employed for all calculations. We employ an open-sourced Python programming language that makes the numerical method easier to develop and analyze. The specific Python libraries and packages, such as NumPy for numerical computations, SciPy (fsolve) for solving differential equations, and Matplotlib for plotting graphs, are used. This tool facilitates a rapid computation and display of the results, which helps to an in-depth understanding of the phenomena under study.

5.4 Results and Discussion

This study examines the effects of viscous dissipation, ion slip, Hall currents, Ohmic (Joule) heating, nonlinear thermal radiation and chemical reactions on the mixed convection flow of an MHD Casson nanofluid across a vertically extending sheet. The numerical results obtained by applying the shooting method in combination with the sixth-order Runge-Kutta (RK6) technique to solve the governing equations of the problem are also discussed.

5.4.1 Validation of the Numerical Method

To verify the accuracy of numerical results, a comparative analysis was conducted with the existing literature. Evaluating the values of $-(1+\frac{1}{\beta})f''(0)$ against M for specific parameter values is summarized in Table 5.2. Similarly, Table 5.3 provides a comparison of the numerical solution of the previously published findings with the present study by calculating the values of $-\theta'(0)$ and $-\phi'(0)$ under specific conditions. The comparison results validate the accuracy as well as reliability of our computational approach by demonstrating excellent agreement with earlier studies.

Table 5.2: The numerical value comparison of Nadeem et al. [3], Sahoo and Nandkeolyar [4] and the current findings by analyzing the values of $-(1+\frac{1}{\beta})f''(0)$ against M for $\beta = 1$, $Pr = 10$, $Nb = Nt = 0.1$ and the absence of Da, Ec, C_r, S, R_n, θ_r, Sc, β_i, β_e, λ_t, and λ_c.

M	$-\left(1+\frac{1}{\beta}\right)f''(0)$		
	Nadeem et al.	Sahoo and Nandkeolyar	Present Study
0	1.4142	1.4142	1.415193
10	4.6904	4.6904	4.690416
100	14.2127	14.2127	14.212670

Table 5.3: A comparison of results of Khan and Pop [1], Sahoo and Nandkeolyar [4] and current study by examining the values of $-\theta'(0)$ and $-\phi'(0)$ under the conditions $Pr = Sc = 10$, $\beta \to \infty$, $Nb = 0.1$ and $M = Da = Ec = C_r = Q_h = R_n = \theta_r = Sc = \beta_i = \beta_e = \lambda_t = \lambda_c = 0$.

N_t	$-\theta'(0)$			$-\phi'(0)$		
	Khan and Pop [1]	Sahoo and Nandkeolyar [4]	Present Study	Khan and Pop [1]	Sahoo and Nandkeolyar [4]	Present Study
0.1	0.9524	0.9524	0.952372	2.1294	2.1294	2.129355
0.2	0.6932	0.6932	0.693173	2.2740	2.2740	2.273956
0.3	0.5201	0.5201	0.520081	2.5286	2.5286	2.528542
0.4	0.4026	0.4026	0.402584	2.7952	2.7952	2.795049
0.5	0.3211	0.3211	0.321059	3.03511	3.03511	3.034979

5.4.2 Profiles of Velocity, Temperature and Nanoparticle Concentration with Prominent Flow Parameters

Physical phenomenon, such as temperature, velocity, nanoparticle concentration, skin friction coefficients, Nusselt number (rate of heat transfer), and Sherwood number (rate of mass transfer), were evaluated in the computations. These analyses were carried out over a wide variety of values of parameter in order to investigate their influence on the properties of mass, momentum, and heat transfer. Thus, several parameters, including the Hall currents (β_e), ion slip (β_i), Casson fluid parameter (β), mixed convection parameters due to temperature difference (λ_t), modified mixed convection parameters due to density difference (λ_c), nonlinear thermal radiation (R_n) parameter, magnetic field parameter (M), the temperature ratio parameter (θ_r), Prandtl number (Pr), Schmidt number (Sc), Eckert number (Ec), Darcy number (Da), chemical reaction (C_r), Brownian diffusion (N_b), heat generation (Q_h), and thermophoretic parameter (N_t), are considered in numerical computations while some of the important parameters effect on temperature distributions, velocity profiles, nanoparticle concentrations, profiles of Nussult number, skin friction and Sherwood number are investigated and plotted graphically from a physical point of view in order to explore and illustrate their effects on the flow field. It is crucial to recognize that, default values were utilized for the parameters as: $\beta = 0.5$, $\beta_e = 2$, $\beta_i = 1$, $\theta_r = 1$, $Ec = 0.1 = N_t = Q_h$, $R_n = 0.5 = C_r = Da = \lambda_t = \lambda_c$, $Pr = 6$, $M = 7$, $N_b = 0.2$, $Sc = 1.5$, unless explicitly indicated otherwise in the plots.

Both the principal (x-direction), $f'(\eta)$, and secondary (z-direction), $h(\eta)$ velocity profiles and their reliance on relevant parameters in particular are analyzed. Figs. 5.2–5.6 provide graphical representations of the effects of different prominent parameters on the principal velocity profiles. These parameters include Hall currents (β_e), ion slip (β_i), Casson parameter (β), mixed convection (λ_t), and modified mixed convection (λ_c) parameters.

Firstly, raising the magnitude of the Hall current, ion slip, mixed convection, and modified mixed convection parameters causes an amplification of the principal velocity profile $f'(\eta)$ within the boundary layer. The application of a transverse magnetic field perpendicular to the fluid flow generates a resisting Lorentz force that opposes and decelerates the fluid motion within the boundary layer. However, incorporating the Hall parameter (β_e) decreases the effective electrical conductivity, which in turn reduces the magnitude of the magnetic resistive Lorentz force. Consequently, this allows for enhanced fluid motion, resulting in an increased profile of principal velocity $f'(\eta)$, as shown in Figure 5.2.

As illustrated in Fig. 5.3, the ion slip parameter (β_i) exhibits a similar effect. Specifically, as the value of the ion slip parameter β_i increases, the damping or retarding force decreases. This reduction in the damping force then leads to an increase in the principal velocity profile $f'(\eta)$.

Additionally, both Figs. 5.5 and 5.6 demonstrate that the mixed convection parameters and the modified mixed convection parameters contribute to the buoyancy-driven flow. Consequently, the fluid experiences further acceleration in the x-direction (streamwise direction) within the boundary layer region.

In contrast, when the Casson parameter rises, the principal velocity profile experiences a decline as dipited in Fig. 5.4. The Casson parameter describes how the Casson nanofluid behaves rheologically, and when its value increases, it leads to a decrease in the velocity component in the x-direction. This occurrence can be explained by the fact that the Casson fluid exhibits shear-thinning behavior, where an increase in viscosity impedes the fluid's movement, ultimately causing a decrease in the principal velocity profile $f'(\eta)$. Asifa et al. [198] also observed that "the flow of nanofluid decelerates with increasing Casson parameter values due to the dominant plasticity effects, which lead to a reduction in the boundary layer." Their observation is consistent with our findings, and this correlation underscores the consistency and reliability of our results with established literature.

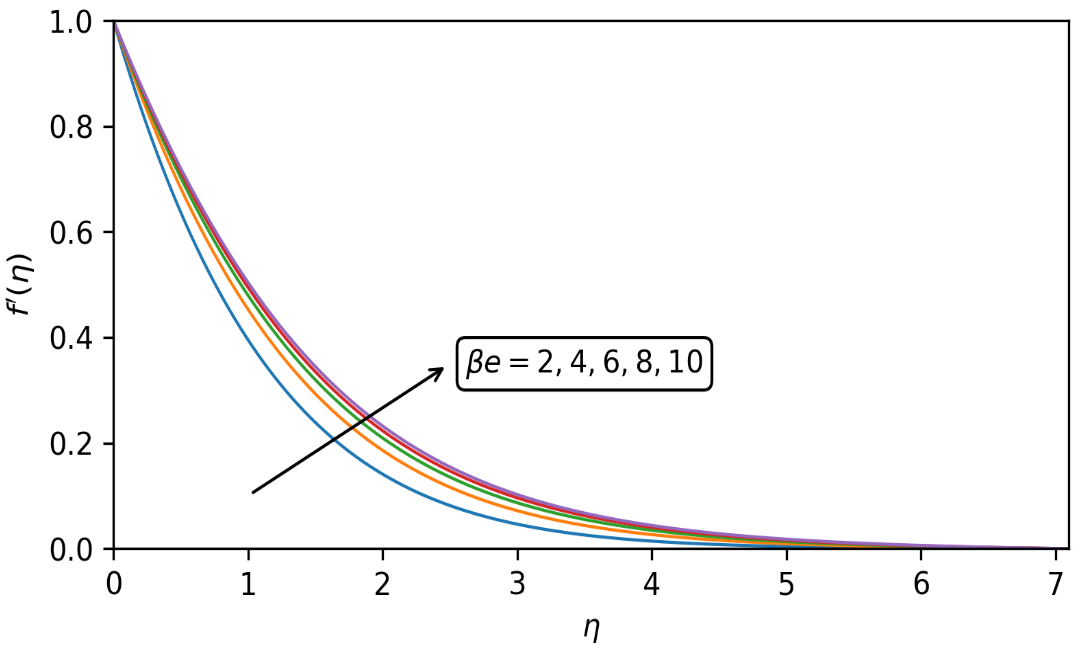

Figure 5.2: Effects of Hall parameter β_e on the principal velocity $f'(\eta)$.

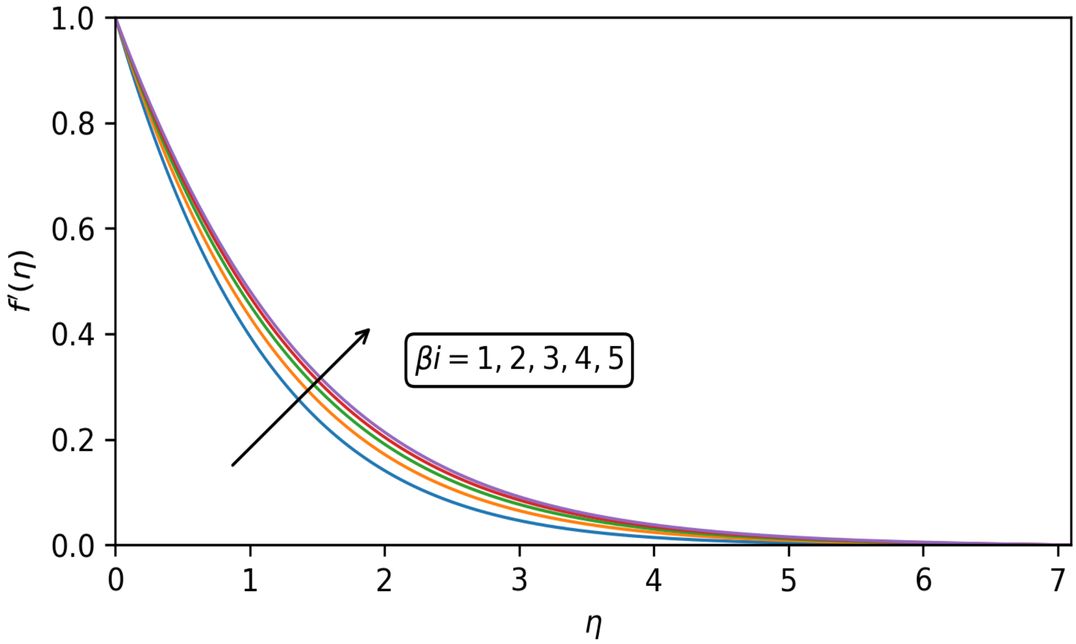

Figure 5.3: Effects of Ion slip parameter β_i on the principal velocity $f'(\eta)$.

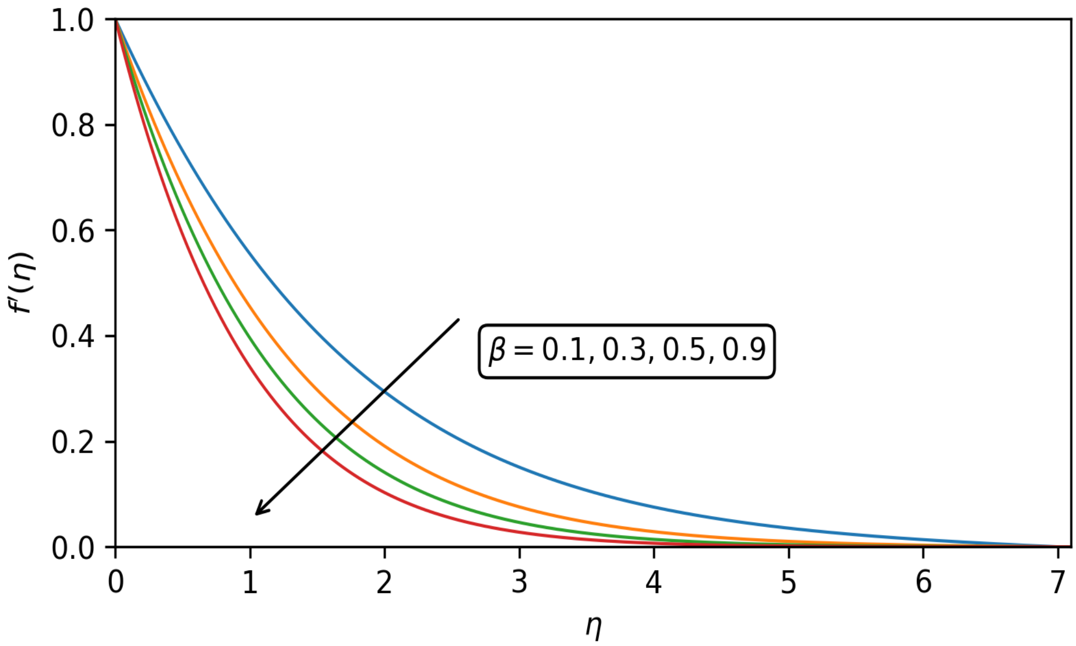

Figure 5.4: Effects of β (Casson parameter) on the principal velocity $f'(\eta)$.

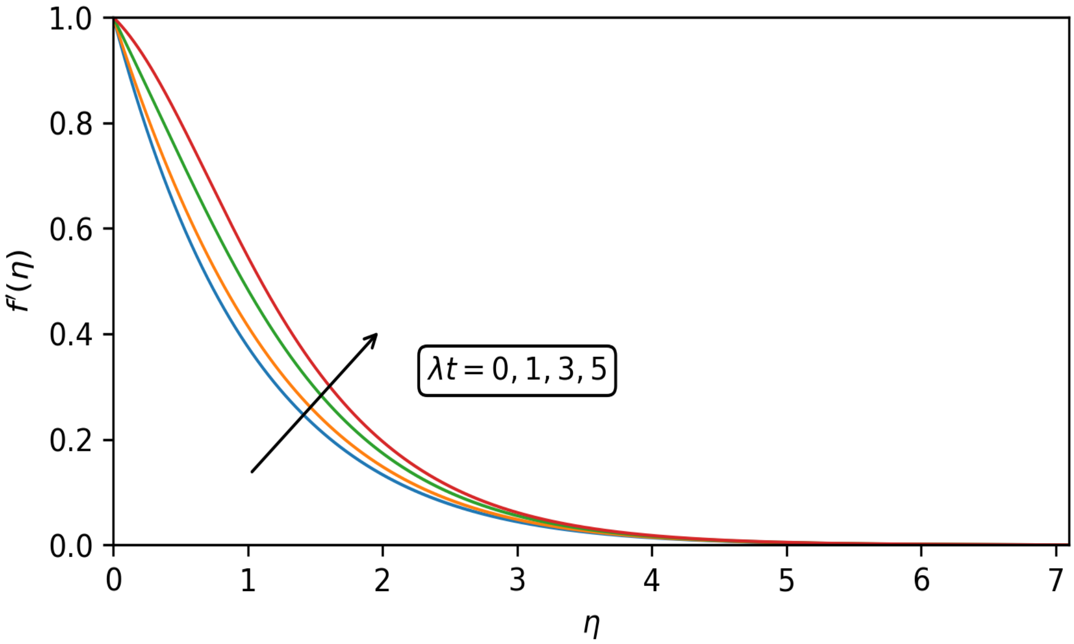

Figure 5.5: Effects of λ_t (mixed convection parameter) on the principal velocity $f'(\eta)$.

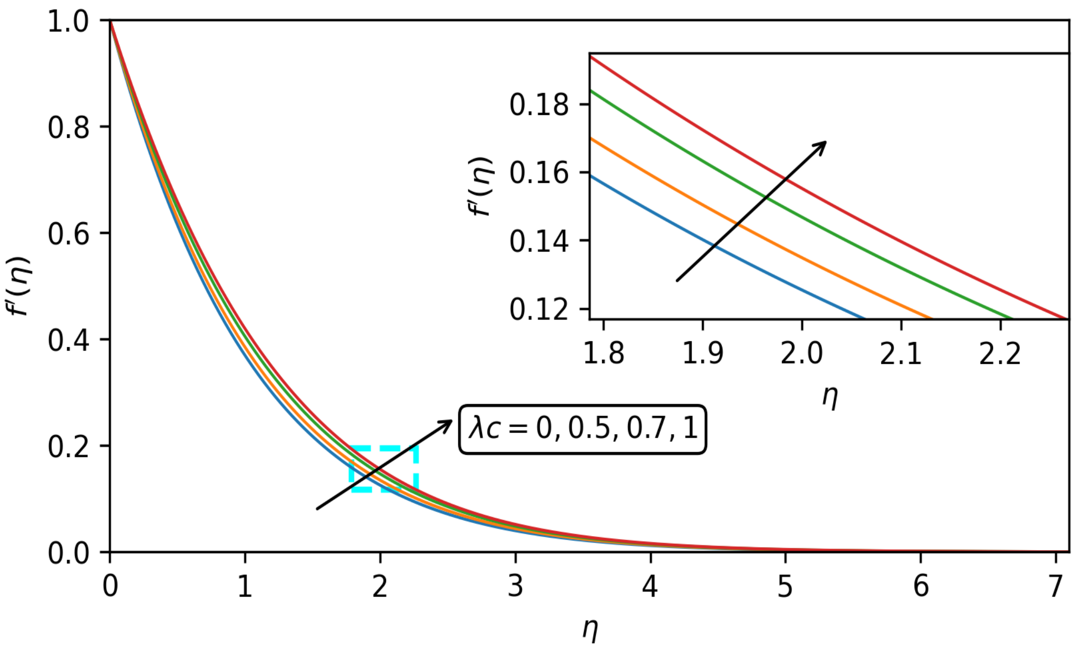

Figure 5.6: Effects of λ_c (modified mixed convection parameter) on the principal velocity $f'(\eta)$.

Moving on to the minor (secondary) velocity profiles $h(\eta)$, Figs. 5.7–5.11 demonstrate the impacts of Hall currents, ion slip, Casson, mixed convection, and modified mixed convection parameters. The secondary velocity profile is influenced by the imposition of a powerful magnetic field, resulting in the generation of Hall currents and ion slip. Figs. 5.7 and 5.8 depict that elevating the values of both the Hall current and ion slip parameters leads to a reduction in the secondary velocity.

Notably, as visualized in Fig. 5.9, increasing the Casson parameter exhibits a dual nature of the secondary velocity profile ($h(\eta)$). Specifically, as the Casson parameter rises, the secondary velocity undergoes a rapid growth near the sheet, followed by a gradual decline away from the sheet within the boundary layer. The observed phenomenon can be ascribed to the combined impact of the rheological characteristics of the Casson fluid and the behavior of the nanofluid in close proximity to the boundary. The elevated Casson parameter results in an enhanced fluid viscosity and a tendency for shear-thinning near the sheet, thereby causing a rapid escalation in the secondary velocity. However, as we traverse away from the sheet, the velocity of the fluid gradually diminishes due to the influence of other parameters.

On the other hand, the minor (secondary) velocity profile $h(\eta)$ is considerably increased when the mixed convection parameters and modified mixed convection parameters are increased, as displayed in Figs. 5.10 and 5.11. This behavior can be elucidated by considering the combined influence of buoyancy force and density difference, which augment the fluid motion within the boundary layer.

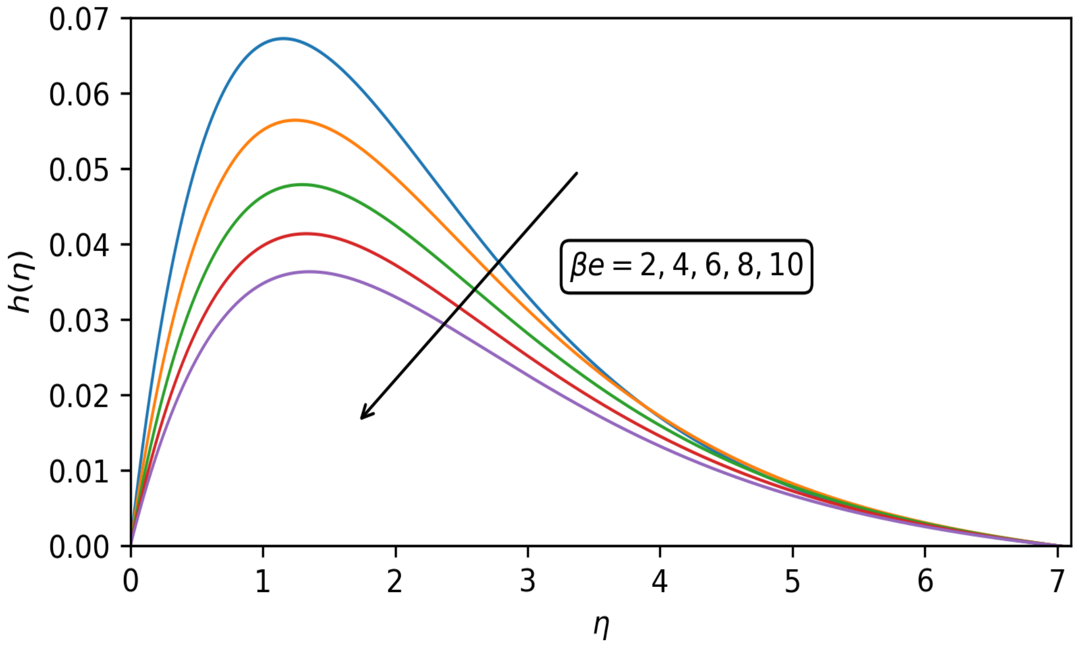

Figure 5.7: Effects of β_e (Hall parameter) on the secondary velocity $h(\eta)$.

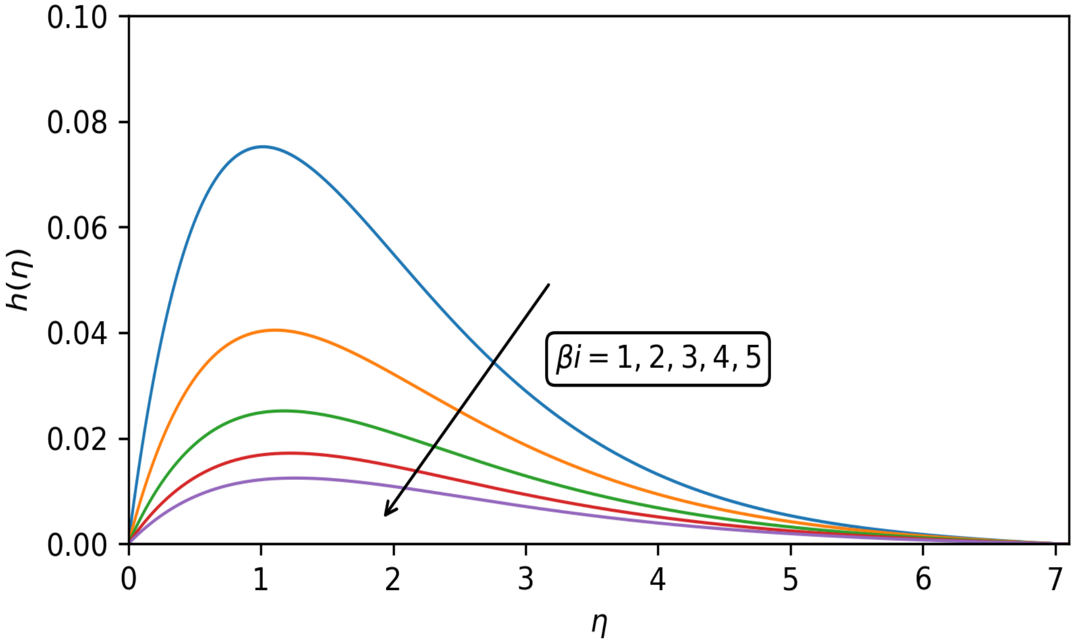

Figure 5.8: Effects of β_i (Ion slip) on the secondary velocity $h(\eta)$.

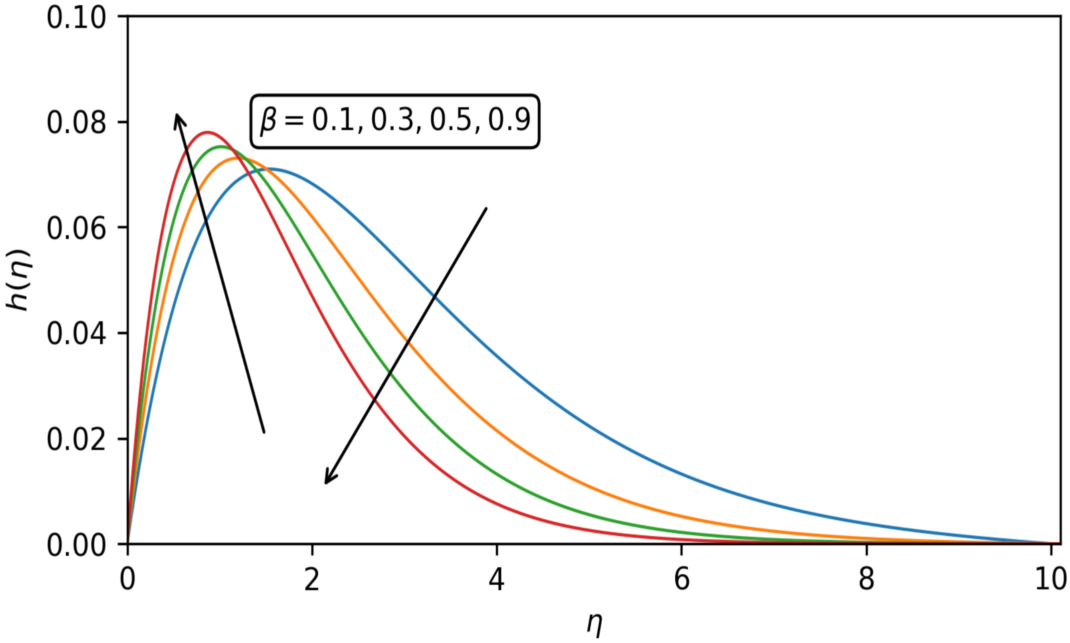

Figure 5.9: Effects of β (Casson parameter) on the secondary velocity $h(\eta)$.

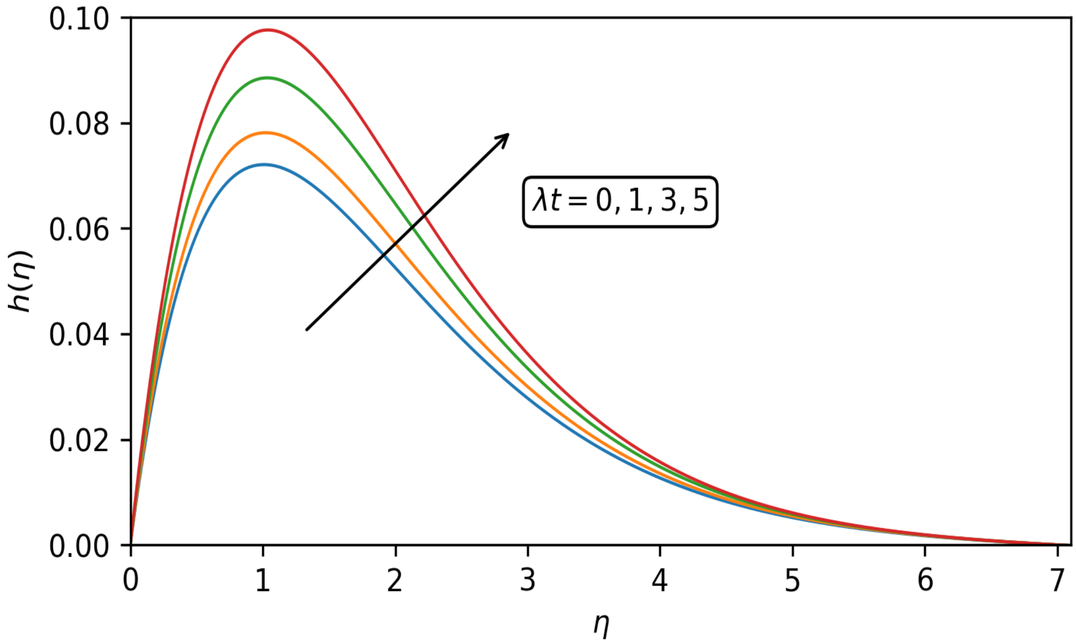

Figure 5.10: Effects of λ_t on the secondary velocity $h(\eta)$.

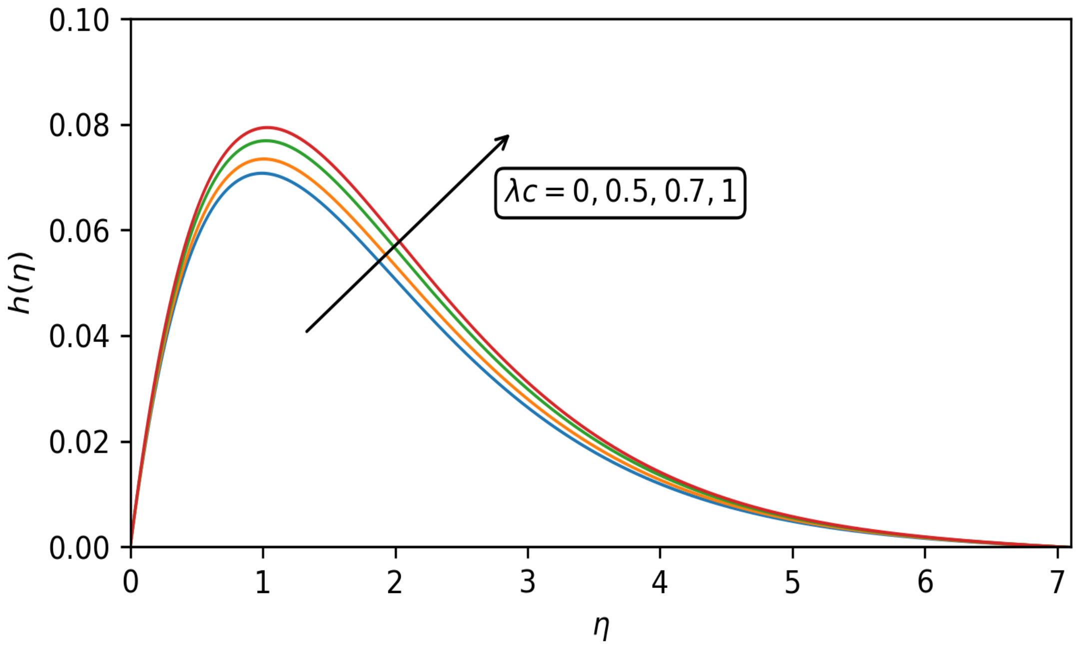

Figure 5.11: Effects of λ_c on the secondary velocity $h(\eta)$.

Figs. 5.12–5.18 present the outcomes of the investigation, focusing on the temperature profiles. Figs. 5.12 and 5.13 illustrate the impact of two parameters, namely Hall currents (β_e) and ion slip (β_i), on the distribution of temperature ($\theta(\eta)$) respectively. It is evident that augmenting the values of the Hall currents (β_e) cause a reduction in the temperature distribution. A similar trend is observed as the ion slip (β_i) parameter is increased. Physically, in an electrically conducting fluid, the presence of Hall currents and ion slip effects introduce additional dissipative mechanisms, ultimately leading to a lowering of fluid temperature within the boundary layer.

The temperature distributions shown in Fig. 5.14 illustrates the profiles associated with different values of the Casson parameter (β). The graph demonstrates that as the Casson parameter (β) increases, the temperature of the fluid within the boundary layer decreases. The Casson parameter characterizes the non-Newtonian behavior of the nanofluid, and a higher value of β indicates an intensified resistance to flow. As a consequence of this heightened resistance, the fluid experiences diminished thermal transport, and hence the fluid temperature drops.

Fig. 5.15 portrays the temperature profiles corresponding to varying values of the mixed convection parameter (λ_t). It is clear that an increase in the mixed convection parameters causes a decline in the temperature profile. This phenomenon can be attributed to the influence of higher temperature differences, which generate stronger buoyancy forces. The intensified buoyancy forces enhance the convective heat transfer, leading to a reduction in the fluid temperature near the stretching sheet.

The impact of nonlinear thermal radiation parameter (R_n) on the fluid temperature profile ($\theta(\eta)$) is demonstrated in Fig. 5.16. The findings indicate that an escalation in the nonlinear thermal radiation parameter results in a substantial increase in the temperature profile. Nonlinear thermal radiation pertains to the radiation heat transfer that deviates from the linear Stefan-Boltzmann law. The parameter R_n represents the relative importance of nonlinear radiation, and its increase enhances the radiative heat transfer, thus elevating the fluid temperature.

Likewise, Fig. 5.17 presents the impact of the temperature ratio parameter (θ_r) on the distribution of temperature. It is evident that an augmentation in the temperature ratio parameter causes an elevation in the fluid temperature. The temperature ratio parameter is a measure of the relationship between the temperature at the surface and the ambient temperature. As this ratio increases, it suggests a greater temperature difference between the surface and the surrounding environment. This higher temperature gradient near the surface leads to an elevated temperature of the fluid within the boundary layer.

Lastly, Fig. 5.18 portrays the influence of the Eckert number (Ec) on the temperature profile ($\theta(\eta)$). The findings demonstrate that augmenting the values of the

Eckert number enhances the temperature profile across the entire boundary layer. Specifically, as the Eckert number increases, a prominent bulge is observed near the sheet, while the temperature gradually approaches the ambient temperature as one moves away from the sheet. Ec represents the ratio of the fluid's kinetic energy to its internal energy, and an increase in this parameter indicates a greater conversion of kinetic energy into thermal energy. Consequently, this intensifies the heating effect, resulting in an elevated temperature profile.

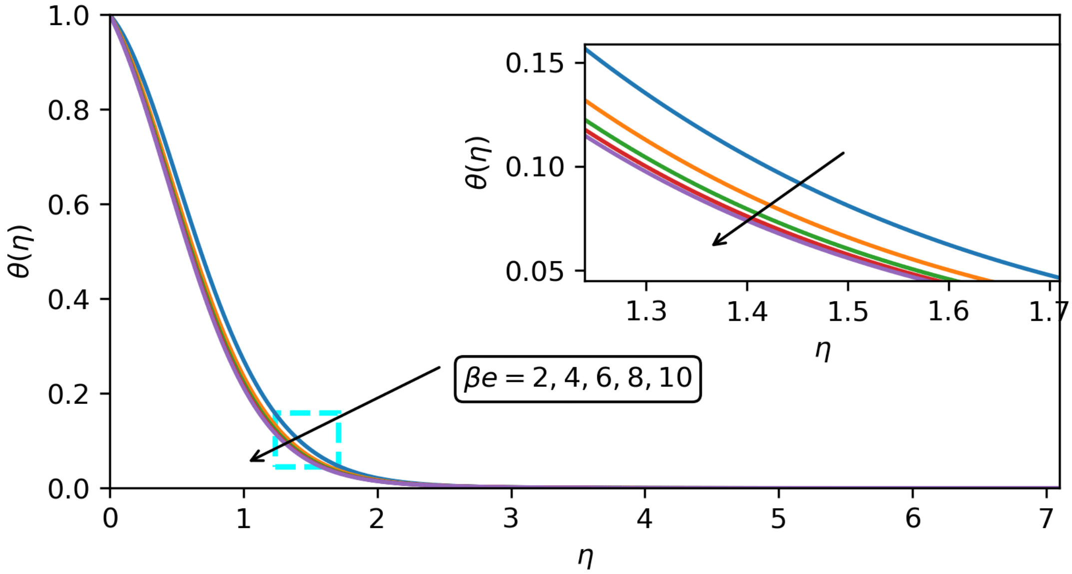

Figure 5.12: Impacts of Hall parameter β_e on temperature $\theta(\eta)$.

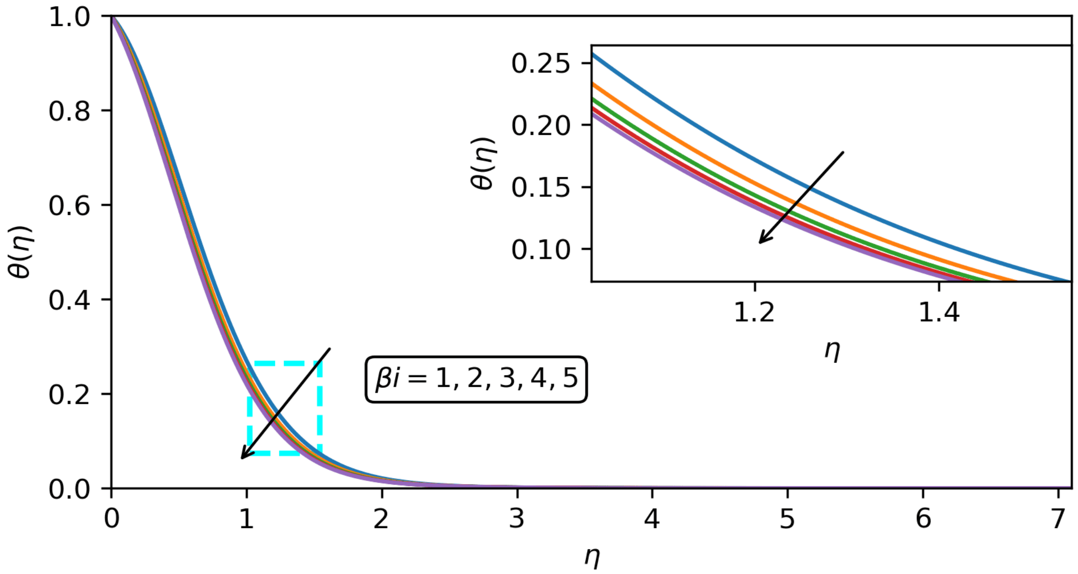

Figure 5.13: Impacts of ion slip parameter β_i on $\theta(\eta)$.

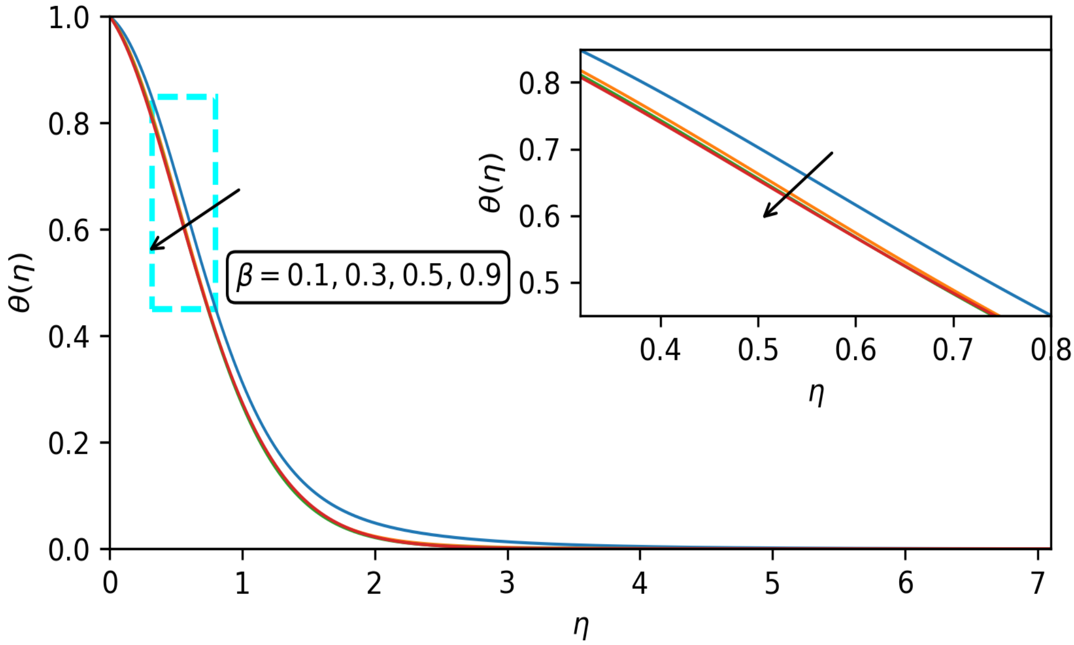

Figure 5.14: Impacts of Casson parameter β on $\theta(\eta)$.

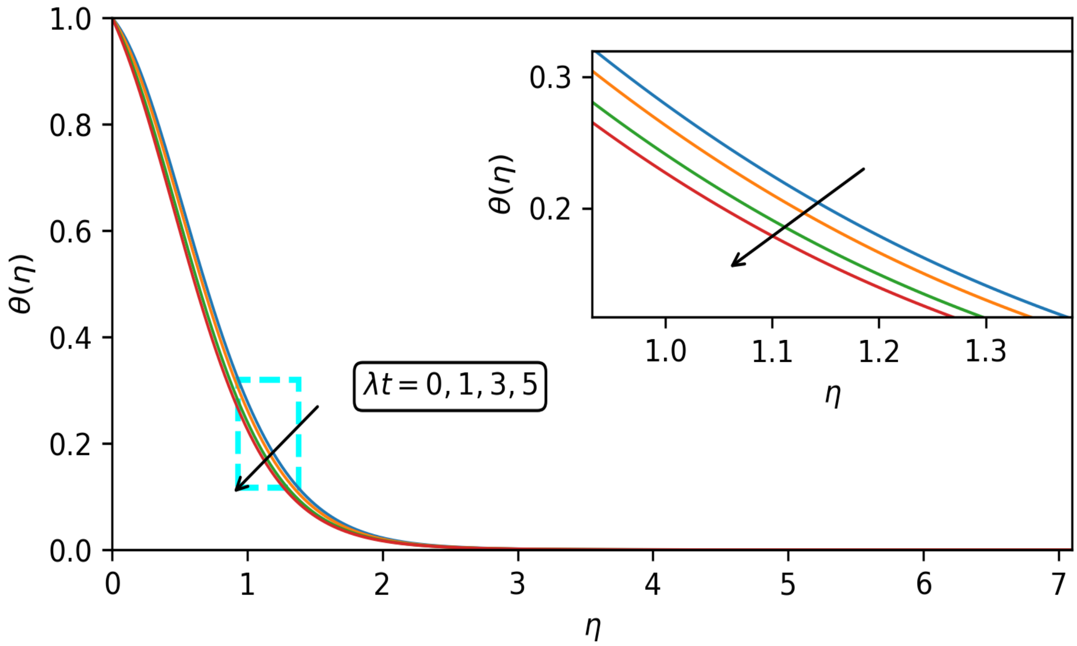

Figure 5.15: Impacts of λ_t on $\theta(\eta)$.

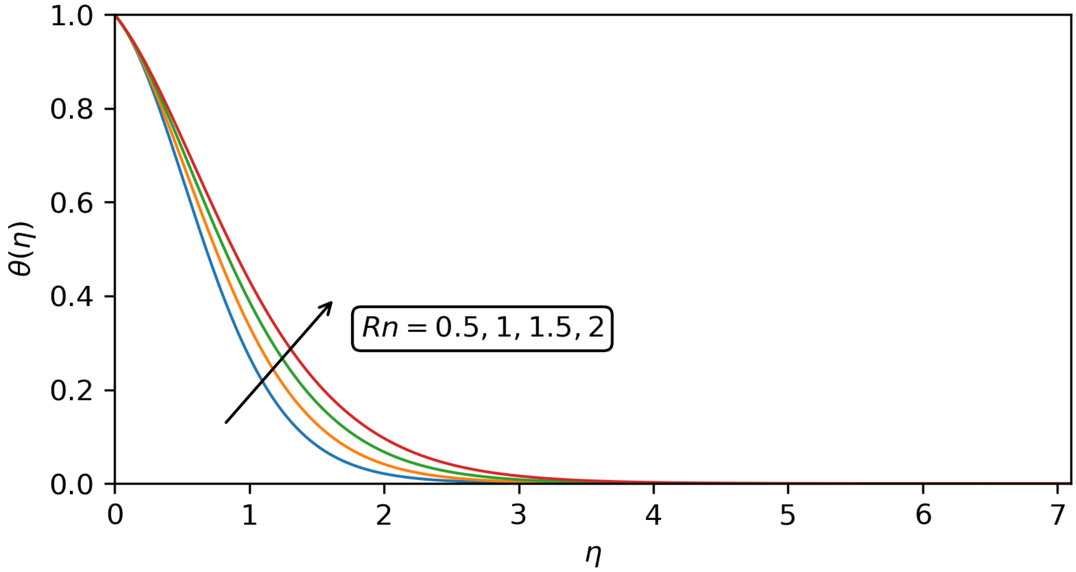

Figure 5.16: Impacts of nonlinear thermal radiation Rn on temperature profile $\theta(\eta)$.

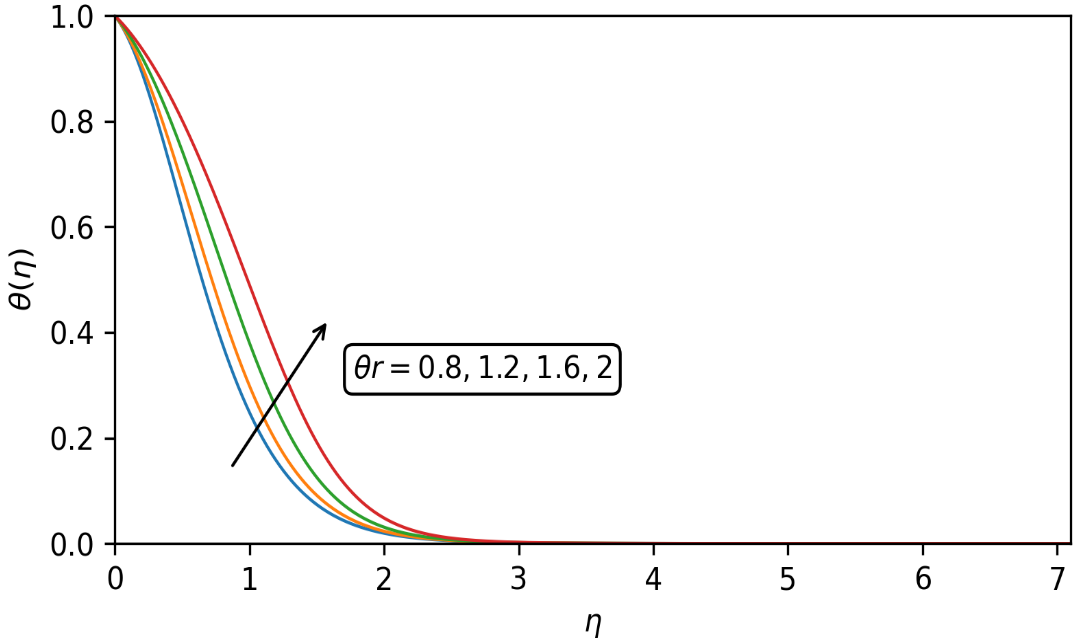

Figure 5.17: Impacts of θ_r on temperature profile $\theta(\eta)$.

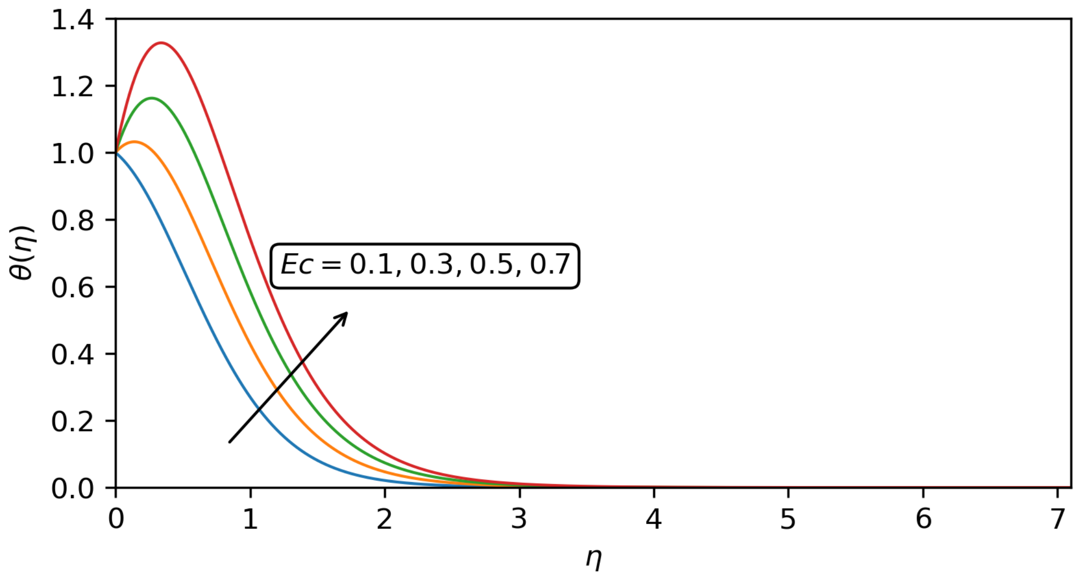

Figure 5.18: Impacts of Ec on temperature profile $\theta(\eta)$.

Fig. 5.19 displays the concentration profile for various values of the Casson parameter β. It is noticed that higher values of β function as an aiding factor in the distribution of nanoparticle concentration within the boundary layer region. This occurrence can be explained by the association between higher values of β and increased fluid viscosity, which impedes the movement of nanoparticles. Consequently, nanoparticles tend to accumulate near the sheet. Therefore, an elevation in the value of β amplifies the distribution of concentration.

Influences of the modified mixed convection parameter, λ_c, on the nanoparticle concentration $\phi(\eta)$ is exhibited in Fig. 5.20. It is observed that λ_c has no significant effect on the distribution of nanoparticle concentration. However, a slight reduction in $\phi(\eta)$ is visualized with increasing values of λ_c. This can be explained by considering that the modified mixed convection parameter influences the fluid flow characteristics, but its effect on nanoparticle concentration is relatively weak.

Fig. 5.21 illustrates the dual nature of the nanoparticle concentration profile, $\phi(\eta)$, with respect to the Eckert number (Ec). As Ec increases, the distribution of nanoparticle concentration decreases rapidly near the sheet. This indicates that the presence of higher thermal energy at the surface reduces the nanoparticle concentration in that region. However, further away from the sheet, the nanoparticle concentration starts to increase within the boundary layer.

Fig. 5.22 highlights the concentration profile for different values of the chemical reaction parameter (Cr). It is noticed that an augmentation in Cr results in a decline in the distribution of nanoparticle concentration $\phi(\eta)$. This can be clarified by considering that elevated values of Cr align with more vigorous chemical reactions, leading to the depletion of nanoparticles. Consequently, the concentration of nanoparticles within the boundary layer decreases.

Similarly, Fig. 5.23 demonstrates the impact of the Schmidt number (Sc) on the distribution of nanoparticle concentration $\phi(\eta)$. It is found that the distribution of nanoparticle concentration in the boundary layer diminishes with increasing Sc. From the definition of a Schmidt number, an increase in Sc indicates a higher momentum diffusivity compared to mass diffusivity, resulting in a reduction in the distribution of nanoparticle concentration.

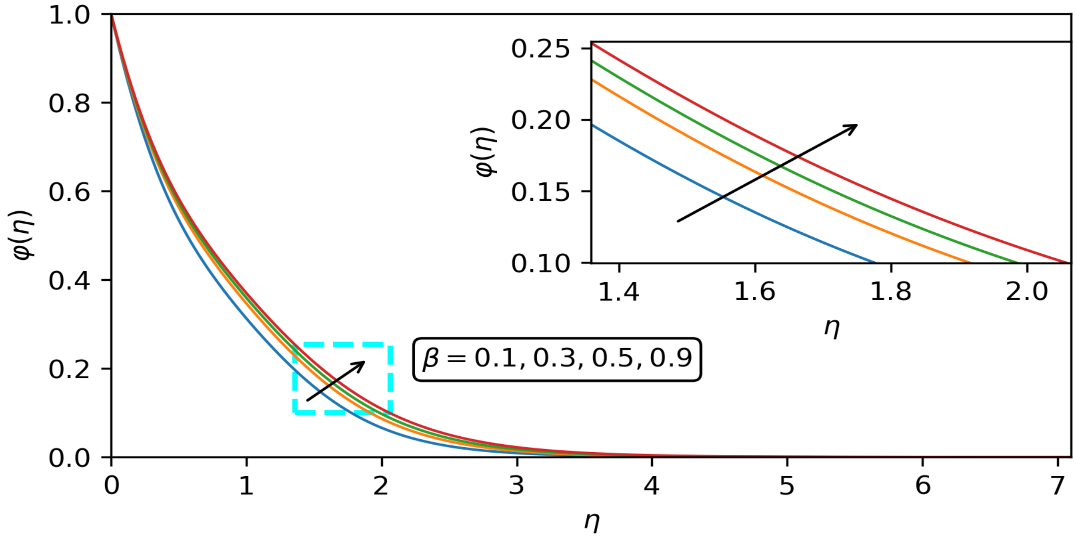

Figure 5.19: Influences of β on nanoparticle concentration $\phi(\eta)$.

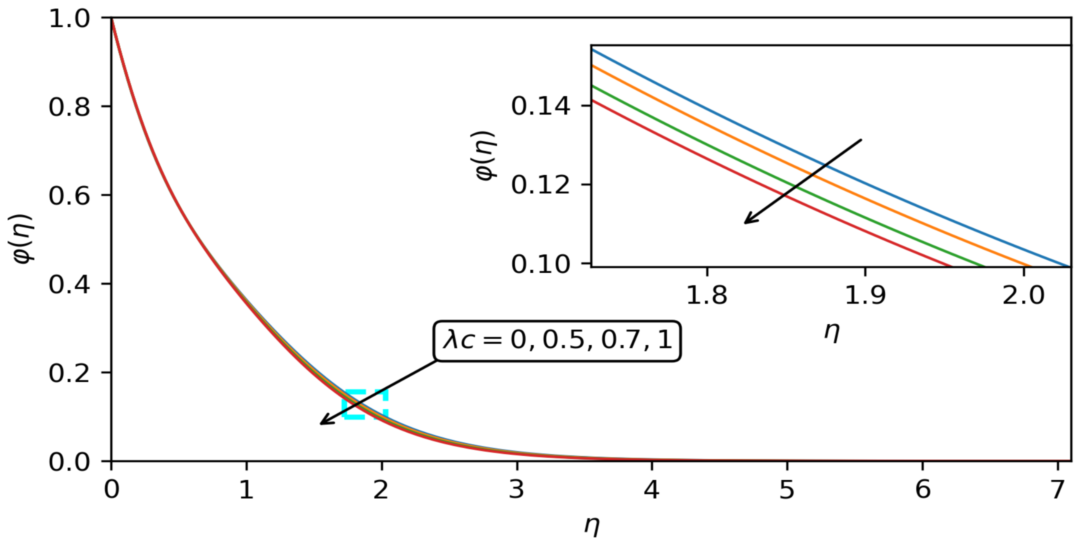

Figure 5.20: Influences of modified mixed convection parameter λ_c on $\phi(\eta)$.

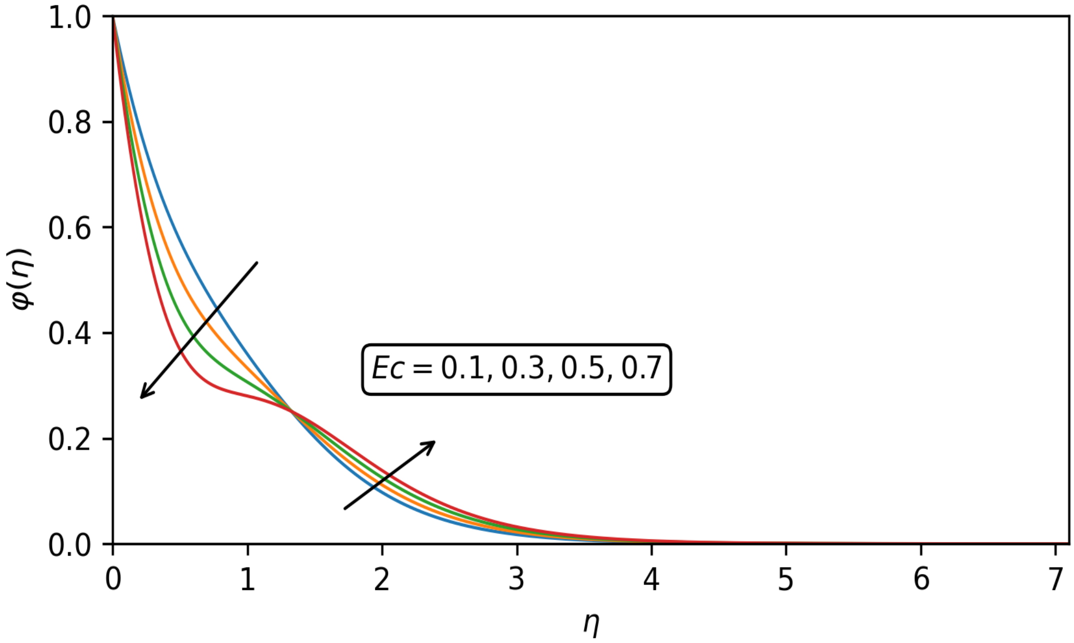

Figure 5.21: Influences of Eckert number Ec on nanoparticle concentration $\phi(\eta)$.

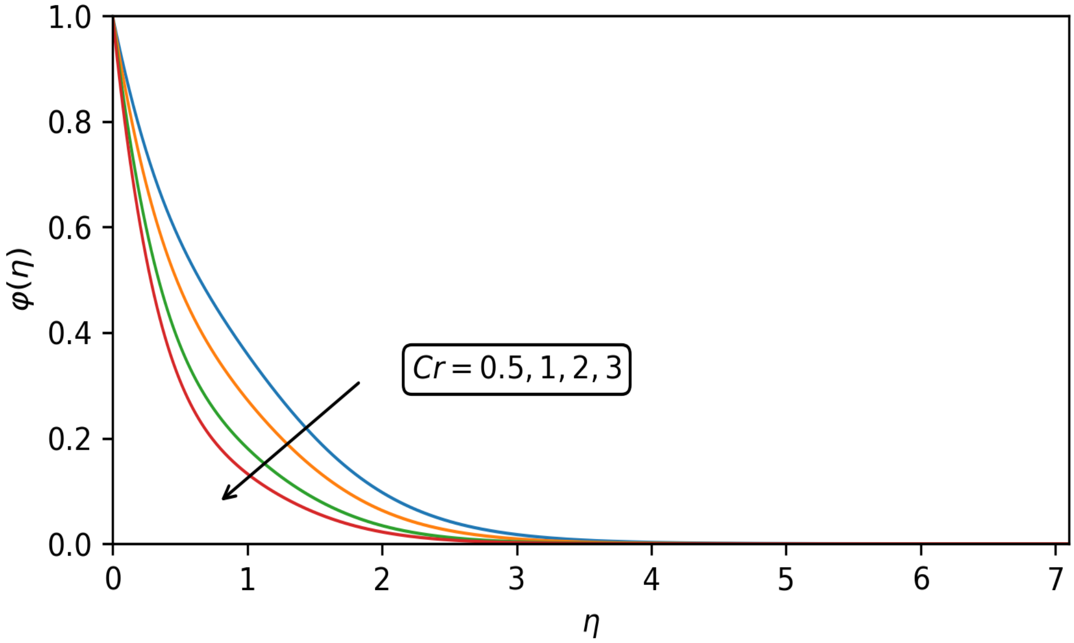

Figure 5.22: Influences of Cr on nanoparticle concentration $\phi(\eta)$.

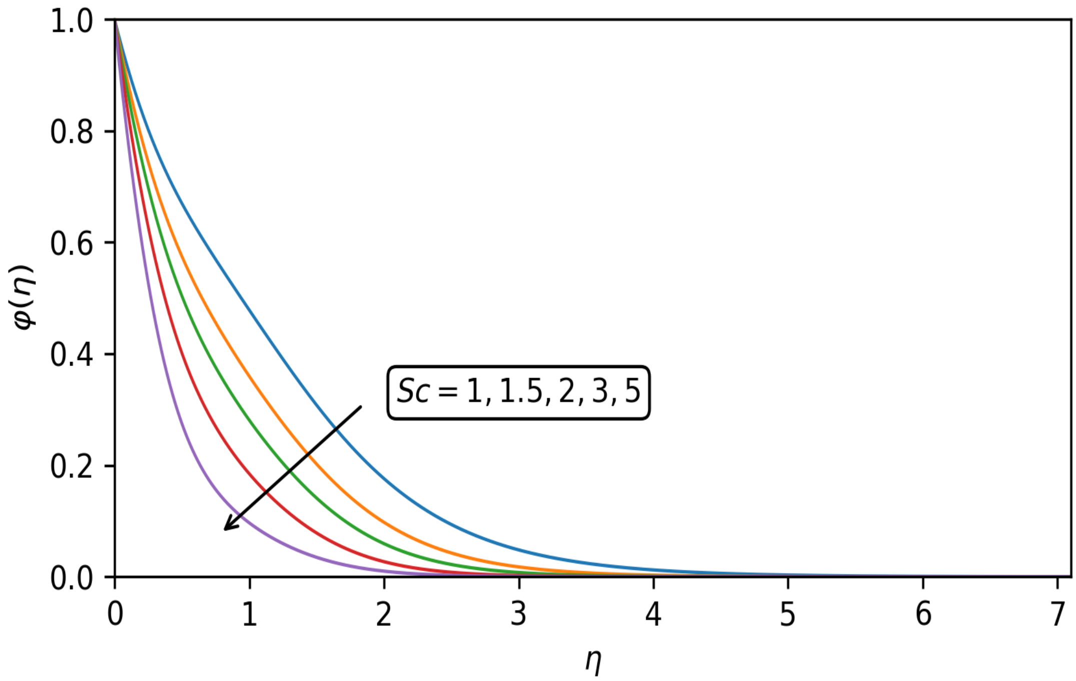

Figure 5.23: Influences of Schmidt number Sc on nanoparticle concentration $\phi(\eta)$.

5.4.3 Effects of Pertinent Flow Parameters on Skin Friction Coefficients, Nusselt Number and Sherwood Number

In this section, we disclose the findings from our study regarding the influence of varying values of relevant parameters on physical properties, such as skin friction coefficients, Nusselt number, and Sherwood number. Tables 5.4 and 5.5 provide a summary of the numerical values obtained for these quantities.

The skin friction coefficients quantify the resistance to the flow along the stretching sheet; the primary in the x-direction and the secondary in the z-direction with the effects of some prominent parameters on these coefficients are summarized in Table 5.4. Observations revealed that the primary skin friction coefficient which quantifies the frictional forces acting in the x-direction exhibits a decreasing trend with respect to the Hall (β_e), ion slip (β_i), mixed convection (λ_t), and modified mixed convection (λ_c) parameters. Physically, the Hall current parameter and ion slip influence the interaction between the magnetic field and fluid flow, resulting in changes to the characteristics of the primary skin friction. As these parameters increase, the impact of electromagnetic forces and ion concentration near the stretching sheet intensifies, leading to a reduction in primary skin friction. Similarly, λ_t and λ_c affect the flow behavior, leading to a reduction in skin friction.

On the other hand, the primary skin friction coefficient exhibits an upward trend when considering the Casson (β), magnetic field (M), and Darcy (Da) parameters. From a physical standpoint, the Casson parameter affects both the flow behavior and viscosity of the Casson nanofluid, consequently impacting the primary skin friction. When the Casson parameter takes higher values, it leads to an increase in viscosity and elevated flow resistance, resulting in an upward trend in primary skin friction. Similarly, the magnetic field parameter (M) and Darcy parameter (Da) have analogous effects, as higher values of these parameters contribute to enhanced flow resistance and consequently lead to an increase in the primary skin friction.

The secondary skin friction coefficient represents the frictional forces acting in the z-direction. It has been observed that variations in certain parameters have an impact on the magnitude of this coefficient. Specifically, an increase in the Casson parameter (β), magnetic field parameter (M), mixed convection parameter (λ_t), and modified mixed convection parameter (λ_c) leads to a increase in the magnitude of the secondary skin friction coefficient. On the other hand, the Hall (β_e), ion slip (β_i), and Darcy (Da) parameters exhibit a decreasing trend with respect to the secondary skin friction coefficient.

Table 5.4: Numerical values of the primary $-(1+\frac{1}{\beta})f''(0)$ and secondary $-(1+\frac{1}{\beta})h'(0)$ skin friction coefficients of some values of parameters for $N_b = 0.2$, $N_t = Ec = Q_h = 0.1$, $Sc = 1.5$, $Da = \lambda_t = \lambda_c = \beta = Rn = Cr = 0.5$, $Pr = 6$, $M = 7, \beta_i = \theta_r = 1$ and $\beta_e = 2$.

Da	M	β_e	β_i	λ_t	λ_c	β	$-\left(1+\frac{1}{\beta}\right)f''(0)$	$\left(1+\frac{1}{\beta}\right)h'(0)$
0							2.39549252	0.64170791
0.5							2.64446937	0.58513186
1.5							3.09942260	0.50428594
	1						1.79620920	0.11979878
	4						2.24635868	0.38924969
	7						2.64446937	0.58513186
		2					2.64446937	0.58513186
		4					2.21486441	0.43781735
		6					2.03772027	0.34235079
			1				2.64446937	0.58513186
			2				2.39267500	0.28791870
			3				2.22712078	0.16842638
				0			2.87598040	0.56985464
				1			2.41850077	0.59964113
				3			1.55437744	0.65231974
					0		2.87153728	0.56593522
					0.5		2.64446937	0.58513186
					0.7		2.55423724	0.59255985
						0.1	1.46500249	0.29113601
						0.3	2.24216775	0.47995759
						0.5	2.64446937	0.58513186

Table 5.5 outlines the impact of various relevant parameters on both the Nusselt number $\left(-\left(1+R_n\theta_r^3\right)\theta'(0)\right)$, which quantifies the rate of heat transfer, and the Sherwood number $(-\phi'(0))$, which represents the rate of mass transfer from the stretching sheet to the surrounding fluid. Flow parameters such as the Hall parameter (β_e), ion slip (β_i), Casson parameter (β), mixed convection parameter (λ_t), modified mixed convection parameter (λ_c) and nonlinear thermal radiation R_n tend to augment the magnitude of the heat transfer rate. From a physical perspective, the Hall and ion slip parameters enhance the influence of electromagnetic forces and ion concentration, which results in an amplified rate of heat transfer. Similarly, the Casson parameter, mixed convection parameter, and modified mixed convection parameter impact the flow behavior and heat transfer characteristics, leading to an augmentation in the rate of heat transfer. The nonlinear thermal radiation parameter specifically influences radiative heat transfer, and an increase in this parameter further enhances the convective heat transfer rates.

Conversely, a contrasting (decreasing) trend is observed for the magnetic field parameter, Eckert number, Darcy number , temperature ratio parameter, chemical reaction parameter and Schmidt number regarding the magnitude of heat transfer rate. Considering the physical aspect, the magnetic field parameter M acts as a suppressor of convective heat transfer, leading to a decrease in the rate of heat transfer. The Eckert number (Ec) indicates a higher dominance of kinetic energy over heat transfer, resulting in a reduction of the heat transfer rate. The Darcy parameter (Da) influences flow resistance in porous media, leading to decreased heat transfer rates. The temperature ratio parameter (θ_r) affects the distribution of temperature and thermal gradients, causing a decrease in the rate of heat transfer. Additionally, higher values of the chemical reaction parameter (Cr) and Schmidt number (Sc) tend to decrease the rate of heat transfer by affecting reaction rates and the diffusion of species, respectively.

In terms of the rate of mass transfer, it is observed that certain parameters, including the magnetic field parameter (M), Eckert number (Ec), Darcy number (Da), chemical reaction parameter (Cr), and Schmidt number (Sc), contribute to an enhancement in magnitude. Conversely, other parameters, such as Hall parameter (β_e), ion slip (β_i), Casso parameter (β), mixed convection parameter (λ_t), modified mixed convection parameter (λ_c), temperature ratio parameter (θ_r), and nonlinear thermal radiation (R_n) tend to retard the rate of mass transfer in magnitude. In reality, the magnetic field parameter, Eckert number, Darcy parameter, chemical reaction parameter, and Schmidt number affect the mass transfer rates and diffusion processes. Higher values of these parameters promote enhanced mass transfer, resulting in an increased rate of mass transfer. On the other hand, the Hall parameter, ion slip, Casson parameter, mixed convection parameters, temperature ratio parameter, and nonlinear thermal radiation parameter influence the flow behavior, temperature distribution, and convective heat transfer characteristics, leading to a retardation of the mass transfer rates.

Table 5.5: The Nusselt number and Sherwood number corresponding to specific parameter values for $N_b = 0.2$, $N_t = Ec = Q_h = 0.1$, $Sc = 1.5$, $Da = \lambda_t = \lambda_c = \beta = Rn = Cr = 0.5$, $Pr = 6$, $M = 7$, $\beta_i = \theta_r = 1$ and $\beta_e = 2$.

β_e	β_i	β	λ_t	λ_c	Da	M	Rn	θ_r	Ec	Cr	Sc	$-\left(1+R_n\theta_r^3\right)\theta'(0)$	$-\phi'(0)$
2												0.48890950	1.23523060
4												0.70373436	1.19408547
6												0.78092632	1.18105029
	1											0.48890950	1.23523060
	2											0.64387730	1.20381316
	3											0.72088605	1.18987049
		0.1										0.28732888	1.33831850
		0.3										0.44601572	1.26405874
		0.5										0.48890950	1.23523060
			0									0.42757910	1.24548294
			1									0.54372446	1.22648575
			3									0.71295744	1.20342371
				0								0.42085166	1.24588014
				0.5								0.48890950	1.23523060
				0.7								0.51424734	1.23139450
					0							0.55726843	1.22560176
					0.5							0.48890950	1.23523060
					1.5							0.35251914	1.25697942
						1						0.85996194	1.17101756
						4						0.66862667	1.20261887
						7						0.48890950	1.23523060
							0.5					0.81484916	1.23523060
							1					0.87832835	1.21041808
							1.5					0.88755490	1.19806324
								1				1.62969832	1.23523060
								1.5				1.50999663	1.22585191
								2				1.24529532	1.22558459
									0.1			0.48890950	1.23523060
									0.3			-0.69763728	1.56358034
									0.5			-1.86401294	1.88567405
										0.5		0.48890950	1.23523060
										1		0.43520938	1.57549089
										2		0.38154524	2.07108269
											1	0.56785674	0.96256563
											1.5	0.48890950	1.23523060
											2	0.44017411	1.45671914

5.5 Conclusion

This study examined the combined impact of various factors, including nonlinear thermal radiation, viscous dissipation, Joule heating, Hall currents, and ion slip, on the mixed convection flow of an MHD Casson nanofluid through a porous medium. The investigation also considered the effects of chemical reactions and heat generation/absorption. To facilitate the numerical analysis, the governing boundary layer equations, which initially comprised nonlinear coupled partial differential equations, were transformed into ordinary differential equations using similarity transformation variables. The methodology employed, involving the sixth-order Runge-Kutta (RK6) method combined with the shooting technique, has proven to be effective for solving the resulting highly nonlinear coupled ordinary differential equations. Numerical simulations were conducted using the open-source Python programming language. The study displayed the concentration, temperature, and velocity profiles under varying parameter influences. The results are presented through comprehensive graphs and tables. Additionally, numerical simulations of the skin friction coefficient, Nusselt number, and Sherwood number are expressed in tabular form to analyze the behavior of shear stress and the heat and mass transfer capabilities of the considered flow scenario. The important conclusions of the study are compactly summarized as follows:

- The velocity profiles in the x-direction were found to be strongly influenced by Hall currents, ion slip, mixed convection parameter, and modified mixed convection parameter. Increasing these parameters led to an enhancement of the principal velocity component within the boundary layer, except for the Casson parameter, which had the opposite effect.

- The Casson parameter displayed a dual behavior in the secondary velocity profile. Initially, it increased near the sheet and subsequently decreased away from the sheet within the boundary layer. Hall currents and ion slip contributed to the reduction of the secondary velocity, whereas the mixed convection and modified mixed convection parameters had an augmenting impact.

- An increase in the fluid temperature was observed when nonlinear thermal radiation, temperature ratio parameter, and Eckert number were augmented. Conversely, a decline in the fluid temperature was resulted when the values of the Casson parameter, Hall currents, ion slip, and mixed convection parameter were increased.

- The nanoparticle concentration profiles were influenced by various parameters. The Casson parameter played a supportive role, while the modified mixed convection parameter had a slight decreasing effect. A higher Eckert number caused a concentration profile with a unique pattern: a rapid decrease near the sheet followed by an increase away from the sheet. On the other hand, the chemical reaction parameter and Schmidt number were found to reduce the nanoparticle concentration within the boundary layer.

- The primary skin friction coefficient exhibited a decremental trend with the augmentation of the Hall parameter, ion slip parameter, mixed convection parameter, and modified mixed convection parameter. Conversely, an opposing effect was observed on the primary skin friction coefficient as a result of increasing the Casson parameter, magnetic field parameter, and Darcy parameter, leading to its amplification.

- The Nusselt number, which signifies the heat transfer rate, was enhanced by increasing the values of the Hall parameter, Casson parameter, mixed convection parameter, ion slip parameter, modified mixed convection parameter, and nonlinear thermal radiation parameter. Conversely, the magnetic field parameter, Darcy parameter, Eckert number, temperature ratio parameter, chemical reaction parameter, and Schmidt number had a contrary impact, causing a decrease in the Nusselt number.

- The Sherwood number, which quantifies the mass transfer rate, exhibited a diminution when the Hall parameter, Casson parameter, mixed convection parameter, ion slip parameter, modified mixed convection parameter, temperature ratio parameter, and nonlinear thermal radiation parameter were augmented. This decline signified a reduction in the mass transfer rate. Conversely, the magnetic field parameter, Eckert number, Darcy parameter, chemical reaction parameter, and Schmidt number demonstrated an opposing influence, amplifying the Sherwood number.

Chapter 6

Investigation on Rotating Flow of MHD Tangent Hyperbolic Nanofluid over a Stretching Permeable Sheet: Impacts of Hall, Ion Slip and Suction velocity

6.1 Introduction

Tangent hyperbolic fluid, a subclass of non-Newtonian fluids, is first introduced by Pop and Ingham [199] in 2001. Tangent hyperbolic fluid reveals shear-thinning behavior where viscosity declines with augmentation of shear rate. The tangent hyperbolic fluid model is an effective tool for modeling complex fluids that exhibit both shear-thinning and yield stress behaviors, making it highly relevant in the study of industrial processes involving such fluids. The behavior of tangent hyperbolic non-Newtonian fluids has been extensively studied in various flow scenarios. For instance, Naseer et al. [200] explored the boundary layer flow of a tangent hyperbolic fluid through a vertical stretching sheet, highlighting the impact of some fluid parameters on the flow characteristics. The extension of this model to include nanoparticles also has been studied by several researchers.

The study of MHD flows of tangent hyperbolic nanofluids is crucial in several engineering and industrial processes, including magnetic drug targeting, magnetic resonance imaging (MRI), and cooling of electronic devices. The interaction of magnetic fields with tangent hyperbolic nanofluids introduces additional complexities but also opportunities for controlling and enhancing processes of heat and mass transfer. Ibrahim [6] and Atif et al. [7] examined the MHD flow of a tangent hyperbolic nanofluid through a stretching sheet, showing how the magnetic field influences the profiles of velocity, concentration, and temperature. Oyelakin et al. [201], Das et al. [202], Amjad et al. [203], Ramasekhar et al. [204], Ali et al. [205] and Alhefthi et al. [206] are among numerous studies conducted on MHD tangent hyperbolic nanofluids.

This study presents a novel investigation into the rotating flow of MHD tangent hyperbolic nanofluid over a permeable stretching sheet, specifically addressing the integration of Hall and ion slip effects alongside other physical phenomena such as viscous dissipation, heat generation/absorption, Ohmic heating, nonlinear thermal radiation, suction velocity, and chemical reactions. While existing research has explored various aspects of MHD flows and nanofluids, significant gaps remain regarding the simultaneous impact of these combined effects, particularly in the context of cooling technologies. By employing advanced numerical methods and considering a comprehensive range of physical influences, the research not only provides valuable insights but also establishes a foundation for future inquiries into optimizing thermal systems in diverse industrial applications. This investigation highlights the need for further exploration of the interplay between these factors, thereby contributing to the advancement of fluid dynamics and heat and mass transfer research.

6.2 Mathematical Formulation

6.2.1 Model Assumptions

The study considers an incompressible, steady, laminar, viscous, homogeneous and electricaly conducting Tangent hyperbolic nanofluid flow through a permeable surface with noslip effect incorporating a strong magnetic constant B_0 perpendicular to the sheet, in the y-axis. The intense magnetic field induces the electrically conductive fluid to undergo Hall and ion-slip phenomena, creating a force in the z-direction that transforms the flow into a three-dimensional pattern. The fluid also flows through a porous medium with stretching velocity $U_w(x) = bx$, where $b > 0$ is the stretching rate. The model is represented by Figure 6.1 in which the suction velocity is taken into account. The study also looks at the influences of ohmic heating, heat generation/absorption, viscous dissipation, chemical reactions and nonlinear thermal radiation. In addition, the Buongiorno model is considered and also the Tangent hyperbolic nanofluid rotates with the angular velocity $\Omega = (0, \Omega, 0)$.

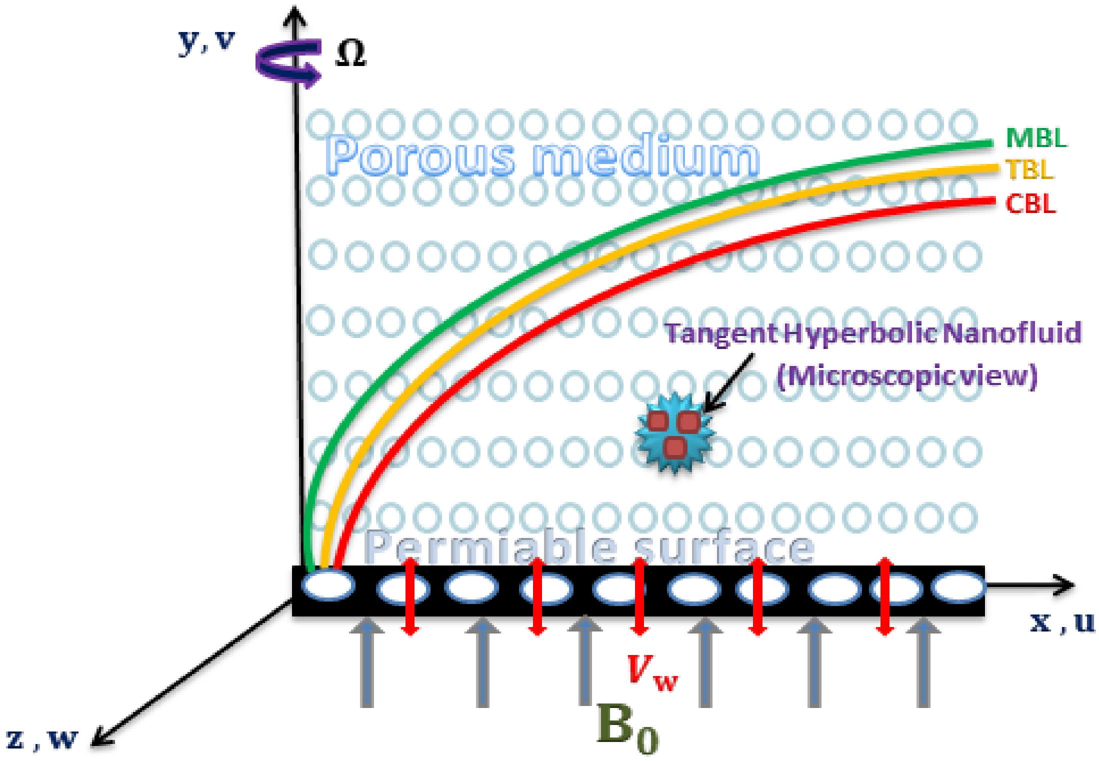

Figure 6.1: Physical model

6.2.2 Conservation Equations

6.2.2.1 Conservation of Mass

For incompressible flow, the mass conservation principle is represented by the equation:

$$\nabla \cdot V = 0, \tag{6.1}$$

where V denote the flow velocity vector. In three-dimensional coordinates, the corresponding velocity field is $\mathbf{V}(u, v, w)$ and the equation for conservation of mass Eq. (6.1) is written as follows.

$$\frac{\partial u}{\partial x} + \frac{\partial v}{\partial y} + \frac{\partial w}{\partial z} = 0, \tag{6.2}$$

6.2.2.2 Conservation of Momentum Equation

In a rotating frame of reference, the governing momentum equation for the fluid flow is expressed as:

$$\rho\left[\frac{\partial \mathbf{V}}{\partial t} + (\mathbf{V}\cdot\nabla)\mathbf{V} + (2\Omega\times\mathbf{V}) + \Omega\times(\Omega\times r)\right] = -\nabla P + \nabla\cdot\tau_{ij} + \mathbf{J}\times\mathbf{B} - \frac{\mu}{K}\mathbf{V} \tag{6.3}$$

where t is the time variable, P is the fluid pressure, τ_{ij} is the Cauchy stress tensor, $B = (0, B_0, 0)$ is external magnetic field, $J = (J_x, J_y, J_z)$ is current density. The constants B_0, ρ, K, represent the external magnetic field, nanofluid density, and porosity of the medium, respectively. Ω is the angular velocity of the rotating reference frame and $\mathbf{r}$ is position vector. $2\Omega \times \mathbf{V}$ is the Coriolis force term, and $\Omega \times (\Omega \times r)$ is the centrifugal acceleration term. Considering the Coriolis forces, the governing momentum equation Eq. (6.3) can be modified as follows.

$$\rho\left[\frac{\partial \mathbf{V}}{\partial t} + (\mathbf{V}\cdot\nabla)\mathbf{V} + (2\Omega \times \mathbf{V})\right] = -\nabla P + \nabla\cdot\tau_{ij} + \mathbf{J}\times\mathbf{B} - \frac{\mu}{K}\mathbf{V} \tag{6.4}$$

The rotation (Corriolis effect) is mathematically derived as follows.

$$2\Omega \times V = 2\begin{vmatrix} \mathbf{i} & \mathbf{j} & \mathbf{k} \\ 0 & \Omega & 0 \\ u & v & w \end{vmatrix} = 2\Omega w\hat{\mathbf{i}} - 2\Omega u\hat{\mathbf{k}}. \tag{6.5}$$

Upon substituting the stress components of Eq. (2.34) into the momentum equations and performing the necessary differentiation, the application of boundary layer approximations yields the following simplified system:

$$\rho_f\left(u\frac{\partial u}{\partial x} + v\frac{\partial u}{\partial y} + w\frac{\partial u}{\partial z} + 2\Omega w\right) = \mu_0\left[(1-n) + n\sqrt{2}\Gamma\frac{\partial u}{\partial y}\right]\frac{\partial^2 u}{\partial y^2} + FB_x, \tag{6.6}$$

$$\rho_f\left(u\frac{\partial w}{\partial x} + v\frac{\partial w}{\partial y} + w\frac{\partial w}{\partial z} - 2\Omega u\right) = \mu_0\left[(1-n) + n\sqrt{2}\Gamma\frac{\partial w}{\partial y}\right]\frac{\partial^2 w}{\partial y^2} + FB_z, \tag{6.7}$$

where μ_0 is zero shear rate viscosity, n is the power law index and $\Gamma > 0$ is a time constant. FB_x, FB_z are the body force components in the x, and z directions, respectively, which include the Lorentz force and the resistance due to porosity. The pressure is approximately constant across the boundary layer, allowing it to be eliminated from the momentum equations.

Considering the Hall current and ion slip effects at extremely high magnetic field strengths, the modified generalized expression for Ohm's law is presented in the simplified form in Eq. (5.11).

$$J \times B = -\frac{\sigma B_0^2\left((1+\beta_e\beta_i)u + \beta_e w\right)}{(1+\beta_e\beta_i)^2 + \beta_e^2}\hat{\mathbf{i}} + \frac{\sigma B_0^2\left(\beta_e u - (1+\beta_e\beta_i)w\right)}{(1+\beta_e\beta_i)^2 + \beta_e^2}\hat{\mathbf{k}} \tag{6.8}$$

where the current density vector is represented by $J = (J_x, J_y, J_z)$. β_e, β_i, *and* B_0 denote the Hall current, ion slip parameter and constant magnetic field, respectively.

6.2.2.3 Conservation of Energy equation

The energy equation is given by

$$\begin{aligned}\left(\rho C_p\right)_f \left[\frac{\partial \mathbf{T}}{\partial t} + (\mathbf{V}\cdot\nabla)\,\mathbf{T}\right] &= \kappa\nabla^2\mathbf{T} + \left(\tau_{ij} : \nabla\right)\mathbf{V} \\ &+ \left(\rho C_p\right)_p \left[D_B \nabla C\cdot\nabla T + \frac{D_T}{T_\infty}\left(\nabla T\cdot\nabla T\right)\right] \\ &+ \frac{1}{\sigma}\left(\mathbf{J}\cdot\mathbf{J}\right) - \nabla q_r + Q_0\left(T - T_\infty\right),\end{aligned} \tag{6.9}$$

where $\left(\rho C_p\right)_f$ and $\left(\rho C_p\right)_p$ are specific heat capacities of the nanofluid and the nanoparticles, respectively, and T is the temperature. κ denotes the thermal conductivity of the fluid; D_B and D_T represent the diffusion coefficients for Brownian and thermophoresis, respectively. T_∞ signifies the ambient temperature, q_r is the radiative heat flux, and the coefficient Q_0 represents heat absorption ($Q_0 < 0$) and generation ($Q_0 > 0$).

In line with the formulations for Williamson and Casson fluid models presented in the preceding chapters, the energy equation for the tangent hyperbolic model incorporates the same fundamental contributions from Joule heating, non-linear thermal radiation, and the presence of a heat source. However, the formulation of the viscous dissipation term is inherently dependent on the non-Newtonian constitutive nature of the fluid; for the tangent hyperbolic nanofluid, it is simplified as follows:

$$\Phi = \frac{\upsilon}{C_p}\left[(1-n) + \frac{n\Gamma}{\sqrt{2}}\sqrt{\left(\frac{\partial u}{\partial y}\right)^2 + \left(\frac{\partial w}{\partial y}\right)^2}\right]\left[\left(\frac{\partial u}{\partial y}\right)^2 + \left(\frac{\partial w}{\partial y}\right)^2\right]. \tag{6.10}$$

6.2.2.4 Conservation of Nanoparticle Concentration Equation

For a homogeneous chemical reaction, the nanoparticle concentration equation is given as:

$$\frac{\partial \mathbf{C}}{\partial t} + (\mathbf{V}\cdot\nabla)\,\mathbf{C} = D_B\nabla^2 C + \frac{D_T}{T_\infty}\nabla^2 T - R_0\left(C - C_\infty\right), \tag{6.11}$$

where the terms represent the rate of change, convective mass transfer, Brownian diffusion, thermophoretic diffusion, and chemical reaction, respectively. C and C_∞ are the near-surface and ambient concentrations, R_0 is the reaction rate constant, and D_B and D_T are the Brownian and thermophoretic coefficients.

6.2.3 Coupled Governing Equations and Boundary Conditions

Based on the aforementioned assumptions, the conservation laws that dictate the flow phenomena are articulated through the continuity, momentum, energy, and concentration equations, presented as follows [7, 108]:

$$\frac{\partial u}{\partial x}+\frac{\partial v}{\partial y}+\frac{\partial w}{\partial z}=0, \tag{6.12}$$

$$\begin{aligned} u\frac{\partial u}{\partial x}+v\frac{\partial u}{\partial y}+w\frac{\partial u}{\partial z}+2\Omega w &= \upsilon\left[(1-n)+n\sqrt{2}\Gamma\frac{\partial u}{\partial y}\right]\frac{\partial^2 u}{\partial y^2}-\frac{\upsilon}{K}u \\ &\quad -\frac{\sigma B_0^2\left[(1+\beta_e\beta_i)u+\beta_e w\right]}{\rho\left[(1+\beta_e\beta_i)^2+\beta_e^2\right]} \end{aligned} \tag{6.13}$$

$$\begin{aligned} u\frac{\partial w}{\partial x}+v\frac{\partial w}{\partial y}+w\frac{\partial w}{\partial z}-2\Omega u &= \upsilon\left[(1-n)+n\sqrt{2}\Gamma\frac{\partial w}{\partial y}\right]\frac{\partial^2 w}{\partial y^2}-\frac{\upsilon}{K}w \\ &\quad +\frac{\sigma B_0^2\left[\beta_e u-(1+\beta_e\beta_i)w\right]}{\rho\left[(1+\beta_e\beta_i)^2+\beta_e^2\right]}, \end{aligned} \tag{6.14}$$

$$\begin{aligned} u\frac{\partial T}{\partial x}+v\frac{\partial T}{\partial y}+w\frac{\partial T}{\partial z} &= \alpha\frac{\partial^2 T}{\partial y^2}+\Lambda\left[D_B\frac{\partial C}{\partial y}\frac{\partial T}{\partial y}+\frac{D_T}{T_\infty}\left(\frac{\partial T}{\partial y}\right)^2\right] \\ &\quad +\frac{16\sigma^*}{3k^*(\rho C_p)_f}\frac{\partial}{\partial y}\left(T^3\frac{\partial T}{\partial y}\right) \\ &\quad +\frac{Q_0(T-T_\infty)}{(\rho C_p)_f}+\frac{\sigma B_0^2(u^2+w^2)}{(\rho C_p)_f\left[(1+\beta_e\beta_i)^2+\beta_e^2\right]} \\ &\quad +\frac{\upsilon}{C_p}\left[(1-n)+\frac{n\Gamma}{\sqrt{2}}\sqrt{\left(\frac{\partial u}{\partial y}\right)^2+\left(\frac{\partial w}{\partial y}\right)^2}\right]\left[\left(\frac{\partial u}{\partial y}\right)^2+\left(\frac{\partial w}{\partial y}\right)^2\right], \end{aligned} \tag{6.15}$$

$$u\frac{\partial C}{\partial x}+v\frac{\partial C}{\partial y}+w\frac{\partial C}{\partial z}=D_B\frac{\partial^2 C}{\partial y^2}+\frac{D_T}{T_\infty}\frac{\partial^2 T}{\partial y^2}-R_0(C-C_\infty) \tag{6.16}$$

where n represents the power law index, k^* and σ^* are representing mean absorption coefficient and the constant of Stefan-Boltzmann respectively. $\left(\upsilon=\frac{\mu}{\rho},\ \alpha=\frac{\kappa}{\left(\rho C_p\right)_f}\right)$ represent the momentum and thermal diffusivity, and $\Lambda=\frac{\left(\rho C_p\right)_p}{\left(\rho C_p\right)_f}$ is the effective heat capacity ratio.

The problem's boundary conditions are provided as follows:

$$\begin{cases} u=U_w(x)=bx,\ \ v=-V_w,\ \ w=0,\ \ T=T_w,\ \ C=C_w,\ \ at\ \ y=0, \\ u\to 0,\ \ w\to 0,\ \ T\to T_\infty,\ \ C\to C_\infty,\ \ as\ \ y\to\infty, \end{cases} \tag{6.17}$$

6.2.4 Similarity Transformation

We examine a set of coupled non-linear PDEs (6.12)−(6.16), which are difficult to solve in closed form. To facilitate the analysis, we introduce the following transformation equations, which convert the governing equations into a system of ordinary differential equations (ODEs).

$$\begin{aligned}&\eta = y\sqrt{\frac{b}{\upsilon}}, \quad \Psi = x\sqrt{b\upsilon}f(\eta), \quad u = bxF'(\eta) \quad v = -\sqrt{b\upsilon}f(\eta) \quad w = bxh(\eta),\\ &\theta(\eta) = \frac{T-T_\infty}{T_w-T_\infty}, \quad \phi(\eta) = \frac{C-C_\infty}{C_w-C_\infty},\end{aligned} \tag{6.18}$$

where η represents the new similarity variable, $f(\eta),\ \ h(\eta),\ \ \theta(\eta)\ \ and\ \ \phi(\eta)$ are the dimensionless stream function, cross flow velocity, temperature distribution and nanoparticles concentration respectively. ψ is the function of flow defined by $u = \frac{\partial\psi}{\partial y} \quad and \quad v = -\frac{\partial\psi}{\partial x}$.

The two momentum equations for the $x-$ and $z-$directions require the following partial derivatives of u and w, which are found using the previously stated similarity transformations.

$$\begin{cases}\dfrac{\partial u}{\partial x} = bf',\\ \dfrac{\partial u}{\partial y} = bxf''\cdot\sqrt{\dfrac{b}{\upsilon}}, \quad \dfrac{\partial u}{\partial z} = 0,\\ \dfrac{\partial^2 u}{\partial y^2} = bxf'''\cdot\dfrac{b}{\upsilon},\end{cases} \tag{6.19}$$

$$\begin{cases}\dfrac{\partial w}{\partial x} = bh,\\ \dfrac{\partial w}{\partial y} = bxh'\sqrt{\dfrac{b}{\upsilon}}, \quad \dfrac{\partial w}{\partial z} = 0,\\ \dfrac{\partial^2 w}{\partial y^2} = bxh''\cdot\dfrac{b}{\upsilon}\end{cases} \tag{6.20}$$

The continuity equation (6.12) automatically satisfied when the previously mentioned similarity transformations are applied.

By applying Eq. (6.19), the x-direction momentum equation given in Eq. (6.13) becomes:

$$\begin{aligned}bxf'\cdot bf' - \sqrt{b\upsilon}f\cdot bxf''\sqrt{\frac{b}{\upsilon}} + 2\Omega bxh =& \upsilon\left[\left((1-n) + n\sqrt{2}\Gamma bxf''\cdot\sqrt{\frac{b}{\upsilon}}\right)bxf'''\cdot\frac{b}{\upsilon}\right]\\ &- \frac{\sigma B_0^2 bx\left[(1+\beta_e\beta_i)f' + \beta_e h\right]}{\rho\left[(1+\beta_e\beta_i)^2 + \beta_e^2\right]} - \frac{\upsilon bx}{K}f'.\end{aligned} \tag{6.21}$$

By dividing the equation by b^2x, the dimensionless ODE for the x-momentum is obtained as follows.

$$\begin{aligned}(1-n)f''' - f'^2 + ff'' - \frac{2\Omega}{b}h + n\sqrt{2}\Gamma b\sqrt{\frac{b}{\upsilon}}f''f''' \\ - \frac{\sigma B_0^2\left[(1+\beta_e\beta_i)f' + \beta_e h\right]}{\rho b\left[(1+\beta_e\beta_i)^2 + \beta_e^2\right]} - \frac{\nu}{bK}f' = 0.\end{aligned} \tag{6.22}$$

Using Eq. (6.20) the $z-$direction momentum equation given in Eq. (6.14) becomes

$$\begin{aligned}bxf'bh - \sqrt{b\upsilon}fbxh'\sqrt{\frac{b}{\upsilon}} - 2\Omega bxf' = \upsilon\left((1+n) + n\sqrt{2}\Gamma bxh'\sqrt{\frac{b}{\upsilon}}\right)bxh''\frac{b}{\upsilon} \\ + \frac{\sigma B_0^2 bx\left[\beta_e f' - (1+\beta_e\beta_i)h\right]}{\rho\left[(1+\beta_e\beta_i)^2 + \beta_e^2\right]} - \frac{\upsilon}{K}bxh.\end{aligned} \tag{6.23}$$

The simplified $z-$ momentum equation is obtained by dividing Eq. (6.23) by b^2x.

$$\begin{aligned}(1-n)h'' - f'h + fh' + \frac{2\Omega}{b}f' + n\sqrt{2}\Gamma bx\sqrt{\frac{b}{\upsilon}}h'h'' \\ + \frac{\sigma B_0^2\left[\beta_e f' - (1+\beta_e\beta_i)h\right]}{\rho b\left[(1+\beta_e\beta_i)^2 + \beta_e^2\right]} - \frac{\upsilon}{bK}h = 0.\end{aligned} \tag{6.24}$$

To transform the energy and concentration equations into dimensionless form using Eq. (6.18), it is necessary to consider the following partial derivatives.

$$\begin{cases}\dfrac{\partial T}{\partial x} = 0, \quad \dfrac{\partial T}{\partial y} = (T_w - T_\infty)\theta'\sqrt{\dfrac{b}{\upsilon}}, \\ \dfrac{\partial T}{\partial z} = 0 \\ \dfrac{\partial^2 T}{\partial y^2} = (T_w - T_\infty)\theta''\dfrac{b}{\upsilon}.\end{cases} \tag{6.25}$$

$$\begin{cases}\dfrac{\partial C}{\partial x} = \dfrac{\partial C}{\partial \phi}\cdot\dfrac{\partial \phi}{\partial x} = (C_w - C_\infty)\cdot\dfrac{\partial \phi}{\partial x} = 0, \\ \dfrac{\partial C}{\partial y} = (C_w - C_\infty)\phi'\sqrt{\dfrac{b}{\upsilon}}, \\ \dfrac{\partial C}{\partial z} = (C_w - C_\infty)\dfrac{\partial \phi}{\partial z} = 0 \\ \dfrac{\partial^2 C}{\partial y^2} = (C_w - C_\infty)\phi''\cdot\dfrac{b}{\upsilon}\end{cases} \tag{6.26}$$

The energy equation in Eq. (6.15) is rewritten as

$$
\begin{aligned}
&(-\sqrt{b\upsilon}f)(T_w-T_\infty)\theta'\sqrt{\frac{b}{\upsilon}}=\alpha(T_w-T_\infty)\theta''\frac{b}{\upsilon}\\
&+\frac{\Lambda b}{\upsilon}\left[D_B(T_w-T_\infty)(C_w-C_\infty)\theta'\phi'+\frac{D_T(T_w-T_\infty)^2}{T_\infty}\theta'^2\right]\\
&+\frac{16\sigma^*T_\infty^3(T_w-T_\infty)}{3k^*(\rho C_p)_f}\frac{b}{\upsilon}\left[3\left((\theta_r-1)\theta+1\right)^2(\theta_r-1)\theta'^2+\left((\theta_r-1)\theta+1\right)^3\theta''\right]\\
&+\frac{Q_0}{(\rho C_p)_f}(T_w-T_\infty)\theta+\frac{\sigma B_0^2(bx)^2\left[f'^2+h^2\right]}{(\rho C_p)_f\left[(1+\beta_e\beta_i)^2+\beta_e^2\right]}\\
&+\frac{\upsilon}{C_p}\left[(1+n)+\frac{n\Gamma}{\sqrt{2}}\sqrt{\left(bxf''\sqrt{\frac{b}{\upsilon}}\right)^2+\left(bxh'\sqrt{\frac{b}{\upsilon}}\right)^2}\right]\left[\left(bxf''\sqrt{\frac{b}{\upsilon}}\right)^2+\left(bxh'\sqrt{\frac{b}{\upsilon}}\right)^2\right],
\end{aligned}
\tag{6.27}
$$

where $\theta_r=\frac{T_w}{T_\infty}$ the temperature ratio parameter.

To simplify Eq. (6.27), divide the entire equation by $\alpha(T_w-T_\infty)\frac{b}{\upsilon}$.

$$
\begin{aligned}
&\frac{\upsilon}{\alpha}f\theta'+\theta''+\frac{\Lambda D_B(C_w-C_\infty)}{\alpha}\theta'\phi'+\frac{\Lambda D_T(T_w-T_\infty)}{\alpha T_\infty}\theta'^2\\
&+\frac{16\sigma^*T_\infty^3}{3k^*(\rho C_p)_f\alpha}\left[3\left((\theta_r-1)\theta+1\right)^2(\theta_r-1)\theta'^2+\left((\theta_r-1)\theta+1\right)^3\theta''\right]\\
&+\frac{Q_0\upsilon}{(\rho C_p)_f\alpha b}\theta+\frac{\sigma B_0^2bx^2\nu\left[f'^2+h^2\right]}{(\rho C_p)_f\alpha(T_w-T_\infty)\left[(1+\beta_e\beta_i)^2+\beta_e^2\right]}\\
&+\frac{b^2x^2\upsilon}{C_p\alpha(T_w-T_\infty)}\left[(1+n)+\frac{n\Gamma}{\sqrt{2}}bx\sqrt{\frac{b}{\upsilon}}\sqrt{(f'')^2+(h')^2}\right]\left[(f'')^2+(h')^2\right]=0.
\end{aligned}
\tag{6.28}
$$

The nanoparticle concentration equation given in Eq. (6.16) can be transformed using the previous partial derivatives.

$$
\begin{aligned}
-\sqrt{b\upsilon}f(C_w-C_\infty)\phi'\sqrt{\frac{b}{\upsilon}}=&D_B(C_w-C_\infty)\phi''\frac{b}{\upsilon}\\
&+\frac{D_T}{T_\infty}(T_w-T_\infty)\theta''\frac{b}{\upsilon}-R_0(C_w-C_\infty)\phi.
\end{aligned}
\tag{6.29}
$$

The dimensionless form of the nanoparticle concentration equation can be simplified by multiplying Eq. (6.29) by $\dfrac{\upsilon}{bD_B(C_w-C_\infty)}$ and becomes

$$
\phi''+\frac{\upsilon}{D_B}f\phi'+\frac{D_T(T_w-T_\infty)}{D_BT_\infty(C_w-C_\infty)}\theta''-\frac{R_0\upsilon}{bD_B}\phi=0.
\tag{6.30}
$$

The boundary conditions can also be expressed in terms of the dimensionless variable η using the previously introduced similarity transformations. At $y = 0$ we have $\eta = 0$ and the boundary conditions are transformed below.

$$\begin{cases} u = bxf'(\eta) \Rightarrow u(0) = bxf'(0) = bx \Rightarrow f'(0) = 1, \\ v = -\sqrt{b\upsilon}f(\eta) \Rightarrow v(0) = -V_w = -\sqrt{b\upsilon}f(0) \Rightarrow f(0) = \dfrac{V_w}{\sqrt{b\upsilon}}, \\ w = bxh(\eta) \Rightarrow h(0) = 0, \\ \theta(0) = \dfrac{T(0) - T_\infty}{T_w - T_\infty} = \dfrac{T_w - T_\infty}{T_w - T_\infty} = 1, \\ \phi(0) = \dfrac{C(0) - C_\infty}{C_w - C_\infty} = \dfrac{C_w - C_\infty}{C_w - C_\infty} = 1. \end{cases} \tag{6.31}$$

Also, transformations as $y \to \infty$, $\eta \to \infty$ are summarized as follows.

$$\begin{cases} u \to 0 \Rightarrow f'(\eta) \to 0, \\ w \to 0 \Rightarrow h(\eta) = 0, \\ \theta(\eta) \to \dfrac{T_\infty - T_\infty}{T_w - T_\infty} = 0, \\ \phi(\eta) \to \dfrac{C_\infty - C_\infty}{C_w - C_\infty} = 0. \end{cases} \tag{6.32}$$

Therefore, Eqs. (6.13)-(6.16) are simplified to the following:

$$(1-n)f''' + nWef''f''' - f'^2 + ff'' - Daf' - \omega h - \frac{M\left[(1+\beta_e\beta_i)f' + \beta_e h\right]}{(1+\beta_e\beta_i)^2 + \beta_e^2} = 0, \tag{6.33}$$

$$(1-n)h'' + nWeh'h'' - f'h + fh' - Dah + \omega f' + \frac{M\left[\beta_e f' - (1+\beta_e\beta_i)h\right]}{(1+\beta_e\beta_i)^2 + \beta_e^2} = 0, \tag{6.34}$$

$$\begin{aligned} \theta'' + Pr\Bigg[Q_h\theta + f\theta' + \frac{ME_c\left(f'^2 + h^2\right)}{(1+\beta_e\beta_i)^2 + \beta_e^2} + Ec\left((1-n) + \frac{n}{2}W_e\left(f''^2 + h'^2\right)^{\frac{1}{2}}\right)\left(f''^2 + h'^2\right) \\ + N_b\theta'\phi' + N_t\left(\theta'\right)^2\Bigg] + R_n\left[\theta''\left(1 + (\theta_r - 1)\theta\right)^3 + 3(\theta_r - 1)\left(1 + (\theta_r - 1)\theta\right)^2\theta'^2\right] = 0, \end{aligned} \tag{6.35}$$

$$\phi'' + S_c f\phi' - S_c C_r\phi + \frac{N_t}{N_b}\theta'' = 0. \tag{6.36}$$

The boundaries conditions that have been transformed are:

$$\begin{aligned} &f'(0) = 1, \quad f(0) = \frac{V_w}{\sqrt{b\upsilon}} = V_0, \quad h(0) = 0, \quad \theta(0) = 1, \quad \phi(0) = 1, \quad at \ \ \eta = 0 \\ &f' \to 0, \quad h \to 0, \quad \theta \to 0, \quad \Phi \to 0 \quad at \ \ \eta \to \infty, \end{aligned} \tag{6.37}$$

Rearranging the equations (6.33)-(6.36)), we obtain

$$f''' = \frac{\left[f'^2 - ff'' + Daf' + \omega h + \frac{M}{(1+\beta_e\beta_i)^2 + \beta_e^2}\left[(1+\beta_e\beta_i)f' + \beta_e h\right]\right]}{[(1-n) + nWef'']}, \tag{6.38}$$

$$h'' = \frac{\left[f'h - fh' + Dah - \omega f' - \frac{M}{(1+\beta_e\beta_i)^2 + \beta_e^2}\left[\beta_e f' - (1+\beta_e\beta_i)h\right]\right]}{[(1-n) + nWeh']}, \tag{6.39}$$

$$\begin{aligned}\theta'' =& \frac{-1}{\left[1 + R_n\left(1 + (\theta_r - 1)\theta\right)^3\right]}\Bigg[Pr\Bigg(Q_h\theta + \theta' f + \frac{MEc\left(f'^2 + h^2\right)}{(1+\beta_e\beta_i)^2 + \beta_e^2} \\ &+ Ec\left((1-n) + \frac{n}{2}We\left(f''^2 + h'^2\right)^{\frac{1}{2}}\right)\left(f''^2 + h'^2\right) + N_b\theta'\phi' + N_t\left(\theta'\right)^2\Bigg) \\ &+ R_n\left[3(\theta_r - 1)\left(1 + (\theta_r - 1)\theta\right)^2\theta'^2\right]\Bigg],\end{aligned} \tag{6.40}$$

$$\phi'' = -Scf\phi' + ScC_r\phi - \frac{N_t}{N_b}\theta''. \tag{6.41}$$

A detailed description of the pertinent dimensionless parameters found in Eqs. (6.33)-(6.36) is provided below.

Table 6.1: Definitions of Dimensionless Parameters

Symbol & Definition	Description
$M = \frac{\sigma B_0^2}{\rho b}$	Hartmann number (magnetic parameter)
$We = \frac{\sqrt{2}\,\Gamma\, b^{3/2} x}{\sqrt{\upsilon}}$	Weissenberg number
$\omega = \frac{2\Omega}{b}$	Rotational parameter
$D_a = \frac{\upsilon}{bK}$	Porous parameter (Darcy number)
$V_0 = \frac{V_w}{\sqrt{b\upsilon}}$	Suction velocity factor
$Pr = \frac{\upsilon}{\alpha}$	Prandtl number
$R_n = \frac{16\sigma^* T_\infty^3}{3\kappa k^*}$	Nonlinear thermal radiation parameter
$\theta_r = \frac{T_w}{T_\infty}$	Temperature ratio parameter

$Sc = \dfrac{\upsilon}{D_B}$	Schmidt number
$C_r = \dfrac{R_0}{b}$	Scaled chemical reaction parameter
$Q_h = \dfrac{Q_0}{(\rho C_p)_f b}$	Heat generation ($Q_h > 0$) or absorption parameter ($Q_h < 0$)
$Ec = \dfrac{U_w^2}{C_p (T_w - T_\infty)}$	Eckert number
$N_b = \dfrac{\Lambda D_B(C_w - C_\infty)}{\upsilon}$	Brownian motion parameter $\left(\Lambda = \dfrac{\left(\rho C_p\right)_p}{\left(\rho C_p\right)_f}\right)$
$N_t = \dfrac{\Lambda D_T (T_w - T_\infty)}{\upsilon T_\infty}$	Thermophoretic parameter

6.2.5 Engineering Relevant Quantities in Boundary Layer

The key physical quantities of interest include local skin friction coefficients (surface drag force coefficient), local Nusselt number (heat transfer rate), and local Sherwood number (mass transfer rate) are written in the dimensionless variables as follows.

6.2.5.1 Skin Friction Coefficients

The primary and secondary skin friction coefficients C_{fx} and C_{fz} in the x and z directions are defined as follows:

$$C_{fx} = \frac{\tau_{wx}}{\rho U_w^2}, \quad C_{fz} = \frac{\tau_{wz}}{\rho U_w^2}, \tag{6.42}$$

where τ_{wx} and τ_{wz} represent the wall shear stresses in the $x-$ and $z-$ directions, respectively.

From the constitutive equation of tangent hyperbolic fluid Eq. (2.34), the stress tensor components at the wall ($y = 0$) are

$$\begin{cases} \tau_{yx} = \mu_0 \left[1 + n(\Gamma\dot{\gamma} - 1)\right] \left(\dfrac{\partial u}{\partial y} + \dfrac{\partial v}{\partial x}\right), \\ \tau_{yz} = \mu_0 \left[1 + n(\Gamma\dot{\gamma} - 1)\right] \left(\dfrac{\partial v}{\partial z} + \dfrac{\partial w}{\partial y}\right). \end{cases} \tag{6.43}$$

where μ_0 is the reference dynamic viscosity of the fluid and Γ is the time constant.

Under boundary layer assumptions and using the shear rate definition, the wall shear stresses Eq. (6.43) reduce to

$$\begin{cases} \tau_{wx} = \mu_0\left[1 + n\left(\Gamma\frac{1}{\sqrt{2}}\frac{\partial u}{\partial y} - 1\right)\right]\left(\frac{\partial u}{\partial y}\right) = \mu_0\left[(1-n)\frac{\partial u}{\partial y} + \frac{n\Gamma}{\sqrt{2}}\left(\frac{\partial u}{\partial y}\right)^2\right], \\ \tau_{wz} = \mu_0\left[1 + n\left(\Gamma\frac{1}{\sqrt{2}}\frac{\partial w}{\partial y} - 1\right)\right]\left(\frac{\partial w}{\partial y}\right) = \mu_0\left[(1-n)\frac{\partial w}{\partial y} + \frac{n\Gamma}{\sqrt{2}}\left(\frac{\partial w}{\partial y}\right)^2\right]. \end{cases} \tag{6.44}$$

Using similarity transformations in Eq. (6.18), the velocity gradients at $y = 0$ ($\eta = 0$) are as follows.

$$\left.\frac{\partial u}{\partial y}\right|_{y=0} = bxf''(0)\sqrt{\frac{b}{\upsilon}}, \quad \left.\frac{\partial w}{\partial y}\right|_{y=0} = bxh'(0)\sqrt{\frac{b}{\upsilon}}. \tag{6.45}$$

Applying Eq. (6.45), Eq. (6.44) simplifies to

$$\begin{cases} \tau_{wx} = \mu_0 bx\sqrt{\frac{b}{\upsilon}}\left[(1-n)\,f''(0) + \frac{n\Gamma}{\sqrt{2}}bx\sqrt{\frac{b}{\upsilon}}\,(f''(0))^2\right], \\ \tau_{wz} = \mu_0 bx\sqrt{\frac{b}{\upsilon}}\left[(1-n)\,h'(0) + \frac{n\Gamma}{\sqrt{2}}bx\sqrt{\frac{b}{\upsilon}}\,(h'(0))^2\right]. \end{cases} \tag{6.46}$$

The skin friction coefficients are then calculated as follows.

$$\begin{aligned} C_{fx} = \frac{\tau_{wx}}{\rho U_w^2} &= \frac{\mu_0 bx}{\rho b^2 x^2}\sqrt{\frac{b}{\upsilon}}\left[(1-n)\,f''(0) + \frac{n\Gamma}{\sqrt{2}}bx\sqrt{\frac{b}{\upsilon}}\,(f''(0))^2\right] \\ &= \sqrt{\frac{\upsilon}{bx^2}}\left[(1-n)\,f''(0) + \frac{n\Gamma}{\sqrt{2}}bx\sqrt{\frac{b}{\upsilon}}\,(f''(0))^2\right], \end{aligned} \tag{6.47}$$

$$\begin{aligned} C_{fz} = \frac{\tau_{wz}}{\rho U_w^2} &= \frac{\mu_0 bx}{\rho b^2 x^2}\sqrt{\frac{b}{\upsilon}}\left[(1-n)\,h'(0) + \frac{n\Gamma}{\sqrt{2}}bx\sqrt{\frac{b}{\upsilon}}\,(h'(0))^2\right] \\ &= \sqrt{\frac{\upsilon}{bx^2}}\left[(1-n)\,h'(0) + \frac{n\Gamma}{\sqrt{2}}bx\sqrt{\frac{b}{\upsilon}}\,(h'(0))^2\right] \end{aligned} \tag{6.48}$$

The skin friction coefficients are reduced to

$$C_{fx}\sqrt{\mathrm{Re}x} = (1-n)\,f''(0) + \frac{nWe}{2}\,(f''(0))^2\,, \tag{6.49}$$

$$C_{fz}\sqrt{\mathrm{Re}_x} = (1-n)\,h'(0) + \frac{nWe}{2}\,(h'(0))^2\,, \tag{6.50}$$

where $We = \sqrt{2}\Gamma bx\sqrt{\frac{b}{\upsilon}}$ is the Weissenberg number and $\mathrm{Re}x = \frac{xU_w}{\upsilon} = \frac{bx^2}{\upsilon}$ is the local Reynolds number.

6.2.5.2 Local Nusselt Number

The Nusselt number is represented by the following equation.

$$Nu_x = \frac{xq_w}{\kappa(T_w - T_\infty)} = \frac{-x}{T_w - T_\infty}\left(1 + \frac{16\sigma^* T_w^3}{3\kappa k^*}\right)\frac{\partial T}{\partial y}\bigg|_{y=0}. \tag{6.51}$$

where q_w is the total wall heat flux, combining conduction and radiative transfer. Using the similarity transformation of Eq. (6.18) for temperature, the dimensionless Nusselt number is simplified to

$$\frac{Nu_x}{\sqrt{\mathrm{Re}_x}} = -\left(1 + R_n\theta_r^3\right)\theta'(0). \tag{6.52}$$

6.2.5.3 Local Sherwood Number

The Sherwood number can also be defined as

$$Sh_x = \frac{xq_m}{D_B(C_w - C_\infty)} = \frac{-x}{C_w - C_\infty}\frac{\partial C}{\partial y}\bigg|_{y=0}. \tag{6.53}$$

with q_m is wall mass flux defined by Fick's law. Using the similarity transformation in Eq. (6.18) for concentration, the dimensionless Sherwood number becomes

$$\frac{Sh_x}{\sqrt{\mathrm{Re}_x}} = -\phi'(0). \tag{6.54}$$

6.3 Method of Solutions

The lack of closed form and/or analytical solution in our existing physical model results from the high degree of nonlinearity present in Eqs. (6.38)-(6.41) with the boundary conditions Eq. (6.37). Nevertheless, by applying the shooting method, the boundary value problems (BVPs) outlined in these equations are transformed into initial value problems (IVPs). Utilizing substitutions ($f = f_1,\ f' = f_2,\ f'' = f_3,\ h = f_4,\ h' = f_5,\ \theta = f_6,\ \theta' = f_7,\ \phi = f_8,\ \phi' = f_9$), the nonlinear ODEs are reformulated into a system of first-order format.

$$\begin{cases} f_1' = f_2 & f_1(0) = V_0, \\ f_2' = f_3 & f_2(0) = 1, \\ f_3' = \dfrac{\left[f_2^2 - f_1 f_3 + Daf_2 + \omega f_4 + \dfrac{M\left[(1+\beta_e\beta_i)f_2 + \beta_e f_4\right]}{(1+\beta_e\beta_i)^2 + \beta_e^2}\right]}{\left[(1-n) + nWef_3\right]} & f_3(0) = \zeta_1, \\ f_4' = f_5 & f_4(0) = 0, \\ f_5' = \dfrac{\left[f_2 f_4 - f_1 f_5 + Daf_4 - \omega f_2 - \dfrac{M\left[\beta_e f_2 - (1+\beta_e\beta_i)f_4\right]}{(1+\beta_e\beta_i)^2 + \beta_e^2}\right]}{\left[(1-n) + nWef_5\right]} & f_5(0) = \zeta_2, \\ f_6' = f_7 & f_6(0) = 1, \\ f_7' = \dfrac{-1}{\left[1 + R_n\left(1 + (\theta_r - 1)f_6\right)^3\right]}\Bigg[Pr\Bigg(f_7 f_1 + \dfrac{MEc\left(f_2^2 + f_4^2\right)}{(1+\beta_e\beta_i)^2 + \beta_e^2} & \\ \qquad + Ec\left(1 + \dfrac{1}{2}We\left(f_3^2 + f_5^2\right)^{\frac{1}{2}}\right)\left(f_3^2 + f_5^2\right) & \\ \qquad + Q_h f_6 + N_b f_7 f_9 + N_t f_7^2\Bigg) & \\ \qquad + R_n\left[3(\theta_r - 1)\left(1 + (\theta_r - 1)f_6\right)^2 f_7^2\right]\Bigg] & f_7(0) = \zeta_3, \\ f_8' = f_9 & f_8(0) = 1, \\ f_9' = -Scf_1 f_9 - \dfrac{N_t}{N_b} f_7' + ScC_r f_8 & f_9(0) = \zeta_4, \end{cases} \tag{6.55}$$

where ζ_1, ζ_2, ζ_3 and ζ_4 denote the initial conditions that are not provided.

Then, using the Runge-Kutta method of the sixth-order (RK6) approach, Eq. (6.55) is numerically computed. As seeking to approximate solutions to ODEs, the high-order accuracy of the Runge-Kutta method proves to be a highly effective technique. To address this issue, it is essential to adjust the problem by guessing suitable initial values for the four unknowns ζ_1, ζ_2, ζ_3 and ζ_4. We iteratively update the initial guess for those unknown initial conditions using the residual. After achieving the required accuracy, we derive the final solution by calculating the values of the variable across the domain.

In all calculations, a step size of 0.1 and an error tolerance of 10^{-6} are used to produce accurate and reliable results. The Python programming language, which is freely available, is used to construct and analyze our numerical method.

6.4 Results and Discussion

6.4.1 Validation of the Numerical Method

In this study, we used the Runge-Kutta sixth order method combined with the shooting technique to solve the provided governing equations (6.33)-(6.36) with corresponding boundary conditions (6.37). To ensure the reliability of our numerical results, we validated the method against previously published work in the literature as summarized in Table 6.2. The comparison was made with the findings of Fathizadeh et al. [5], Ibrahim [6] and Atif et al. [7]. Our numerical results demonstrated excellent agreement, confirming the accuracy and robustness of the numerical approach.

Table 6.2: Numerical value comparison between Fathizadeh et al. [5], Ibrahim [6], Atif et al. [7] and the findings of our study by evaluating the values of $-f''(0)$ against M for $Pr = 1$, $Nb = 0.0001$, $Nt = 0.0$ and the absence of Da, Ec, Cr, Q_h, R_n, θ_r, Sc, V_0, We, n, β_i, β_e and ω.

	$-f''(0)$			
M	Fathizadeh et al. [5]	Ibrahim [6]	Atif et al. [7]	Present Study
1	1.41421	1.4142	1.41421	1.41421643
5	2.44948	2.4495	2.44949	2.44948974
10	3.31662	3.3166	3.31662	3.31662479
50	7.14142	7.1414	7.14142	7.14142843

6.4.2 Profiles of Velocity, Temperature and Nanoparticle Concentration with Prominent Flow Parameters

Several parameters, including Hall (β_e), ion slip (β_i), power law index (n), Weissenberg number(We), suction velocity (V_0), rotation parameter (ω), magnetic field parameter (M), nonlinear thermal radiation parameter (R_n), the ratio temperature parameter (θ_r), Prandtl number (Pr), Schmidt number (Sc), heat generation (Q_h), chemical reaction parameter (Cr), Eckert number (Ec), porous parameter (Darcy number) (Da), Brownian motion parameter (N_b), and thermophoretic parameter (N_t), are considered in numerical computations while some of the effects of Key parameters were systematically varied to assess their impact on velocity profiles ($f'(\eta)$, $h(\eta)$), temperature distributions ($\theta(\eta)$), nanoparticle concentration ($\phi(\eta)$), skin friction coefficients (surface drag force coefficients), rate of heat transfer and rate of mass transfer. The results are illustrated graphically to provide a comprehensive understanding of how these parameters influence the flow dynamics and thermal behavior of the fluid.

To perform the numerical simulations, we establish the non-dimensional parameters at fixed values: $Pr = 3$, $M = 5$, $Sc = 1.5$, $We = 0.2$, $\beta_e = 2$, $n = 0.3$, $V_0 = 0.7$, $\beta_i = \omega = \theta_r = 1$, $Ec = 0.1$, $R_n = Cr = N_b = N_t = D_a = Q_h = 0.5$. Throughout the study, these parameters will remain unchanged, except for the parameter that varies and is illustrated in the corresponding figure.

The effects of Hall currents on the principal (leading) velocity profiles (x-direction velocity, denoted as $f'(\eta)$), secondary (auxiliary) velocity (z-direction velocity, denoted as $h(\eta)$), temperature ($\theta(\eta)$) and nanoparticle concentration ($\phi(\eta)$) profiles are depicted in Figs. 6.2–6.5. Fig. 6.2 clearly shows that increasing the Hall current parameter (β_e) enhances the principal velocity ($f'(\eta)$) within the boundary layer. This increase can be attributed to the enhanced electromagnetic interactions within the nanofluid, which facilitate better momentum transfer. The Hall currents generate a transverse electric field that influences the flow dynamics, thereby accelerating the fluid particles in the x-direction. As shown in Fig. 6.3, increasing the Hall current (β_e) boosts the secondary velocity. The Hall effect alters the lateral flow by modifying the Lorentz force distribution and enhancing the secondary velocity. Fig. 6.4 shows that as the Hall current parameter increases, a notable decrease in the temperature distribution $\theta(\eta)$ is observed. Physically, the reduction in temperature with increased Hall current can be attributed to enhanced momentum transfer and the resultant increase in the convective heat transport within the fluid. This indicates that the electromagnetic interaction effectively dissipates thermal energy, thereby cooling the fluid. Fig. 6.5 portrays that augmenting the Hall parameter (β_e) enhances nanoparticle concentration ($\phi(\eta)$) near the sheet, followed by a decrease away from it.

Figs. 6.6–6.9 display the principal velocity ($f'(\eta)$), secondary (auxiliary) velocity ($h(\eta)$), temperature ($\theta(\eta)$) and nanoparticle concentration ($\phi(\eta)$) profiles for varying values of ion slip parameter (β_i). Similarly to Hall currents, increasing the ion slip parameter β_i boosts the principal velocity as illustrated in Fig. 6.6. Ion slip effects arise from the disparity in ion and electron movement, which modifies the current density and, subsequently, the velocity. Fig. 6.7 shows a dual nature of the secondary velocity. Initially, $h(\eta)$ decreases near the sheet but increases farther away, indicating complex interactions between the ion slip and the electric field of the boundary layer. Figs. 6.8 and 6.9 reflect the influence of ion slip (β_i) on the temperature and nanoparticle concentration profiles and align with the behavior observed for Hall currents.

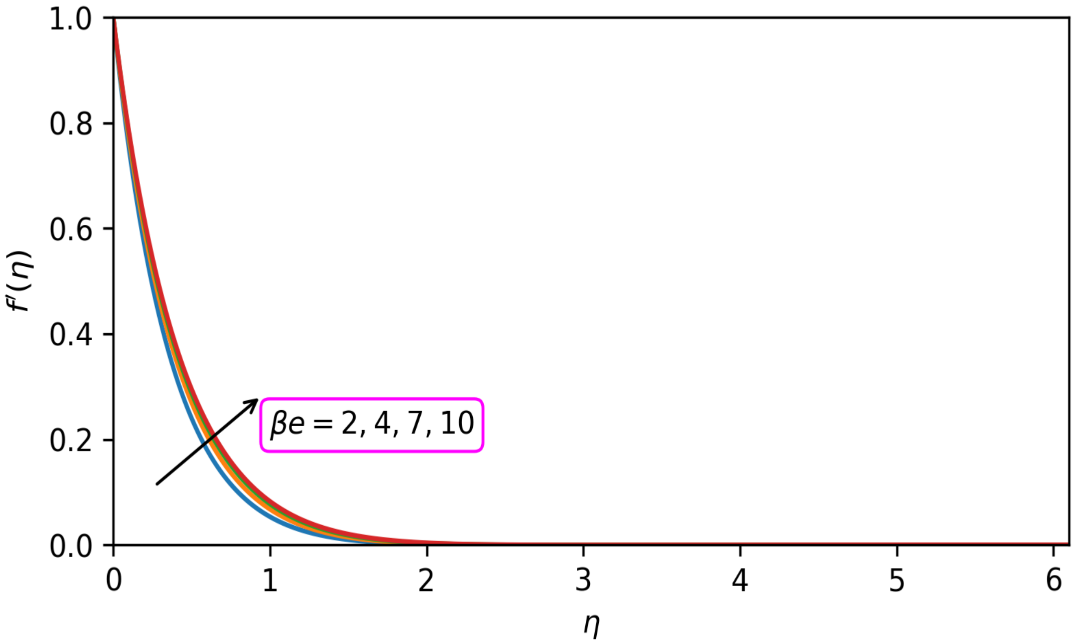

Figure 6.2: Profiles of principal velocity $f'(\eta)$ with Hall parameter β_e.

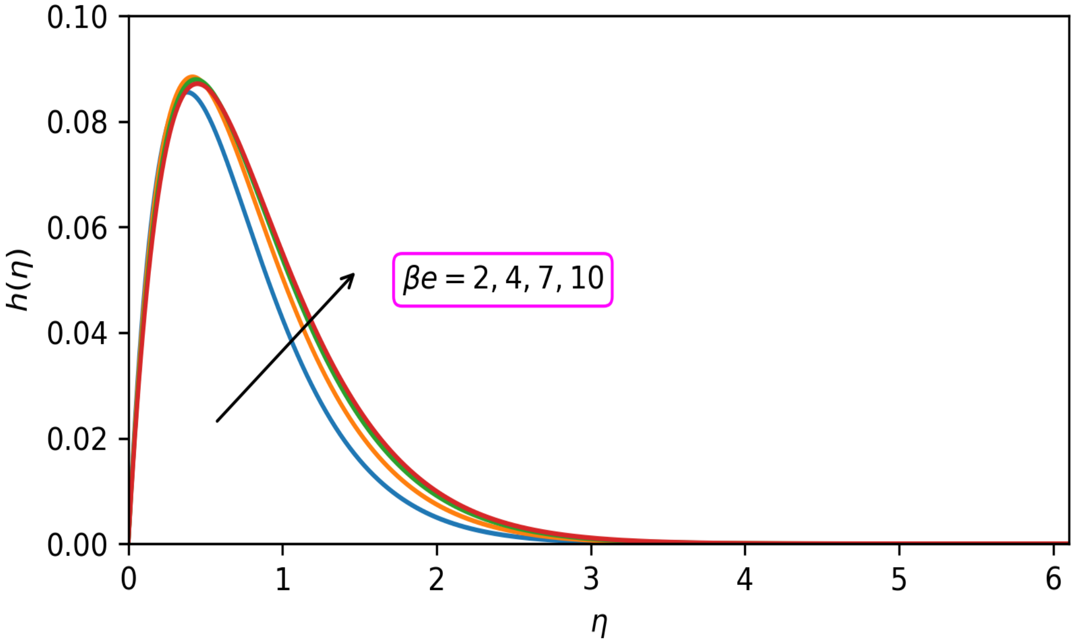

Figure 6.3: Profiles of secondary velocity $h(\eta)$ with β_e.

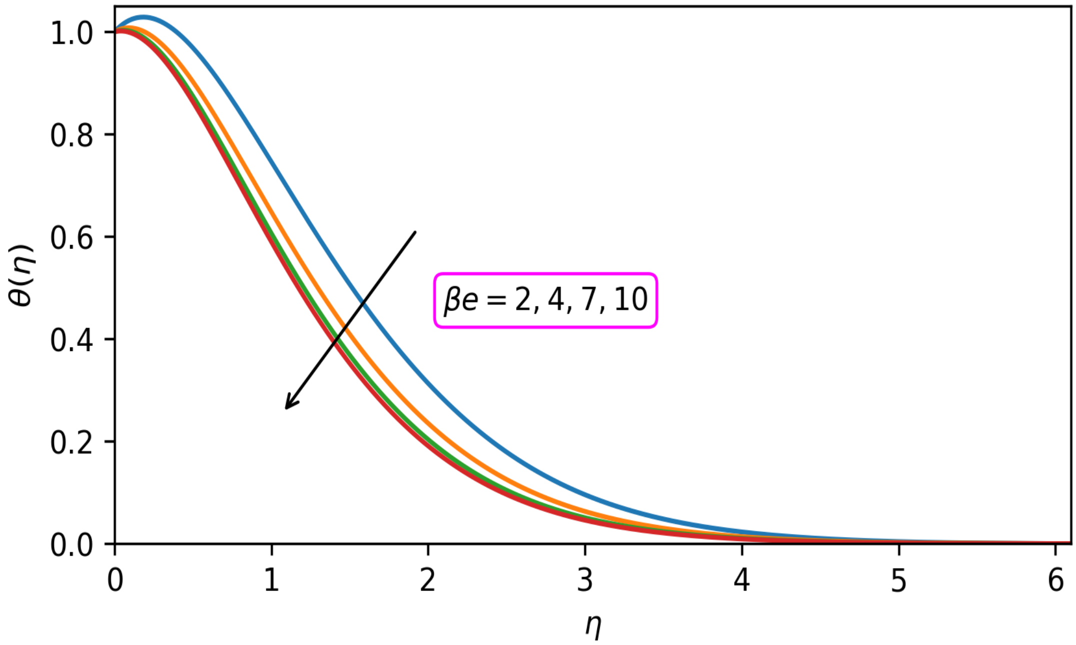

Figure 6.4: Profiles of Temperature $\theta(\eta)$ with β_e.

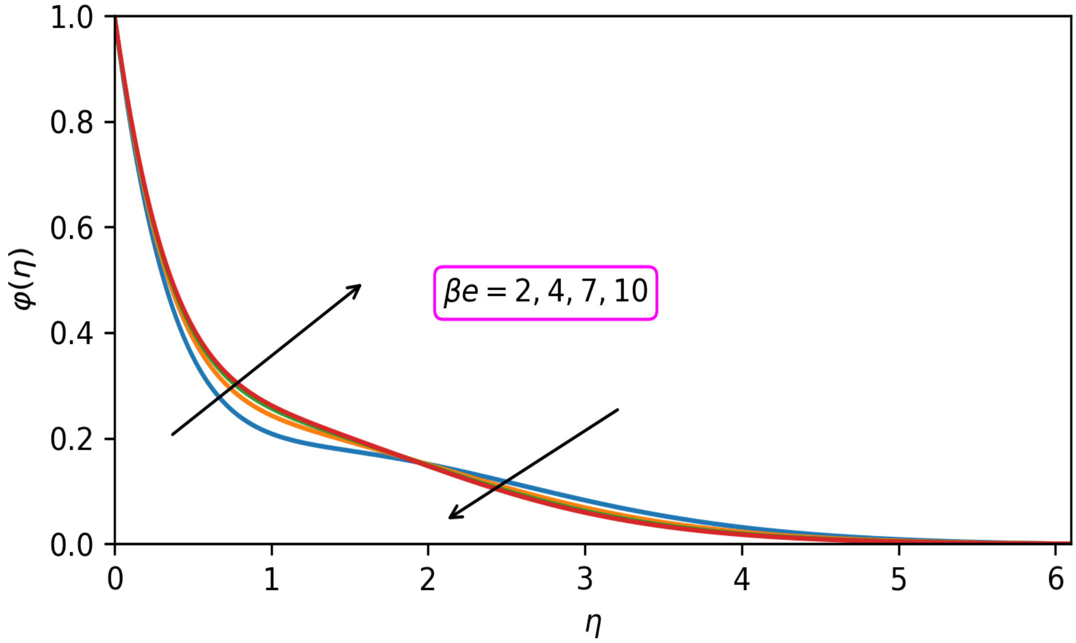

Figure 6.5: Profiles of nanoparicle concentration $\phi(\eta)$ with β_e.

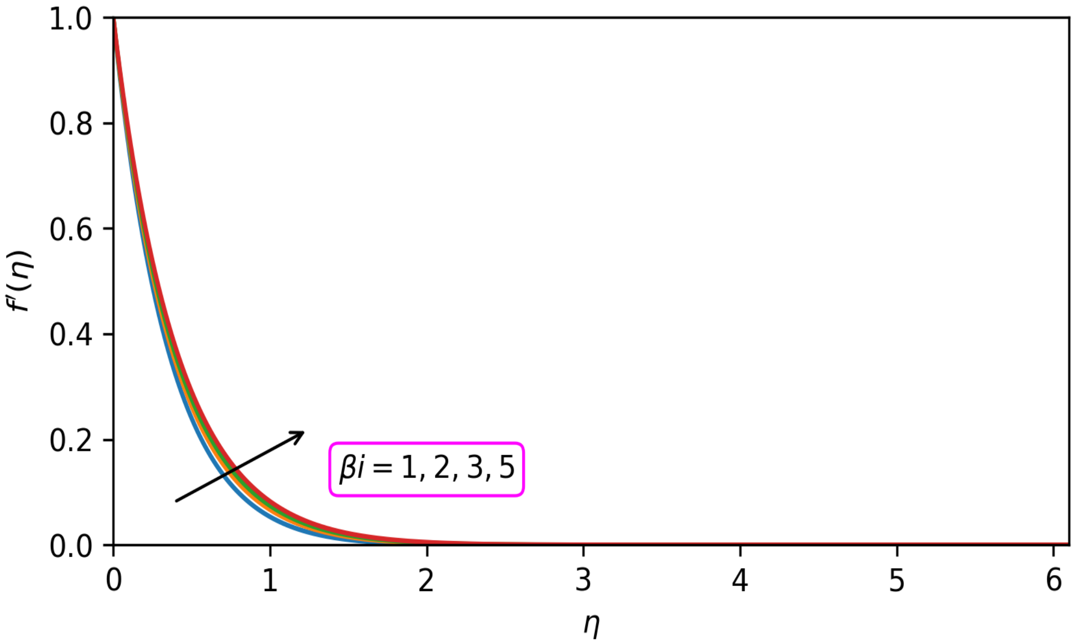

Figure 6.6: Profiles of principal velocity $f'(\eta)$ with ion slip parameter β_i.

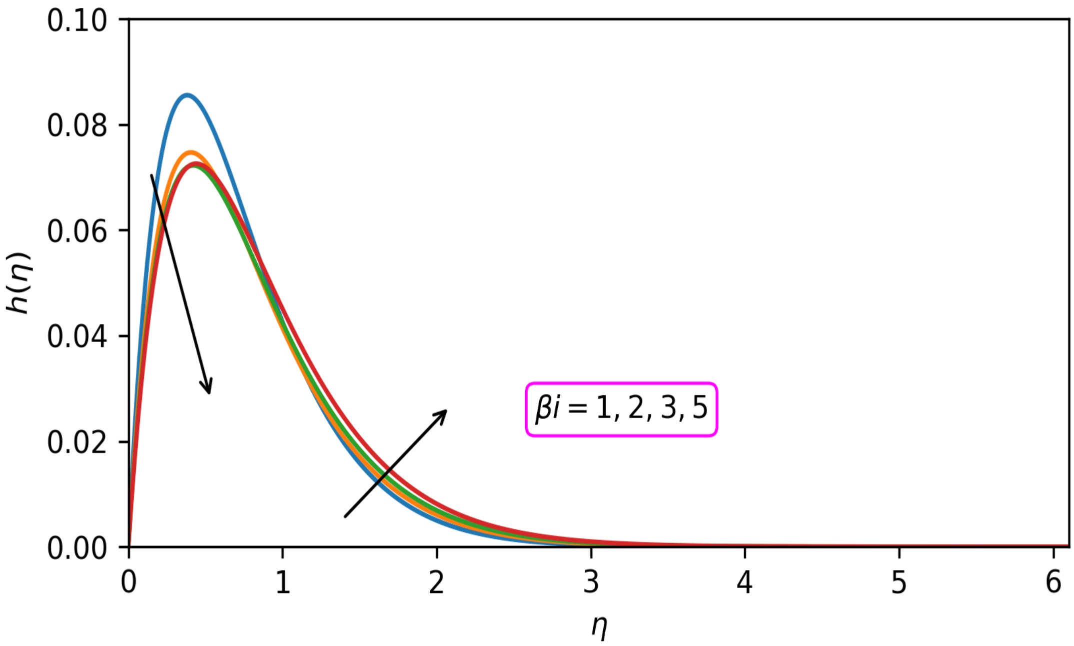

Figure 6.7: Profiles of secondary velocity $h(\eta)$ with β_i.

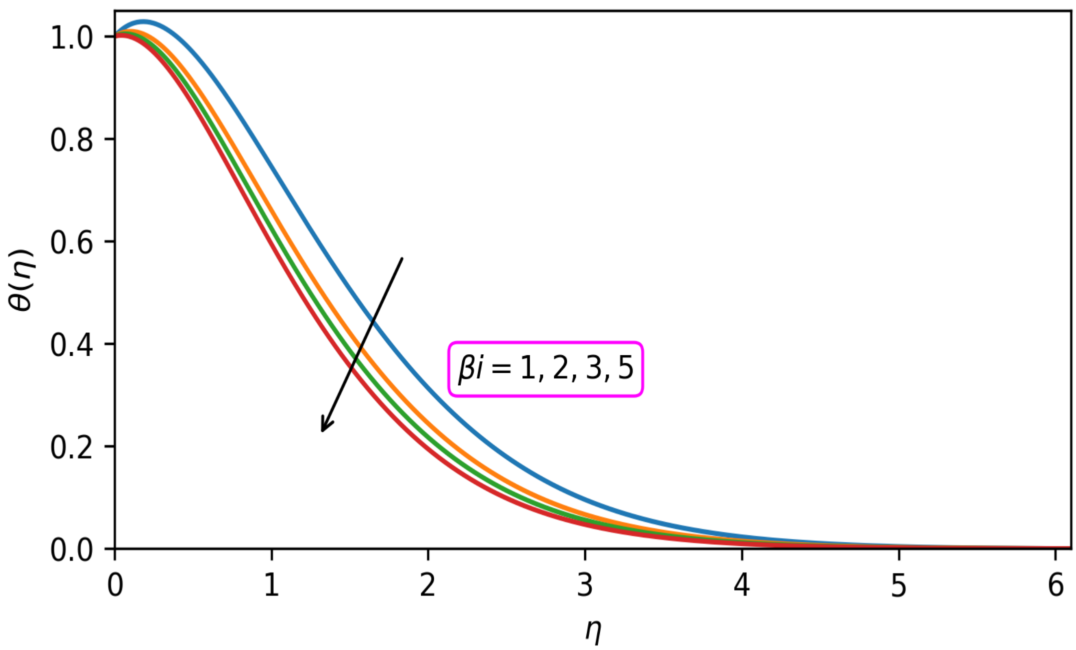

Figure 6.8: Profiles of Temperature $\theta(\eta)$ with β_i.

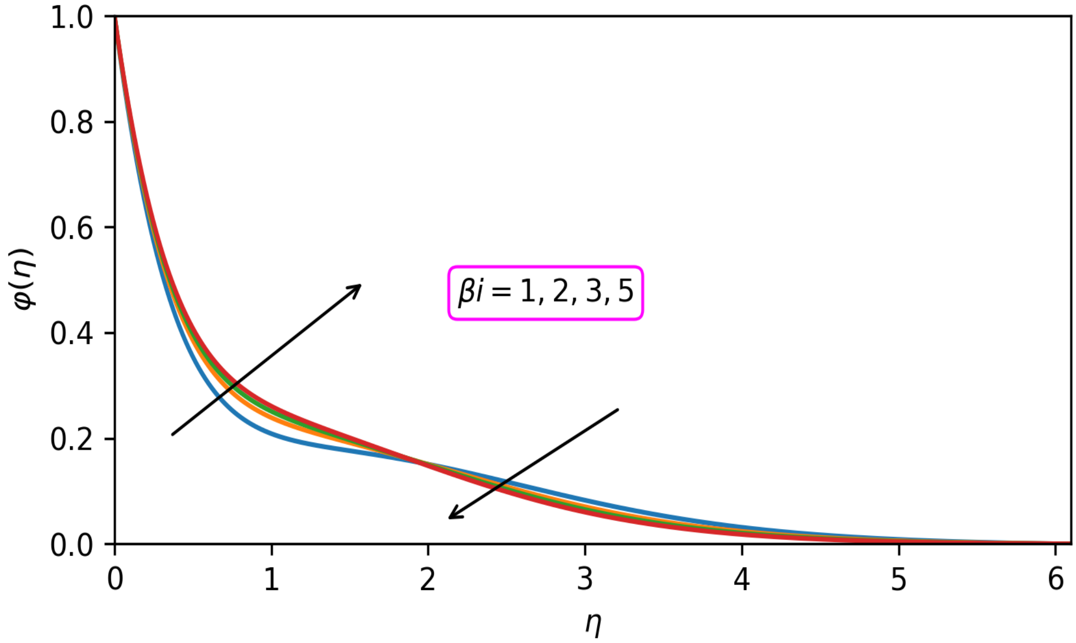

Figure 6.9: Profiles of nanoparicle concentration $\phi(\eta)$ with β_i.

Figs. 6.10–6.13 illustrate how the Power law index (n) influences the profiles of principal velocity, secondary velocity, temperature and nanoparticle concentration. As portrayed in fig. 6.10, it is shown that an increase in the Power law index (n) results in a reduction in the principal velocity. Similarly, the secondary velocity also declines as the values of the Power law index (n) increase, as witnessed by Fig. 6.11. The power law index, indicative of the fluid's non-Newtonian behavior, suggests that as the fluid becomes more viscous, the resistance to flow increases, leading to lower velocities. In contrast, increasing the power law index (n) tends to elevate the fluid temperature as displayed in Fig. 6.12. In fact, an elevation in the power law index (a rise in the liquid's viscosity) typically enhances the non-Newtonian characteristics of the fluid, leading to improved thermal conductivity. Fig. 6.13 demonstrates a dual nature in ($\phi(\eta)$).

Similarly to the power law index (n), the Weissenberg number (We) contributes to the reduction of both the principal and secondary velocities but to the amplification of the temperature profile as presented in Figs. 6.14, 6.15, and 6.16, respectively. The Weissenberg number, representing the ratio of relaxation time (the time it takes for a fluid to relax after being deformed) to processing time (the time scale of the flow or deformation process), suggests that higher values can also enhance the relaxation time and hence dampen fluid motion, whereas the fluid temperature is enhanced. Fig. 6.17 depicts the dual nature in the concentration profile $\phi(\eta)$ as we vary Weissenberg number (We).

Alhefthi et al. [206] also found that "an increase in both the power law index n and the Weissenberg number We results in a decrease in the tangent hyperbolic nanofluid flow velocity field." This observation aligns with our findings, reinforcing the consistency and reliability of our results in relation to the existing literature.

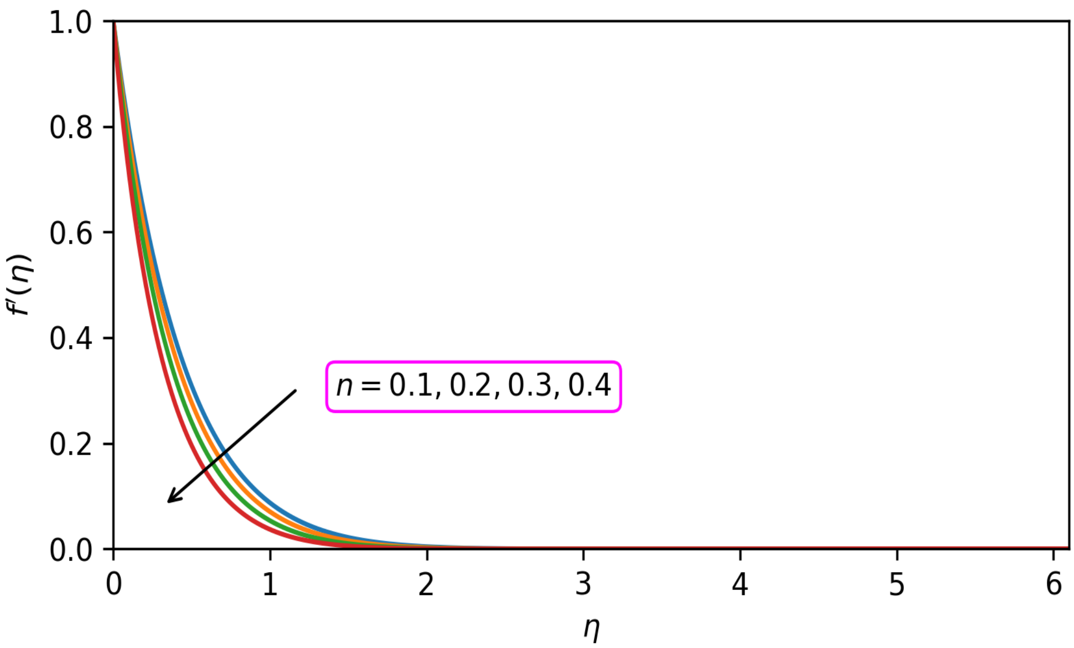

Figure 6.10: Profiles of principal velocity $f'(\eta)$ with power index parameter n.

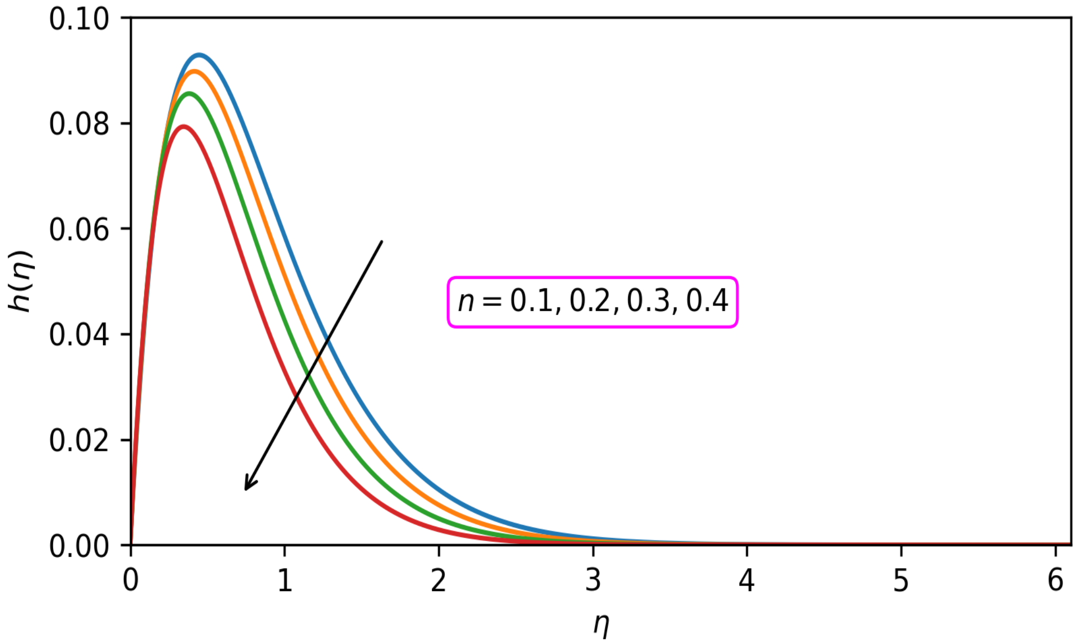

Figure 6.11: Profiles of secondary velocity $h(\eta)$ with n.

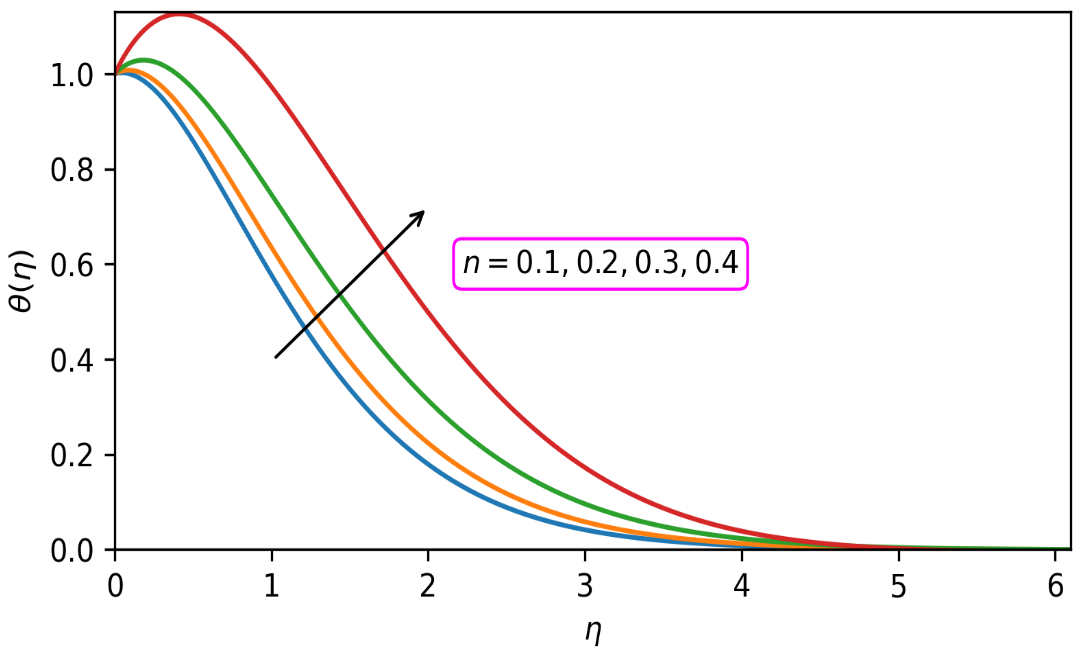

Figure 6.12: Profiles of Temperature $\theta(\eta)$ with n.

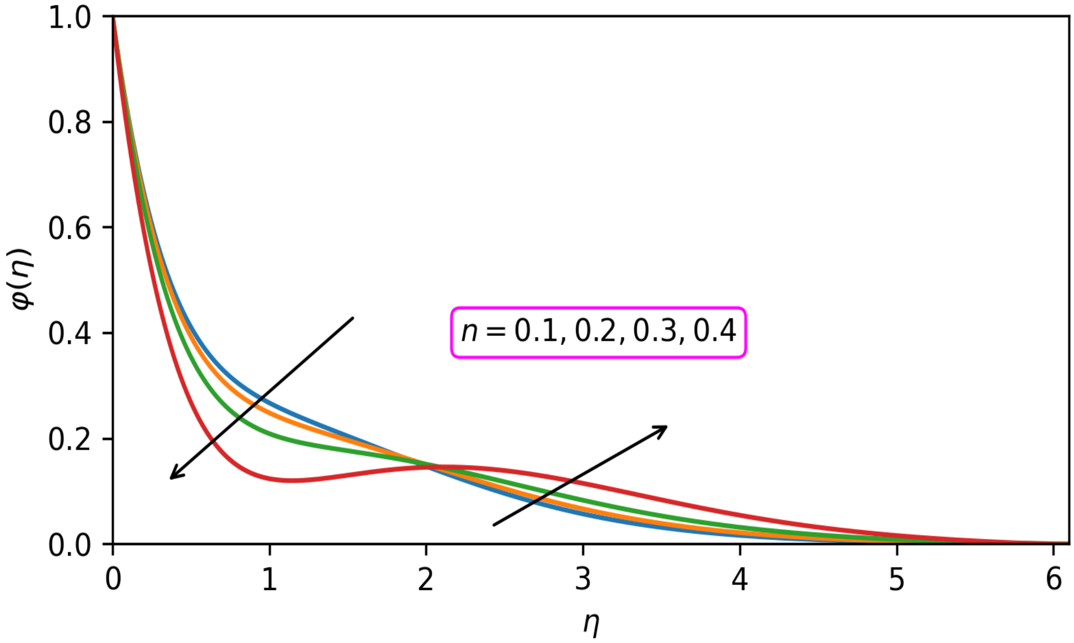

Figure 6.13: Profiles of nanoparicle concentration $\phi(\eta)$ with n.

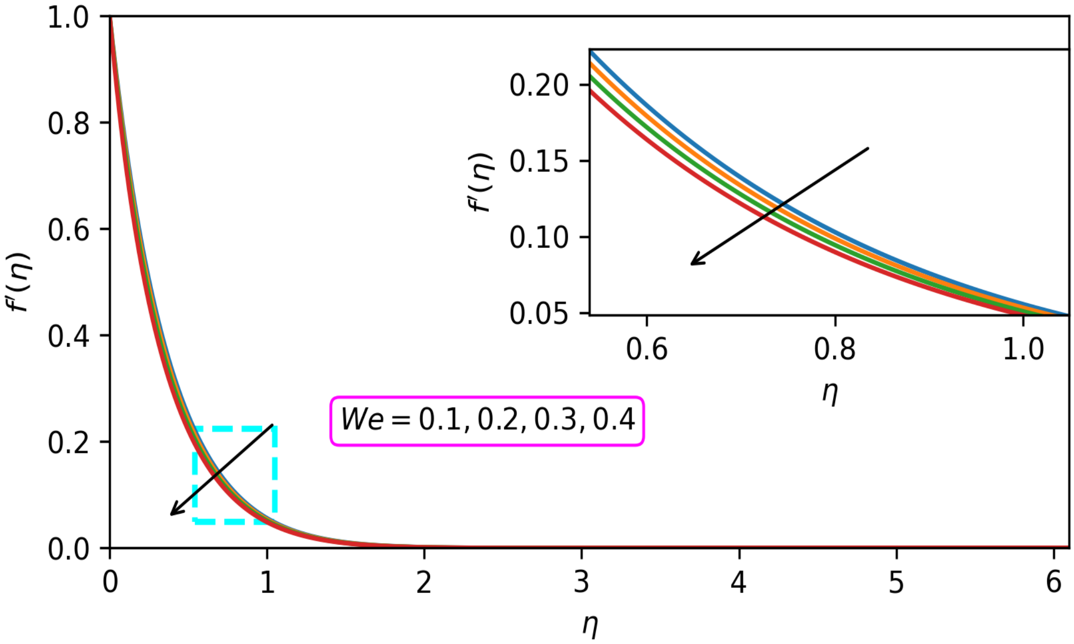

Figure 6.14: Profiles of principal velocity $f'(\eta)$ with Weissenberg number (We).

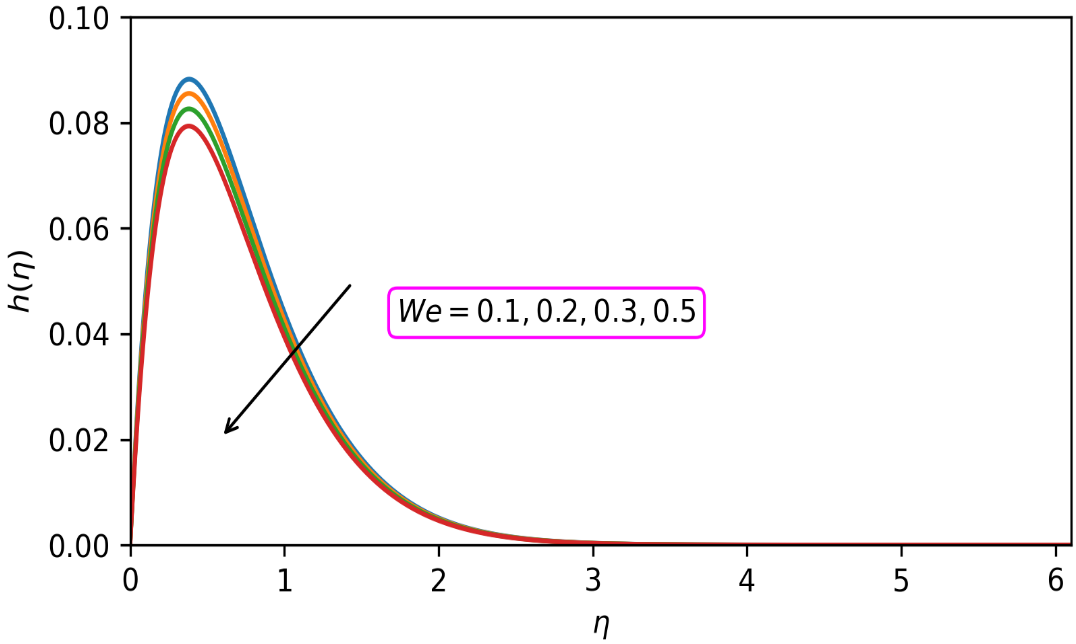

Figure 6.15: Profiles of secondary velocity $h(\eta)$ with We.

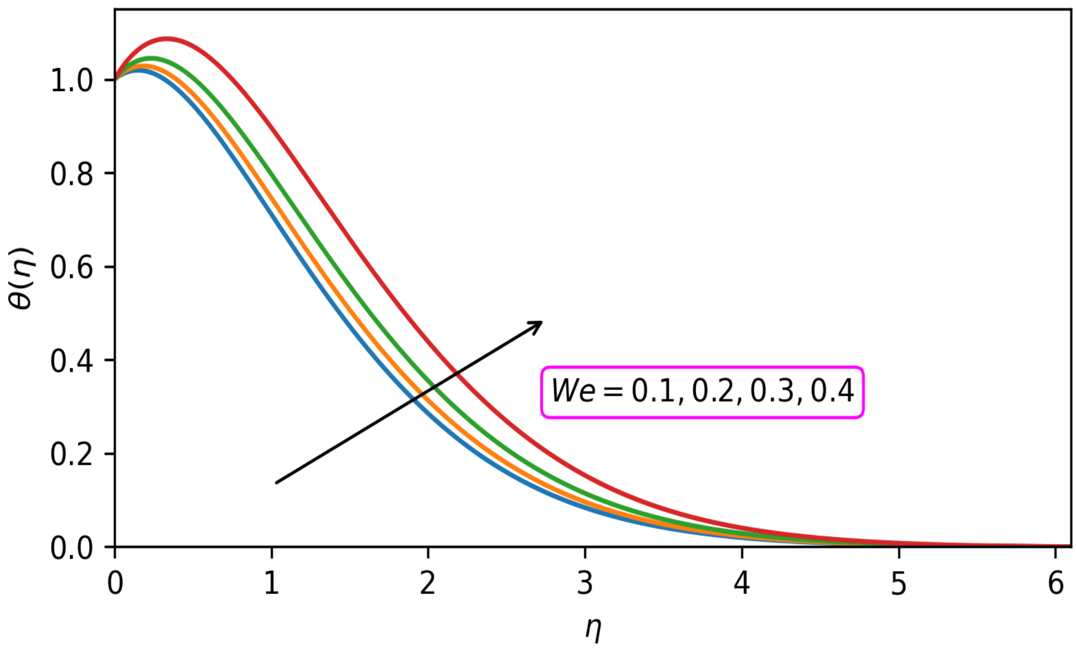

Figure 6.16: Profiles of Temperature $\theta(\eta)$ with We.

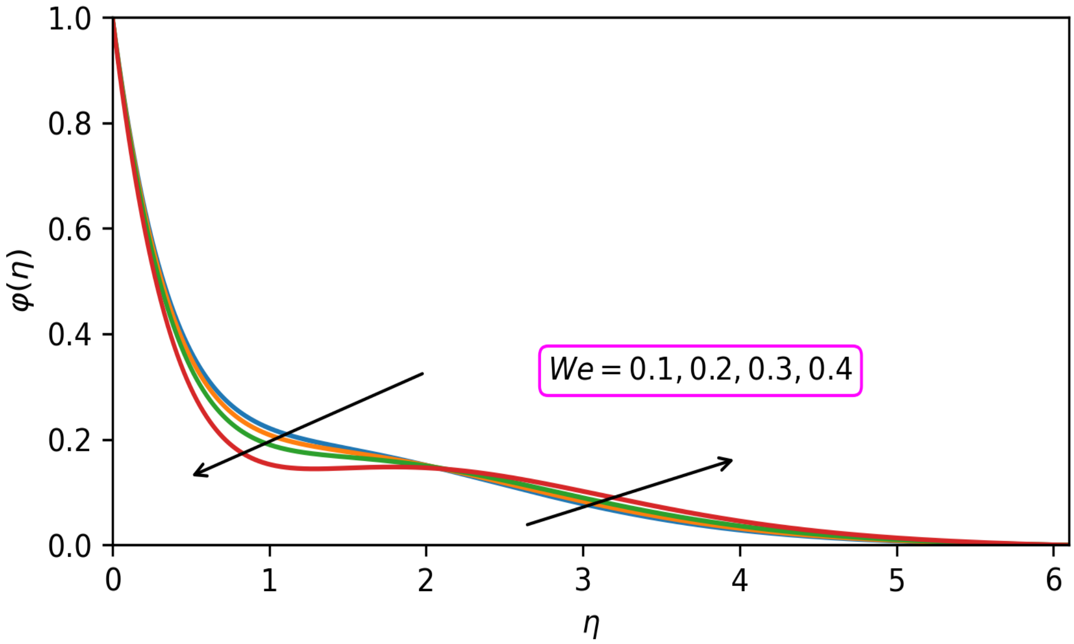

Figure 6.17: Profiles of nanoparicle concentration $\phi(\eta)$ with We.

Figs. 6.18–6.21 explore the impacts of the suction factor on the profiles of velocities, temperature, and nanoparticle concentration. As sketched in Figs. 6.18, 6.19, and 6.20, enhanced suction reduces the principal and secondary velocities, as well as the fluid temperature, respectively. The suction factor (V_0) exerts a negative influence, as enhanced suction removes fluid from the boundary layer, thus decreasing both fluid velocities. The increase in suction effectively removes warmer fluid from the boundary layer, promoting cooler fluid inflow from the surroundings. This process not only decreases the temperature but also enhances the stability of the thermal boundary layer, promoting efficient heat removal from the surface. Figure 6.21 reveals trends similar to Hall currents and ion slip.

The significance of the rotation parameter on the velocities, and temperature profiles are presented in Figs. 6.22–6.24. As indicated in Fig. 6.22, increasing (ω) diminishes the principal velocity. Physically, the Coriolis force, resulting from rotation, adds an apparent force that opposes the flow direction. Interestingly, the rotation parameter (ω) exhibits a positive influence on the auxiliary velocity, as illustrated in Fig. 6.23, which means that rotation generates a centrifugal effect that enhances lateral flow, thus increasing $h(\eta)$. Fig. 6.24 indicates that increasing the rotation parameter (ω) tends to elevate the fluid temperature. Physically, the rotation parameter influences the centrifugal forces in the fluid, promoting heat retention.

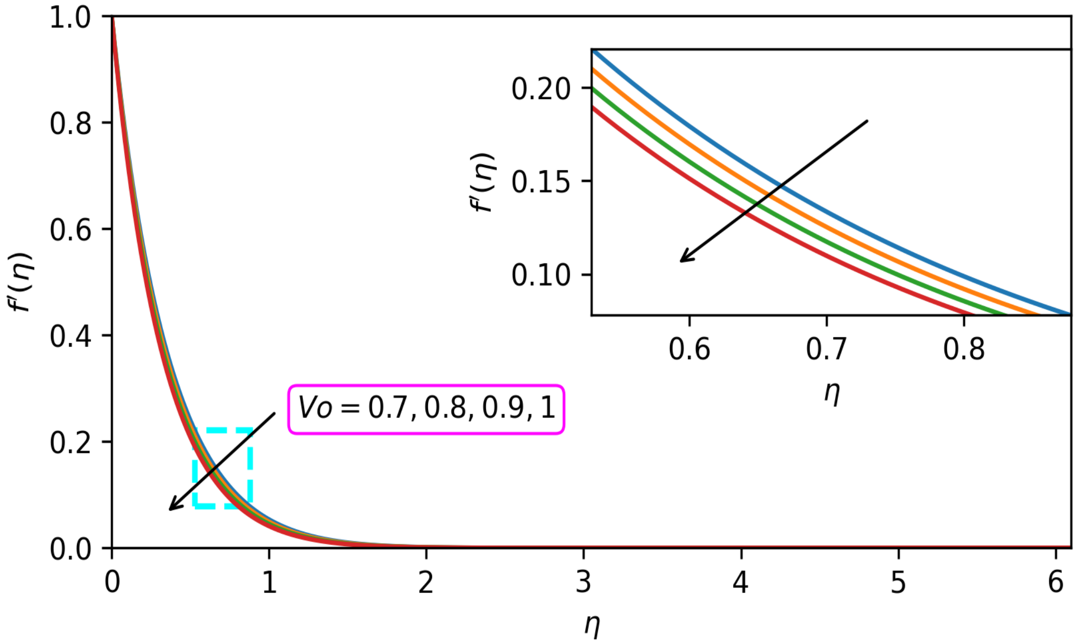

Figure 6.18: Profiles of principal velocity $f'(\eta)$ with Suction Velocity parameter (V_0).

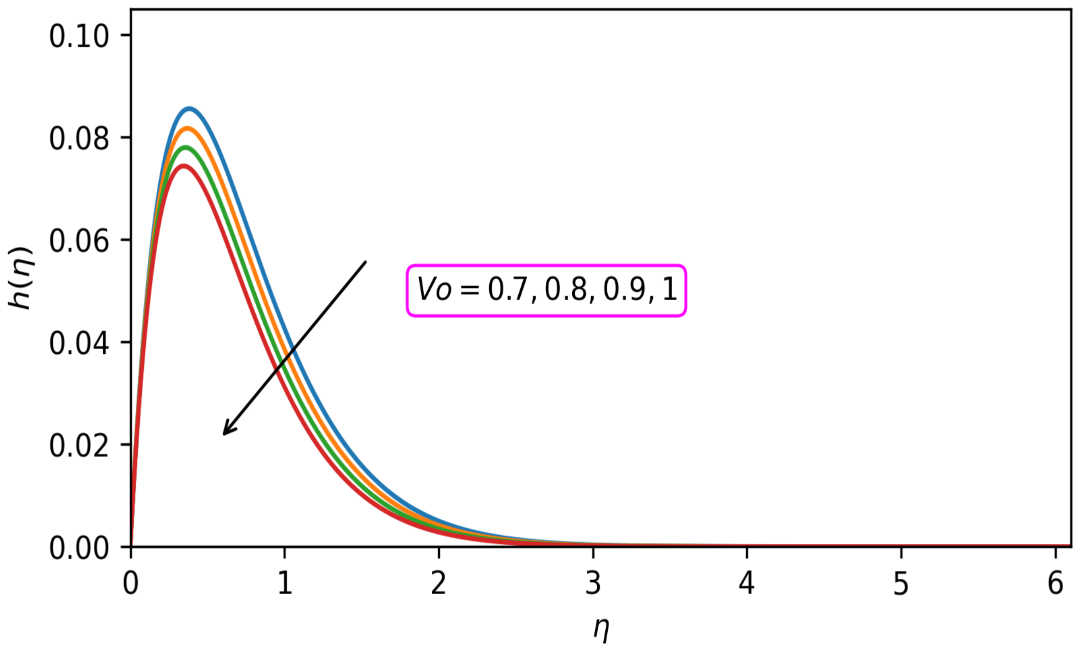

Figure 6.19: Profiles of secondary velocity $h(\eta)$ with V_0.

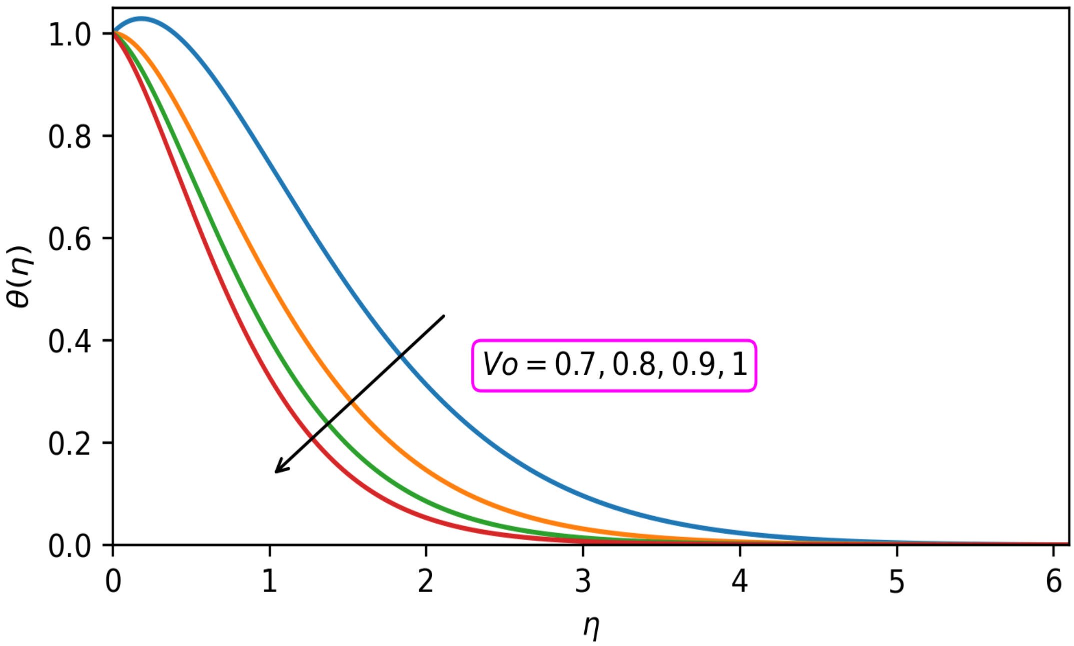

Figure 6.20: Profiles of Temperature $\theta(\eta)$ with V_0.

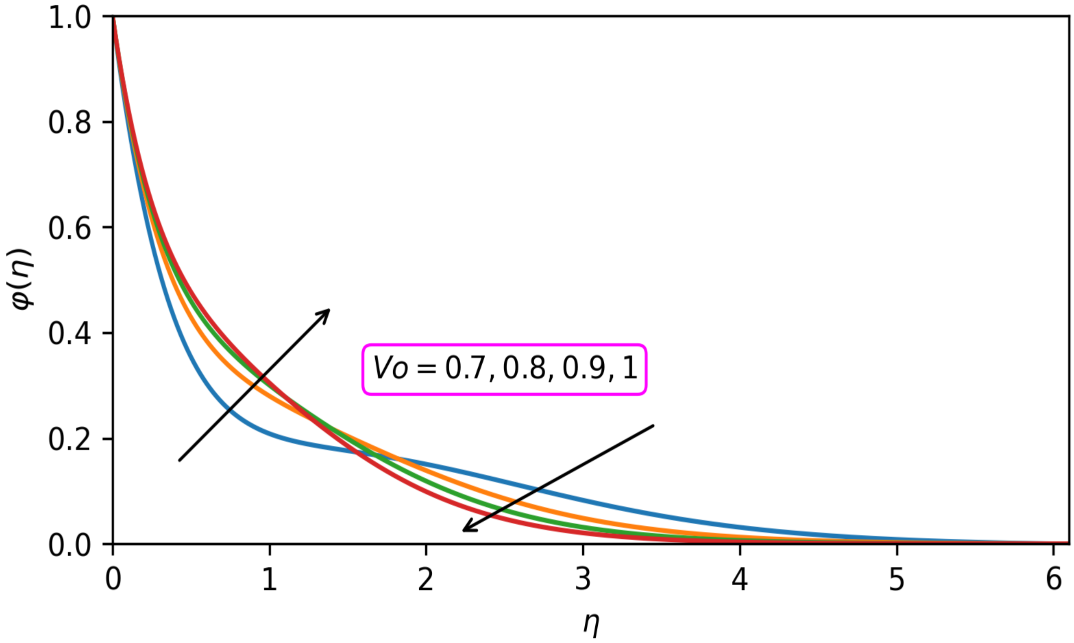

Figure 6.21: Profiles of nanoparicle concentration $\phi(\eta)$ with V_0.

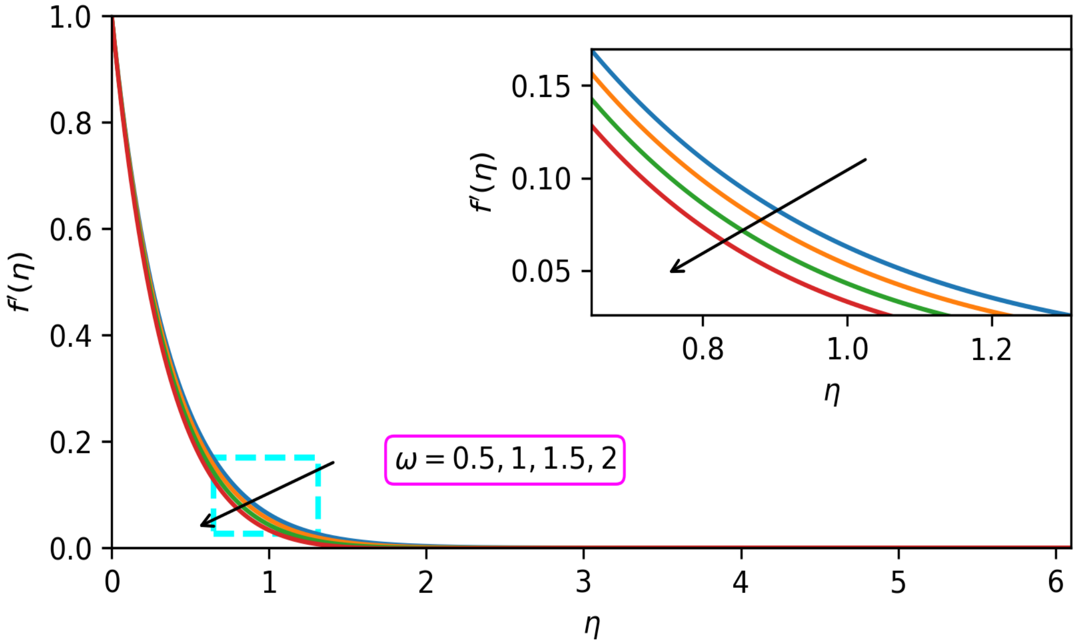

Figure 6.22: Profiles of leading velocity $f'(\eta)$ with rotation parameter (ω).

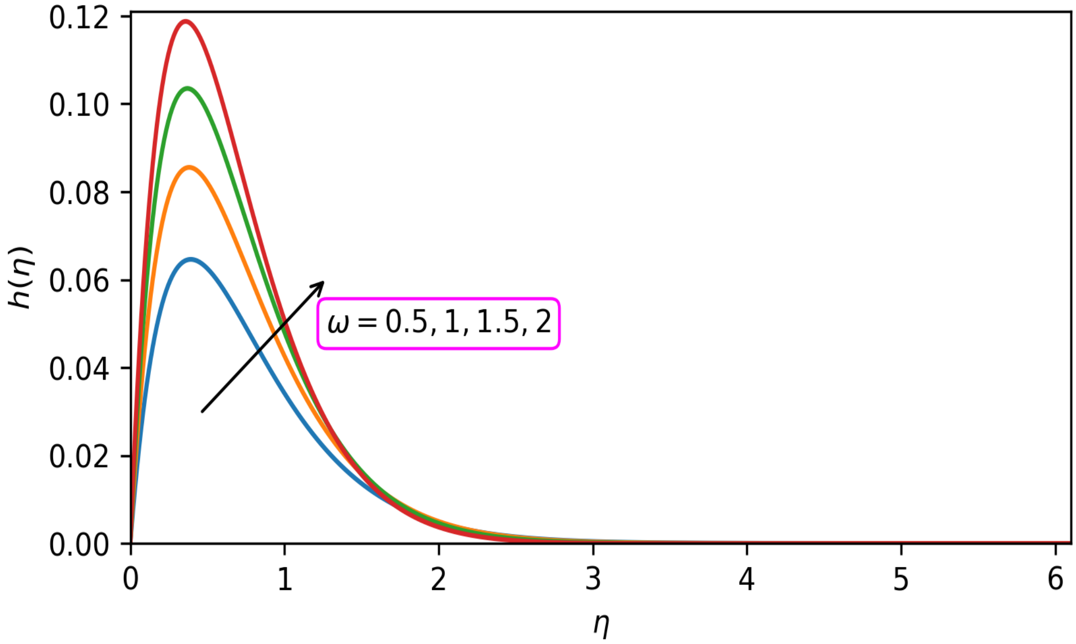

Figure 6.23: Profiles of auxiliary velocity $h(\eta)$ with ω.

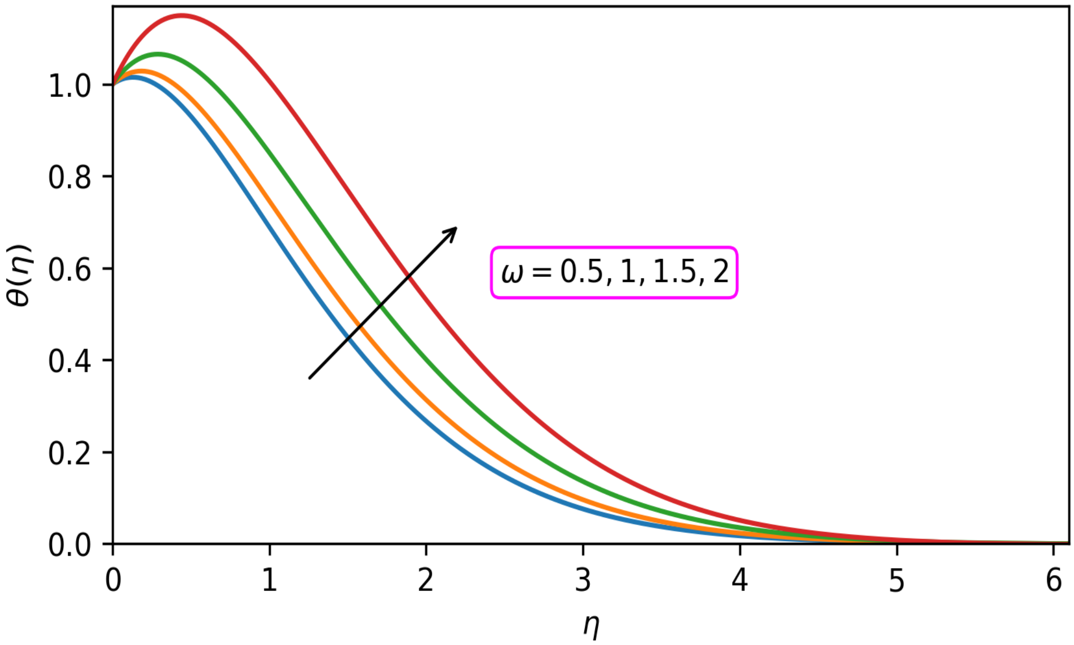

Figure 6.24: Profiles of Temperature $\theta(\eta)$ with ω.

Figs. 6.25 and 6.27 illustrate the effects of the nonlinear thermal radiation parameter (R_n) and the temperature ratio parameter (θ_r) on the temperature distribution. The results show a significant rise in temperature with increasing R_n and θ_r. Physically, nonlinear thermal radiation contributes to heat transfer by allowing the fluid to absorb more radiant energy, thereby elevating its temperature. The temperature ratio parameter, which compares the temperature of the fluid at the surface to that outside the boundary layer, underscores the importance of surface conditions in dictating thermal behavior. A higher ratio indicates an effective heat transfer from the surface, resulting in increased fluid temperatures.

Figs. 6.26 and 6.28 indicate variations in nanoparticle concentration profile due to the effects of nonlinear thermal radiation and the temperature ratio parameters. For each of these parameters, an increase leads to a rapid decline in concentration of nanoparticle near the wall, followed by growth as we move away from it.

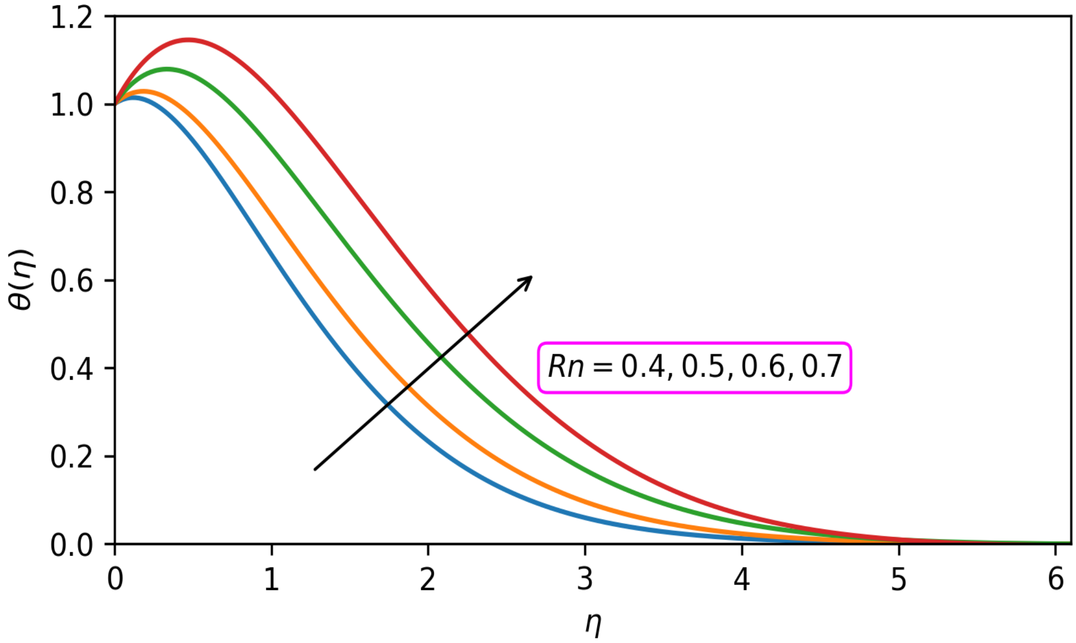

Figure 6.25: Profiles of Temperature $\theta(\eta)$ with nonlinear thermal radiation parameter R_t.

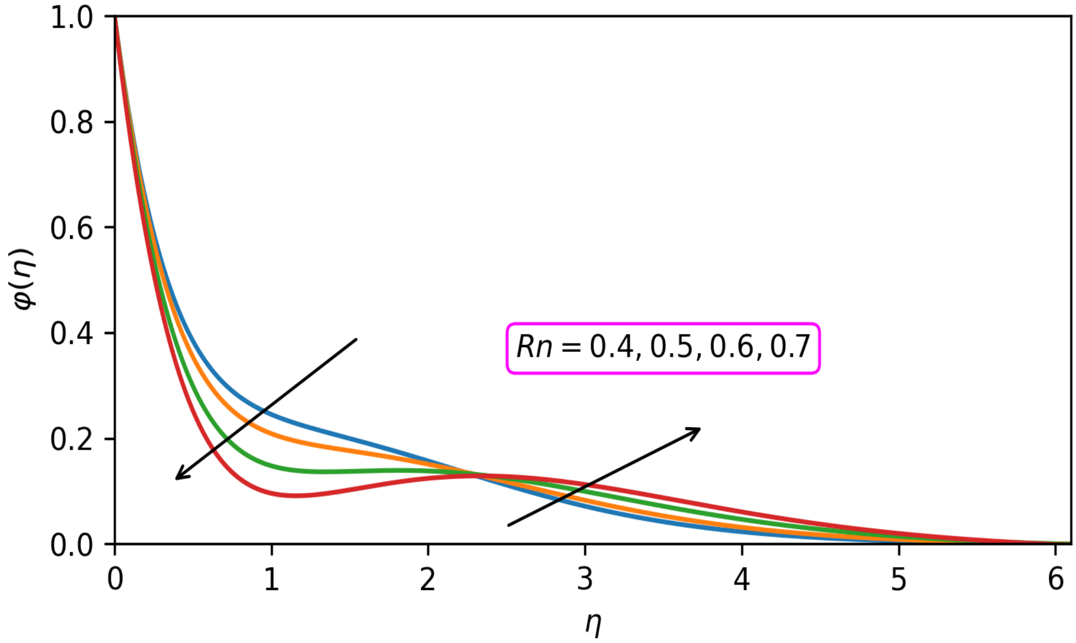

Figure 6.26: Profiles of nanoparicle concentration $\phi(\eta)$ with R_t.

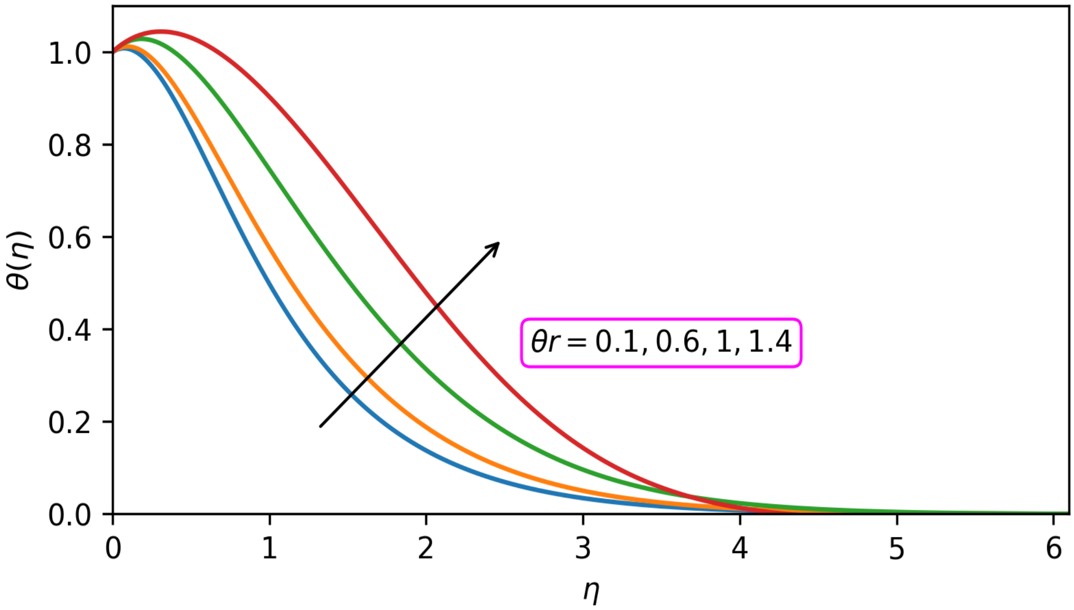

Figure 6.27: Profiles of Temperature $\theta(\eta)$ with ratio of temperature parameter θ_r.

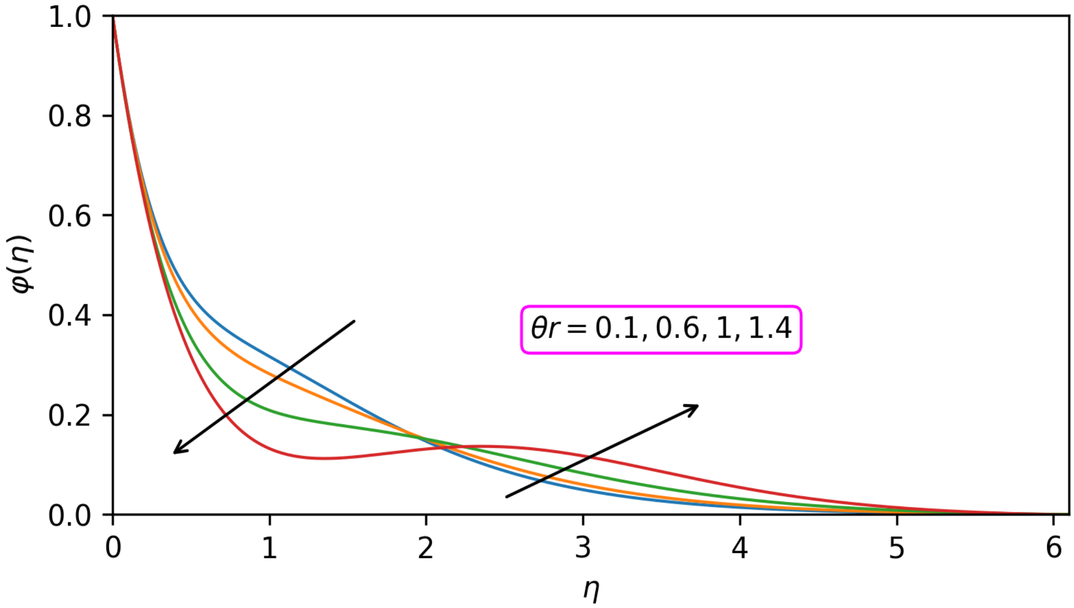

Figure 6.28: Profiles of nanoparicle concentration $\phi(\eta)$ with θ_r.

Fig. 6.29 examines the impact of varying Eckert number (Ec) on the temperature profile $\theta(\eta)$. An increase in the Eckert number enhances the temperature throughout the boundary layer, with a distinct hump observed near the sheet.

Fig. 6.30 shows that escalating the chemical reaction parameter (C_r) leads to a decrease in the temperature distribution, as chemical reactions often absorb heat, leading to a cooling effect in the fluid. Fig. 6.31 demonstrates that higher C_r levels diminish nanoparticle concentration in the boundary layer, as chemical reactions may deplete reactants or generate by-products that influence the overall presence of nanoparticles.

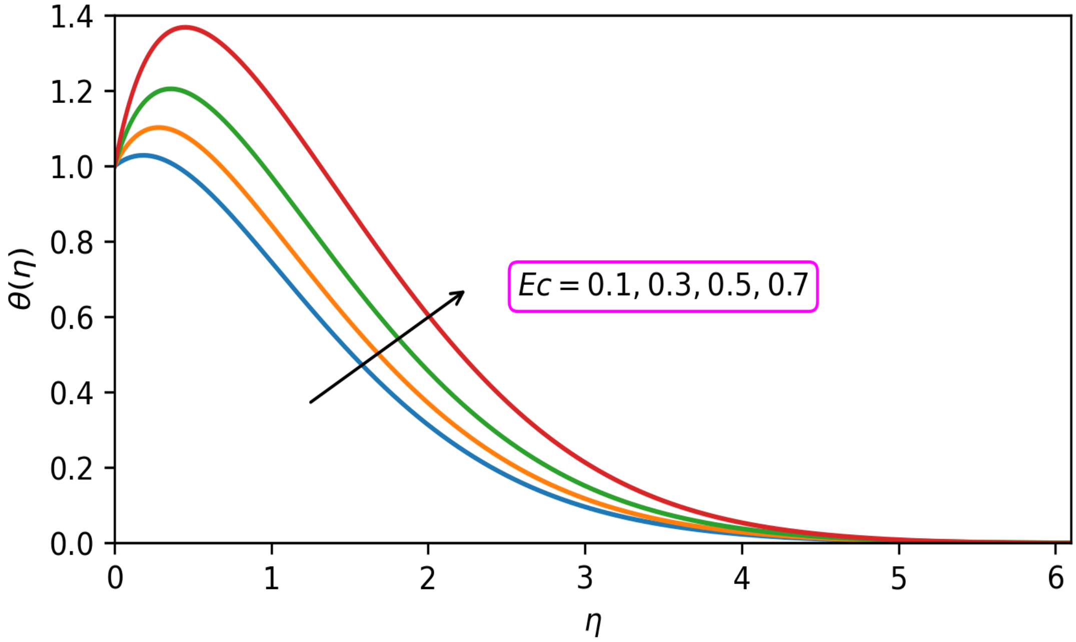

Figure 6.29: Profiles of Temperature $\theta(\eta)$ with Eckert number Ec.

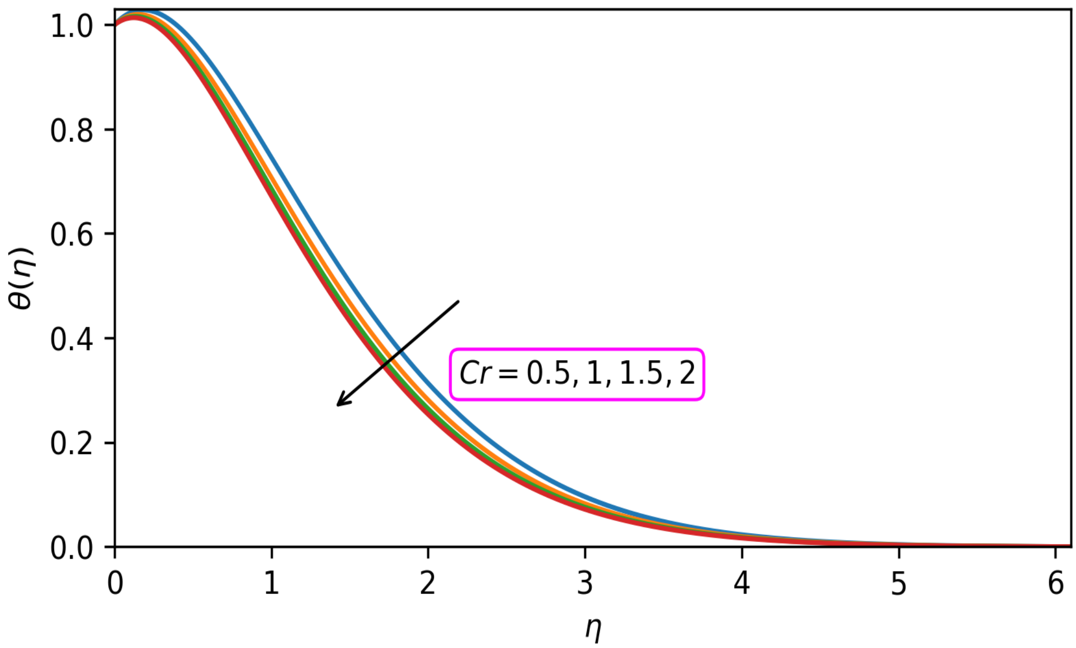

Figure 6.30: Profiles of Temperature $\theta(\eta)$ with chemical reaction parameter Cr.

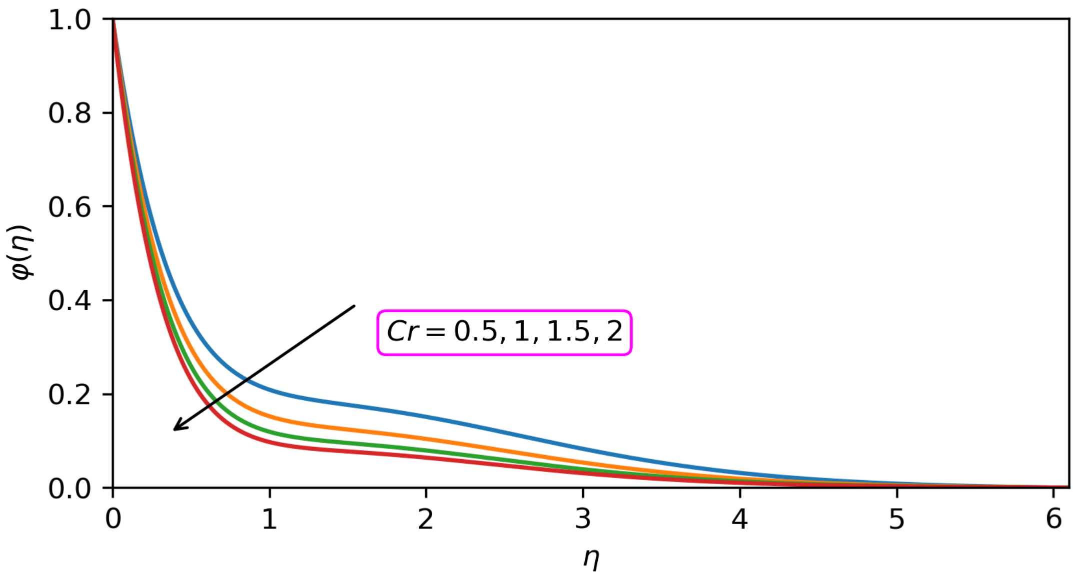

Figure 6.31: Profiles of nanoparicle concentration $\phi(\eta)$ with Cr.

6.4.3 Effects of Pertinent Flow Parameters on Skin Friction Coefficients, Nusselt Number and Sherwood Number

The skin friction coefficients are indispensable measures of the resistance to flow over the stretching sheet. This study emphasizes them in both the x and z directions. Table 6.3 presents the numerical results for the surface drag force in these directions across varying estimates of evolving parameters, including the Hall parameter β_e, ion slip β_i, power law index n, suction factor V_0, rotation parameter ω, Weissenberg number We, porous parameter Da, and magnetic field parameter M. The table make it evident that all these parameters exert a significant influence.

Table 6.3 reveals that the skin friction coefficient in the x-direction diminishes as the Hall parameter β_e and the ion slip β_i rise. In contrast, the parameters of the power law index n, the suction factor V_0, the rotation ω, the Weissenberg number We, the porous Da, and the magnetic field M display an opposite trend. Tangibly, the Hall effect introduces a cross-coupling between the magnetic field and fluid velocity, thereby reducing the effective Lorentz force in the x-direction and diminishing flow resistance. Similarly, the ion slip effects enhance the fluid's mobility, consequently reducing the resistance encountered along the x-direction. Conversely, the power law index which enhances the primary skin friction indicates a more viscous fluid, which increases resistance to motion in the x-direction due to shear-thinning effects. Moreover, the suction factor also influences the surface drag force positively; suction removes fluid from the boundary layer, thereby increasing the velocity gradient on the surface and enhancing the drag force coefficient. The rotation parameter also contributes to this increase in $-C_{fx}\sqrt{Re}$ by introducing centrifugal forces that elevate the effective viscosity of the fluid, further increasing resistance along the x-direction. In addition, as Weissenberg number reflects elasticity of the fluid; elevated values indicate that elastic effects become more pronounced, which raises flow resistance. Finally, as the increased porosity allows more fluid to permeate the medium, heightening interaction with the surface, and hence increasing skin friction. Similarly, elevating the magnetic parameter leads to a higher $-C_{fx}\sqrt{Re}$, as the magnetic field generates a Lorentz force that opposes fluid motion, augmenting resistance.

Table 6.3: Numerical values of the skin friction coefficients of some values of parameters for $Pr = 3,\ M = 5,\ Sc = 1.5,\ We = 0.2,\ \beta_e = 2,\ n = 0.3,\ V_0 = 0.7,\ \beta_i = \omega = \theta_r = 1,\ Ec = 0.1,\ R_n = Cr = N_b = N_t = D_a = Q_h = 0.5$.

β_e	β_i	n	V_0	ω	We	Da	M	$-C_{fx}\sqrt{Re}$	$C_{fz}\sqrt{Re}$
2								1.76931554	0.42768365
4								1.63667663	0.40415767
7								1.56529749	0.38123469
	1							1.76931554	0.42768365
	2							1.68253705	0.35060734
	3							1.62783050	0.32592104
		0.1						1.44122438	0.39671089
		0.2						1.57590975	0.41244172
		0.3						1.76931554	0.42768365
			0.7					1.76931554	0.42768365
			0.8					1.82962675	0.42268887
			0.9					1.89145046	0.41731040
				0.5				1.74128020	0.31447923
				1				1.76931554	0.42768365
				1.5				1.80208827	0.53323836
					0.1			1.57586265	0.44655056
					0.2			1.64454726	0.43300770
					0.3			1.73556603	0.41885580
						0		1.66719567	0.46687169
						0.5		1.76931554	0.42768365
						1		1.86663545	0.39581414
							1	1.52353956	0.35065873
							3	1.65293036	0.39118528
							5	1.76931554	0.42768365

In Table 6.3, it is observed that the coefficient of skin friction in the z-direction $C_{fz}\sqrt{Re}$ increases under the power law index n, rotation parameter ω, and the magnetic field parameter M, and conversely, the Hall parameter β_e, ion slip parameter β_i, suction factor V_0, Weissenberg number We, and porous parameter Da all exert a decreasing influence on the secondary skin friction coefficient, $C_{fz}\sqrt{Re}$.

The values and trends of the rate of heat transfer (Nusselt number) under some key parameters are presented in Table 6.4. The table clearly demonstrates that elevated values of ion slip (β_i), Hall current (β_e), and suction factor (V_0) result in a significant increase in the rate of heat transfer, whereas higher values of power low index (n), rotation (ω), Weissenberg number (We), magnetic field (M), Eckert number (Ec), temperature ratio (θ_r), and nonlinear thermal radiation (R_n) lead to a notable decrease in the rate of heat transfer.

From a physical point of view, increased ion slip allows for a more efficient energy distribution within the fluid, enhancing thermal conductivity, and thus the heat transfer rate amplifies. The Hall parameter has a trend similar to the ion slip, significantly amplifying the rate of heat transfer. Enhanced suction at the permeable surface removes warmer fluid layers near the surface, replacing them with cooler fluid. This process promotes a higher rate of heat transfer from the sheet to the fluid. In contrast, increasing the power law index (n) makes the fluid more viscous, reducing its ability to facilitate heat transfer. The rotation parameter also negatively impacts the transfer rate since increased rotation leads to a centrifugal effect that can suppress fluid motion near the surface, reducing the convective heat transfer efficiency. Furthermore, an increase in Weissenberg number (We) can lead to a decrease in the rate of heat transfer, as the fluid's elastic properties dominate, impeding the flow, and thus the heat transfer. Increasing the magnetic field parameter (M) also functions as a dampener of convective heat transfer, yielding a reduction in the rate of heat transfer. Furthermore, as the Eckert number (Ec) increases, viscous heating decreases the temperature gradient required for efficient heat transfer, which in turn diminishes the rate of heat transfer. An increase in the temperature ratio (θ_r) lowers the rate of heat transfer, as the reduced temperature gradient weakens the driving force of heat transfer. The effect of nonlinear thermal radiation (R_n) on the rate of heat transfer also has a similar trend to the ratio temperature (θ_r).

Contrary to the rate of heat transfer, the rate of mass transfer (Sherwood number) exhibits an opposing trend across all parameters considered, as summarized in Table 6.4. It is observed that rate of mass transfer increases with rising values of power law index, rotation parameter, Weissenberg number, magnetic field parameter, Eckert number, ratio temperature, and nonlinear thermal radiation, while it decreases as ion slip, Hall current, and suction parameter increase.

Realistically, the ion slip effect attenuates the mobility of ions, resulting in a dampened mass transfer rate. An increase in the Hall parameter reduces the Sherwood number, indicating less mass transfer. Increased suction at the surface tends to draw fluid away from the sheet, thereby reducing the mass transfer rate. In contrast, a higher power law index value indicates a more pronounced non-Newtonian behavior, which can enhance the transport characteristics of the fluid, facilitating greater mass transfer.

The rotation parameter also boosts the Sherwood number by enhancing the mixing in the boundary layer through centrifugal forces, resulting in improved mass transfer rates as the fluid is drawn away from the surface. A higher Weissenberg number suggests that the elastic properties of the fluid contribute to better flow characteristics, promoting mass transfer. An increase in the magnetic field parameter generally enhances the Sherwood number, likely as a result of the induced secondary flows that improve mass transfer. Higher Eckert number values indicate that increased viscous heating contributes to the overall energy of the fluid, enhancing the mass transport capabilities.

Table 6.4: Numerical values of the rate of heat transfer and rate of mass transfer of some parameters values for $Pr = 3$, $M = 5$, $Sc = 1.5$, $We = 0.2$, $\beta_e = 2$, $n = 0.3$, $V_0 = 0.7$, $\beta_i = \omega = \theta_r = 1$, $Ec = 0.1$, $R_n = Cr = N_b = N_t = D_a = Q_h = 0.5$.

β_e	β_i	n	V_0	ω	We	M	Rn	θ_r	Ec	$\frac{Nu_x}{\sqrt{Re_x}}$	$\frac{Sh_x}{\sqrt{Re_x}}$
2										−0.50206225	2.29643951
4										−0.25617688	2.17199040
7										−0.1514496	2.12085948
	1									−0.50206225	2.29643951
	2									−0.28988801	2.18856094
	3									−0.20134570	2.14483946
		0.1								−0.13278852	2.12384919
		0.2								−0.25744973	2.17895162
		0.3								−0.50206225	2.29643951
			0.7							−0.50206225	2.29643951
			0.8							0.00233426	2.13485823
			0.9							0.27997285	2.08698216
				0.5						−0.36950463	2.22921386
				1						−0.50206225	2.29643951
				1.5						−0.74559799	2.42273411
					0.1					−0.40583900	2.24643736
					0.2					−0.50206225	2.29643951
					0.3					−0.63889258	2.36814451
						1				−0.09300313	2.09352279
						3				−0.27620507	2.18251274
						5				−0.50206225	2.29643951
							0.4			−0.40275687	2.23913777
							0.5			−0.53553306	2.29643951
							0.6			−0.82757099	2.43194560
								0.1		−0.34407570	2.25419714
								0.6		−0.39291494	2.26758128
								1		−0.50206225	2.29643951
									0.1	−0.50206225	2.29643951
									0.3	−1.29342177	2.78369099
									0.5	−2.18119335	3.32455083

6.5 Conclusion

In this investigation, the 3D flow of MHD Tangent hyperbolic nanofluid has been investigated on a stretching sheet through a permeable surface considering factors such as Hall (β_e), ion slip (β_i), power law index (n), Weissenberg number(We), suction factor (V_0), rotation parameter (ω), magnetic field parameter (M), nonlinear thermal radiation (R_n), the ratio temperature (θ_r), Prandtl number (Pr), Schmidt number (Sc), Brownian diffusion parameter (N_b), chemical reaction parameter (Cr), heat generation (Q_h), Eckert number (Ec), porous parameter (Darcy number) (Da), and thermophoretic parameter (N_t) on the profiles of leading and auxiliary velocities ($f'(\eta)$, $h(\eta)$), temperature ($\theta(\eta)$), nanparticle concentration ($\phi(\eta)$), surface drag force coefficients along the two ($x\&z$) directions, heat and mass transfers; utilizing the Runge-Kutta sixth-order method (RK6) along with shooting scheme, the systems of nonlinear ODEs were solved in which simulations were conducted using Python programming. The key conclusions of the study are succinctly summarized as follows:

- The principal velocity in the x-direction was positively influenced by the ion slip (β_i) and Hall (β_e) parameters, while it was reduced by the power law index (n), Weissenberg number (We), suction velocity (V_0), and rotation parameter (ω).

- The ion slip parameter resulted in a dual behavior in the secondary velocity profile. Initially, it decreased near the sheet and then decreased away from the sheet. The Hall parameter contributed to the enhancement of the secondary velocity ($h(\eta)$), while the parameters power law index, suction factor, rotation parameter and Weissenberg number had a reducing impact.

- The fluid temperature was intensified with the elevation of the power law index, rotation parameter, Weissenberg number, nonlinear thermal radiation, ratio temperature, and Eckert number, but a decline was caused due to parameter values of ion slip, Hall current, suction factor, and chemical reaction.

- A growth in the chemical reaction parameter C_r reduced the concentration of the nanoparticles while a dual nature was observed for the remaining parameters considered with different patterns such that a reduction near the sheet followed by rising away from the sheet was recorded by the power law index, rotation parameter, Weissenberg number, nonlinear thermal radiation, ratio temperature parameter and Eckert number, and vice versa by the increment of the ion slip, Hall current, and suction factor.

- The coefficient of surface drag force (skin friction coefficient) in the x direction was negatively affected by the augmentation of Hall and ion slip parameters. However, an opposing effect was noted by increasing the power-law index, suction factor, rotation parameter, Weissenberg number, Darcy number, and magnetic field parameters.

- Unlike rate of heat transfer, the rate of mass transfer exhibited an incremental growth with rising values of the power law index, rotation parameter, Weissenberg number, magnetic field, ratio temperature and nonlinear thermal radiation, while it was declined by the increment of ion slip, Hall, and suction factor.

Chapter 7

Python-Based Simulation of Rotating MHD Jeffrey Nanofluid Flow over a Permeable Stretching Surface Subject to Hall and Ion Slip Effects

7.1 Introduction

In real-world applications such as polymer processing, biological systems, and lubrication technologies, many fluids exhibit non-Newtonian behavior, meaning that their viscosity depends on shear rate or time rather than remaining constant as in Newtonian fluids. Accurately modeling such fluids requires sophisticated constitutive relationships to capture their complex stress-strain behavior, especially when combined with nanoparticle transport in nanofluids. Among the various rheological models developed to describe non-Newtonian behavior, the Jeffrey fluid model stands out for its effectiveness in capturing both relaxation and retardation effects, making it a valuable tool in simulating the dynamic behavior of non-Newtonian nanofluids. This fluid has received considerable attention due to its ability to simulate real-world materials like polymers and biological fluids. Hayat et al. [207] conducted a comprehensive study of Jeffrey fluid flow in three-dimensional boundary layers. El-Zahar et al. [208] also studied Jeffrey nanofluid in different flow scenarios.

Combining the physics of magnetohydrodynamics (MHD) with Jeffrey nanofluids introduces additional complexity and practical relevance. The presence of magnetic fields significantly alters the transport characteristics of conducting fluids, which is vital in numerous applications, including electromagnetic pumping, metallurgical processing, and magnetic drug targeting. Notably, Shehzad et al. [127, 209], Prasannakumara et al. [210], Biswas et al. [211], Shahzad et al. [125] and Ur Rasheed et al. [212] have extensively studied MHD Jeffrey nanofluid flows incorporating various thermal and mass transfer mechanisms. Recent studies by Dawar et al. [213], Krishna and Kumar [114] and Moltot et al. [214] further demonstrated how Lorentz forces modify the dynamics boundary layer, with applications in industry.These investigations have highlighted the critical influence of magnetic field strength, fluid elasticity, and boundary interactions on heat and mass transport.

Although extensive research has been conducted on MHD Jeffrey nanofluid flows considering individual or limited coupled physical effects, a unified investigation addressing the simultaneous interplay of multiple transport and electromagnetic mechanisms over a permeable surface remains largely unexplored. The present work introduces a novel computational framework for analyzing the three-dimensional rotating flow of an MHD Jeffrey nanofluid, wherein the combined influences of nonlinear thermal radiation, viscous dissipation, Joule heating, and internal heat generation/absorption are incorporated to capture realistic energy transport dynamics. The model further accounts for the effects of Hall and ion slip currents induced by strong magnetic fields, which significantly modify both the momentum and electromagnetic field distributions. In addition, the influence of chemical reactions on nanoparticle mass transfer and the role of Coriolis forces arising from system rotation are examined. The flow is considered through a porous medium in contact with a permeable stretching surface, enabling suction control for boundary layer regulation. The governing equations are solved using a high accuracy sixth-order, seven-stage Runge–Kutta method (RK6,7) with the shooting technique, implemented in the Python programming language, ensuring stable and precise solutions for this highly coupled, nonlinear system. The study offers new insights into the coupled thermal hydrodynamic–electromagnetic behavior of non-Newtonian nanofluids under complex multiphysics conditions.

7.2 Mathematical Formulation

7.2.1 Model Assumptions

The present study considers a steady, laminar, incompressible, and electrically conducting flow of a Jeffrey nanofluid over a linearly stretching permeable surface embedded in a porous medium. The stretching surface moves along the x-axis with a velocity $U_w(x) = a_1 x$, where $a_1 > 0$ denotes the stretching rate. A uniform and strong magnetic field of intensity B_0 is applied perpendicular to the surface, along the

y-direction. The induced magnetic field is neglected under the assumption of a low magnetic Reynolds number. A schematic of the physical model is shown in Figure 7.1. The interaction of the magnetic field with the electrically conducting nanofluid generates Hall and ion slip currents, resulting in a three-dimensional flow structure due to the development of an additional force component along the z-axis. The fluid is assumed to rotate uniformly with constant angular velocity $\Omega = (0, \Omega, 0)$ about the y-axis, introducing Coriolis forces that further influence the spanwise motion. A first-order homogeneous chemical reaction is also considered, affecting the nanoparticle concentration. Furthermore, the Buongiorno nanofluid model is employed to account for Brownian motion and thermophoresis effects in nanoparticle diffusion. The surface is assumed to be subject to suction, characterized by a constant normal velocity $V_w < 0$, which helps control the boundary layer thickness and stabilize the flow. The no-slip boundary condition is assumed at the surface for both velocity and temperature fields. The porous medium is modeled using Darcy's resistance law, contributing an additional drag force proportional to the velocity.

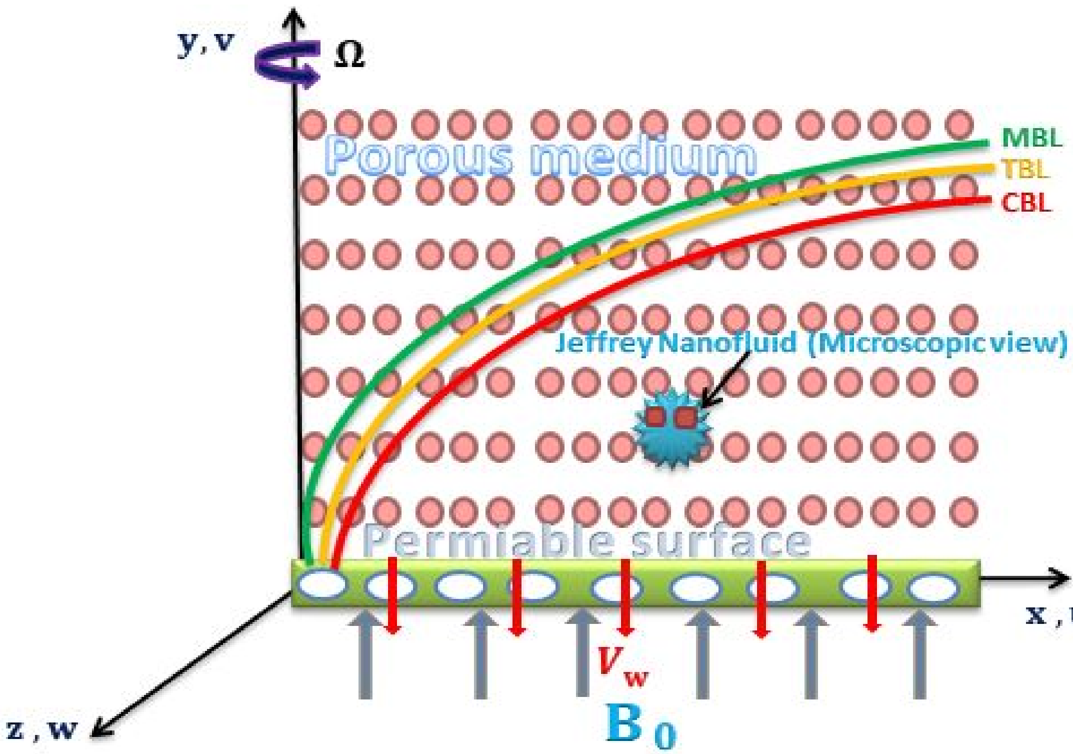

Figure 7.1: A schematic of the physical model

7.2.2 Conservation Equations

7.2.2.1 Conservation of Mass

The continuity equation for incompressible flow can be written as

$$\frac{\partial u}{\partial x} + \frac{\partial v}{\partial y} + \frac{\partial w}{\partial z} = 0, \tag{7.1}$$

7.2.2.2 Conservation of Momentum Equation

The governing momentum equation for fluid flow in a rotating frame, when Coriolis forces are taken into account, can be written as

$$\rho\left[\frac{\partial \mathbf{V}}{\partial t} + (\mathbf{V}\cdot\nabla)\mathbf{V} + (2\Omega\times\mathbf{V})\right] = -\nabla P + \nabla\cdot\tau_{ij} + \mathbf{J}\times\mathbf{B} - \frac{\mu}{K}\mathbf{V} \tag{7.2}$$

where t is the time variable, P is the fluid pressure, τ_{ij} is the Cauchy stress tensor, $\vec{B}$ is external magnetic field, $\vec{J}$ is current density. The constants ρ and K, represent the nanofluid density, and porosity of the medium, respectively. Ω is the angular velocity of the rotating reference frame. The Corriolis term is mathematically written as

$$2\Omega\times V = 2\Omega w\hat{\mathbf{i}} - 2\Omega u\hat{\mathbf{k}}. \tag{7.3}$$

By evaluating the partial derivatives of the stress tensor components from Eq. (2.39) within the momentum balances and applying boundary layer approximations, we obtain the following simplified momentum equations:

$$\rho_f\left(u\frac{\partial u}{\partial x} + v\frac{\partial u}{\partial y} + w\frac{\partial u}{\partial z} + 2\Omega w\right) = \frac{\mu}{1+\lambda_1}\left[\frac{\partial^2 u}{\partial y^2} + \lambda_2\left(u\frac{\partial^3 u}{\partial x\partial y^2} + v\frac{\partial^3 u}{\partial y^3} + \frac{\partial u}{\partial y}\frac{\partial^2 u}{\partial x\partial y} + \frac{\partial v}{\partial y}\frac{\partial^2 u}{\partial y^2}\right)\right] + FB_x, \tag{7.4}$$

$$\rho_f\left(u\frac{\partial w}{\partial x} + v\frac{\partial w}{\partial y} + w\frac{\partial w}{\partial z} - 2\Omega u\right) = \frac{\upsilon}{1+\lambda_1}\left[\frac{\partial^2 w}{\partial y^2} + \lambda_2\left(u\frac{\partial^3 w}{\partial x\partial y^2} + v\frac{\partial^3 w}{\partial y^3} + \frac{\partial u}{\partial y}\frac{\partial^2 w}{\partial x\partial y} + \frac{\partial v}{\partial y}\frac{\partial^2 w}{\partial y^2}\right)\right] + FB_z, \tag{7.5}$$

where the parameter λ_1 signifies the ratio of relaxation time to retardation time and λ_2 corresponds to the retardation time. Since the pressure remains approximately constant normal to the surface within the boundary layer, its gradient vanishes. The remaining body forces, FB_x and FB_z in the respective $x-$, and $z-$ directions, account for the electromagnetic Lorentz force and the Darcy resistance due to porosity.

By incorporating the Hall current and ion slip phenomena occurring at high magnetic field intensities, the modified generalized Ohm's law can be written in the simplified form provided in Eq. (5.11).

$$J \times B = -\frac{\sigma B_0^2\left((1+\beta_e\beta_i)u+\beta_e w\right)}{(1+\beta_e\beta_i)^2+\beta_e^2}\hat{\mathbf{i}} + \frac{\sigma B_0^2\left(\beta_e u-(1+\beta_e\beta_i)w\right)}{(1+\beta_e\beta_i)^2+\beta_e^2}\hat{\mathbf{k}}, \tag{7.6}$$

where the current density vector is expressed as $J = (J_x, J_y, J_z)$. The parameters $\beta_e,\quad \beta_i,\quad and\quad B_0$ denote correspond to the Hall current, the ion slip parameter, and constant magnetic field, respectively.

7.2.2.3 Conservation of Energy equation

The governing energy equation is expressed as

$$\begin{aligned}\left(\rho C_p\right)_f\left[\frac{\partial \mathbf{T}}{\partial t}+(\mathbf{V}\cdot\nabla)\,\mathbf{T}\right] &= \kappa\nabla^2\mathbf{T}+\left(\tau_{ij}:\nabla\right)\mathbf{V}\\ &\quad+\left(\rho C_p\right)_p\left[D_B\nabla C\cdot\nabla T+\frac{D_T}{T_\infty}(\nabla T\cdot\nabla T)\right]\\ &\quad+\frac{1}{\sigma}(\mathbf{J}\cdot\mathbf{J})-\nabla q_r+Q_0\,(T-T_\infty)\,,\end{aligned} \tag{7.7}$$

Consistent with the governing energy equations for the Williamson, Casson, and tangent hyperbolic nanofluid models developed in Chapters 4, 5, and 6, the expressions for Joule heating ($\frac{1}{\sigma}(\mathbf{J}\cdot\mathbf{J})$), non-linear thermal radiation ($-\nabla q_r$), and the heat source term ($Q_0\,(T-T_\infty)$) remain unaltered for the Jeffrey nanofluid. The viscous dissipation term, however, is uniquely defined by the constitutive relationship of the Jeffrey fluid and is derived for this model as follows.

$$\begin{aligned}\Phi = \frac{\upsilon}{C_p(1+\lambda_1)}\Bigg[\left(\frac{\partial u}{\partial y}\right)^2+\left(\frac{\partial w}{\partial y}\right)^2+\lambda_2\Bigg(u\frac{\partial u}{\partial y}\frac{\partial^2 u}{\partial x\partial y}+v\frac{\partial u}{\partial y}\frac{\partial^2 u}{\partial y^2}\\ +u\frac{\partial w}{\partial y}\frac{\partial^2 w}{\partial x\partial y}+v\frac{\partial w}{\partial y}\frac{\partial^2 w}{\partial y^2}\Bigg)\Bigg].\end{aligned} \tag{7.8}$$

7.2.2.4 Conservation of Nanoparticle Concentration Equation

The equation governing nanoparticle concentration in a homogeneous chemical reaction is

$$\frac{\partial \mathbf{C}}{\partial t}+(\mathbf{V}\cdot\nabla)\,\mathbf{C} = D_B\nabla^2 C+\frac{D_T}{T_\infty}\nabla^2 T-R_0\,(C-C_\infty)\,. \tag{7.9}$$

This model accounts for the rate of change in concentration, convective mass transfer, diffusion due to Brownian motion, thermophoretic effects, and the depletion of nanoparticles from a chemical reaction. Here, C and C_∞ represent the concentration near the surface and in the ambient environment, respectively, while R_0, D_B, and D_T are the reaction rate constant, Brownian diffusion coefficient, and thermophoretic diffusion coefficient.

7.2.3 Coupled Governing Equations and Boundary Conditions

The formulation leads to a system of nonlinear partial differential equations governed by the principles of conservation of mass, momentum, energy, and nanoparticle concentration, written as follows [215].

$$\frac{\partial u}{\partial x} + \frac{\partial v}{\partial y} + \frac{\partial w}{\partial z} = 0, \tag{7.10}$$

$$\begin{aligned} u\frac{\partial u}{\partial x} + v\frac{\partial u}{\partial y} + w\frac{\partial u}{\partial z} + 2\Omega w =& \frac{\upsilon}{1+\lambda_1}\left[\frac{\partial^2 u}{\partial y^2} + \lambda_2\left(u\frac{\partial^3 u}{\partial x \partial y^2} + v\frac{\partial^3 u}{\partial y^3} + \frac{\partial u}{\partial y}\frac{\partial^2 u}{\partial x \partial y} + \frac{\partial v}{\partial y}\frac{\partial^2 u}{\partial y^2}\right)\right] \\ & - \frac{\upsilon}{K}u - \frac{\sigma B_0^2\left[(1+\beta_e\beta_i)u + \beta_e w\right]}{\rho\left[(1+\beta_e\beta_i)^2 + \beta_e^2\right]}, \end{aligned} \tag{7.11}$$

$$\begin{aligned} u\frac{\partial w}{\partial x} + v\frac{\partial w}{\partial y} + w\frac{\partial w}{\partial z} - 2\Omega u =& \frac{\upsilon}{1+\lambda_1}\left[\frac{\partial^2 w}{\partial y^2} + \lambda_2\left(u\frac{\partial^3 w}{\partial x \partial y^2} + v\frac{\partial^3 w}{\partial y^3} + \frac{\partial u}{\partial y}\frac{\partial^2 w}{\partial x \partial y} + \frac{\partial v}{\partial y}\frac{\partial^2 w}{\partial y^2}\right)\right] \\ & - \frac{\upsilon}{K}w + \frac{\sigma B_0^2\left[\beta_e u - (1+\beta_e\beta_i)w\right]}{\rho\left[(1+\beta_e\beta_i)^2 + \beta_e^2\right]}, \end{aligned} \tag{7.12}$$

$$\begin{aligned} u\frac{\partial T}{\partial x} + v\frac{\partial T}{\partial y} + w\frac{\partial T}{\partial z} =& \alpha\frac{\partial^2 T}{\partial y^2} + \frac{(\rho C)_p}{(\rho C)_f}\left(D_B\frac{\partial T}{\partial y}\frac{\partial C}{\partial y} + \frac{D_T}{T_\infty}\left(\frac{\partial T}{\partial y}\right)^2\right) + \frac{16\sigma^*}{3k^*(\rho C)_f}\frac{\partial}{\partial y}\left(T^3\frac{\partial T}{\partial y}\right) \\ & + \frac{Q_0(T-T_\infty)}{(\rho C)_f} + \frac{\sigma B_0^2(u^2+w^2)}{(\rho C)_f\left[(1+\beta_e\beta_i)^2 + \beta_e^2\right]} \\ & + \frac{\upsilon}{C_p(1+\lambda_1)}\left[\left(\frac{\partial u}{\partial y}\right)^2 + \left(\frac{\partial w}{\partial y}\right)^2\right. \\ & \left. + \lambda_2\left(u\frac{\partial u}{\partial y}\frac{\partial^2 u}{\partial x \partial y} + v\frac{\partial u}{\partial y}\frac{\partial^2 u}{\partial y^2} + u\frac{\partial w}{\partial y}\frac{\partial^2 w}{\partial x \partial y} + v\frac{\partial w}{\partial y}\frac{\partial^2 w}{\partial y^2}\right)\right], \end{aligned} \tag{7.13}$$

$$u\frac{\partial C}{\partial x} + v\frac{\partial C}{\partial y} + w\frac{\partial C}{\partial z} = D_B\frac{\partial^2 C}{\partial y^2} + \frac{D_T}{T_\infty}\frac{\partial^2 T}{\partial y^2} - R_0\left(C - C_\infty\right). \tag{7.14}$$

The problem's boundary conditions are provided as follows.

$$\begin{cases} u = U_w(x) = a_1 x, \;\; v = -V_w, \;\; w = 0, \;\; T = T_w, \;\; C = C_w, \quad at \;\; y = 0, \\ \\ u \to 0, \;\; \frac{\partial u}{\partial y} \to 0, \;\; w \to 0, \;\; \frac{\partial w}{\partial y} \to 0, \;\; T \to T_\infty, \;\; C \to C_\infty, \quad as \;\; y \to \infty, \end{cases} \tag{7.15}$$

where α, K, $(c_p$, κ, υ, and ρ_f represent the thermal diffusivity, porosity, specific heat capacity, base fluid thermal conductivity, kinematic viscosity and fluid density.

7.2.4 Similarity Transformation

Eqs. (7.10)–(7.14) are transformed into a dimensionless form using similarity transformations and are further reduced to a system of ODEs subject to appropriate boundary conditions.

$$\begin{aligned} &\eta = y\sqrt{\frac{a_1}{\upsilon}}, \quad \psi = x\sqrt{a_1\upsilon} f(\eta), \quad u = a_1 x f'(\eta), \quad v = -\sqrt{a_1 \upsilon} f(\eta), \\ &w = a_1 x h(\eta), \quad \theta(\eta) = \frac{T - T_\infty}{T_w - T_\infty}, \quad \phi(\eta) = \frac{C - C_\infty}{C_w - C_\infty}, \end{aligned} \tag{7.16}$$

where η is similarity variable; $f(\eta)$ is dimensionless stream function; $h(\eta)$ is dimensionless cross-flow velocity; $\theta(\eta)$ is dimensionless temperature; $\phi(\eta)$ is dimensionless nanoparticle concentration. ψ is the function of flow defined by $u = \frac{\partial \psi}{\partial y}$ *and* $v = -\frac{\partial \psi}{\partial x}$.

We now compute the necessary partial derivatives of u and w.

$$\begin{cases} \dfrac{\partial u}{\partial x} = a_1 f', \quad \dfrac{\partial u}{\partial y} = a_1 x f''\sqrt{\dfrac{a_1}{\upsilon}}, \quad \dfrac{\partial u}{\partial z} = 0, \\ \dfrac{\partial^2 u}{\partial y^2} = a_1 x f''' \dfrac{a_1}{\upsilon}, \\ \dfrac{\partial^3 u}{\partial x \partial y^2} = a_1 f''' \cdot \dfrac{a_1}{\upsilon}, \\ \dfrac{\partial^3 u}{\partial y^3} = a_1 x f^{(4)} \left(\dfrac{a_1}{\upsilon}\right)^{3/2}, \\ \dfrac{\partial^2 u}{\partial x \partial y} = a_1 f'' \sqrt{\dfrac{a_1}{\upsilon}}, \end{cases} \tag{7.17}$$

$$\begin{cases} \dfrac{\partial w}{\partial x} = a_1 h, \quad \dfrac{\partial w}{\partial y} = a_1 x h' \sqrt{\dfrac{a_1}{\upsilon}}, \quad \dfrac{\partial w}{\partial z} = 0, \\ \dfrac{\partial^2 w}{\partial y^2} = a_1 x h'' \dfrac{a_1}{\upsilon}, \\ \dfrac{\partial^3 w}{\partial x \partial y^2} = a_1 h'' \dfrac{a_1}{\upsilon}, \\ \dfrac{\partial^3 w}{\partial x \partial y^2} = a_1 h'' \dfrac{a_1}{\upsilon}, \\ \dfrac{\partial^3 w}{\partial y^3} = a_1 x h^{(3)} \left(\dfrac{a_1}{\upsilon}\right)^{3/2}, \\ \dfrac{\partial^2 w}{\partial x \partial y} = a_1 h' \sqrt{\dfrac{a_1}{\upsilon}}. \end{cases} \tag{7.18}$$

When the derived similarity transformations are applied, they satisfy the continuity equation Eq. (7.10) identically. We then systematically transform the remaining governing equations: streamwise momentum Eq. (7.11), spanwise momentum Eq. (7.12), energy Eq. (7.13), and nanoparticle concentration Eq. (7.14) into their dimensionless ODE through sequential application of these transformations.

Substituting Eq. (7.17) on the left-hand side (LHS) of Eq. (7.11), we have

$$\begin{aligned} u\frac{\partial u}{\partial x} + v\frac{\partial u}{\partial y} + w\frac{\partial u}{\partial z} + 2\Omega w &= a_1 x f' \cdot a_1 f' - \sqrt{a_1 \upsilon} f \cdot a_1 x f'' \sqrt{\frac{a_1}{\upsilon}} + 0 + 2\Omega a_1 x h \\ &= a_1^2 x f'^2 - a_1^2 x f f'' + 2\Omega a_1 x h \\ &= a_1^2 x \left(f'^2 - f f'' + \frac{2\Omega}{a_1} h \right). \end{aligned} \tag{7.19}$$

Similarly, the right-hand side (RHS) of Eq. (7.11) becomes

$$\begin{aligned} &\frac{\upsilon}{1+\lambda_1}\left[\frac{\partial^2 u}{\partial y^2} + \lambda_2\left(u\frac{\partial^3 u}{\partial x \partial y^2} + v\frac{\partial^3 u}{\partial y^3} + \frac{\partial u}{\partial y}\frac{\partial^2 u}{\partial x \partial y} + \frac{\partial v}{\partial y}\frac{\partial^2 u}{\partial y^2}\right)\right] \\ &\qquad - \frac{\upsilon}{K}u - \frac{\sigma B_0^2\left[(1+\beta_e\beta_i)u + \beta_e w\right]}{\rho\left[(1+\beta_e\beta_i)^2 + \beta_e^2\right]} \\ &= \frac{\upsilon}{1+\lambda_1}\left[a_1 x f''' \cdot \frac{a_1}{\upsilon} + \lambda_2\left(\frac{a_1^3 x}{\upsilon} f' f''' + -\frac{a_1^3 x}{\nu} f f^{(4)} + a_1^2 x f''^2 \cdot \frac{a_1}{\upsilon} - \frac{a_1^3 x}{\upsilon} f' f'''\right)\right] \\ &\qquad - \frac{\upsilon}{K} a_1 x f' - \frac{\sigma B_0^2 a_1 x\left[(1+\beta_e\beta_i)f' + \beta_e h\right]}{\rho\left[(1+\beta_e\beta_i)^2 + \beta_e^2\right]} \\ &= a_1^2 x\left[\frac{1}{1+\lambda_1}\left[f''' + \lambda_2 a_1\left(f''^2 - f f^{(4)}\right)\right] - \frac{\upsilon}{a_1 K} f' - \frac{\sigma B_0^2\left[(1+\beta_e\beta_i)f' + \beta_e h\right]}{\rho a_1\left[(1+\beta_e\beta_i)^2 + \beta_e^2\right]}\right]. \end{aligned} \tag{7.20}$$

Multiplaying the entire equation by $\dfrac{1+\lambda_1}{a_1^2 x}$, we obtain the non-dimensionalized form of $x-$ momentum Eq. (7.11) as

$$
\begin{aligned}
&f''' + \lambda_2 a_1\left(f''^2 - f f^{(4)}\right) - (1+\lambda_1)\left(f'^2 - f f'' + \frac{2\Omega}{a_1}h\right)\\
&\quad - \frac{\upsilon(1+\lambda_1)}{a_1 K}f' - \frac{\sigma B_0^2(1+\lambda_1)\left[(1+\beta_e\beta_i)f' + \beta_e h\right]}{\rho a_1\left[(1+\beta_e\beta_i)^2 + \beta_e^2\right]} = 0.
\end{aligned}
\tag{7.21}
$$

We now also apply the similarity transformations to the equation of z-momentum. Substitute Eq. (7.18) in Eq. (7.12)), we have

$$
\begin{aligned}
&a_1 x f' a_1 h - \sqrt{a_1\upsilon} f a_1 x h' \sqrt{\frac{a_1}{\upsilon}} + 0 - 2\Omega a_1 x f'\\
&= \frac{\upsilon}{1+\lambda_1}\left[a_1 x h'' \frac{a_1}{\upsilon} + \lambda_2\left(\frac{a_1^3 x}{\upsilon} f' h'' - \frac{a_1^3 x}{\upsilon} f h^{(3)} + \frac{a_1^3 x}{\upsilon} f'' h' - \frac{a_1^3 x}{\upsilon} f' h''\right)\right]\\
&\quad - \frac{\upsilon}{K}a_1 x h + \frac{\sigma B_0^2 a_1 x\left[\beta_e f' - (1+\beta_e\beta_i)h\right]}{\rho\left[(1+\beta_e\beta_i)^2 + \beta_e^2\right]}.
\end{aligned}
\tag{7.22}
$$

Multiplaying Eq. (7.22) by $\dfrac{1+\lambda_1}{a_1^2 x}$, the non-dimensional form of the equation of the z-momentum becomes

$$
\begin{aligned}
&h'' + \lambda_2 a_1\left(f'' h' - f h'''\right) + (1+\lambda_1)\left(f h' - f' h + \frac{2\Omega}{a_1} f'\right)\\
&\quad - \frac{\upsilon(1+\lambda_1)}{a_1 K}h + \frac{\sigma B_0^2(1+\lambda_1)\left(\beta_e f' - (1+\beta_e\beta_i)h\right)}{\rho a_1\left[(1+\beta_e\beta_i)^2 + \beta_e^2\right]} = 0.
\end{aligned}
\tag{7.23}
$$

To non-dimensionalize the energy equation using the similarity transformations (7.16), we compute the following necessary partial derivatives in addition to Eq. (7.17) and (7.18).

$$
\begin{cases}
\dfrac{\partial T}{\partial x} = 0, \quad \dfrac{\partial T}{\partial y} = (T_w - T_\infty)\theta'\sqrt{\dfrac{a_1}{\upsilon}}, \quad \dfrac{\partial T}{\partial z} = 0,\\[2ex]
\dfrac{\partial^2 T}{\partial y^2} = (T_w - T_\infty)\theta''\dfrac{a_1}{\upsilon}, \dfrac{\partial C}{\partial y} = (C_w - C_\infty)\phi'\sqrt{\dfrac{a_1}{\upsilon}}.
\end{cases}
\tag{7.24}
$$

Now, the transformations of each term of the energy equation are computed as follows. Transforming the convection term (LHS)

$$
u\frac{\partial T}{\partial x} + v\frac{\partial T}{\partial y} + w\frac{\partial T}{\partial z} = -a_1(T_w - T_\infty) f\theta'.
\tag{7.25}
$$

and the thermal diffusion term is

$$\alpha \frac{\partial^2 T}{\partial y^2} = \alpha(T_w - T_\infty)\theta'' \frac{a_1}{\upsilon} \tag{7.26}$$

Nanoparticle diffusion (Brownian and thermophoresis diffusion) term can be transformed as

$$\tau\left(D_B \frac{\partial T}{\partial y}\frac{\partial C}{\partial y} + \frac{D_T}{T_\infty}\left(\frac{\partial T}{\partial y}\right)^2\right) = \frac{\tau a_1}{\upsilon}\Bigg[D_B(T_w - T_\infty)(C_w - C_\infty)\theta'\phi' + \frac{D_T}{T_\infty}(T_w - T_\infty)^2\theta'^2\Bigg] \tag{7.27}$$

The nonlinear thermal radiation term can also be transformed to the following.

$$\frac{16\sigma^*}{3k^*(\rho c)_f}\frac{\partial}{\partial y}\left(T^3\frac{\partial T}{\partial y}\right) = \frac{16\sigma^*}{3k^*(\rho c)_f}T_\infty^3(T_w - T_\infty)\cdot\frac{a_1}{\upsilon}\cdot\left[3\left((\theta_r - 1)\theta + 1\right)^2(\theta_r - 1)\theta'^2 + \left((\theta_r - 1)\theta + 1\right)^3\theta''\right] \tag{7.28}$$

where the temperature ratio parameter, $\theta_r = \frac{T_w}{T_\infty}$ and then $T = T_\infty\left[(\theta_r - 1)\theta + 1\right]$. Nondimensionalizing the heat source term, we obtain

$$\frac{Q_0(T - T_\infty)}{(\rho c)_f} = \frac{Q_0}{(\rho C)_f}(T_w - T_\infty)\theta. \tag{7.29}$$

The magnetic dissipation (Joule heating) term can also be transformed as follows.

$$\frac{\sigma B_0^2(u^2 + w^2)}{(\rho C)_f\left[(1 + \beta_e\beta_i)^2 + \beta_e^2\right]} = \frac{\sigma B_0^2(a_1 x)^2\left[f'^2 + h^2\right]}{(\rho C)_f\left[(1 + \beta_e\beta_i)^2 + \beta_e^2\right]} \tag{7.30}$$

The nondimensionalized form of the viscous dissipation term is derived using the given similarity transformations as follows.

$$\begin{aligned}
&\frac{\mu}{(\rho C)_f(1 + \lambda_1)}\left[\left(\frac{\partial u}{\partial y}\right)^2 + \left(\frac{\partial w}{\partial y}\right)^2 + \lambda_2\left(u\frac{\partial u}{\partial y}\frac{\partial^2 u}{\partial x\partial y} + v\frac{\partial u}{\partial y}\frac{\partial^2 u}{\partial y^2} + u\frac{\partial w}{\partial y}\frac{\partial^2 w}{\partial x\partial y} + v\frac{\partial w}{\partial y}\frac{\partial^2 w}{\partial y^2}\right)\right]\\
&= \frac{\mu}{(\rho C)_f(1 + \lambda_1)}\Bigg[\left(a_1 x f''\sqrt{\frac{a_1}{\upsilon}}\right)^2 + \left(a_1 x h'\sqrt{\frac{a_1}{\upsilon}}\right)^2\\
&\qquad + \lambda_2\left(a_1^4 x^2\frac{f'(f'')^2}{\upsilon} - a_1^4 x^2\frac{f f'' f'''}{\upsilon} + a_1^4 x^2\frac{f'(h')^2}{\upsilon} - a_1^4 x^2\frac{f h' h''}{\upsilon}\right)\Bigg]\\
&= \frac{a_1^3 x^2}{C_f(1 + \lambda_1)}\left[f''^2 + h'^2 + \lambda_2 a_1\left(f' f''^2 - f f'' f''' + f' h'^2 - f h' h''\right)\right].
\end{aligned} \tag{7.31}$$

Combining Eqs.(7.25)– (7.31) and dividing by $\alpha(T_w - T_\infty)\frac{a_1}{\upsilon}$, the non-dimensional form of the energy equation is written as

$$
\begin{aligned}
&\theta'' + \frac{\upsilon}{\alpha} f\theta' + \frac{\tau D_B (C_w - C_\infty)}{\alpha}\theta'\phi' + \frac{\tau D_T (T_w - T_\infty)}{\alpha T_\infty}\theta'^2 \\
&+ \frac{16\sigma^* T_\infty^3}{3k^*(\rho C)_f \alpha}\left[3\left((\theta_r - 1)\theta + 1\right)^2(\theta_r - 1)\theta'^2 + \left((\theta_r - 1)\theta + 1\right)^3\theta''\right] \\
&+ \frac{Q_0 \upsilon}{(\rho C)_f \alpha a_1}\theta + \frac{\sigma B_0^2 a_1 x^2 \upsilon\left[f'^2 + h^2\right]}{(\rho C)_f \alpha (T_w - T_\infty)\left[(1 + \beta_e\beta_i)^2 + \beta_e^2\right]} \\
&+ \frac{a_1^2 x^2 \upsilon}{C_f(1 + \lambda_1)\alpha(T_w - T_\infty)}\Bigg[f''^2 + h'^2 \\
&\qquad + \lambda_2 a_1\left(f' f''^2 - f f'' f''' + f' h'^2 - f h' h''\right)\Bigg] = 0.
\end{aligned}
\tag{7.32}
$$

To non-dimensionalize the nanoparticle concentration equation, we need to apply the following partial derivatives.

$$
\begin{cases}
\dfrac{\partial C}{\partial x} = \dfrac{\partial C}{\partial \phi}\dfrac{\partial \phi}{\partial x} = (C_w - C_\infty)\dfrac{\partial \phi}{\partial x} = 0 \\
\dfrac{\partial C}{\partial z} = (C_w - C_\infty)\dfrac{\partial \phi}{\partial z} = 0, \\
\dfrac{\partial^2 C}{\partial y^2} = (C_w - C_\infty)\phi'' \cdot \dfrac{a_1}{\upsilon}.
\end{cases}
\tag{7.33}
$$

By substituting the partial derivatives of Eqs. (7.17), (7.18), (7.24) and (7.33) into Eq. (7.14), the nanoparticle concentration is transformed to

$$
\begin{aligned}
&- \sqrt{a_1 \upsilon} f (C_w - C_\infty)\phi' \sqrt{\frac{a_1}{\upsilon}} \\
&= D_B (C_w - C_\infty)\phi'' \cdot \frac{a_1}{\upsilon} + \frac{D_T}{T_\infty}(T_w - T_\infty)\theta'' \cdot \frac{a_1}{\upsilon} - R_0 (C_w - C_\infty)\phi.
\end{aligned}
\tag{7.34}
$$

Dividing Eq. (7.34) by $D_B(C_w - C_\infty)\dfrac{a_1}{\upsilon}$, the non-dimensional ODE form of the nanoparticle concentration equation becomes

$$
\phi'' + \frac{\upsilon}{D_B} f\phi' + \frac{D_T (T_w - T_\infty)}{D_B T_\infty (C_w - C_\infty)}\theta'' - \frac{R_0 \upsilon}{D_B a_1}\phi = 0.
\tag{7.35}
$$

From the definition of the similarity variable of Eq. (7.16) given by $\eta = y\sqrt{\frac{a_1}{\upsilon}}$, it is evident that when $y = 0$, we have $\eta = 0$, and as $y \to \infty$, it follows that $\eta \to \infty$. This relationship enables the boundary conditions to be conveniently expressed in terms of the dimensionless variable η. The transformations of velocity, temperature, and concentration boundary conditions at $y = 0$ can be summarized as follows.

$$\begin{cases} u = a_1 x f'(\eta) \Rightarrow a_1 x f'(0) = a_1 x \Rightarrow f'(0) = 1, \\ v = -\sqrt{a_1 \upsilon} f(\eta) \Rightarrow v(0) = -V_w = -\sqrt{a_1 \upsilon} f(0) \Rightarrow f(0) = \dfrac{V_w}{\sqrt{a_1 \upsilon}}, \\ w = a_1 x h(\eta) \Rightarrow h(0) = 0, \\ \theta(0) = \dfrac{T(0) - T_\infty}{T_w - T_\infty} = \dfrac{T_w - T_\infty}{T_w - T_\infty} = 1, \\ \phi(0) = \dfrac{C(0) - C_\infty}{C_w - C_\infty} = \dfrac{C_w - C_\infty}{C_w - C_\infty} = 1. \end{cases} \tag{7.36}$$

Also, as $y \to \infty$ we have $\eta \to \infty$ and consequently

$$\begin{cases} u \to 0 \Rightarrow f'(\eta) \to 0, \quad \dfrac{\partial u}{\partial y} \to 0 \Rightarrow f''(\eta) \to 0, \\ w \to 0 \Rightarrow h(\eta) = 0, \quad \dfrac{\partial w}{\partial y} \to 0 \Rightarrow h'(\eta) \to 0, \\ \theta(\eta) \to \dfrac{T_\infty - T_\infty}{T_w - T_\infty} = 0, \\ \phi(\eta) \to \dfrac{C_\infty - C_\infty}{C_w - C_\infty} = 0. \end{cases} \tag{7.37}$$

Through the introduction of non-dimensional parameters, the transformed governing equations for linear momentum, energy, and nanoparticle concentration are simplified, yielding the following system of coupled, nonlinear ODEs.

$$\begin{aligned} & f''' + \beta_1 \left(f''^2 - f f^{(4)} \right) - (1 + \lambda_1) \left(f'^2 - f f'' + \omega h \right) \\ & \quad - Da(1 + \lambda_1) f' - \frac{M(1 + \lambda_1) \left[(1 + \beta_e \beta_i) f' + \beta_e h \right]}{\left[(1 + \beta_e \beta_i)^2 + \beta_e^2 \right]} = 0, \end{aligned} \tag{7.38}$$

$$\begin{aligned} & h'' + \beta_1 \left(f'' h' - f h''' \right) + (1 + \lambda_1) \left(f h' - f' h + \omega f' \right) \\ & \quad - Da(1 + \lambda_1) h + \frac{M(1 + \lambda_1) \left(\beta_e f' - (1 + \beta_e \beta_i) h \right)}{\left[(1 + \beta_e \beta_i)^2 + \beta_e^2 \right]} = 0, \end{aligned} \tag{7.39}$$

$$\begin{aligned} & \theta'' + Prf\theta' + PrNb\theta'\phi' + PrNt\theta'^2 + PrQ_h\theta + \frac{PrMEc\left[f'^2 + h^2 \right]}{\left[(1 + \beta_e \beta_i)^2 + \beta_e^2 \right]} \\ & + \frac{PrEc}{(1 + \lambda_1)} \left[f''^2 + h'^2 + \beta_1 \left(f' f''^2 - f f'' f''' + f' h'^2 - f h' h'' \right) \right] \\ & + R_n \left[3 \left((\theta_r - 1)\theta + 1 \right)^2 (\theta_r - 1) \theta'^2 + \left((\theta_r - 1)\theta + 1 \right)^3 \theta'' \right] = 0, \end{aligned} \tag{7.40}$$

$$\phi'' + Scf\phi' + \frac{Nt}{Nb}\theta'' - CrSc\phi = 0. \tag{7.41}$$

Therefore, the dimensionless boundary conditions are

$$\begin{cases} f'(0) = 1, \quad f(0) = V_0, \quad h(0) = 0, \quad \theta(0) = 1, \quad \phi(0) = 1, \quad at \quad \eta = 0, \\ f' \to 0, \quad f'' \to 0, \quad h \to 0, \quad h' \to 0, \quad \theta \to 0, \quad \phi \to 0, \quad as \quad \eta \to \infty. \end{cases} \tag{7.42}$$

Dimensionless parameters used in the above mentioned equations are defined as follows.

Table 7.1: Definitions of Dimensionless Parameters

Symbol & Definition	Description
$\beta_1 = \lambda_2 a_1$	Deborah number
$\omega = \dfrac{2\Omega}{a_1}$	Rotational parameter
$D_a = \dfrac{\upsilon}{a_1 K}$	Porous (Darcy) parameter
$M = \dfrac{\sigma B_0^2}{\rho a_1}$	Hartmann (magnetic) parameter
$Pr = \dfrac{\upsilon}{\alpha}$	Prandtl number
$Nb = \dfrac{\tau D_B (C_w - C_\infty)}{\upsilon}$	Brownian motion parameter
$Nt = \dfrac{\tau D_T (T_w - T_\infty)}{\upsilon T_\infty}$	Thermophoresis parameter
$R_n = \dfrac{16\sigma^* T_\infty^3 a_1}{3k^* (\rho c)_f \upsilon}$	Nonlinear thermal radiation parameter
$Q_h = \dfrac{Q_0}{(\rho C)_f a_1}$	Heat generation/absorption parameter
$Ec = \dfrac{a_1^2 x^2}{C_p (T_w - T_\infty)}$	Eckert number
$Sc = \dfrac{\upsilon}{D_B}$	Schmidt number
$Cr = \dfrac{R_0}{a_1}$	Scaled chemical reaction rate
$\theta_r = \dfrac{T_w}{T_\infty}$	Temperature ratio parameter
$V_0 = \dfrac{V_w}{\sqrt{a_1 \upsilon}}$	Suction velocity (factor)

7.2.5 Engineering Relevant Quantities in Boundary Layer

Boundary layer analysis provides essential metrics to quantify surface transport phenomena. For this non-Newtonian fluid model with linear stretching, we define three critical engineering parameters: the dual-component skin friction coefficient, the Nusselt number, and the Sherwood number. These quantities capture the complex interplay between fluid rheology, surface kinematics, and transport mechanisms.

7.2.5.1 Skin Friction Coefficients

The three-dimensional nature of the flow gives rise to two distinct skin friction components that define the surface drag characteristics.

$$C_{fx} = \frac{\tau_{wx}}{\rho U_w^2}, \quad C_{fz} = \frac{\tau_{wz}}{\rho U_w^2}, \tag{7.43}$$

where τ_{wx} and τ_{wz} represent the wall shear stresses in the streamwise (x) and cross-stream (z) directions, respectively. From the constitutive equation of the Jeffrey fluid model Eq. (2.39), the stress tensor components at the wall ($y = 0$) are defined as follows.

$$\begin{cases} \tau_{wx} = \dfrac{\mu}{1+\lambda_1}\left[\left(\dfrac{\partial u}{\partial y}\right)_{y=0} + \lambda_2\left(u\dfrac{\partial}{\partial x}\left(\dfrac{\partial u}{\partial y}\right) + v\dfrac{\partial}{\partial y}\left(\dfrac{\partial u}{\partial y}\right)\right)_{y=0}\right], \\ \tau_{wz} = \dfrac{\mu}{1+\lambda_1}\left[\left(\dfrac{\partial w}{\partial y}\right)_{y=0} + \lambda_2\left(u\dfrac{\partial}{\partial x}\left(\dfrac{\partial w}{\partial y}\right) + v\dfrac{\partial}{\partial y}\left(\dfrac{\partial w}{\partial y}\right)\right)_{y=0}\right]. \end{cases} \tag{7.44}$$

Through similarity transformation Eq. (7.16), these reduce to the dimensionless forms using the following derivatives.

$$\begin{cases} \left.\dfrac{\partial u}{\partial y}\right|_{y=0} = a_1 x f''(0)\sqrt{\dfrac{a_1}{\upsilon}}, \quad \left.\dfrac{\partial^2 u}{\partial x \partial y}\right|_{y=0} = a_1\sqrt{\dfrac{a_1}{\upsilon}} f''(0), \\ \left.\dfrac{\partial^2 u}{\partial y^2}\right|_{y=0} = a_1 x f'''(0)\cdot\dfrac{a_1}{\upsilon}, \\ \left.u\dfrac{\partial^2 u}{\partial x \partial y}\right|_{y=0} = a_1^2 x f'(0) f''(0)\sqrt{\dfrac{a_1}{\upsilon}}, \quad \left.v\dfrac{\partial^2 u}{\partial y^2}\right|_{y=0} = -a_1^2 x f(0) f'''(0)\sqrt{\dfrac{a_1}{\upsilon}}, \end{cases} \tag{7.45}$$

$$\begin{cases} \left.\dfrac{\partial w}{\partial y}\right|_{y=0} = a_1 x h'(0)\sqrt{\dfrac{a_1}{\upsilon}}, \quad \left.\dfrac{\partial^2 w}{\partial x \partial y}\right|_{y=0} = a_1\sqrt{\dfrac{a_1}{\upsilon}} h'(0), \\ \left.\dfrac{\partial^2 w}{\partial y^2}\right|_{y=0} = a_1 x h''(0)\cdot\dfrac{a_1}{\upsilon}, \\ \left.u\dfrac{\partial^2 w}{\partial x \partial y}\right|_{y=0} = a_1^2 x f'(0) h'(0)\sqrt{\dfrac{a_1}{\upsilon}}, \quad \left.v\dfrac{\partial^2 w}{\partial y^2}\right|_{y=0} = -a_1^2 x f(0) h''(0)\sqrt{\dfrac{a_1}{\upsilon}}. \end{cases} \tag{7.46}$$

Thus, the non-dimensional form of Eq. (7.44) becomes

$$\begin{cases} \tau_{wx} = \dfrac{\mu a_1 x}{1+\lambda_1}\sqrt{\dfrac{a_1}{\upsilon}}\left[f''(0) + \lambda_2 a_1 \left(f'(0)f''(0) - f(0)f'''(0)\right)\right], \\ \tau_{wz} = \dfrac{\mu a_1 x}{1+\lambda_1}\sqrt{\dfrac{a_1}{\upsilon}}\left[h'(0) + \lambda_2 a_1 \left(f'(0)h'(0) - f(0)h''(0)\right)\right]. \end{cases} \tag{7.47}$$

Substituting Eq. (7.47) in Eq. (7.43), we obtain the two skin friction coefficients in the x- and z-directions, respectively.

$$C_{fx}\sqrt{\mathrm{Re}_x} = \frac{1}{1+\lambda_1}\left[f''(0) + \beta_1 \left(f'(0)f''(0) - f(0)f'''(0)\right)\right], \tag{7.48}$$

$$C_{fz}\sqrt{\mathrm{Re}_x} = \frac{1}{1+\lambda_1}\left[h'(0) + \beta_1 \left(f'(0)h'(0) - f(0)h''(0)\right)\right]. \tag{7.49}$$

where $\mathrm{Re}_x = \dfrac{xU_w}{\upsilon} = \dfrac{a_1 x^2}{\upsilon}$ is the local Reynolds number, $U(x)$ is the characteristic velocity, and $\beta_1 = \lambda_2 a_1$ is the dimensionless retardation parameter (Deborah number).

7.2.5.2 Local Nusselt Number

This term indicates that the total wall heat flux must account for both the conductive and radiative contributions. Thus, the Nusselt number becomes

$$\begin{aligned} Nu_x &= \frac{xq_w}{\kappa\left(T_w - T_\infty\right)} = -\frac{x}{k\left(T_w - T_\infty\right)} \cdot \left(\kappa + \frac{16\sigma^*}{3k^*}T_w^3\right)\left(\frac{\partial T}{\partial y}\bigg|_{y=0}\right) \\ &= -\frac{x}{T_w - T_\infty}\left(1 + \frac{16\sigma^* T_w^3}{3\kappa k^*}\right)\left(\frac{\partial T}{\partial y}\bigg|_{y=0}\right). \end{aligned} \tag{7.50}$$

Applying similarity transformation of Eq. (7.16), the nondimensional form becomes

$$\begin{aligned} Nu_x &= -x\sqrt{\frac{a_1}{\upsilon}}\left(1 + \frac{16\sigma^*\theta_r^3 T_\infty^3}{3kk^*}\right)\theta'(0) \\ &= -\sqrt{Re_x}\left(1 + R_n\theta_r^3\right)\theta'(0). \end{aligned} \tag{7.51}$$

Therefore,

$$\frac{Nu_x}{\sqrt{Re_x}} = -\left(1 + R_n\theta_r^3\right)\theta'(0). \tag{7.52}$$

7.2.5.3 Local Sherwood Number

The Sherwood number describes convective-diffusive mass transfer efficiency

$$Sh_x = \frac{xq_m}{D_B(C_w - C_\infty)}, \tag{7.53}$$

with q_m defined by Fick's law for wall mass flux

$$q_m = -D_B \left(\frac{\partial C}{\partial y} \right)_{y=0}. \tag{7.54}$$

This reduces to the concentration gradient expression

$$Sh_x = -\frac{x}{C_w - C_\infty} \left(\frac{\partial C}{\partial y} \right)_{y=0}. \tag{7.55}$$

Applying Eq. (7.33), we have

$$\left.\frac{\partial C}{\partial y}\right|_{y=0} = (C_w - C_\infty)\, \phi'(0) \sqrt{\frac{a_1}{\upsilon}} \Rightarrow \quad Sh_x = -\, x \sqrt{\frac{a_1}{\upsilon}}\, \phi'(0). \tag{7.56}$$

Consequently,

$$\frac{Sh_x}{\sqrt{Re_x}} = \phi'(0). \tag{7.57}$$

The dimensionless form directly relates to the thickness of the concentration boundary layer.

7.3 Method of Solution

Due to the strong non-linearities, obtaining closed-form analytical solutions to the governing system of equations (7.38)–(7.41) with boundary conditions (7.42) becomes impractical. Therefore, a numerical approach is employed. Specifically, the classical boundary value problem (BVP) is transformed into an initial value problem (IVP) through the application of the shooting method, facilitating effective numerical integration. To implement this transformation, the system of higher-order nonlinear ordinary differential equations (ODEs) is first reduced to a system of first-order equations. Through the substitutions $f = f_1$, $f' = f_2$, $f'' = f_3$, $f''' = f_4$, $h = f_5$, $h' = f_6$, $h'' = f_7$, $\theta = f_8$, $\theta' = f_9$, $\phi = f_{10}$, and $\phi' = f_{11}$, the system is recast into eleven first-order ordinary differential equations as follows.

$$
\begin{cases}
f_1' = f_2 & f_1(0) = V_0 \\
f_2' = f_3 & f_2(0) = 1 \\
f_3' = f_4 & f_3(0) = \xi_1 \\
f_4' = \dfrac{1}{\beta_1 f_1}\Big[f_4 + \beta_1 f_3^2 - (1+\lambda_1)\left(f_2^2 - f_1 f_3 + \omega f_5\right) & \\
\qquad - Da(1+\lambda_1) f_2 - \dfrac{M(1+\lambda_1)\left[(1+\beta_e\beta_i) f_2 + \beta_e f_5\right]}{\left[(1+\beta_e\beta_i)^2 + \beta_e^2\right]}\Big] & f_4(0) = \xi_2 \\
f_5' = f_6 & f_5(0) = 0 \\
f_6' = f_7 & f_6(0) = \xi_3 \\
f_7' = \dfrac{1}{\beta_1 f_1}\Big[(1+\lambda_1)(f_1 f_6 - f_2 f_5 + \omega f_2) + f_7 - \beta_1 f_3 f_6 & \\
\qquad - Da(1+\lambda_1) f_5 + \dfrac{M(1+\lambda_1)(\beta_e f_2 - (1+\beta_e\beta_i) f_5)}{\left[(1+\beta_e\beta_i)^2 + \beta_e^2\right]}\Big] & f_7(0) = \xi_4 \\
f_8' = f_9 & f_8(0) = 1 \\
f_9' = \dfrac{-1}{1 + R_n\left(1 + (\theta_r - 1) f_8\right)^3}\Big[Pr\Big(f_1 f_9 + Nb f_9 f_{11} + Nt f_9^2 & \\
\qquad + Q_h f_8 + \dfrac{ME_c(f_2^2 + f_5^2)}{(1+\beta_e\beta_i)^2 + \beta_e^2} + \dfrac{Ec}{(1+\lambda_1)}\Big(f_3^2 + f_6^2 & \\
\qquad\qquad + \beta_1(f_2 f_3^2 - f_1 f_3 f_4 + f_2 f_6^2 - f_1 f_6 f_7)\Big)\Big) & \\
\qquad + R_n\left[3(\theta_r - 1)(1 + (\theta_r - 1) f_8)^2 f_9^2\right]\Big] & f_9(0) = \xi_5 \\
f_{10}' = f_{11} & f_{10}(0) = 1 \\
f_{11}' = -Sc f_1 f_{11} - \dfrac{Nt}{Nb} f_9' + CrSc f_{10} & f_{11}(0) = \xi_6
\end{cases}
\tag{7.58}
$$

where $\xi_1, \xi_2, \xi_3, \xi_4, \xi_5$, and ξ_6 represent unknown initial conditions.

This system is then numerically solved using the sixth-order Runge-Kutta (RK6) method. The RK6 algorithm is particularly effective for solving highly non-linear ODEs due to its superior accuracy and stability properties. In this process, the missing initial conditions $\xi_1, \xi_2, \xi_3, \xi_4, \xi_5$, and ξ_6 are iteratively estimated. The iterative scheme updates these shooting parameters by minimizing the residuals at the boundary through a root-finding algorithm. Convergence is achieved when the computed values satisfy the asymptotic boundary conditions in a sufficiently large domain with a prespecified tolerance. In this study, a step size of 0.1 and a convergence tolerance of 10^{-6} are used throughout the domain to ensure numerical stability and precision.

All computations are carried out using Python, an open source high-level programming language that provides robust numerical libraries suitable for scientific computing. The modularity and flexibility of Python enable efficient coding, result visualization, and parametric analysis of the governing model.

7.4 Results and Discussion

7.4.1 Validation of the Numerical Method

To ensure the reliability and accuracy of the numerical scheme developed based on the sixth-order Runge-Kutta method (RK6) with the shooting technique, a comparative validation is carried out against benchmark studies available in the literature. Specifically, the present results for the reduced Nusselt number $Nu_r = -\theta'(0)$ and the reduced Sherwood number $Sh_r = -\phi'(0)$ are compared with the results obtained by Khan and Pop [1], who employed an implicit finite difference method, and Goyal and Bhargava [216], who used the finite element method. The comparison is performed for various values of the thermophoresis parameter N_t, while other parameters are kept fixed. As presented in Table 7.2, the computed values of both $-\theta'(0)$ and $-\phi'(0)$ using the RK6 method are in excellent agreement with those reported in the literature, with only negligible numerical discrepancies. This high level of agreement strongly validates the accuracy, consistency, and robustness of the present computational approach, thereby confirming its suitability for solving the complex coupled nonlinear boundary layer equations arising in the current physical model involving magnetic nanofluid flow with multiple considerations beyond classical effects.

Table 7.2: Comparison of Nu_r and Sh_r with N_t for $Pr = Le = 10$, $Nb = 0.1$, and $Ec = Cr = Da = \lambda_1 = V_0 = Rn = Qh = M = \beta_i = \omega = \theta_r = \beta_1 = \beta_e = 0$

N_t	$-\theta'(0)$			$-\phi'(0)$		
	Khan and Pop [1]	Goyal and Bhargava [216]	Present (RK6)	Khan and Pop [1]	Goyal and Bhargava [216]	Present (RK6)
0.1	0.9524	0.95248	0.95236251	2.1294	2.12922	2.12928802
0.2	0.6932	0.69329	0.69317135	2.2740	2.27389	2.27384176
0.3	0.5201	0.52020	0.52008359	2.5286	2.52857	2.52837316
0.4	0.4026	0.40271	0.40259044	2.7952	2.79516	2.79481371
0.5	0.3211	0.32117	0.32106763	3.0351	3.03350	3.03469089

7.4.2 Profiles of Velocity, Temperature and Nanoparticle Concentration with Prominent Flow Parameters

This section presents a detailed numerical investigation of the steady MHD flow of Jeffrey nanofluids over a permeable surface, incorporating Hall and ion slip phenomena, fluid rotation, nonlinear thermal radiation, viscous dissipation, Joule heating, internal heat generation/absorption, and chemical reactions. The boundary-layer governing equations, formulated using appropriate similarity transformations, were solved numerically using the sixth-order Runge-Kutta shooting method. The discussion elaborates on the influence of key physical parameters: Hall current (β_e), ion slip effect (β_i), relaxation time parameter (λ_1), Deborah number (β_1), rotation parameter (ω), suction parameter (V_0), non-linear radiation (Rn), temperature ratio (θ_r), Eckert number (Ec), and chemical reaction parameter (Cr) on stream-wise and span-wise velocity profiles, temperature distribution, and nanoparticle concentration.

To conduct the numerical simulations, the dimensionless parameters are assigned the following fixed baseline values: $\lambda_1 = 0.5$, $\beta_1 = 0.5$, $Da = 0.5$, $\omega = 1$, $V_0 = 1.5$, $M = 5$, $\beta_e = 2$, $\beta_i = 1$, $Pr = 7$, $R_n = 0.5$, $\theta_r = 1.2$, $Q_h = 0.5$, $Ec = 0.1$, $N_b = 0.1$, $N_t = 0.1$, $Sc = 10$, $Cr = 0.1$ These values are maintained constant throughout the analysis unless a specific parameter is intentionally varied to examine its influence, as indicated in the respective figure captions and discussions. The ranges of parameters used in the study are as follows: $1 \leq M \leq 7$, $2 \leq \beta_e \leq 10$, $1 \leq \beta_i \leq 4$, $0.5 \leq \lambda_1 \leq 2$, $0.5 \leq \beta_1 \leq 0.8$, $1 \leq \omega \leq 4$, $0.5 \leq V_0 \leq 2$, $0.5 \leq R \leq 1.1$, $1.2 \leq \theta_r \leq 1.8$, $0.1 \leq Ec \leq 1.3$, $0.1 \leq C_r \leq 3$, and $2 \leq Pr \leq 7$.

Figs. 7.2 − 7.6 illustrate the behavior of the stream-wise (principal) velocity component under the influence of several key parameters.

Fig. 7.2 illustrates the variation of the principal velocity $f'(\eta)$ with the magnetic parameter (Hartmann number, M). It is observed that $f'(\eta)$ decreases as M increases. Physically, the imposition of a transverse magnetic field generates a Lorentz force that opposes the motion of the conducting Jeffrey nanofluid. This resistive force enhances the overall drag and suppresses the fluid momentum, thereby reducing $f'(\eta)$.

As depicted in Fig. 7.3, an increase in the Hall current improves the principal velocity. This is due to the induced secondary currents which alter the Lorentz force distribution, reducing the electromagnetic drag along the primary flow direction.

Similarly to the Hall current, an increase in the ion slip parameter (β_i) as illustrated in Fig. 7.4 facilitates fluid motion by modifying the current density and reducing magnetic resistance, thus enhancing the principal velocity.

Increasing values of the relaxation time parameter (λ_1), a characteristic of the Jeffrey fluid model, are observed to diminish the principal velocity profile. This behavior arises from an enhanced resistance introduced by the viscoelastic nature of the fluid, which counteracts momentum development due to internal molecular memory effects. Hence, as shown in Fig. 7.5, a higher λ_1 effectively delays velocity propagation through the fluid layers.

In contrast, an increase in the Deborah number (β_1) leads to an enhancement in the x-direction velocity as guaranteed in Fig. 7.6. Since β_1 quantifies the ratio of fluid elasticity to its relaxation time, larger values denote a stronger elastic response in the Jeffrey fluid, promoting velocity amplification due to elastic energy storage and subsequent release along the streamlines. This enhances the flow acceleration beyond viscous limitations.

Fig. 7.7 showed that increasing the rotation parameter (ω) induces Coriolis forces that deflect the flow direction, resulting in a suppression of the principal velocity due to the diversion of momentum into the transverse direction.

In general, the streamwise (principal) velocity profile is governed by a balance between electromagnetic, elastic, rotational, and permeability effects. Hall and ion slip promote axial motion, while viscoelastic relaxation and rotation hinder it. These observations underscore the need for precise control of such parameters in practical MHD applications involving viscoelastic nanofluids.

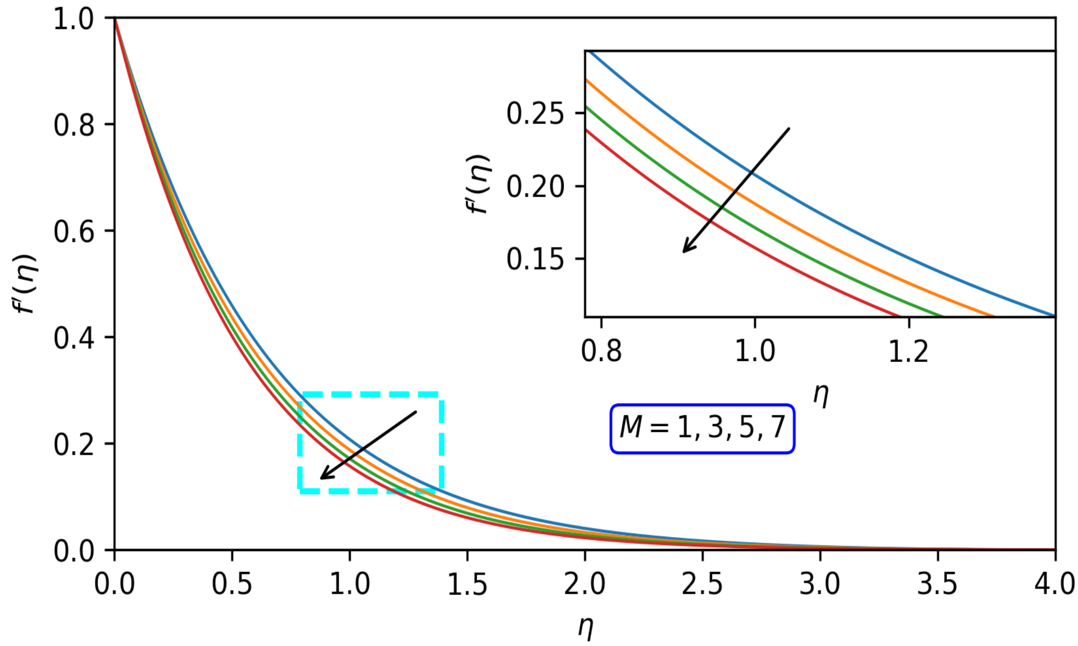

Figure 7.2: Principal velocity profiles with magnetic parameter M.

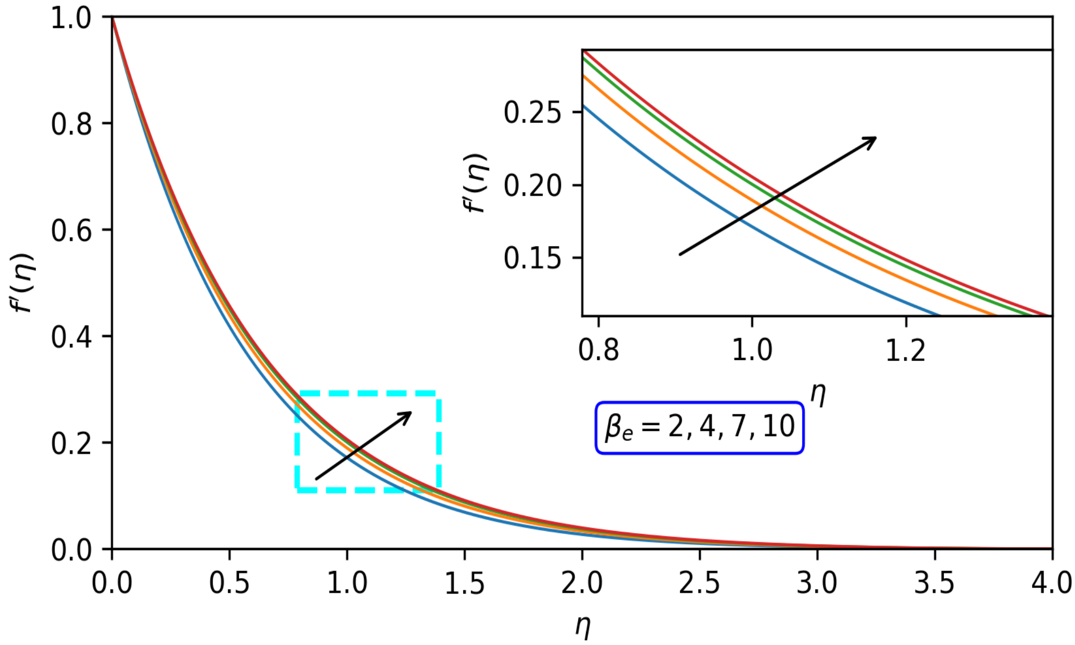

Figure 7.3: Principal velocity profiles with Hall parameter β_e.

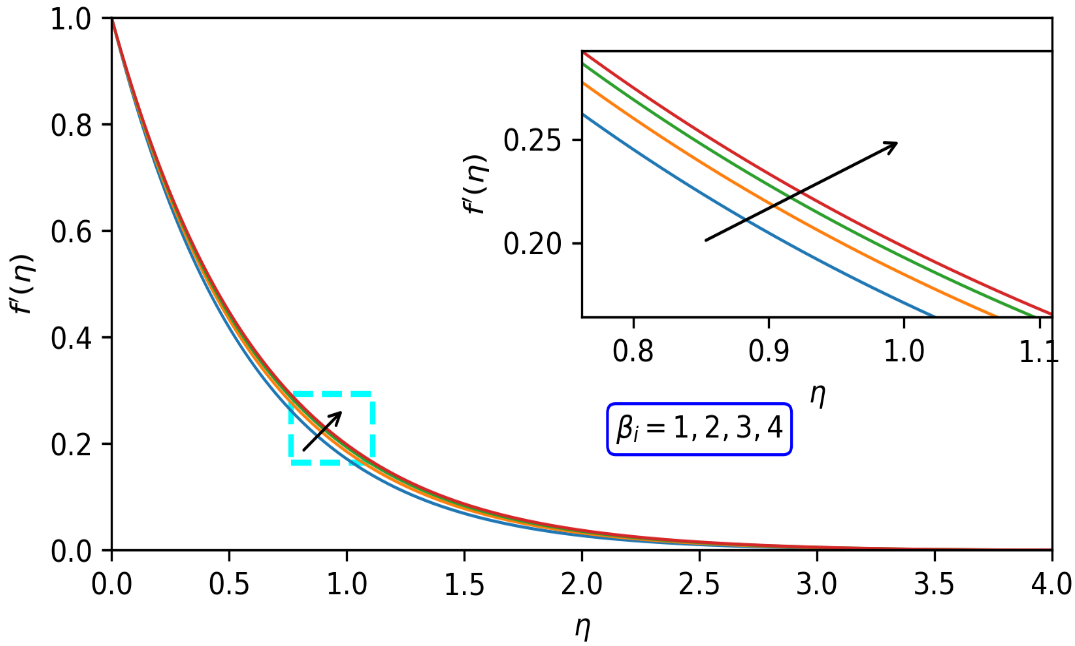

Figure 7.4: Streamwise velocity profiles with ion slip parameter β_i.

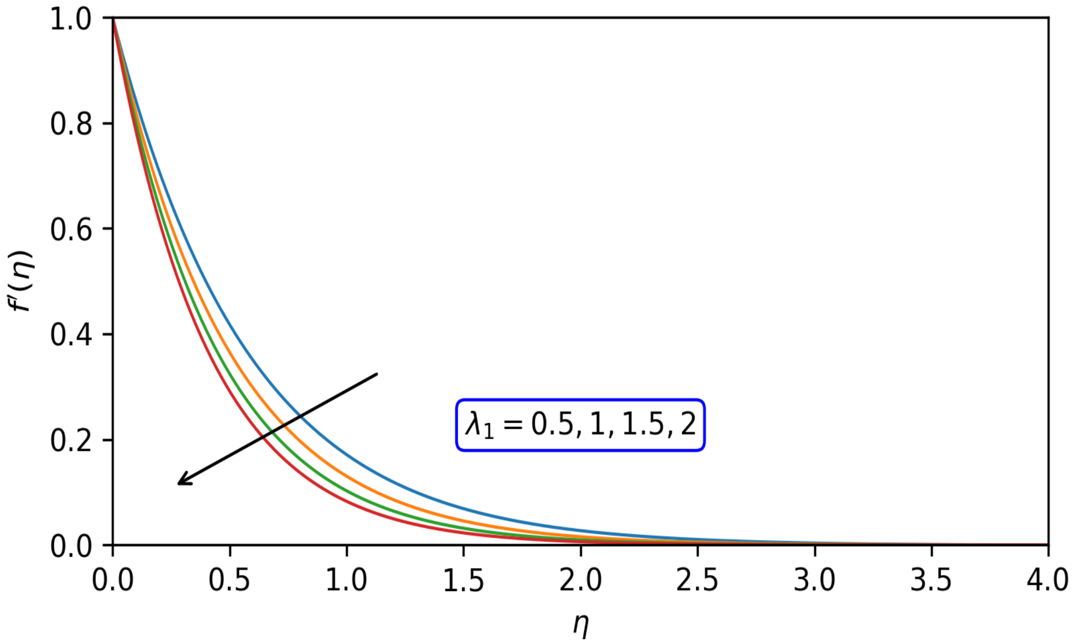

Figure 7.5: Principal velocity profiles with λ_1.

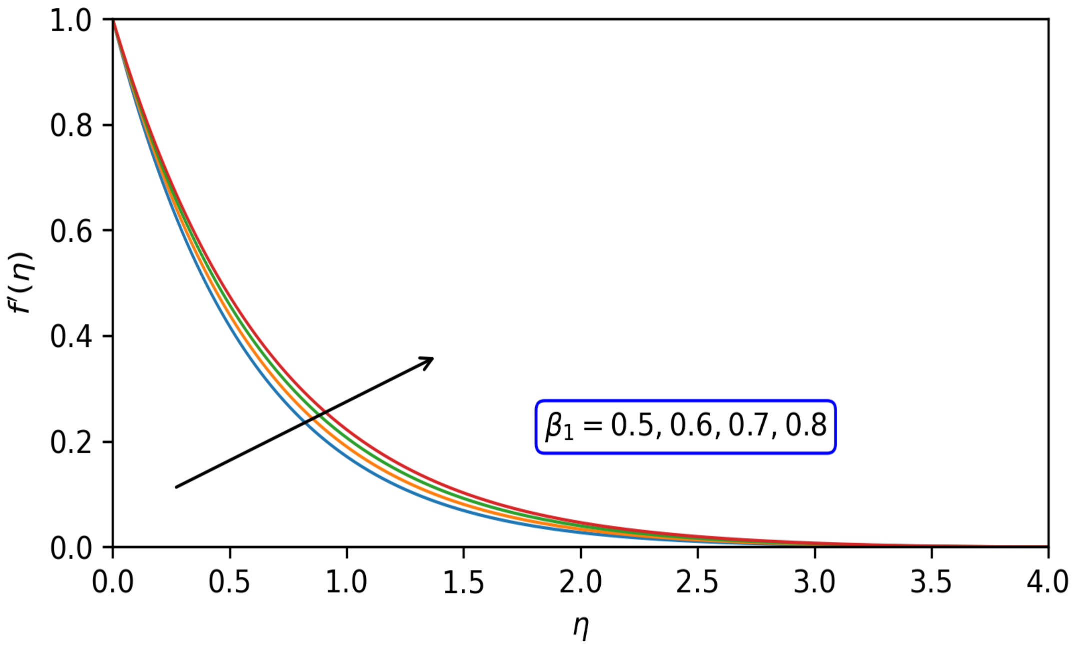

Figure 7.6: Principal velocity profiles with Deborah number β_1.

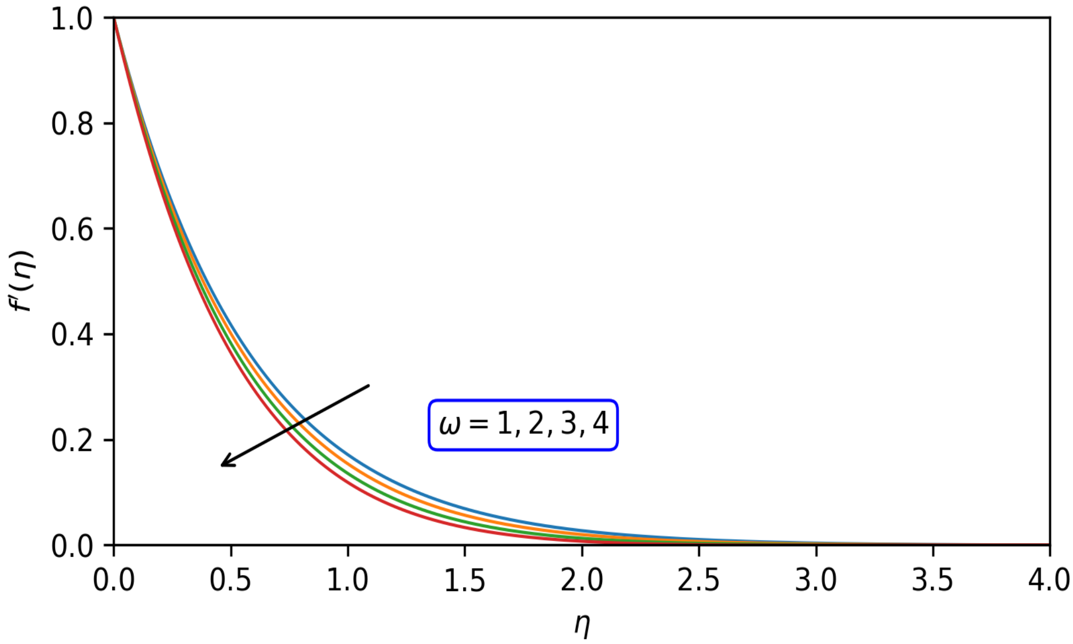

Figure 7.7: Principal velocity profiles with rotation parameter ω.

Figs. 7.8–7.11 exhibit the trends in the spanwise (z-direction) velocity. As depicted in Fig. 7.8, an increasing trend in λ_1 introduces fluid memory effects that resist velocity in all directions, thus reducing secondary velocity.

Interestingly, an elevated Deborah number (β_1) improves the secondary velocity as indicated in Fig. 7.9. As elasticity becomes dominant over viscous forces, the stored elastic energy promotes deformation and lateral fluid motion.

The fluid rotation, quantified by ω, significantly elevates the secondary velocity as displayed in Fig. 7.10. Unlike the stream-wise direction, rotation tends to increase secondary velocity by transferring some of the flow momentum from the x-direction into the z-direction due to Coriolis acceleration.

The suction parameter (V_0) shown in Fig. 7.11, on the other hand, acts as a stabilizing mechanism by extracting fluid from the domain, thus reducing the lateral expansion. Increased suction results in lower spanwise velocities, effectively damping out perturbations and confining the flow closer to the wall. These findings are essential for managing flow stability in rotating MHD systems.

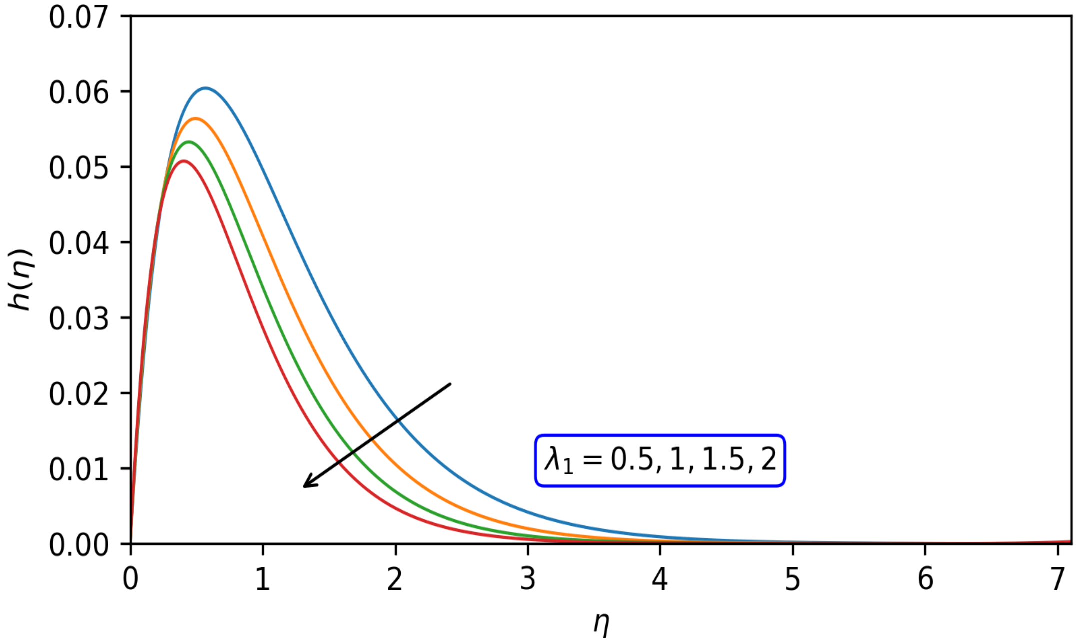

Figure 7.8: Secondary velocity profiles with λ_1.

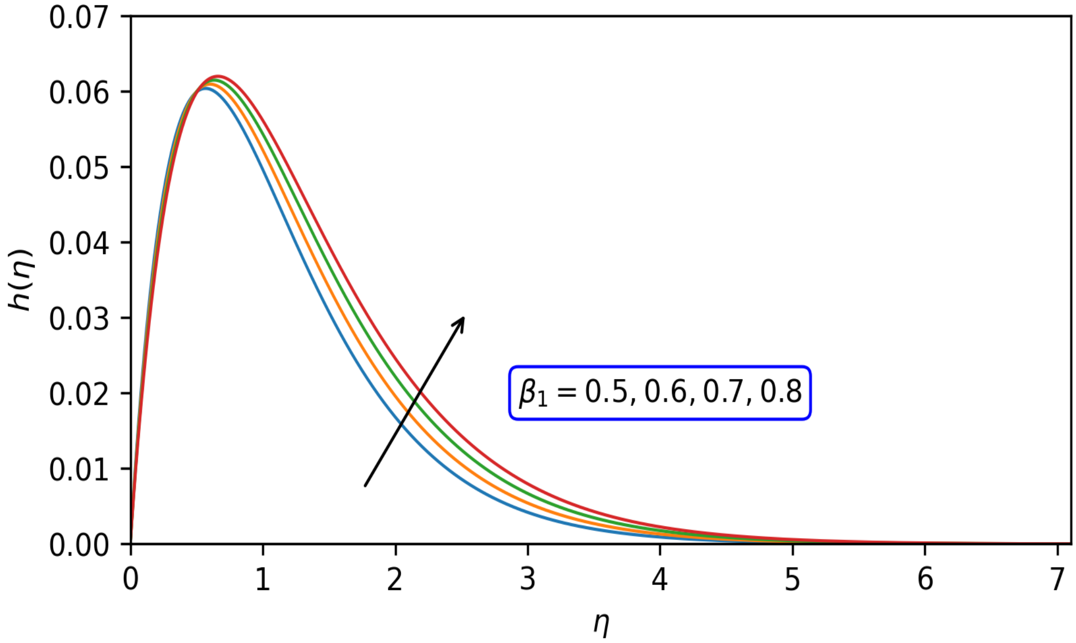

Figure 7.9: Secondary velocity profiles with Diborah number ($beta_1$).

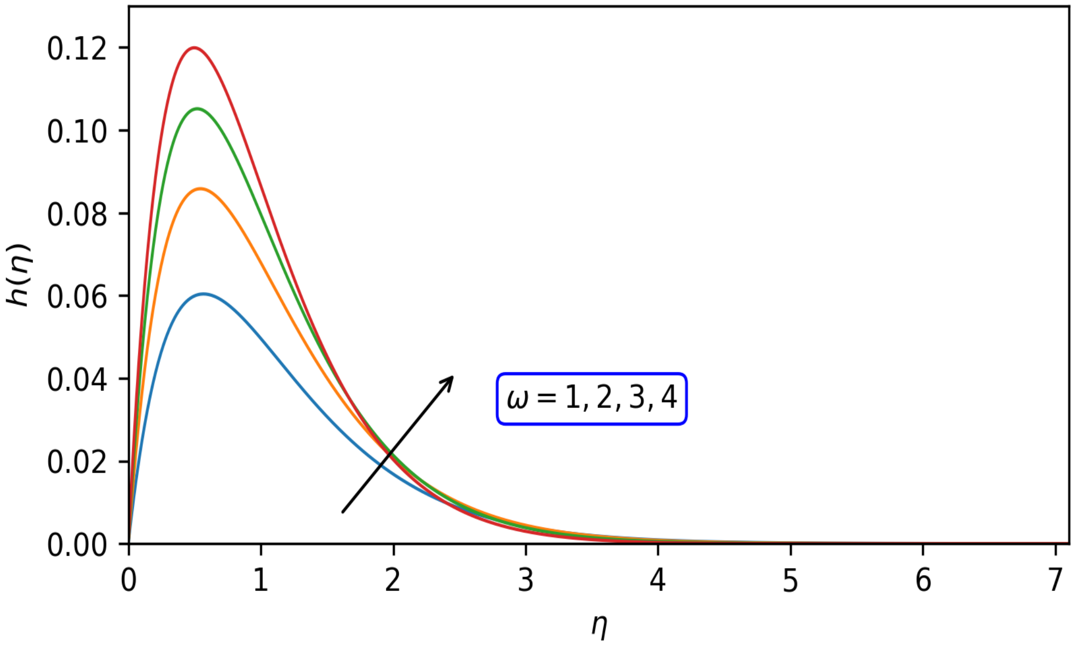

Figure 7.10: Secondary velocity profiles with rotation parameter (ω).

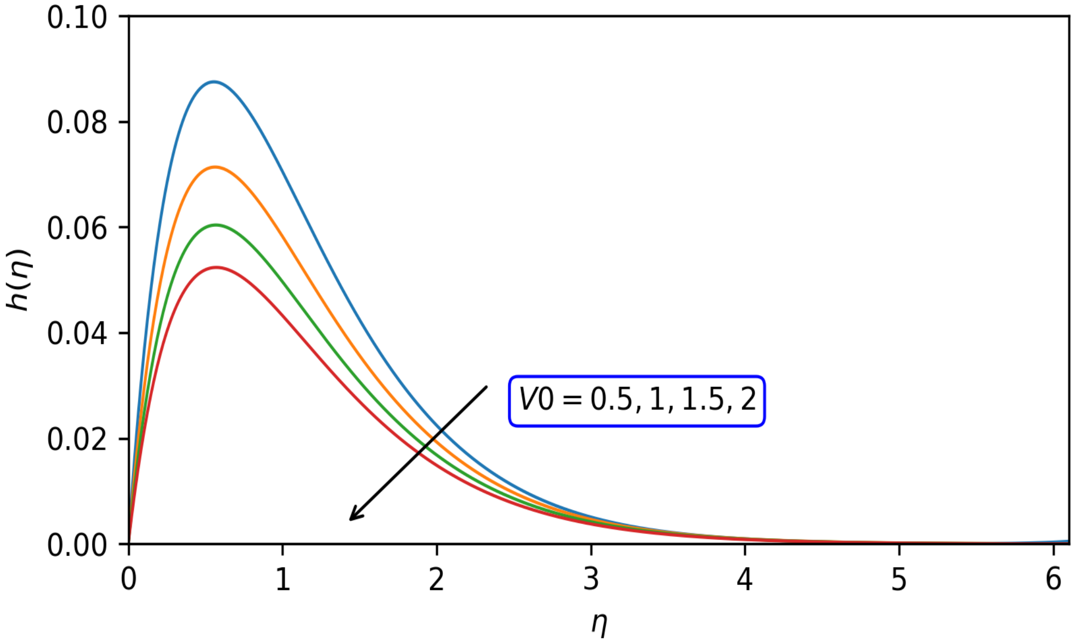

Figure 7.11: Secondary velocity profiles with suction parameter (V_0).

The behavior of the thermal boundary layer is significantly influenced by multiple interacting physical mechanisms, as shown in Figs. 7.12–7.17.

The temperature distribution $\theta(\eta)$ within the boundary layer is enhanced by an increase in the Hartmann number (M), as clearly shown in Fig. 7.12. The rise in temperature is a direct and logical consequence of the velocity damping. The work done by the Lorentz force in opposing the fluid motion is converted into thermal energy through a process known as Joule dissipation or Ohmic heating. This constitutes an additional internal heat source within the fluid medium. As M increases, the stronger Lorentz force does more work against the motion of the fluid, generating more Joule heating. This injects additional thermal energy into the system.

Figs. 7.13 and 7.14 portray that the Hall (β_e) and ion slip (β_i) parameters contribute to a decline in the fluid temperature. These electromagnetic effects reduce the intensity of induced currents, and hence Joule heating, which is a source of thermal energy in MHD flows.

Radiative heat transfer is significantly affected by the non-linear radiation parameter (Rn) and the temperature ratio (θ_r) as provided graphically in Figs. 7.15 and 7.16, respectively. Both parameters are shown to enhance fluid temperature. The non-linear radiation term accounts for the strong dependence of radiative heat flux on temperature, particularly in high-energy systems. Similarly, a larger wall-to-ambient temperature difference (θ_r) increases thermal gradients, promoting radiative heat inflow.

Viscous dissipation, represented by the Eckert number (Ec), also causes a noticeable rise in fluid temperature as presented in Fig. 7.17, which aligns with the study of Shahzad et al. [125]. As Ec increases, more kinetic energy is irreversibly converted into internal energy, heating the fluid layers. This phenomenon becomes more significant in high-speed or highly viscous flow conditions.

These temperature trends highlight the synergistic influence of electromagnetic suppression (via β_e, β_i) and dissipative amplification (via Ec, Rn) on the thermal behavior of nanofluids. Effective management of these parameters is crucial in thermal management systems such as cooling devices and radiative heat exchangers.

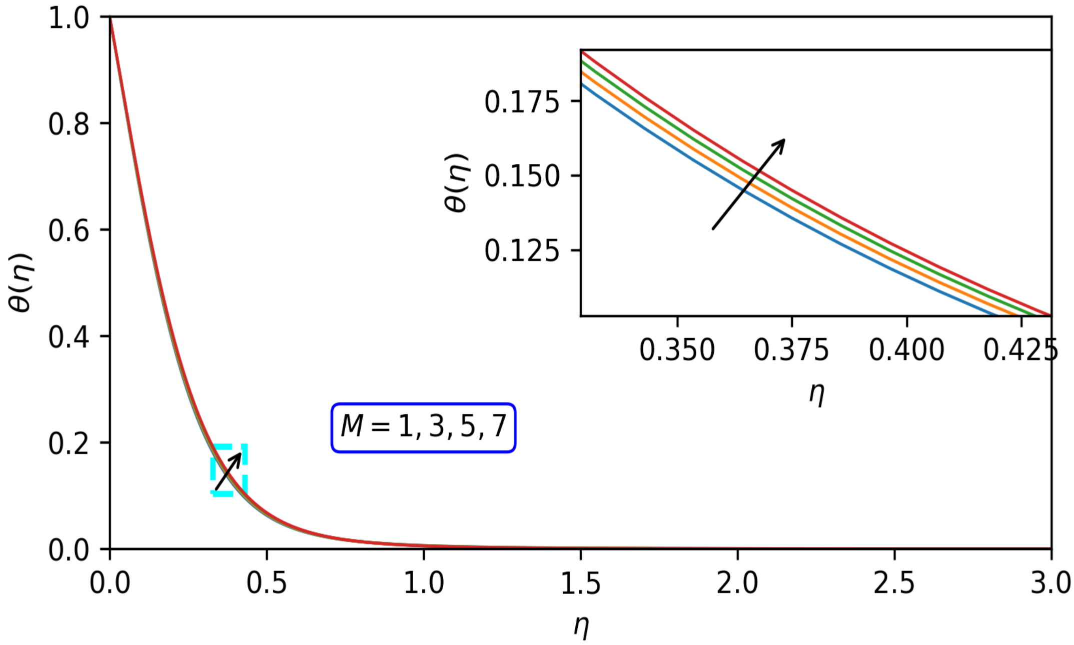

Figure 7.12: Temperature ($\theta(\eta)$) profiles for Hall parameter (β_e).

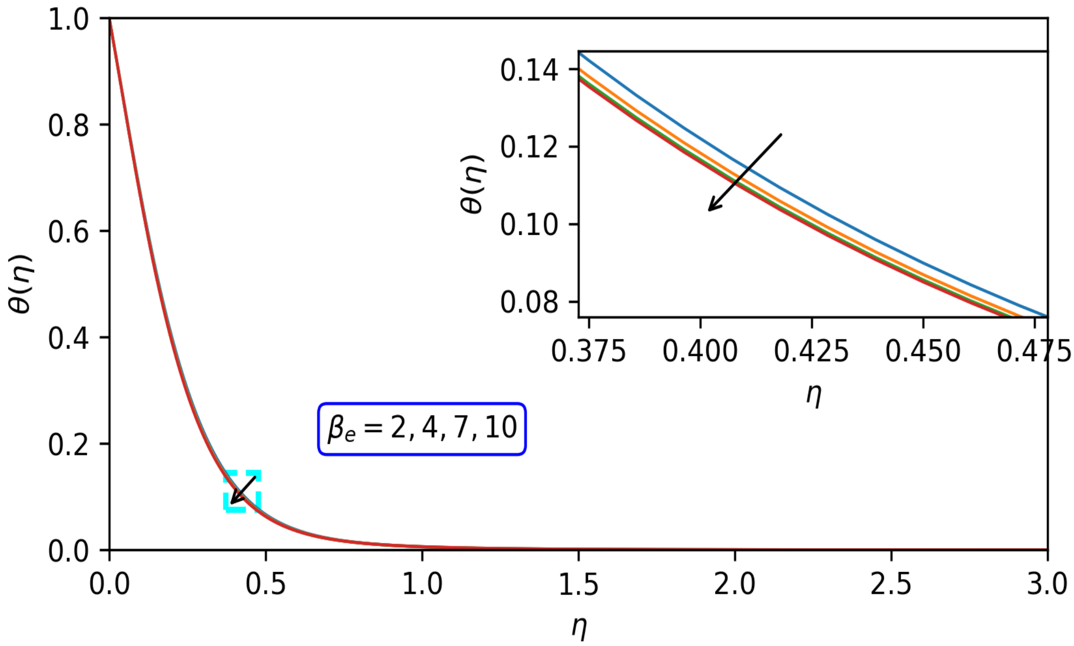

Figure 7.13: Temperature ($\theta(\eta)$) profiles for Hall parameter (β_e).

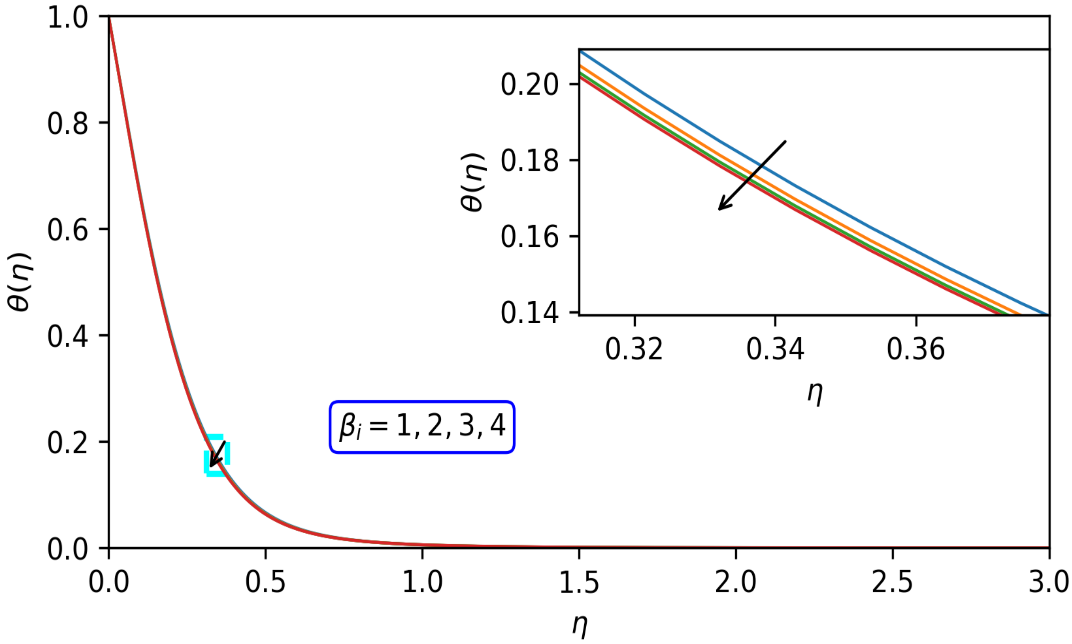

Figure 7.14: Temperature ($\theta(\eta)$) profiles for ion slip parameter (β_i).

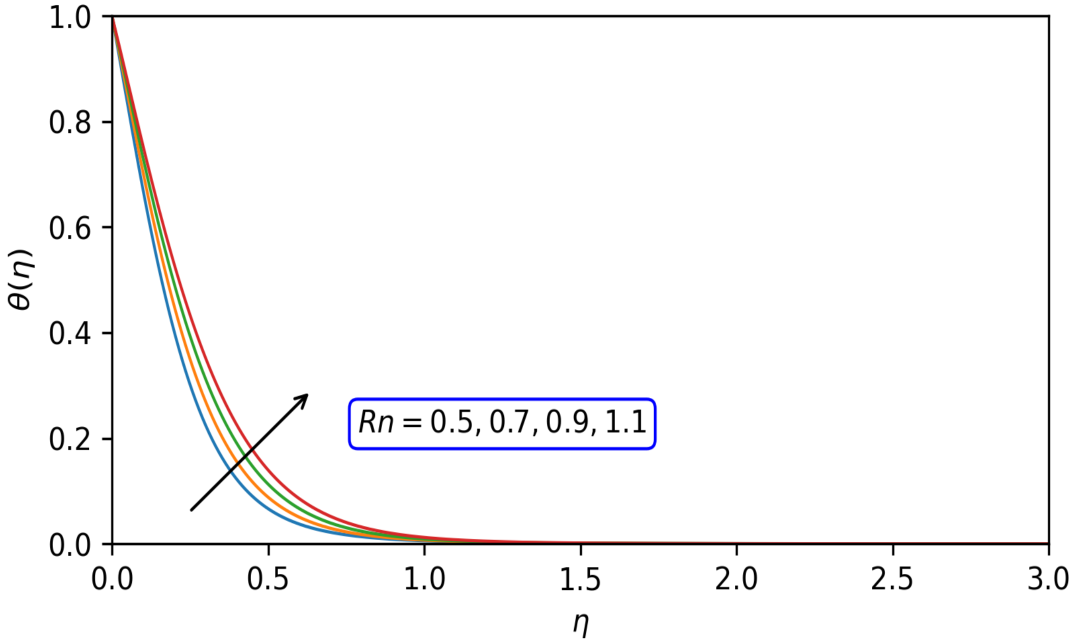

Figure 7.15: Temperature ($\theta(\eta)$) profiles for nonlinear thermal radiation parameter (Rn).

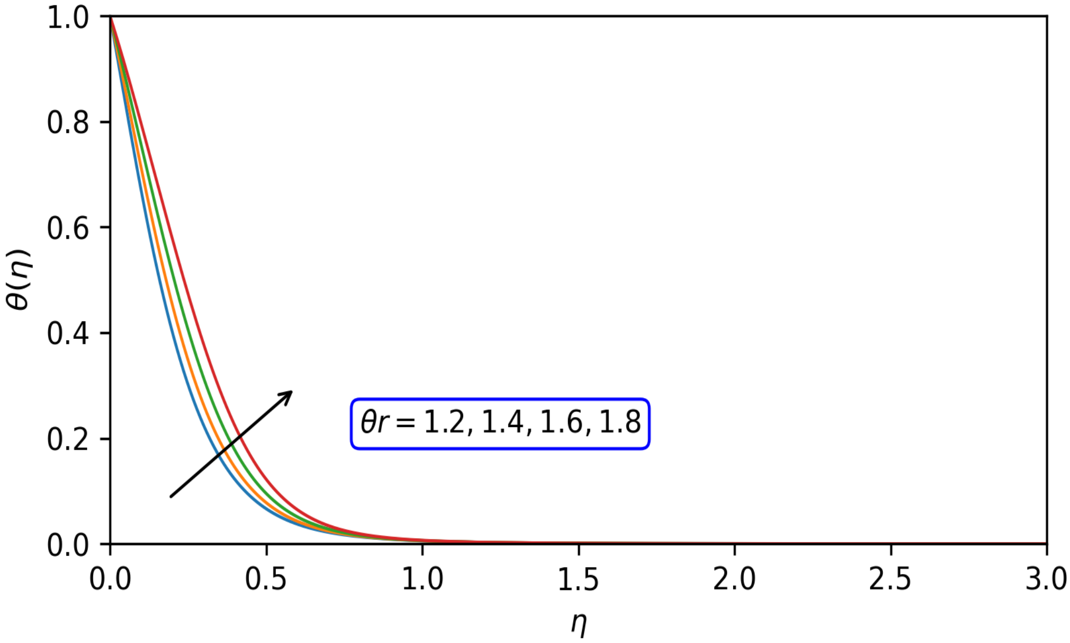

Figure 7.16: Temperature ($\theta(\eta)$) profiles for ratio of temperature parameter (θ_r).

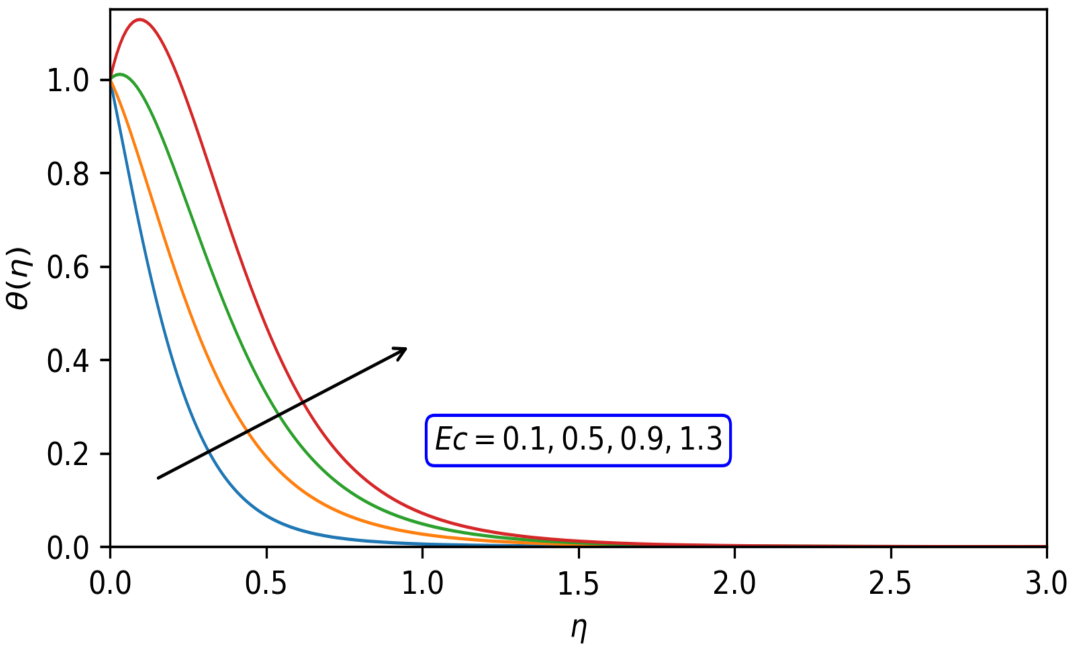

Figure 7.17: Temperature ($\theta(\eta)$) profiles for Eckert number(Ec).

Figs. 7.18 to 7.20 detail the variation in nanoparticle concentration across the boundary layer.

Figs. 7.18 and 7.19 illustrated that the Hall and ion slip parameters (β_e, β_i) are observed to lower concentration profiles. This reduction stems from diminished electromigration of nanoparticles, a consequence of reduced Lorentz forces under these conditions, leading to less effective particle transport toward the wall.

As illustrated in Fig. 7.20, increasing Cr intensifies the chemical reaction rate, consuming more nanoparticles in the reaction process, leading to a reduction in the concentration profile.

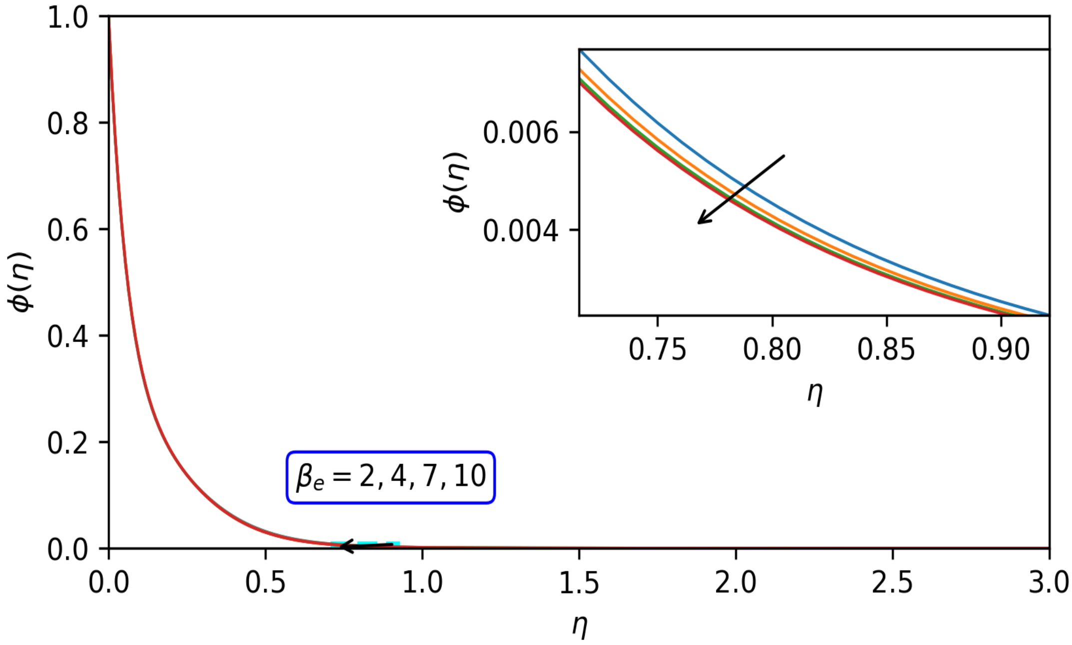

Figure 7.18: Nanoparticle concentration profiles for Hall parameter (β_e).

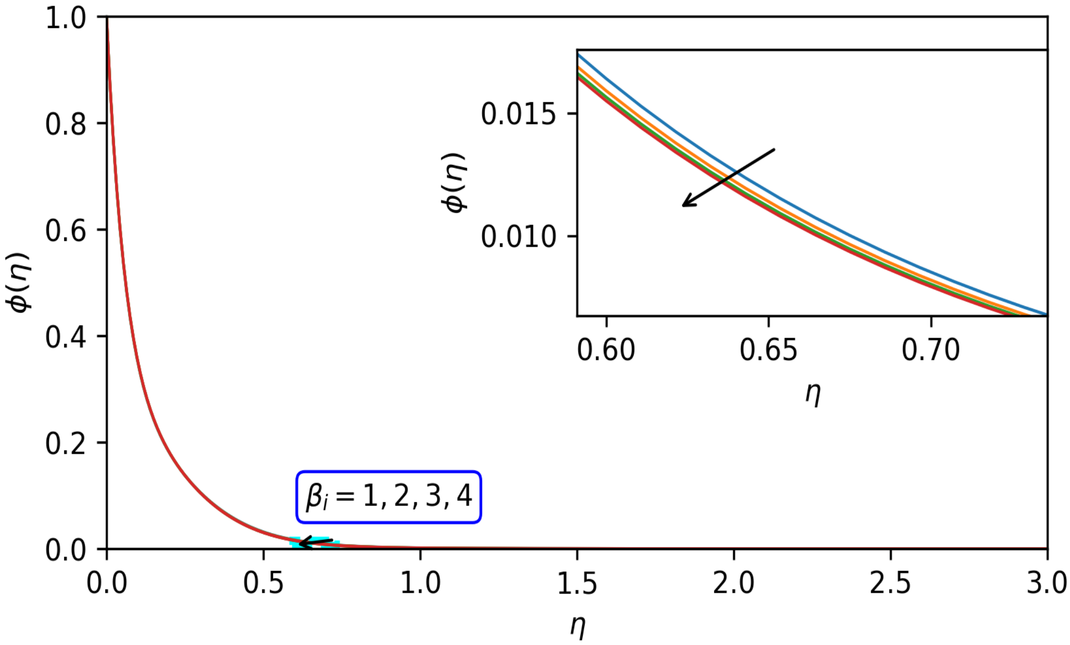

Figure 7.19: Nanoparticle concentration profiles for ion slip parameter (β_i).

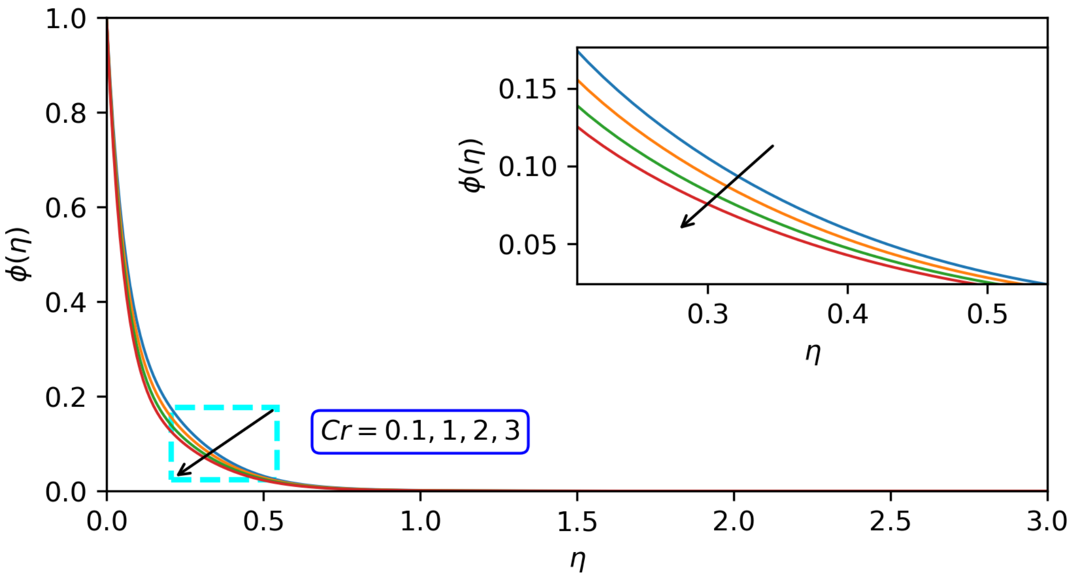

Figure 7.20: Nanoparticle concentration profiles for chemical reaction parameter (Cr).

The collective findings offer a comprehensive framework for optimizing engineering applications such as MHD power generation, nanofluid cooling systems, electrochemical reactors, and polymeric fluid processing. By carefully modulating the physical parameters, it becomes possible to tailor the flow and transport properties for specific industrial or biomedical applications.

7.4.3 Effects of Pertinent Flow Parameters on Skin Friction Coefficients, Nusselt Number and Sherwood Number

This subsection presents the numerical results and physical interpretations of the dimensionless engineering quantities: the skin friction coefficients in both x- and z-directions, the Nusselt number (rate of heat transfer), and the Sherwood number (rate of mass transfer). Tables 7.3 and 7.4 list the effects of varying different flow parameters on these quantities.

The skin friction coefficients in the stream-wise ($-C_{fx}\sqrt{Re}$) and spanwise ($C_{fz}\sqrt{Re}$) directions represent the shear stress exerted by the fluid on the surface. Table 7.3 outlines how various dimensionless parameters influence the skin friction coefficients. An increase in the Hall parameter (β_e) leads to a noticeable reduction in both x- and z-direction skin friction. Physically, this implies that the Hall current weakens the resistance of the fluid to the surface due to enhanced electromagnetic diffusion and reduced Lorentz drag. Similarly, increasing the ion slip parameter (β_i) results in decreased values for both stream-wise and transverse shear stresses, reinforcing the notion that ion slip effects diminish the influence of magnetic braking forces on fluid motion. On the other hand, an increase in the relaxation time parameter (λ_1) causes both components of the skin friction coefficients to rise. The enhanced relaxation time allows the Jeffrey fluid to gradually respond to imposed deformations, increasing shear stress on the wall. Contrastingly, a higher Deborah number (β_1) exhibits a decrease in shear stress, suggesting that at elevated β_1, elastic relaxation overcomes viscous resistance, leading to smoother fluid behavior on the wall. Furthermore, both the rotation parameter (ω) and the suction parameter (V_0) amplify the shear stresses significantly. The Coriolis force associated with rotation transfers angular momentum toward the wall, strengthening the velocity gradient, while suction adheres the fluid closer to the surface, thickening the boundary layer and consequently increasing friction. Lastly, a stronger magnetic field (M) elevates both skin friction coefficients due to intensified Lorentz forces that resist fluid motion and increase surface drag.

The local Nusselt number, expressed as $\left(\frac{Nu_x}{\sqrt{Re_x}}\right)$, quantifies the relative efficiency of convective to conductive heat transfer at the boundary surface. The analysis of the results, detailed in Table 7.4, reveals a pronounced sensitivity of this parameter to thermophysical, electromagnetic, and rheological influences. Specifically, the Nusselt number exhibits a positive correlation with the Hall current parameter, the ion slip parameter, the relaxation time (λ_1), and the Prandtl number, indicating enhanced heat transfer under these conditions. In contrast, it demonstrates an inverse relationship

Table 7.3: Numerical values of the skin friction coefficients of some values of parameters for $N_b = N_t = Ec = Cr = 0.1$, $Sc = 10$, $Da = \lambda_1 = V_0 = Rn = Qh = 0.5$, $Pr = 7$, $M = 5$, $Cr = 0.1$ $\beta_i = 1 = \omega$, $\theta_r = 1.2$, $\beta_1 = 0.5$ and $\beta_e = 2$.

β_e	β_i	λ_1	β_1	ω	V_0	M	$-C_{fx}\sqrt{Re}$	$C_{fz}\sqrt{Re}$
2							3.16833616	0.7985078
4							2.91476018	0.72968286
7							2.78354335	0.67418624
	1						3.16833616	0.7985078
	2						3.01071729	0.63954400
	3						2.90985103	0.58548169
		0.5					1.90100169	0.47910468
		1					2.35243085	0.56478752
		1.5					2.78524482	0.64144504
			0.5				3.97568843	1.04084906
			0.6				3.63558826	0.95520047
			0.7				3.36564329	0.88745159
				1			3.16833616	0.79850780
				2			3.26994636	1.20380100
				3			3.38887069	1.57291957
					0.5		2.19332358	0.68538670
					1		2.67992498	0.75258852
					1.5		3.16833616	0.79850780
						2	2.83179109	0.66140758
						3	2.94792556	0.70897169
						5	3.16833616	0.79850780

with the Deborah number (β_1), the nonlinear thermal radiation parameter, the temperature ratio parameter, the Eckert number, and the chemical reaction parameter, reflecting a suppression of thermal transport efficiency as these parameters intensify. The increased Hall and ion slip parameters marginally enhance the Nusselt number, indicating improved convective heat transfer. These phenomena likely occur due to thinning of the thermal boundary layer, as Joule heating is mitigated by electromagnetically induced flow alterations. An increase in the relaxation time parameter (λ_1) enhances the Nusselt number (Nu_x), as dominant elastic effects promote a thinner thermal boundary layer by storing deformation energy, which steepens the temperature gradient near the wall. Conversely, an increase in the Deborah number (β_1) results in a decrease in heat transfer, as the heightened viscous retardation character intensifies internal dissipation, leading to a thicker thermal boundary layer and a reduced temperature gradient. Similarly, both the non-linear thermal radiation parameter (Rn) and the temperature ratio parameter (θ_r) dramatically reduce the Nusselt number, confirming that intense radiative heating elevates the bulk fluid temperature and thereby reduces the temperature gradient near the surface. An increase in the Eckert number (Ec) intensifies both viscous dissipation and ohmic heating, generating substantial internal thermal energy that elevates the bulk fluid temperature. This thermal saturation effect reduces the temperature gradient at the wall, thereby suppressing the wall-to-fluid heat flux and diminishing the Nusselt number as internal energy conversion progressively overpowers conductive heat transfer. Additionally, the chemical reaction parameter (Cr) slightly lowers the Nusselt number, reflecting the influence of endothermic processes that absorb heat during chemical transformation. In contrast, the Prandtl number (Pr) exhibits a positive correlation with the Nusselt number (Nu_x). Higher Pr values, which correspond to lower thermal diffusivity, promote the development of thinner thermal boundary layers and improve the efficiency of convective heat transfer, thus increasing the rate of surface heat transfer.

The Sherwood number $\left(\frac{Sh_x}{\sqrt{Re_x}}\right)$ quantifies the convective mass transfer of nanoparticles at the surface. Parametric variations, as shown in Table 7.4, yield insightful trends in the dynamics of mass transport under the effects of MHD. Increasing β_e and β_i slightly decreases the Sherwood number, indicating a reduction in the flux of nanoparticles to the wall. The diminished Lorentz force, due to Hall and ion slip effects, weakens the electromigration of nanoparticles, thus lowering concentration gradients near the wall. Additionally, an increase in the relaxation time parameter (λ_1) slightly reduces mass transfer, suggesting improved particle retention in the region near the wall due to slow response time. In contrast, a rising Deborah number (β_1) enhances the Sherwood number, highlighting the role of elastic turbulence in dispersing nanoparticles more effectively. Furthermore, elevated values of the radiation parameter (Rn) and the temperature ratio (θ_r) significantly increase the Sherwood number, indicating that the thermophoretic effects induced by radiative heating stimulate the migration of nanoparticles toward cooler regions. Moreover, Eckert number (Ec) positively influences Sherwood number, consistent with enhanced thermophoretic forces due to viscous heating. This facilitates the transport of the nanoparticle away from high-temperature zones. In particular, increasing the chemical reaction parameter (Cr) substantially increases the Sherwood number, which can be attributed to reaction-induced consumption of nanoparticles near the wall, intensifying the concentration gradient. However, elevated values of the Prandtle number (Pr) correspond to a reduction in the Sherwood number, as the dominance of momentum diffusivity over species diffusivity hinders effective mass transport.

Table 7.4: Numerical values of the rate of heat transfer $\left(1 + R_n\theta_r^3\right)\theta'(0)$ and rate of mass transfer $(-\phi'(0))$ of some parameters values for $N_b = N_t = Ec = Cr = 0.1$, $Sc = 10$, $Da = \lambda_1 = V_0 = Rn = Qh = 0.5$, $Pr = 7$, $M = 5$, $Cr = 0.1$ $\beta_i = 1 = \omega$, $\theta_r = 1.2$, $\beta_1 = 0.5$ and $\beta_e = 2$.

β_e	β_i	λ_1	β_1	R_n	θ_r	Ec	C_r	Pr	$\frac{Nu_x}{\sqrt{Re_x}}$	$\frac{Sh_x}{\sqrt{Re_x}}$
2									6.04606990	12.79346594
4									6.15811855	12.74402886
7									6.21093330	12.72143243
	1								6.04606990	12.79346594
	2								6.13174781	12.75503881
	3								6.17509645	12.73621105
		0.5							6.04606990	12.79346594
		1							6.08202549	12.75242133
		1.5							6.10545419	12.72118625
			0.5						6.04606990	12.79346594
			0.6						6.03029116	12.81019399
			0.7						6.01511331	12.82515169
				0.5					8.28804603	12.79346594
				0.7					7.38371316	13.13269272
				0.9					6.66566830	13.40008901
					1.2				9.88649198	12.79346594
					1.4				8.25985220	13.31259150
					1.6				6.81623157	13.76932880
						0.1			6.04606990	12.79346594
						0.5			2.51766691	14.61629399
						0.9			-1.27727201	16.57940255
							0.1		6.04606990	12.79346594
							1		6.00695199	13.72260081
							2		5.97130297	14.62741222
								2	2.27534221	14.66990932
								5	4.81396369	13.42114615
								7	6.04606990	12.79346594

In conclusion, the analysis of skin friction, the Nusselt number, and the Sherwood number provides a comprehensive understanding of the momentum, thermal, and mass transport behaviors of MHD Jeffrey nanofluids over permeable rotating surfaces. Skin friction is notably influenced by Hall/ion slip, viscoelastic, and rotational effects, while convective heat and mass transfer respond significantly to electromagnetic, radiative, and chemical parameters. These findings are instrumental in optimizing heat and mass transfer devices, including MHD generators, rotating thermal exchangers, and nanofluid-based solar energy systems.

7.5 Conclusion

The present chapter offers a comprehensive numerical investigation of the rotating MHD flow of a Jeffrey nanofluid induced by a permeable stretching surface, encompassing a broad spectrum of influential physical effects.

The system of nonlinear ordinary differential equations resulting from similarity transformations was solved numerically using the sixth-order Runge-Kutta method with a shooting technique, implemented in Python programming. The convergence and stability of the algorithm were ensured by iteratively adjusting the initial guesses to satisfy the boundary conditions at infinity.

Key findings from the numerical simulations can be summarized as follows.

- The stream-wise velocity increases with Hall current, ion slip, and Deborah number but decreases with rotation and the relaxation parameter.
- The spanwise velocity increases with the Deborah number and rotation parameter but decreases with the relaxation time and suction parameters.
- Thermal profiles decrease with Hall and ion slip effects but increase significantly with effects of nonlinear thermal radiation, temperature ratio, and Eckert number.
- The nanoparticle concentration decreases with stronger Hall and ion slip currents and chemical reaction rates.
- Skin friction coefficients in both x- and z-directions increase with magnetic field strength, relaxation time, and suction, while Deborah number, Hall and ion slip reduce wall shear stress.
- The local Nusselt number (heat transfer rate) increases with Hall current, ion slip, relaxation time, and Prandtl number but decreases with Deborah number, nonlinear thermal radiation, temperature ratio, Eckert number, and chemical reaction. Conversely, the Sherwood number exhibits opposite dependencies, increasing with the Deborah number, radiation, temperature ratio, Eckert number, and chemical reaction, but decreasing with Hall current, ion slip, relaxation time, and Prandtl number.

The overall analysis reveals that magneto-rotational and non-Newtonian effects, along with suction control mechanisms, play a critical role in modulating flow, thermal, and concentration behaviors. The observed sensitivity to physical parameters offers practical insights for optimizing cooling systems, energy conversion devices, and magnetic-targeted drug delivery where advanced nanofluid models are applicable.

Chapter 8

Conclusions, Recommendations and Future Works

This dissertation presents a comprehensive theoretical and numerical investigation of MHD Non-Newtonian nanofluid flow over a stretching sheet, with particular emphasis on the combined effects of Hall current and ion slip. Four distinct non-Newtonian fluid models—namely Williamson, Casson, tangent hyperbolic, and Jeffrey fluids—are examined to elucidate the complex interactions between electromagnetic forces, fluid rheology, and transport phenomena. The analysis further incorporates the effects of nonlinear thermal radiation, chemical reaction, viscous dissipation, Joule heating, internal heat generation or absorption, system rotation, and porous medium permeability, thereby providing a unified and detailed understanding of the underlying flow, heat transfer, and mass transport mechanisms.

This chapter is organized as follows: the first section presents the main conclusions drawn from the present study, the second section outlines recommendations based on the key findings, and the third section discusses potential directions for future research.

8.1 Conclusions

The principal findings of the present investigation are summarized as follows.

- Across all considered fluid models, Hall current and ion slip effects enhance streamwise momentum transfer, while suppressing thermal and nanoparticle transport due to their interaction with the Lorentz force.
- Elevated values of the Williamson fluid parameter lead to a progressive

advancement in the temperature and concentration distributions, accompanied by a reduction in the velocity profiles.

- An increase in the Casson parameter results in a diminishing effect on the primary velocity component.
- For tangent hyperbolic fluids, the power-law index, suction velocity, Weissenberg number, and rotation parameter contribute to reductions in the velocity profiles.
- Fluid elasticity, represented by the Deborah number (β_1), enhances both principal and transverse velocity components.
- The temperature field increases with nonlinear thermal radiation, temperature ratio, Eckert number, power-law index, rotation parameter, and Weissenberg number, while it decreases with Hall current, ion slip, suction, Casson parameter, and chemical reaction in various flow configurations.
- The nanoparticle concentration consistently decreases with increasing chemical reaction parameter.
- Primary skin friction is reduced by Hall current, ion slip, and Weissenberg number, whereas it is enhanced by the Casson parameter, magnetic field strength, and Darcy number.
- The skin friction coefficient in the x-direction increases with magnetic field strength, relaxation time, and suction velocity, while it decreases with increasing Deborah number, Hall current, and ion slip.
- The rate of heat transfer, characterized by the Nusselt number, increases with Hall current, ion slip, Casson parameter, nonlinear thermal radiation, temperature ratio, and power-law index, but decreases with magnetic field strength, Darcy number, chemical reaction parameter, and Eckert number for most fluid models.
- The rate of mass transfer increases with magnetic field strength, Darcy number, Schmidt number, Deborah number, and chemical reaction parameter, and decreases with Hall current, ion slip, suction, and the ratio of relaxation to retardation times in certain models.

In addition, a systematic quantitative assessment was performed to evaluate the sensitivity of different non-Newtonian fluid models to the magnetic parameter M. The influence of the applied magnetic field on the wall shear stress, $-f''(0)$, was examined for the Williamson, Casson, Tangent Hyperbolic, and Jeffrey fluid models over a wide range of magnetic strengths ($M = 0$–100). The corresponding results are presented in Table 8.1.

Table 8.1: Effect of the magnetic parameter M on the wall shear stress $-f''(0)$ for different non-Newtonian fluid models

M	Williamson	Casson	Tangent Hyperbolic	Jeffrey
0	1.00004793	0.70759669	1.00048363	1.06322305
5	2.44948974	1.73205081	2.44948974	1.75110070
10	3.31662479	2.34520788	3.31662479	2.13936544
50	7.14142843	5.04975247	7.14142843	3.65053020
100	10.1335910	7.10633520	10.53939201	4.65217223

The results indicate that the Williamson, Casson, and Tangent Hyperbolic fluid models exhibit strong sensitivity to the magnetic parameter, with the wall shear stress increasing by nearly ten times as M increases from 0 to 100. This behavior reflects a significant enhancement of flow resistance due to the intensification of the Lorentz force and highlights the strong magneto-responsive nature of shear-dependent non-Newtonian fluids. In contrast, the Jeffrey fluid model demonstrates a comparatively weaker response to variations in the magnetic parameter, with the wall shear stress increasing by approximately 4.4 times over the same range of M. This reduced sensitivity is attributed to the viscoelastic nature of the Jeffrey fluid, wherein elastic effects partially counteract magnetic damping.

Overall, the analysis confirms that the influence of the magnetic field on wall shear stress is strongly dependent on the rheological characteristics of the fluid. Shear-thinning and yield-stress-based Non-Newtonian fluids exhibit pronounced magnetic sensitivity, whereas viscoelastic fluids display greater stability under strong magnetic fields. These findings provide valuable insights for the modeling, control, and optimization of non-Newtonian MHD flow systems.

8.2 Recommendations

Based on the findings of this study, the following practical recommendations are proposed:

- Engineers and system designers can utilize Hall and ion slip effects as control mechanisms to regulate flow velocity and heat transfer in MHD-based thermal systems.

- The selection of non-Newtonian fluids in industrial applications should consider rheological properties, as they significantly influence momentum and thermal transport characteristics under magnetic fields.

- Nonlinear thermal radiation effects should be incorporated in the design of high-temperature MHD systems, as they substantially enhance thermal energy transport.

- The results of this study can serve as benchmark solutions for validating numerical simulations and developing simplified design correlations for MHD nanofluid systems.

- Practitioners are encouraged to consider the combined influence of electromagnetic, thermal, and chemical effects when modeling nanofluid-based cooling and processing technologies.

8.3 Future Research Work

Although the present study has advanced the understanding of MHD Non-Newtonian nanofluid flow over stretching surfaces, several important avenues remain open for further investigation. Building upon the findings of this dissertation, future research can be systematically directed toward the development of advanced numerical methodologies, the extension of physical modeling assumptions, experimental validation, and comprehensive parametric and sensitivity analyses.

1. **Advanced Numerical and Computational Approaches**

   Future investigations may benefit from the adoption of alternative high-accuracy numerical techniques, such as the Finite Element Method (FEM) or spectral methods, for solving the governing nonlinear equations. In addition, data-driven approaches based on machine learning offer promising opportunities for accelerating parametric studies. Artificial Neural Networks (ANNs) may be developed as surrogate models for rapid prediction of key engineering quantities, including the Nusselt and Sherwood numbers. Furthermore, inverse modeling frameworks based on Physics-Informed Neural Networks (PINNs) may be employed to estimate unknown boundary conditions, material properties, or transport coefficients from limited experimental or observational data.

2. **Extension of Physical Models and Governing Assumptions**

   To improve the physical realism of the heat and mass transfer modeling, future studies may incorporate non-Fourier heat conduction models, such as the Cattaneo–Christov formulation, as well as non-Fickian mass diffusion theories. These models account for finite thermal and solutal relaxation times and are particularly relevant in high-frequency, high-gradient, or microscale transport processes. Additionally, the current model may be further refined by incorporating velocity and thermal slip boundary conditions, which become significant in micro- and nano-scale flows. The consideration of more advanced multiphase nanofluid models, including nanoparticle aggregation, sedimentation, and migration effects, as well as hybrid nanofluids containing multiple nanoparticle species, would substantially enhance the applicability and predictive capability of the model.

3. **Experimental Validation and Benchmarking**

   An important extension of the present work involves the design and implementation of controlled experimental studies to validate the theoretical and numerical predictions. This would require the development of experimental configurations that closely replicate the modeled physical system, such as a stretching surface subjected to an externally applied magnetic field. Experimental validation would not only strengthen the credibility and robustness of the proposed mathematical model but also facilitate the determination of empirical correlations and material constants for specific nanofluid systems. Such validation studies would play a critical role in bridging the gap between theoretical analysis and practical engineering applications.

4. **Comprehensive Sensitivity and Scenario-Based Analyses**

   Future research should include rigorous global sensitivity analyzes using established techniques, such as Sobol indices or the Morris screening method. These approaches enable a quantitative assessment of the relative influence of governing parameters. Such analyzes would move beyond qualitative trend identification and provide objective parameter ranking and uncertainty quantification. In addition, targeted scenario-based investigations can be conducted to evaluate system behavior under extreme or optimal operating conditions relevant to specific applications. Examples include maximizing heat transfer performance in compact heat exchangers or minimizing hydrodynamic resistance in biomedical and microfluidic flow systems.

Bibliography

[1] W. Khan and I. Pop, "Boundary-layer flow of a nanofluid past a stretching sheet," *International journal of heat and mass transfer*, vol. 53, no. 11-12, pp. 2477–2483, 2010.

[2] J. Bouslimi, M. Omri, R. Mohamed, K. Mahmoud, S. Abo-Dahab, and M. Soliman, "Mhd williamson nanofluid flow over a stretching sheet through a porous medium under effects of joule heating, nonlinear thermal radiation, heat generation/absorption, and chemical reaction," *Advances in Mathematical Physics*, vol. 2021, 2021.

[3] S. Nadeem, R. U. Haq, N. S. Akbar, and Z. H. Khan, "Mhd three-dimensional casson fluid flow past a porous linearly stretching sheet," *Alexandria Engineering Journal*, vol. 52, no. 4, pp. 577–582, 2013.

[4] A. Sahoo and R. Nandkeolyar, "Entropy generation and dissipative heat transfer analysis of mixed convective hydromagnetic flow of a casson nanofluid with thermal radiation and hall current," *Scientific Reports*, vol. 11, no. 1, p. 3926, 2021.

[5] M. Fathizadeh, M. Madani, Y. Khan, N. Faraz, A. Yıldırım, and S. Tutkun, "An effective modification of the homotopy perturbation method for mhd viscous flow over a stretching sheet," *Journal of King Saud University-Science*, vol. 25, no. 2, pp. 107–113, 2013.

[6] W. Ibrahim, "Magnetohydrodynamics (mhd) flow of a tangent hyperbolic fluid with nanoparticles past a stretching sheet with second order slip and convective boundary condition," *Results in physics*, vol. 7, pp. 3723–3731, 2017.

[7] S. Atif, S. Hussain, and M. Sagheer, "Effect of viscous dissipation and joule heating on mhd radiative tangent hyperbolic nanofluid with convective and

slip conditions," *Journal of the Brazilian Society of Mechanical Sciences and Engineering*, vol. 41, pp. 1–17, 2019.

[8] G. K. Batchelor, *An introduction to fluid dynamics*. Cambridge university press, 2000.

[9] F. M. White *et al.*, "Fluid mechanics," 2011.

[10] M. Sadeghi-Goughari and M. Hosseini, "The effects of non-uniform flow velocity on vibrations of single-walled carbon nanotube conveying fluid," *Journal of Mechanical Science and Technology*, vol. 29, no. 2, pp. 723–732, 2015.

[11] D. A. Lockerby, J. M. Reese, and M. A. Gallis, "Capturing the knudsen layer in continuum-fluid models of nonequilibrium gas flows," *AIAA journal*, vol. 43, no. 6, pp. 1391–1393, 2005.

[12] P. K. Kundu, I. M. Cohen, D. R. Dowling, and J. Capecelatro, *Fluid mechanics*. Elsevier, 2024.

[13] G. Karniadakis, A. Beskok, and N. Aluru, *Microflows and nanoflows: fundamentals and simulation*. Springer, 2005.

[14] G. A. Bird, *Molecular gas dynamics and the direct simulation of gas flows*. Oxford university press, 1994.

[15] R. L. Panton, *Incompressible flow*. John Wiley & Sons, 2024.

[16] R. Danchin and P. B. Mucha, "Incompressible flows with piecewise constant density," *Archive for Rational Mechanics and Analysis*, vol. 207, no. 3, pp. 991–1023, 2013.

[17] P. H. Oosthuizen and W. E. Carscallen, *Compressible fluid flow*. McGraw-Hill New York, 1997, vol. 179.

[18] P. Liu, "Fundamentals of compressible aerodynamics," in *Aerodynamics*. Springer, 2022, pp. 395–489.

[19] T. Colonius, "Modeling artificial boundary conditions for compressible flow," *Annu. Rev. Fluid Mech.*, vol. 36, no. 1, pp. 315–345, 2004.

[20] F. M. White and J. Majdalani, *Viscous fluid flow*. McGraw-Hill New York, 2006, vol. 3.

[21] M. Saldana, S. Gallegos, E. Gálvez, J. Castillo, E. Salinas-Rodríguez, E. Cerecedo-Sáenz, J. Hernández-Ávila, A. Navarra, and N. Toro, "The reynolds number: A journey from its origin to modern applications," *Fluids*, vol. 9, no. 12, p. 299, 2024.

[22] X. D. Chen, "Laminar-to-turbulence transition revealed through a reynolds number equivalence," *Engineering*, vol. 5, no. 3, pp. 576–579, 2019.

[23] J. Pozorski and M. Wacławczyk, "Mixing in turbulent flows: An overview of physics and modelling," *Processes*, vol. 8, no. 11, p. 1379, 2020.

[24] D. Christodoulou, "The euler equations of compressible fluid flow," *Bulletin of the American Mathematical Society*, vol. 44, no. 4, pp. 581–602, 2007.

[25] A. Schröder and D. Schanz, "3d lagrangian particle tracking in fluid mechanics," *Annual Review of Fluid Mechanics*, vol. 55, no. 1, pp. 511–540, 2023.

[26] F. Toschi and E. Bodenschatz, "Lagrangian properties of particles in turbulence," *Annual review of fluid mechanics*, vol. 41, no. 1, pp. 375–404, 2009.

[27] Z. Zhang and Q. Chen, "Comparison of the eulerian and lagrangian methods for predicting particle transport in enclosed spaces," *Atmospheric environment*, vol. 41, no. 25, pp. 5236–5248, 2007.

[28] J. Ferry and S. Balachandar, "A fast eulerian method for disperse two-phase flow," *International journal of multiphase flow*, vol. 27, no. 7, pp. 1199–1226, 2001.

[29] S. Balachandar and J. K. Eaton, "Turbulent dispersed multiphase flow," *Annual review of fluid mechanics*, vol. 42, no. 1, pp. 111–133, 2010.

[30] S. Pirker, D. Kahrimanovic, C. Kloss, B. Popoff, and M. Braun, "Simulating coarse particle conveying by a set of eulerian, lagrangian and hybrid particle models," *Powder Technology*, vol. 204, no. 2-3, pp. 203–213, 2010.

[31] J. M. Franco and P. Partal, "The newtonian fluid," *Rheology*, vol. 1, pp. 74–95, 2010.

[32] R. P. Chhabra and J. F. Richardson, *Non-Newtonian flow and applied rheology: engineering applications*. Butterworth-Heinemann, 2011.

[33] F. Irgens, *Rheology and non-newtonian fluids*. Springer, 2014, vol. 1.

[34] R. P. Chhabra, "Non-newtonian fluids: an introduction," in *Rheology of complex fluids*. Springer, 2010, pp. 3–34.

[35] T. Shende, V. J. Niasar, and M. Babaei, “An empirical equation for shear viscosity of shear thickening fluids,” *Journal of Molecular Liquids*, vol. 325, p. 115220, 2021.

[36] N. J. Balmforth, I. A. Frigaard, and G. Ovarlez, “Yielding to stress: recent developments in viscoplastic fluid mechanics,” *Annual review of fluid mechanics*, vol. 46, no. 1, pp. 121–146, 2014.

[37] E. Fatahian, N. Kordani, and H. Fatahian, “The application of computational fluid dynamics (cfd) method and several rheological models of blood flow: a review,” *Gazi University Journal of Science*, vol. 31, no. 4, pp. 1213–1227, 2018.

[38] H. Sun, Y. Jiang, Y. Zhang, and L. Jiang, “A review of constitutive models for non-newtonian fluids,” *Fractional Calculus and Applied Analysis*, vol. 27, no. 4, pp. 1483–1526, 2024.

[39] S. U. Choi and J. A. Eastman, “Enhancing thermal conductivity of fluids with nanoparticles,” Argonne National Lab.(ANL), Argonne, IL (United States), Tech. Rep., 1995.

[40] S. Kumar and A. Kumar, “A comprehensive review on the heat transfer and nanofluid flow characteristics in different shaped channels,” *International Journal of Ambient Energy*, vol. 42, no. 3, pp. 345–361, 2021.

[41] D. Wen, G. Lin, S. Vafaei, and K. Zhang, “Review of nanofluids for heat transfer applications,” *Particuology*, vol. 7, no. 2, pp. 141–150, 2009.

[42] Y. Li, J. Zhou, S. Tung, E. Schneider, and S. Xi, “A review on development of nanofluid preparation and characterization,” *Powder technology*, vol. 196, no. 2, pp. 89–101, 2009.

[43] J. BUONGIORNO, “Convective transport in nanofluids,” *Journal of heat transfer*, vol. 128, no. 3, pp. 240–250, 2006.

[44] R. K. Tiwari and M. K. Das, “Heat transfer augmentation in a two-sided lid-driven differentially heated square cavity utilizing nanofluids,” *International Journal of heat and Mass transfer*, vol. 50, no. 9-10, pp. 2002–2018, 2007.

[45] T. Hayat, T. Muhammad, S. A. Shehzad, and A. Alsaedi, “A mathematical study for three-dimensional boundary layer flow of jeffrey nanofluid,” *Zeitschrift für Naturforschung a*, vol. 70, no. 4, pp. 225–233, 2015.

[46] C.-G. Fälthammar, "The discovery of magnetohydrodynamic waves," *Journal of atmospheric and solar-terrestrial physics*, vol. 69, no. 14, pp. 1604–1608, 2007.

[47] N. B. Morley, S. Smolentsev, L. Barleon, I. R. Kirillov, and M. Takahashi, "Liquid magnetohydrodynamics—recent progress and future directions for fusion," *Fusion Engineering and design*, vol. 51, pp. 701–713, 2000.

[48] D. Homfray, M. GORLEY, C. HARRINGTON, A. HOLLINGSWORTH, J. MORRIS, and T. M. DE CARVALHO, "Technology roadmap for a magnetically confined fusion powered spacecraft," *Journal of the British Interplanetary Society*, vol. 70, pp. 319–336, 2017.

[49] A. Farzin, S. A. Etesami, J. Quint, A. Memic, and A. Tamayol, "Magnetic nanoparticles in cancer therapy and diagnosis," *Advanced healthcare materials*, vol. 9, no. 9, p. 1901058, 2020.

[50] K. Sarada, R. J. P. Gowda, I. E. Sarris, R. N. Kumar, and B. C. Prasannakumara, "Effect of magnetohydrodynamics on heat transfer behaviour of a non-newtonian fluid flow over a stretching sheet under local thermal non-equilibrium condition," *Fluids*, vol. 6, no. 8, p. 264, 2021.

[51] J. Raza, F. Mebarek-Oudina, and B. Mahanthesh, "Magnetohydrodynamic flow of nano williamson fluid generated by stretching plate with multiple slips," *Multidiscipline Modeling in Materials and Structures*, vol. 15, no. 5, pp. 871–894, 2019.

[52] R. Mohamed, S. Ahmed, A. Aly, A. Chamkha, and M. Soliman, "Mhd casson nanofluid flow over a stretching surface embedded in a porous medium: effects of thermal radiation and slip conditions," *Lat. Am. Appl. Res*, vol. 51, no. 4, pp. 229–239, 2021.

[53] M. Z. Ashraf, S. U. Rehman, S. Farid, A. K. Hussein, B. Ali, N. A. Shah, and W. Weera, "Insight into significance of bioconvection on mhd tangent hyperbolic nanofluid flow of irregular thickness across a slender elastic surface," *Mathematics*, vol. 10, no. 15, p. 2592, 2022.

[54] R. Abdullah Mohamed, A. Mahmoud Aly, S. Elsayed Ahmed, and M. Sayed Soliman, "Mhd jeffrey nanofluids flow over a stretching sheet through a porous medium in presence of nonlinear thermal radiation and heat generation/absorption," *Challenges in Nano and Micro Scale Science and Technology*, vol. 8, no. 1, pp. 9–22, 2020.

[55] K. Anantha Kumar, A. Venkata Ramudu, V. Sugunamma, and N. Sandeep, “Effect of non-linear thermal radiation on mhd casson fluid flow past a stretching surface with chemical reaction,” *International Journal of Ambient Energy*, vol. 43, no. 1, pp. 8400–8407, 2022.

[56] M. B. Jeelani and A. Abbas, “Al2o3-cu\ethylene glycol-based magnetohydrodynamic non-newtonian maxwell hybrid nanofluid flow with suction effects in a porous space: energy saving by solar radiation,” *Symmetry*, vol. 15, no. 9, p. 1794, 2023.

[57] S. Kanchi, P. R. Gaddala, and S. Gurram, “Impact of activation energy, diffusion thermo, thermal diffusion and hall current on mhd casson fluid flow with inclined plates,” *CFD Letters*, vol. 16, no. 6, pp. 90–108, 2024.

[58] B. C. Sakiadis, “Boundary-layer behavior on continuous solid surfaces: I. boundary-layer equations for two-dimensional and axisymmetric flow,” *AIChE Journal*, vol. 7, no. 1, pp. 26–28, 1961.

[59] S. Nadeem, S. Hussain, and C. Lee, “Flow of a williamson fluid over a stretching sheet,” *Brazilian journal of chemical engineering*, vol. 30, pp. 619–625, 2013.

[60] H. Ullah, I. Khan, M. Fiza, N. N. Hamadneh, M. Fayz-Al-Asad, S. Islam, I. Khan, M. A. Z. Raja, and M. Shoaib, “Mhd boundary layer flow over a stretching sheet: A new stochastic method,” *Mathematical Problems in Engineering*, vol. 2021, pp. 1–26, 2021.

[61] M. A. Iqbal, M. Usman, F. Allehiany, M. Hussain, and K. A. Khan, “Rotating mhd williamson nanofluid flow in 3d over exponentially stretching sheet with variable thermal conductivity and diffusivity,” *Heliyon*, vol. 9, no. 11, 2023.

[62] H. Muzara and S. Shateyi, “Magnetohydrodynamics williamson nanofluid flow over an exponentially stretching surface with a chemical reaction and thermal radiation,” *Mathematics*, vol. 11, no. 12, p. 2740, 2023.

[63] A. M. Rashad, M. A. Nafe, and D. A. Eisa, “Heat variation on mhd williamson hybrid nanofluid flow with convective boundary condition and ohmic heating in a porous material,” *Scientific Reports*, vol. 13, no. 1, p. 6071, 2023.

[64] N. Kumar, R. N. Jat, S. Sinha, P. K. Dadheech, P. Agrawal, S. D. Purohit, and K. S. Nisar, “Radiation and slip effects on mhd point flow of nanofluid towards a stretching sheet with melting heat transfer,” *Heat Transfer*, vol. 51, no. 4, pp. 3018–3034, 2022.

[65] S. Irshad, A. H. Majeed, S. Jahan, A. Riaz, S. M. Eldin, and H. Shahzad, "Numerical simulations of mhd generalized newtonian fluid flow effects on a stretching sheet in the presence of permeable media: A finite difference-based study," *Frontiers in Physics*, vol. 11, p. 130, 2023.

[66] A.-R. Khaled and K. Vafai, "The role of porous media in modeling flow and heat transfer in biological tissues," *International Journal of Heat and Mass Transfer*, vol. 46, no. 26, pp. 4989–5003, 2003.

[67] S. M. Razi, S. K. Soid, A. S. Abd Aziz, N. Adli, and Z. M. Ali, "Williamson nanofluid flow over a stretching sheet with varied wall thickness and slip effects," in *Journal of Physics: Conference Series*, vol. 1366, no. 1. IOP Publishing, 2019, p. 012007.

[68] T. Kebede, E. Haile, G. Awgichew, and T. Walelign, "Heat and mass transfer in unsteady boundary layer flow of williamson nanofluids," *Journal of Applied Mathematics*, vol. 2020, pp. 1–13, 2020.

[69] A. Abbas, M. B. Jeelani, A. S. Alnahdi, and A. Ilyas, "Mhd williamson nanofluid fluid flow and heat transfer past a non-linear stretching sheet implanted in a porous medium: Effects of heat generation and viscous dissipation," *Processes*, vol. 10, no. 6, p. 1221, 2022.

[70] S. Abdal, S. Hussain, I. Siddique, A. Ahmadian, and M. Ferrara, "On solution existence of mhd casson nanofluid transportation across an extending cylinder through porous media and evaluation of priori bounds," *Scientific Reports*, vol. 11, no. 1, p. 7799, 2021.

[71] A. Mahdy and A. J. Chamkha, "Unsteady mhd boundary layer flow of tangent hyperbolic two-phase nanofluid of moving stretched porous wedge," *International Journal of Numerical Methods for Heat & Fluid Flow*, vol. 28, no. 11, pp. 2567–2580, 2018.

[72] K. Ramesh, A. Patel, and M. Rawal, "Electroosmosis and transverse magnetic effects on radiative tangent hyperbolic nanofluid flow through porous medium," *International Journal of Ambient Energy*, pp. 1–8, 2020.

[73] S. Choudhary, P. Choudhary, and B. Pattanaik, "Tangent hyperbolic fluid flow under condition of divergent channel in the presence of porous medium with suction/blowing and heat source: Emergence of the boundary layer," *International Journal of Mathematics and Mathematical Sciences*, vol. 2023, no. 1, p. 6282130, 2023.

[74] M. A. Ur Rehman, M. A. Farooq, and M. Irfan, "Numerical analysis of magnetohydrodynamic free stream and radiative heat transfer flow of nanofluid in a permeable medium over a linearly stretched cylinder with arrhenius activation energy," *Numerical Heat Transfer, Part B: Fundamentals*, pp. 1–21, 2024.

[75] M. Naveed Khan, A. Alhowaity, Z. Wang, K. A. Gepreel, and M. Hussien, "Numerical analysis of the heat transfer application on a convective tangent hyperbolic nanofluid flow over a porous stretching cylinder with stratification effects," *Numerical Heat Transfer, Part A: Applications*, pp. 1–17, 2024.

[76] A. Divya, T. Jithendra, and S. Balakrishna, "Application of artificial neural networks modelling for analyzing non-newtonian fluid flow over porous media with an induced magnetic field," *Journal of Nanofluids*, vol. 13, no. 3, pp. 721–734, 2024.

[77] D. Bhargavi, A. Kumar, P. Anantha Lakshmi Narayana, and N. Gupta, "An analytical study of fluid flow through a porous filled channel with permeable wall: Suction/injection wall conditions," *Journal of Nanofluids*, vol. 13, no. 2, pp. 371–380, 2024.

[78] N. Tarakaramu, N. Sivakumar, P. Satya Narayana, and R. Sivajothi, "Viscous dissipation and joule heating effects on 3d magnetohydrodynamics flow of williamson nanofluid in a porous medium over a stretching surface with melting condition," *ASME Open Journal of Engineering*, vol. 1, 2022.

[79] W. Ibrahim and T. Anbessa, "Hall and ion-slip effects on mixed convection flow of williamson nanofluid over a nonlinear porous stretching sheet with variable thermal conductivity," *Heat Transfer*, vol. 50, no. 6, pp. 5627–5651, 2021.

[80] M. Taj and T. Salahuddin, "Analysis of viscously dissipated three-dimensional flow of williamson fluid with nonlinear radiation and activation energy," *Alexandria Engineering Journal*, vol. 76, pp. 595–607, 2023.

[81] T. Walelign, T. Kebede, E. Haile, and A. Walelgn, "Analytical study of heat and mass transfer in unsteady mhd radiant flow of williamson nanofluid over stretching sheet with heat generation and chemical reaction," *Heat Transfer*, vol. 49, no. 8, pp. 4246–4263, 2020.

[82] H. Hunegnaw, "Unsteady boundary layer flow of williamson nanofluids over a heated permeable stretching sheet embedded in porous medium in the presence of viscous dissipation," *Journal of Naval Architecture and Marine Engineering*, vol. 18, no. 1, pp. 83–96, 2021.

[83] M. I. Khan, M. Waqas, T. Hayat, and A. Alsaedi, "Chemically reactive flow of micropolar fluid accounting viscous dissipation and joule heating," *Results in physics*, vol. 7, pp. 3706–3715, 2017.

[84] M. Qamar, "Mhd tangent hyperbolic nanofluid past a stretching sheet with the effect of joule heating and chemical reaction," Ph.D. dissertation, CAPITAL UNIVERSITY, 2019.

[85] F. Shahzad, M. Sagheer, and S. Hussain, "Mhd tangent hyperbolic nanofluid with chemical reaction, viscous dissipation and joule heating effects," *AIP advances*, vol. 9, no. 2, 2019.

[86] M. Sohail, Y.-M. Chu, E. R. El-Zahar, U. Nazir, and T. Naseem, "Contribution of joule heating and viscous dissipation on three dimensional flow of casson model comprising temperature dependent conductance utilizing shooting method," *Physica Scripta*, vol. 96, no. 8, p. 085208, 2021.

[87] M. M. Muduly, P. K. Rath, P. Kar, and K. Swain, "Effects of joule heating and viscous dissipation on casson nanofluid flow over a stretched sheet with chemical reaction," *Journal of Computational Applied Mechanics*, vol. 53, no. 4, pp. 478–493, 2022.

[88] M. Waqas, M. R. Almutiri, B. Yagoob, H. Ahmad, and M. Bilal, "Numerical analysis of mhd tangent hyperbolic nanofluid flow over a stretching surface subject to heat source/sink," *Pramana*, vol. 98, no. 1, p. 27, 2024.

[89] S. Nandi and B. Kumbhakar, "Viscous dissipation and chemical reaction effects on tangent hyperbolic nanofluid flow past a stretching wedge with convective heating and navier's slip conditions," *Iranian Journal of Science and Technology, Transactions of Mechanical Engineering*, vol. 46, no. 2, pp. 379–397, 2022.

[90] K. Nagaraja, U. Khan, J. Madhukesh, A. M. Hassan, B. Prasannakumara, N. Ben Kahla, S. Elattar, and J. Singh Chohan, "Heat and mass transfer analysis of assisting and opposing radiative flow conveying ternary hybrid nanofluid over an exponentially stretching surface," *Scientific Reports*, vol. 13, no. 1, p. 14795, 2023.

[91] N. Tarakaramu, P. Satya Narayana, N. Sivakumar, D. Harish Babu, and K. Bhagya Lakshmi, "Convective conditions on 3d magnetohydrodynamic (mhd) non-newtonian nanofluid flow with nonlinear thermal radiation and heat absorption: a numerical analysis," *Journal of Nanofluids*, vol. 12, no. 2, pp. 448–457, 2023.

[92] W. Younas and M. Sagheer, “Enhanced nanofluid dynamics and heat transfer with brownian motion, chemical reaction, and thermophoresis at stagnation point,” *Journal of Nanofluids*, vol. 13, no. 4, pp. 999–1008, 2024.

[93] M. Archana, B. Gireesha, B. Prasannakumara, and R. Gorla, “Influence of nonlinear thermal radiation on rotating flow of casson nanofluid,” *Nonlinear Engineering*, vol. 7, no. 2, pp. 91–101, 2018.

[94] S. Ghadikolaei, K. Hosseinzadeh, D. D. Ganji, and B. Jafari, “Nonlinear thermal radiation effect on magneto casson nanofluid flow with joule heating effect over an inclined porous stretching sheet,” *Case studies in thermal engineering*, vol. 12, pp. 176–187, 2018.

[95] W. Akaje and B. Olajuwon, “Impacts of nonlinear thermal radiation on a stagnation point of an aligned mhd casson nanofluid flow with thompson and troian slip boundary condition,” *Journal of Advanced Research in Experimental Fluid Mechanics and Heat Transfer*, vol. 6, no. 1, pp. 1–15, 2021.

[96] M. Shamshuddin, F. Mebarek-Oudina, S. Salawu, and A. Shafiq, “Thermophoretic movement transport of reactive casson nanofluid on riga plate surface with nonlinear thermal radiation and uneven heat sink/source,” *Journal of Nanofluids*, vol. 11, no. 6, pp. 833–844, 2022.

[97] Y. Li, M. Imtiaz, W. Jamshed, S. Rehman, M. R. Eid, N. A. A. M. Nasir, N. A. Aminuddin, A. Abd-Elmonem, N. S. E. Abdalla, R. W. Ibrahim *et al.*, “Nonlinear thermal radiation and the slip effect on a 3d bioconvection flow of the casson nanofluid in a rotating frame via a homotopy analysis mechanism,” *Nanotechnology Reviews*, vol. 12, no. 1, p. 20230161, 2023.

[98] T. Hayat, S. Qayyum, M. Imtiaz, and A. Alsaedi, “Three-dimensional rotating flow of jeffrey fluid for cattaneo-christov heat flux model,” *AIP Advances*, vol. 6, no. 2, p. 025012, 02 2016. [Online]. Available: https://doi.org/10.1063/1.4942091

[99] M. V. Krishna, “Hall and ion slip impacts on unsteady mhd free convective rotating flow of jeffreys fluid with ramped wall temperature,” *International Communications in Heat and Mass Transfer*, vol. 119, p. 104927, 2020.

[100] M. V. Krishna, N. A. Ahamad, and A. J. Chamkha, “Hall and ion slip impacts on unsteady mhd convective rotating flow of heat generating/absorbing second grade fluid,” *Alexandria Engineering Journal*, vol. 60, no. 1, pp. 845–858, 2021.

[101] S. A. Anand Kumar, S. Sreedhar, M. V. Krishna, and A. Chamkha, "Chemical reaction, radiation and hall effects on mhd rotating nanofluid past an infinite vertical moving smooth plate," *Journal of Nanofluids*, vol. 12, no. 8, pp. 2170–2180, 2023.

[102] M. Preetham and S. Kumbinarasaiah, "Analysis of hybrid nanofluid mhd flow and heat transfer between two surfaces in a rotating system in the presence of joule heating and thermal radiation by fibonacci wavelet," *Journal of Nanofluids*, vol. 13, no. 1, pp. 1–14, 2024.

[103] U. Hani and M. Ali, "Analyzing the effect of coriolis force on mhd boundary layer flow over a cylindrical-shaped geometry with chemical reaction and heat generation: A statistical and numerical approach," *Journal of Nanofluids*, vol. 13, no. 4, pp. 907–929, 2024.

[104] V. R. R. Vaddemani, Y. R. Reddy, and D. R. Srinivasan, "Activation energy, rotational and hall current effects of magnetohydrodynamic 3d flow of non-newtonian hybrid nanofluid over a stretched plate," *Journal of Advanced Research in Numerical Heat Transfer*, vol. 20, no. 1, pp. 36–52, 2024.

[105] A. Ishak, R. Nazar, and I. Pop, "Uniform suction/blowing effect on flow and heat transfer due to a stretching cylinder," *Applied Mathematical Modelling*, vol. 32, no. 10, pp. 2059–2066, 2008.

[106] U. Shahzad, M. Mushtaq, S. Farid, K. Jabeen, and R. Muntazir, "A numerical approach for an unsteady tangent hyperbolic nanofluid flow past a wedge in the presence of suction/injection," *Mathematical Problems in Engineering*, vol. 2021, no. 1, p. 8653091, 2021.

[107] A. Alkaoud, M. M. Khader, A. Eid, and A. M. Megahed, "Numerical simulation of the flow of a tangent hyperbolic fluid over a stretching sheet within a porous medium, accounting for slip conditions," *Heliyon*, vol. 10, no. 8, 2024.

[108] A. Amer, S. A. Al Rashdi, N. I. Ghoneim, and A. M. Megahed, "Tangent hyperbolic nanofluid flowing over a stretching sheet through a porous medium with the inclusion of magnetohydrodynamic and slip impact," *Results in Engineering*, vol. 19, p. 101370, 2023.

[109] M. Seddeek, "Effects of hall and ion–slip currents on magneto–micropolar fluid and heat transfer over a non–isothermal stretching sheet with suction and blowing," *Proceedings of the Royal Society of London. Series A: Mathematical, Physical and Engineering Sciences*, vol. 457, no. 2016, pp. 3039–3050, 2001.

[110] X. Su *et al.*, "Hall and ion-slip effects on the unsteady mhd mixed convection of cu-water nanofluid over a vertical stretching plate with convective heat flux," *Indian Journal of Pure & Applied Physics (IJPAP)*, vol. 55, no. 8, pp. 564–573, 2017.

[111] A. A. Opanuga, J. A. Gbadeyan, H. I. Okagbue, and O. O. Agboola, "Hall current and suction/injection effects on the entropy generation of third grade fluid," *International Journal of Advanced and Applied Sciences*, vol. 5, no. 7, pp. 108–115, 2018.

[112] W. Ibrahim and T. Anbessa, "Mixed convection flow of nanofluid with hall and ion-slip effects using spectral relaxation method," *Journal of the Egyptian Mathematical Society*, vol. 27, no. 1, pp. 1–21, 2019.

[113] I. EL GLILI and M. Driouich, "The effect of nonlinear thermal radiation on emhd casson nanofluid over a stretchable riga plate with temperature-dependent viscosity and chemical reaction," *Physical Chemistry Research*, vol. 12, no. 1, pp. 157–173, 2024.

[114] M. V. Krishna and A. V. Kumar, "Chemical reaction, slip effects and non-linear thermal radiation on unsteady mhd jeffreys nanofluid flow over a stretching sheet," *Case Studies in Thermal Engineering*, vol. 55, p. 104129, 2024.

[115] M. Abbas, M. Qamar, M. Khan, and S. Hussain, "Chemically reactive flow of williamson nanofluid with nonlinear thermal radiation over an exponentially stretching/shrinking surface," *Journal of Radiation Research and Applied Sciences*, vol. 18, no. 3, p. 101630, 2025.

[116] P. S. Kumari, S. M. Ibrahim, P. V. Kumar, and G. Lorenzini, "Magnetohydrodynamic jeffrey nanofluid flow across an inclined stretching sheet via porous media with slip effects," *Frontiers in Heat and Mass Transfer*, vol. 23, no. 5, pp. 1639–1660, 2025.

[117] Z. Mingliang, Z. Asghar, D. Hussain, E. A. Ismail, F. A. Awwad, A. Zeeshan, and N. Ijaz, "Thermal dynamics in electrically conducting tangent hyperbolic nanofluid flow: Hybrid-empirical modelling approach using rsm," *ZAMM-Journal of Applied Mathematics and Mechanics/Zeitschrift für Angewandte Mathematik und Mechanik*, vol. 105, no. 2, p. e202400770, 2025.

[118] K. Khalil, F. Mohammed, W. Abbas, and A. M. Megahed, "Exploring slip boundary impacts on magnetohydrodynamic casson nanofluid flow over a vertical

stretching sheet with nonlinear thermal radiation," *Journal of Taibah University for Science*, vol. 19, no. 1, p. 2565855, 2025.

[119] L. Ahmad, H. U. Rahman, S. Javed, U. Khan, and D. H. Elkamchouchi, "Thermal radiation in a non-newtonian (williamson) mhd flow between the two rotating disks," *Chemical Engineering & Technology*, vol. 48, no. 12, p. e70143, 2025.

[120] W. D. Alamirew, G. A. Zergaw, and E. H. Gorfie, "Effects of hall, ion slip, viscous dissipation and nonlinear thermal radiation on mhd williamson nanofluid flow past a stretching sheet," *International Journal of Thermofluids*, vol. 22, p. 100646, 2024.

[121] W. D. Alamirew, G. Awgichew, and E. Haile, "Mixed convection flow of mhd casson nanofluid over a vertically extending sheet with effects of hall, ion slip and nonlinear thermal radiation," *International Journal of Thermofluids*, vol. 23, p. 100762, 2024.

[122] W. D. Alamirew, G. Awgichew, E. Haile, E. Yetbarek, and E. Birara, "Investigation on rotating flow of magnetohydrodynamic tangent hyperbolic nanofluid over a stretching permeable sheet: Impacts of hall, ion slip and suction velocity," *Journal of Nanofluids*, vol. 13, no. 6, pp. 1255–1270, 2024.

[123] W. D. Alamirew, G. Awgichew, and E. Haile, "Python-based simulation of rotating mhd jeffrey nanofluid flow over a permeable stretching surface subject to hall and ion slip effects," *International Journal of Thermofluids*, vol. 31, p. 101517, 2026.

[124] S. Pramanik, "Casson fluid flow and heat transfer past an exponentially porous stretching surface in presence of thermal radiation," *Ain shams engineering journal*, vol. 5, no. 1, pp. 205–212, 2014.

[125] F. Shahzad, M. Sagheer, and S. Hussain, "Numerical simulation of magnetohydrodynamic jeffrey nanofluid flow and heat transfer over a stretching sheet considering joule heating and viscous dissipation," *AIP Advances*, vol. 8, no. 6, 2018.

[126] G. Kumar and S. Rizvi, "Casson fluid flow past on vertical cylinder in the presence of chemical reaction and magnetic field," *Applications and Applied Mathematics: An International Journal (AAM)*, vol. 16, no. 1, p. 28, 2021.

[127] S. A. Shehzad, T. Hayat, A. Alsaedi, and M. A. Obid, "Nonlinear thermal radiation in three-dimensional flow of jeffrey nanofluid: a model for solar energy," *Applied Mathematics and Computation*, vol. 248, pp. 273–286, 2014.

[128] B. E. Launder, "Heat and mass transport," *Turbulence*, pp. 231–287, 2005.

[129] C. Y. Han, "Effect of a magnetic field on natural convection of an electrically conducting fluid in a tilted cavity," *Journal of the Korean Physical Society*, vol. 55, no. 5, pp. 2193–2199, 2009.

[130] S. Nazir, M. Kashif, A. Zeeshan, H. Alsulami, and M. Ghamkhar, "A study of heat and mass transfer of non-newtonian fluid with surface chemical reaction," *Journal of the Indian Chemical Society*, vol. 99, no. 5, p. 100434, 2022.

[131] R. Rajput, *A textbook of heat and mass transfer*. S. Chand Publishing, 2015.

[132] A. Salazar, "On thermal diffusivity," *European journal of physics*, vol. 24, no. 4, p. 351, 2003.

[133] B. Zohuri and B. Zohuri, "Forced convection heat transfer," *Thermal-Hydraulic Analysis of Nuclear Reactors*, pp. 323–345, 2017.

[134] S. Sazhin, V. Gol'dshtein, and M. Heikal, "A transient formulation of newton's cooling law for spherical bodies," *J. Heat Transfer*, vol. 123, no. 1, pp. 63–64, 2001.

[135] M. Awais, T. Hayat, N. Muqaddass, A. Ali, S. E. Awan *et al.*, "Nanoparticles and nonlinear thermal radiation properties in the rheology of polymeric material," *Results in physics*, vol. 8, pp. 1038–1045, 2018.

[136] S. Qayyum, M. I. Khan, T. Hayat, and A. Alsaedi, "A framework for nonlinear thermal radiation and homogeneous-heterogeneous reactions flow based on silver-water and copper-water nanoparticles: a numerical model for probable error," *Results in physics*, vol. 7, pp. 1907–1914, 2017.

[137] J. Benitez, *Principles and modern applications of mass transfer operations*. John Wiley & Sons, 2011.

[138] S. S. Bavera, T. Fragos, M. Zevin, C. P. Berry, P. Marchant, J. J. Andrews, S. Coughlin, A. Dotter, K. Kovlakas, D. Misra *et al.*, "The impact of mass-transfer physics on the observable properties of field binary black hole populations," *Astronomy & Astrophysics*, vol. 647, p. A153, 2021.

[139] L. Deike, “Mass transfer at the ocean–atmosphere interface: the role of wave breaking, droplets, and bubbles,” *Annual Review of Fluid Mechanics*, vol. 54, no. 1, pp. 191–224, 2022.

[140] J. C. Wong, V. K. Pareek, and B. Sun, “Cfd analysis of phase change behaviour and frost growth under various conditions using mass transfer theory,” *International Journal of Heat and Mass Transfer*, vol. 198, p. 123396, 2022.

[141] M. B. Riaz, M. Asgir, A. Zafar, and S. Yao, “Combined effects of heat and mass transfer on mhd free convective flow of maxwell fluid with variable temperature and concentration,” *Mathematical Problems in Engineering*, vol. 2021, no. 1, p. 6641835, 2021.

[142] H. A. Nabwey, F. Rahbar, T. Armaghani, A. M. Rashad, and A. J. Chamkha, “A comprehensive review of non-newtonian nanofluid heat transfer,” *Symmetry*, vol. 15, no. 2, p. 362, 2023.

[143] M. Sheremet, D. Cimpean, and I. Pop, “Free convection in a partially heated wavy porous cavity filled with a nanofluid under the effects of brownian diffusion and thermophoresis,” *Applied Thermal Engineering*, vol. 113, pp. 413–418, 2017.

[144] I. Ullah, S. Shafie, I. Khan, and K. L. Hsiao, “Brownian diffusion and thermophoresis mechanisms in casson fluid over a moving wedge,” *Results in Physics*, vol. 9, pp. 183–194, 2018.

[145] M. I. Khan, S. A. Khan, T. Hayat, M. I. Khan, and A. Alsaedi, “Nanomaterial based flow of prandtl-eyring (non-newtonian) fluid using brownian and thermophoretic diffusion with entropy generation,” *Computer Methods and Programs in Biomedicine*, vol. 180, p. 105017, 2019.

[146] H. Waqas, S. A. Khan, B. Ali, D. Liu, T. Muhammad, and E. Hou, “Numerical computation of brownian motion and thermophoresis effects on rotational micropolar nanomaterials with activation energy,” *Propulsion and Power Research*, vol. 12, no. 3, pp. 397–409, 2023.

[147] Z. Abdelmalek, A. Hussain, S. Bilal, E.-S. M. Sherif, and P. Thounthong, “Brownian motion and thermophoretic diffusion influence on thermophysical aspects of electrically conducting viscoinelastic nanofluid flow over a stretched surface,” *Journal of Materials Research and Technology*, vol. 9, no. 5, pp. 11 948–11 957, 2020.

[148] S. Ahmed, H. Xu, Y. Zhou, and Q. Yu, "Modelling convective transport of hybrid nanofluid in a lid driven square cavity with consideration of brownian diffusion and thermophoresis," *International Communications in Heat and Mass Transfer*, vol. 137, p. 106226, 2022.

[149] M. Amir, M. Ramzan, A. Shafique, S. Abbas, A. Alhushaybari, E. A. Az-Zo'bi, and Y. M. A. and, "Effect of brownian and thermophoresis motion on fluid flow with chemical reaction and heat transfer," *Radiation Effects and Defects in Solids*, vol. 0, no. 0, pp. 1–17, 2025.

[150] N. Thamaraikannan, S. Karthikeyan, D. K. Chaudhary, and S. Kayikci, "Analytical investigation of magnetohydrodynamic non-newtonian type casson nanofluid flow past a porous channel with periodic body acceleration," *Complexity*, vol. 2021, no. 1, p. 7792422, 2021.

[151] M. Kothandapani and J. Prakash, "Influence of heat source, thermal radiation, and inclined magnetic field on peristaltic flow of a hyperbolic tangent nanofluid in a tapered asymmetric channel," *IEEE transactions on nanobioscience*, vol. 14, no. 4, pp. 385–392, 2014.

[152] F. Hussain, M. Nazeer, I. Ghafoor, A. Saleem, B. Waris, and I. Siddique, "Perturbation solution of couette flow of casson nanofluid with composite porous medium inside a vertical channel," *Nanoscience and Technology: An International Journal*, vol. 13, no. 4, 2022.

[153] A. Z. Kohilavani Naganthran, M. F. Basir, N. Shehzad, R. Nazar, R. Choudhary, and S. Balaji, "Concentration flux dependent on radiative mhd casson flow with arrhenius activation energy: homotopy analysis method (ham) with an evolutionary algorithm," *Int J Heat Technol*, vol. 38, no. 4, pp. 785–93, 2020.

[154] V. J. Prajapati and R. Meher, "Analysis of mhd tangent hyperbolic hybrid nanofluid flow with different base fluids over a porous stretched sheet," *Journal of Taibah University for Science*, vol. 18, no. 1, p. 2300851, 2024.

[155] S. Liao, "An optimal homotopy-analysis approach for strongly nonlinear differential equations," *Communications in Nonlinear Science and Numerical Simulation*, vol. 15, no. 8, pp. 2003–2016, 2010.

[156] S. Akbar, M. Sohail, S. T. Abbas, and N. Badi, "Optimal homotopic strategy for thermal and mass transport in williamson model flow pdes under heat generation/absorption and joule heating," *Advances in Mechanical Engineering*, vol. 16, no. 11, p. 16878132241294262, 2024.

[157] L. Ali, X. Liu, B. Ali, S. Mujeed, and S. Abdal, "Finite element analysis of thermo-diffusion and multi-slip effects on mhd unsteady flow of casson nanofluid over a shrinking/stretching sheet with radiation and heat source," *Applied Sciences*, vol. 9, no. 23, p. 5217, 2019.

[158] W. Ibrahim and D. Gamachu, "Finite element method solution of mixed convection flow of williamson nanofluid past a radially stretching sheet," *Heat Transfer*, vol. 49, no. 2, pp. 800–822, 2020.

[159] B. Ali, R. A. Naqvi, A. Mariam, L. Ali, and O. M. Aldossary, "Finite element study for magnetohydrodynamic (mhd) tangent hyperbolic nanofluid flow over a faster/slower stretching wedge with activation energy," *Mathematics*, vol. 9, no. 1, p. 25, 2020.

[160] U. Nazir, M. Sohail, H. Alrabaiah, M. M. Selim, P. Thounthong, and C. Park, "Inclusion of hybrid nanoparticles in hyperbolic tangent material to explore thermal transportation via finite element approach engaging cattaneo-christov heat flux," *PLoS one*, vol. 16, no. 8, p. e0256302, 2021.

[161] M. S. Arif, W. Shatanawi, and Y. Nawaz, "Finite element study of electrical mhd williamson nanofluid flow under the effects of frictional heating in the view of viscous dissipation," *Energies*, vol. 16, no. 6, p. 2778, 2023.

[162] H. B. Keller, "A new difference scheme for parabolic problems," in *Numerical solution of partial differential equations–II*. Elsevier, 1971, pp. 327–350.

[163] M. I. Anwar, K. Rafique, M. Misiran, S. A. Shehzad, and G. Ramesh, "Keller-box analysis of inclination flow of magnetized williamson nanofluid," *SN Applied Sciences*, vol. 2, pp. 1–9, 2020.

[164] M. Z. Swalmeh, F. A. Alwawi, M. S. Kausar, M. A. H. Ibrahim, A. S. Hamarsheh, I. M. Sulaiman, A. M. Awwal, N. Pakkaranang, and B. Panyanak, "Numerical simulation on energy transfer enhancement of a williamson ferrofluid subjected to thermal radiation and a magnetic field using hybrid ultrafine particles," *Scientific Reports*, vol. 13, no. 1, p. 3176, 2023.

[165] K. Rafique, A. M. Alqahtani, S. Ahmad, S. Aslam, I. Khan, and A. Singh, "Numerical simulations of williamson fluid containing hybrid nanoparticles via keller box technique," *Discover Applied Sciences*, vol. 6, no. 3, p. 80, 2024.

[166] S. Bilal, Z. Shah, P. Kumam, and P. Thounthong, "Mathematical and engineering aspects of chemically reactive tangent hyperbolic nanofluid over a cone and

plate with mixed convection," *Mathematical Problems in Engineering*, vol. 2020, no. 1, p. 9090185, 2020.

[167] W. Iqbal, M. Jalil, M. A. Khadimallah, M. Hussain, M. N. Naeem, A. F. Al Naim, and A. Tounsi, "Interaction of casson nanofluid with brownian motion: Temperature profile with shooting method," *Advances in nano research*, vol. 10, no. 4, pp. 349–357, 2021.

[168] K. Muhammad, S. A. Abdelmohsen, A. M. Abdelbacki, and B. Ahmed, "Darcy-forchheimer flow of hybrid nanofluid subject to melting heat: A comparative numerical study via shooting method," *International Communications in Heat and Mass Transfer*, vol. 135, p. 106160, 2022.

[169] S. Sakinder and T. Salahuddin, "A numerical study of electro-osmosis williamson nanofluid flow in a permeable tapered channel," *Alexandria Engineering Journal*, vol. 81, pp. 620–625, 2023.

[170] H. Maiti and S. K. Nandy, "The unified impact of thermal radiation and heat source on unsteady flow of tangent hyperbolic nanofluid through a permeable shrinking sheet," *Chemical Engineering Journal Advances*, vol. 15, p. 100502, 2023.

[171] S. Jangid, R. Mehta, A. Bhatnagar, M. F. Alotaibi, H. Ahmad *et al.*, "Heat and mass transfer of hydromagnetic williamson nanofluid flow study over an exponentially stretched surface with suction/injection, buoyancy, radiation and chemical reaction impacts," *Case Studies in Thermal Engineering*, vol. 59, p. 104278, 2024.

[172] H. Basha, "Dynamics of chemically reactive magnetized casson nanofluid flow over a sensor surface under joule heating and viscous dissipation effects," *BioNanoScience*, vol. 14, no. 1, pp. 241–267, 2024.

[173] Z. Adegboye, Y. Yahaya, and U. Ahmed, "Direct integration of general fourth order ordinary differential equations using fifth order runge-kutta method," *Journal of the Nigerian Mathematical Society*, vol. 39, no. 1, pp. 69–78, 2020.

[174] N. Ahamad and S. Charan, "Study of numerical solution of fourth order ordinary differential equations by fifth order runge-kutta method," *Int. J. Sci. Res. Sci. Eng. Technol*, vol. 6, no. 1, pp. 230–237, 2019.

[175] G. D. Trikkaliotis and M. C. Gousidou-Koutita, "Derivation of the reduction formula of sixth order and seven stages runge-kutta method for the solution of

an ordinary differential equation," *Applied Mathematics*, vol. 13, no. 4, pp. 338–355, 2022.

[176] C. R. Harris, K. J. Millman, S. J. Van Der Walt, R. Gommers, P. Virtanen, D. Cournapeau, E. Wieser, J. Taylor, S. Berg, N. J. Smith *et al.*, "Array programming with numpy," *Nature*, vol. 585, no. 7825, pp. 357–362, 2020.

[177] P. Virtanen, R. Gommers, T. E. Oliphant, M. Haberland, T. Reddy, D. Cournapeau, E. Burovski, P. Peterson, W. Weckesser, J. Bright *et al.*, "Scipy 1.0: fundamental algorithms for scientific computing in python," *Nature methods*, vol. 17, no. 3, pp. 261–272, 2020.

[178] J. D. Hunter, "Matplotlib: A 2d graphics environment," *Computing in science & engineering*, vol. 9, no. 03, pp. 90–95, 2007.

[179] K. Vajravelu, S. Sreenadh, K. Rajanikanth, and C. Lee, "Peristaltic transport of a williamson fluid in asymmetric channels with permeable walls," *Nonlinear Analysis: Real World Applications*, vol. 13, no. 6, pp. 2804–2822, 2012.

[180] I. Zehra, M. M. Yousaf, and S. Nadeem, "Numerical solutions of williamson fluid with pressure dependent viscosity," *Results in Physics*, vol. 5, pp. 20–25, 2015.

[181] M. V. Krishna and A. J. Chamkha, "Hall and ion slip effects on mhd rotating boundary layer flow of nanofluid past an infinite vertical plate embedded in a porous medium," *Results in Physics*, vol. 15, p. 102652, 2019.

[182] M. Ali and F. Al-Yousef, "Laminar mixed convection from a continuously moving vertical surface with suction or injection," *Heat and Mass transfer*, vol. 33, no. 4, pp. 301–306, 1998.

[183] M. E. Ali, "The effect of variable viscosity on mixed convection heat transfer along a vertical moving surface," *International Journal of Thermal Sciences*, vol. 45, no. 1, pp. 60–69, 2006.

[184] A. Ishak, R. Nazar, and I. Pop, "Unsteady mixed convection boundary layer flow due to a stretching vertical surface," *Arabian Journal for Science and Engineering*, vol. 31, no. 2, pp. 165–182, 2006.

[185] S. Harris, D. Ingham, and I. Pop, "Mixed convection boundary-layer flow near the stagnation point on a vertical surface in a porous medium: Brinkman model with slip," *Transport in Porous Media*, vol. 77, pp. 267–285, 2009.

[186] M. A. Ismael, I. Pop, and A. J. Chamkha, "Mixed convection in a lid-driven square cavity with partial slip," *International Journal of Thermal Sciences*, vol. 82, pp. 47–61, 2014.

[187] J. Merkin, "Mixed convection in a falkner–skan system," *Journal of Engineering Mathematics*, vol. 100, no. 1, pp. 167–185, 2016.

[188] N. Casson, "Flow equation for pigment-oil suspensions of the printing ink-type," *Rheology of disperse systems*, pp. 84–104, 1959.

[189] S. Mukhopadhyay, P. R. De, K. Bhattacharyya, and G. Layek, "Casson fluid flow over an unsteady stretching surface," *Ain Shams Engineering Journal*, vol. 4, no. 4, pp. 933–938, 2013.

[190] M. M. Nandeppanavar, S. Vaishali, M. Kemparaju, and N. Raveendra, "Theoretical analysis of thermal characteristics of casson nano fluid flow past an exponential stretching sheet in darcy porous media," *Case Studies in Thermal Engineering*, vol. 21, p. 100717, 2020.

[191] M. Awais, M. A. Z. Raja, S. E. Awan, M. Shoaib, and H. M. Ali, "Heat and mass transfer phenomenon for the dynamics of casson fluid through porous medium over shrinking wall subject to lorentz force and heat source/sink," *Alexandria Engineering Journal*, vol. 60, no. 1, pp. 1355–1363, 2021.

[192] S. Abo-Dahab, M. Abdelhafez, F. Mebarek-Oudina, and S. Bilal, "Mhd casson nanofluid flow over nonlinearly heated porous medium in presence of extending surface effect with suction/injection," *Indian Journal of Physics*, pp. 1–15, 2021.

[193] B. N. Reddy and P. Maddileti, "Casson nanofluid and joule parameter effects on variable radiative flow of mhd stretching sheet," *Partial Differential Equations in Applied Mathematics*, vol. 7, p. 100487, 2023.

[194] T. Gubena and W. Ibrahim, "A 3d flow analysis of casson nano-fluid flow over a stretching surface with non-fourier heat and non-fick's mass flux," *International Journal of Thermofluids*, vol. 20, p. 100488, 2023.

[195] M. Y. Ali, S. Reza-E-Rabbi, S. F. Ahmmed, M. N. Nabi, A. K. Azad, and S. Muyeen, "Hydromagnetic flow of casson nano-fluid across a stretched sheet in the presence of thermoelectric and radiation," *International Journal of Thermofluids*, vol. 21, p. 100484, 2024.

[196] W. Ibrahim and T. Anbessa, “Three-dimensional mhd mixed convection flow of casson nanofluid with hall and ion slip effects,” *Mathematical Problems in Engineering*, vol. 2020, pp. 1–15, 2020.

[197] R. Koka and A. Gajikunta, “Investigating the impact of magnetohydrodynamic (mhd) and radiation on the casson-based nanofluid flow over a linear stretching sheet in a porous medium with heat source or sink,” *Journal of Advanced Research in Fluid Mechanics and Thermal Sciences*, vol. 111, no. 2, pp. 170–194, 2023.

[198] Asifa, T. Anwar, P. Kumam, Z. Shah, and K. Sitthithakerngkiet, “Significance of shape factor in heat transfer performance of molybdenum-disulfide nanofluid in multiple flow situations; a comparative fractional study,” *Molecules*, vol. 26, no. 12, p. 3711, 2021.

[199] I. Pop and D. B. Ingham, *Convective heat transfer: mathematical and computational modelling of viscous fluids and porous media*. Elsevier, 2001.

[200] M. Naseer, M. Y. Malik, S. Nadeem, and A. Rehman, “The boundary layer flow of hyperbolic tangent fluid over a vertical exponentially stretching cylinder,” *Alexandria engineering journal*, vol. 53, no. 3, pp. 747–750, 2014.

[201] I. S. Oyelakin, P. Lalramneihmawii, S. Mondal, S. K. Nandy, and P. Sibanda, “Thermophysical analysis of three-dimensional magnetohydrodynamic flow of a tangent hyperbolic nanofluid,” *Engineering Reports*, vol. 2, no. 4, p. e12144, 2020.

[202] M. Das, S. Nandi, B. Kumbhakar, and G. Shanker Seth, “Soret and dufour effects on mhd nonlinear convective flow of tangent hyperbolic nanofluid over a bidirectional stretching sheet with multiple slips,” *Journal of Nanofluids*, vol. 10, no. 2, pp. 200–213, 2021.

[203] M. Amjad, M. Khan, K. Ahmed, I. Ahmed, T. Akbar, and S. M. Eldin, “Magnetohydrodynamics tangent hyperbolic nanofluid flow over an exponentially stretching sheet: Numerical investigation,” *Case Studies in Thermal Engineering*, vol. 45, p. 102900, 2023.

[204] G. Ramasekhar, M. Jawad, A. Divya, S. Jakeer, H. A. Ghazwani, M. R. Almutiri, A. Hendy, and M. R. Ali, “Heat transfer exploration for bioconvected tangent hyperbolic nanofluid flow with activation energy and joule heating induced by riga plate,” *Case Studies in Thermal Engineering*, vol. 55, p. 104100, 2024.

[205] B. Ali, S. Liu, H. J. Liu, and M. I. H. Siddiqui, "Magnetohydrodynamics tangent hyperbolic nanofluid flow across a vertical stretching surface using levengberg-marquardt back propagation artificial neural networks," *Numerical Heat Transfer, Part A: Applications*, pp. 1–23, 2024.

[206] R. K. Alhefthi, I. Shahzadi, H. A. Khan, N. Khan, M. Hashmi, and M. Inc, "Convective boundary layer flow of mhd tangent hyperbolic nanofluid over stratified sheet with chemical reaction," *AIMS Mathematics*, vol. 9, no. 7, pp. 16 901–16 923, 2024.

[207] T. Hayat, T. Muhammad, S. A. Shehzad, and A. Alsaedi, "Three-dimensional flow of jeffrey nanofluid with a new mass flux condition," *Journal of Aerospace Engineering*, vol. 29, no. 2, p. 04015054, 2016.

[208] E. R. El-Zahar, A. M. Rashad, and L. F. Seddek, "Impacts of viscous dissipation and brownian motion on jeffrey nanofluid flow over an unsteady stretching surface with thermophoresis," *Symmetry*, vol. 12, no. 9, p. 1450, 2020.

[209] S. Shehzad, T. Hayat, and A. Alsaedi, "Mhd flow of jeffrey nanofluid with convective boundary conditions," *Journal of the Brazilian Society of Mechanical Sciences and Engineering*, vol. 37, no. 3, pp. 873–883, 2015.

[210] B. Prasannakumara, M. Krishnamurthy, B. Gireesha, and R. S. Gorla, "Effect of multiple slips and thermal radiation on mhd flow of jeffery nanofluid with heat transfer," *Journal of Nanofluids*, vol. 5, no. 1, pp. 82–93, 2016.

[211] P. Biswas, S. Arifuzzaman, I. Karim, and M. S. Khan, "Impacts of magnetic field and radiation absorption on mixed convective jeffrey nano fluid flow over a vertical stretching sheet with stability and convergence analysis," *Journal of nanofluids*, vol. 6, no. 6, pp. 1082–1095, 2017.

[212] H. Ur Rasheed, A. AL-Zubaidi, S. Islam, S. Saleem, Z. Khan, and W. Khan, "Effects of joule heating and viscous dissipation on magnetohydrodynamic boundary layer flow of jeffrey nanofluid over a vertically stretching cylinder," *Coatings*, vol. 11, no. 3, p. 353, 2021.

[213] A. Dawar, A. Wakif, A. Saeed, Z. Shah, T. Muhammad, and P. Kumam, "Significance of lorentz forces on jeffrey nanofluid flows over a convectively heated flat surface featured by multiple velocity slips and dual stretching constraint: a homotopy analysis approach," *Journal of Computational Design and Engineering*, vol. 9, no. 2, pp. 564–582, 2022.

[214] A. T. Moltot, E. Haile, G. Awgichew, and H. Dessie, “Influences of non-linear thermal radiation and cattaneo-christov heat and mass fluxes on electrical conductivity of jeffrey ternary hybrid nanofluid flow,” *Journal of Nanofluids*, vol. 13, no. 6, pp. 1226–1245, 2024.

[215] M. Awais, H. Rehman, M. A. Z. Raja, S. E. Awan, A. Ali, M. Shoaib, and M. Y. Malik, “Hall effect on mhd jeffrey fluid flow with cattaneo–christov heat flux model: An application of stochastic neural computing,” *Complex & Intelligent Systems*, vol. 8, no. 6, pp. 5177–5201, 2022.

[216] M. Goyal and R. Bhargava, “Boundary layer flow and heat transfer of viscoelastic nanofluids past a stretching sheet with partial slip conditions,” *Applied Nanoscience*, vol. 4, no. 6, pp. 761–767, 2014.

Appendix A

Mesh Independence Analysis

To ensure the reliability and numerical accuracy of the proposed computational scheme, a comprehensive mesh independence (grid convergence) analysis was carried out. The governing nonlinear ordinary differential equations (5.77) were solved using different step sizes, namely $\Delta\eta = 0.025$, 0.020, and 0.010. The variations in velocity, temperature, and concentration profiles, along with their corresponding gradients, were carefully examined. The results confirm that the numerical solutions are independent of the grid size, thereby validating the robustness of the adopted numerical methodology.

A.1 Mesh Independence Analysis for Principal and Spanwise Velocity Components

A mesh independence analysis (grid convergence) was carried out for both the principal velocity component $f'(\eta)$ and the spanwise velocity component $h(\eta)$ in order to ensure the numerical accuracy, stability, and reliability of the computed velocity fields. The governing momentum equations were solved using three different step sizes, namely $\Delta\eta = 0.025$, 0.020, and 0.010, and the resulting velocity profiles together with their corresponding gradients were systematically compared.

A.1.1 Principal Velocity Profile

The convergence characteristics of the principal velocity gradient $|f''(\eta)|$ and the corresponding principal velocity profile $f'(\eta)$ for different grid resolutions are presented in Table A.1. The numerical values exhibit negligible variation with decreasing step size, indicating that the obtained solutions are insensitive to further mesh refinement.

Table A.1: Grid convergence study for principal velocity gradient and velocity profile

(a) Velocity gradient $|f''(\eta)|$

η	$\Delta\eta = 0.025$	$\Delta\eta = 0.020$	$\Delta\eta = 0.010$
0.0	0.708051	0.708051	0.708051
1.0	0.251242	0.251238	0.251233
2.0	0.084682	0.084680	0.084676
3.0	0.035380	0.035379	0.035377
4.0	0.035188	0.035187	0.035186
5.0	0.024777	0.024777	0.024776
6.0	0.016868	0.016867	0.016866
7.0	0.004346	0.004346	0.004346

(b) Velocity profile $f'(\eta)$

η	$\Delta\eta = 0.025$	$\Delta\eta = 0.020$	$\Delta\eta = 0.010$
0.0	1.000000	1.000000	1.000000
1.0	0.556242	0.556239	0.556234
2.0	0.403049	0.403046	0.403044
3.0	0.348897	0.348896	0.348895
4.0	0.316424	0.316425	0.316425
5.0	0.268820	0.268821	0.268822
6.0	0.176145	0.176146	0.176148
7.0	0.000000	0.000000	0.000000

The excellent agreement among the numerical results reported in Table A.1 confirms that further grid refinement does not yield any significant improvement in solution accuracy. This observation verifies that the selected grid resolution is sufficient to capture the essential flow characteristics.

The mesh independence of the principal velocity profile is further illustrated in Figure A.1, where the overlapping curves corresponding to different step sizes clearly demonstrate numerical convergence.

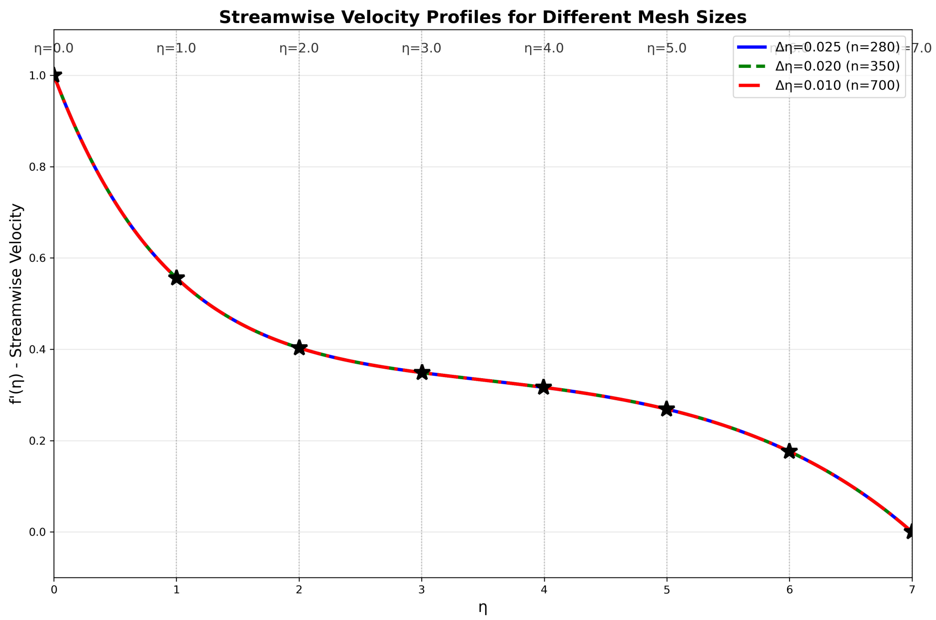

Figure A.1: Mesh independence of the principal velocity profile $f'(\eta)$ for different grid resolutions

A.1.2 Spanwise Velocity Profile

The grid convergence behavior of the spanwise velocity component $h(\eta)$ is presented in Table A.2. The numerical values obtained for different step sizes are nearly identical throughout the computational domain, confirming that the solution is independent of the chosen grid resolution.

Table A.2: Grid convergence study for the spanwise velocity profile $h(\eta)$

η	$\Delta\eta = 0.025$	$\Delta\eta = 0.020$	$\Delta\eta = 0.010$
0.0	0.000000	0.000000	0.000000
1.0	0.127690	0.127692	0.127694
2.0	0.142888	0.142889	0.142889
3.0	0.130483	0.130484	0.130484
4.0	0.108362	0.108362	0.108362
5.0	0.077356	0.077357	0.077357
6.0	0.038203	0.038203	0.038203
7.0	0.000000	-0.000000	-0.000000

Figure A.2 shows the mesh independence of the spanwise velocity profile. The superposition of the curves corresponding to different step sizes clearly indicates numerical convergence and validates the adequacy of the selected computational grid.

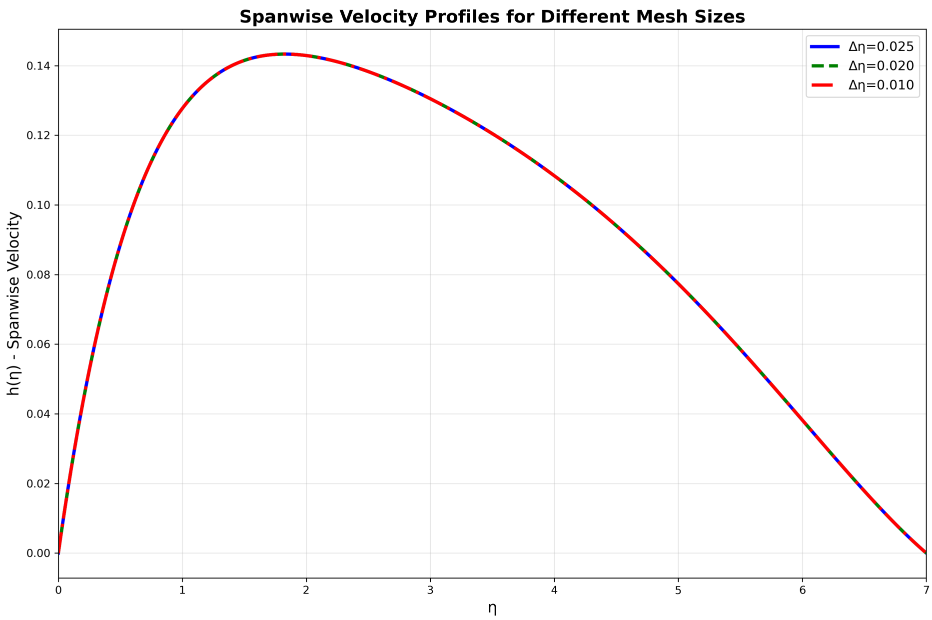

Figure A.2: Mesh independence of the spanwise velocity profile $h(\eta)$ for different grid resolutions

Overall, the mesh independence analysis for both principal and spanwise velocity components confirms that the numerical solutions are stable, accurate, and insensitive to further grid refinement.

A.2 Temperature Profile and Gradient

The grid convergence results for the temperature gradient $|\theta'(\eta)|$ and the temperature profile $\theta(\eta)$ are presented in Table A.3. Perfect agreement across all step sizes is observed, confirming excellent numerical stability.

Table A.3: Grid convergence study for temperature gradient and temperature profile

(a) Temperature gradient $|\theta'(\eta)|$

η	$\Delta\eta = 0.025$	$\Delta\eta = 0.020$	$\Delta\eta = 0.010$
0.0	0.325940	0.325940	0.325940
1.0	0.580232	0.580232	0.580232
2.0	0.057636	0.057636	0.057636
3.0	0.003799	0.003799	0.003799
4.0	0.000353	0.000353	0.000353
5.0	0.000041	0.000041	0.000041
6.0	0.000005	0.000005	0.000005
7.0	0.000001	0.000001	0.000001

(b) Temperature profile $\theta(\eta)$

η	$\Delta\eta = 0.025$	$\Delta\eta = 0.020$	$\Delta\eta = 0.010$
0.0	1.000000	1.000000	1.000000
1.0	0.270457	0.270457	0.270457
2.0	0.021122	0.021122	0.021122
3.0	0.001575	0.001575	0.001575
4.0	0.000163	0.000163	0.000163
5.0	0.000020	0.000020	0.000020
6.0	0.000002	0.000002	0.000002
7.0	0.000000	0.000000	0.000000

The corresponding temperature profile convergence is depicted in Figure A.3.

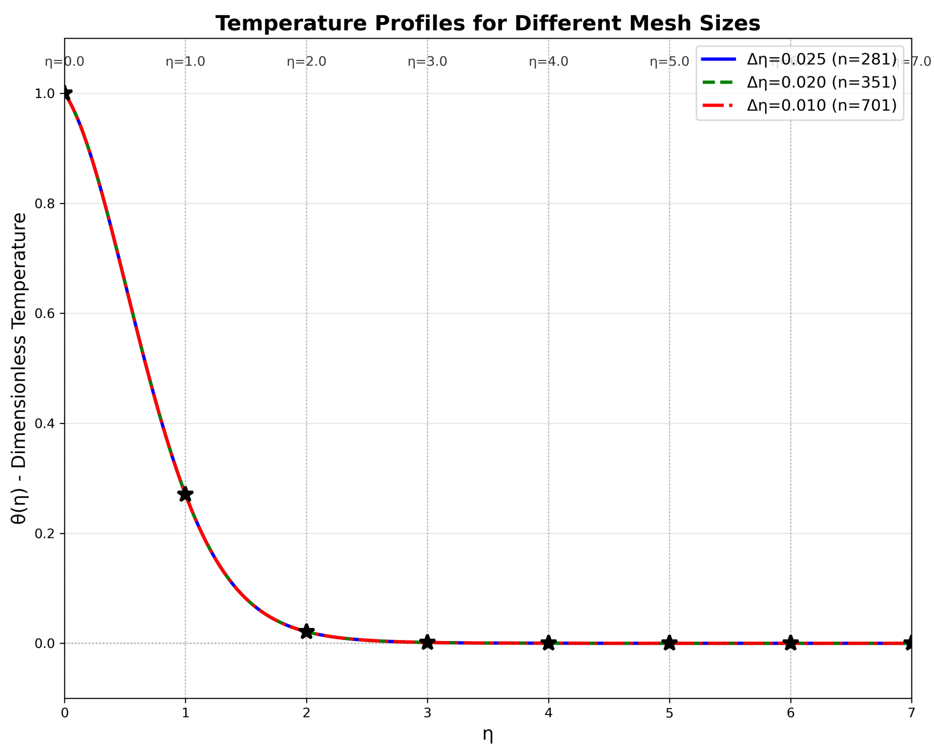

Figure A.3: Mesh independence of the temperature profile for different grid resolutions

A.3 Concentration Profile and Gradient

Table A.4 shows the convergence behavior of the concentration gradient $|\phi'(\eta)|$ and the concentration profile $\phi(\eta)$. The results reveal perfect agreement across all grid sizes.

Table A.4: Grid convergence study for concentration gradient and concentration profile

(a) Concentration gradient $|\phi'(\eta)|$

η	$\Delta\eta = 0.025$	$\Delta\eta = 0.020$	$\Delta\eta = 0.010$
0.0	1.235231	1.235231	1.235231
1.0	0.359388	0.359388	0.359388
2.0	0.153767	0.153767	0.153767
3.0	0.031665	0.031665	0.031665
4.0	0.005175	0.005175	0.005175
5.0	0.000799	0.000799	0.000799
6.0	0.000123	0.000123	0.000123
7.0	0.000022	0.000022	0.000022

(b) Concentration profile $\phi(\eta)$

η	$\Delta\eta = 0.025$	$\Delta\eta = 0.020$	$\Delta\eta = 0.010$
0.0	1.000000	1.000000	1.000000
1.0	0.359438	0.359438	0.359438
2.0	0.097511	0.097511	0.097511
3.0	0.017512	0.017512	0.017512
4.0	0.002765	0.002765	0.002765
5.0	0.000418	0.000418	0.000418
6.0	0.000057	0.000057	0.000057
7.0	0.000000	0.000000	0.000000

The mesh independence of the concentration profile is illustrated in Figure A.4.

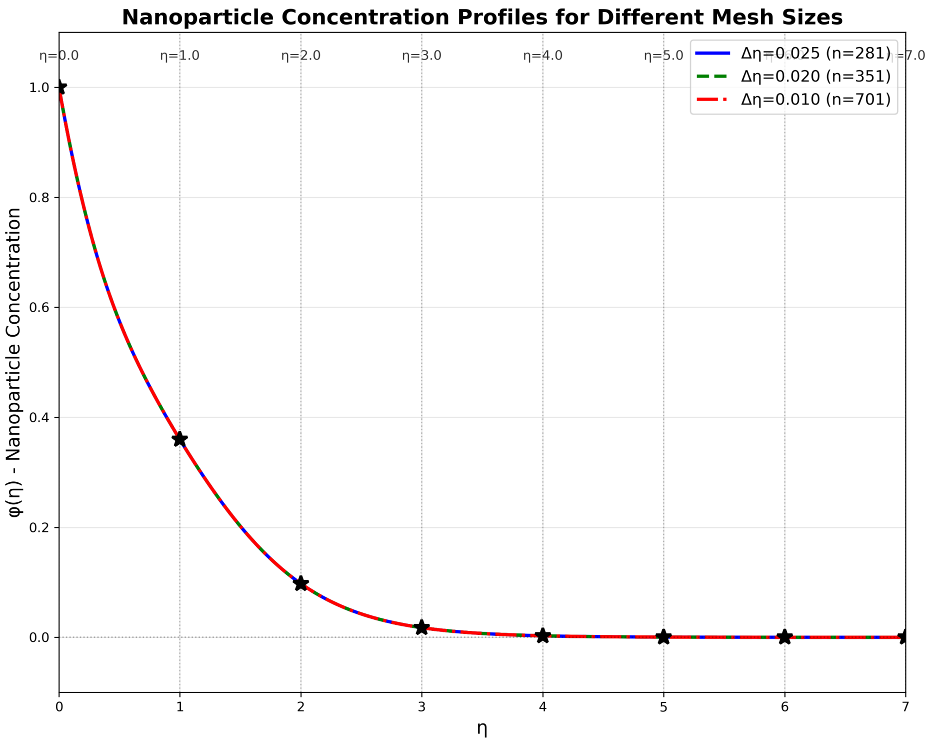

Figure A.4: Mesh independence of the concentration profile for different grid resolutions

Appendix B

Computational Performance and Accuracy

Table B.1 presents the computational performance and accuracy for different choices of the truncated boundary η_∞. The results demonstrate that $\eta_\infty \geq 7$ is sufficient to accurately capture the boundary layer behavior.

Table B.1: Computational performance and accuracy for different domain truncations of chapter 5

η_∞	n	Time (s)	$\lvert f' \rvert$	$\lvert h \rvert$	$\lvert \theta \rvert$	$\lvert \phi \rvert$	Total Error
5	1000	4.73	5.77×10^{-9}	1.09×10^{-9}	1.73×10^{-9}	4.87×10^{-9}	1.35×10^{-8}
7	1400	3.75	4.40×10^{-12}	7.29×10^{-12}	1.79×10^{-11}	5.41×10^{-12}	3.54×10^{-11}
10	2000	5.38	1.29×10^{-13}	1.37×10^{-12}	3.81×10^{-14}	7.71×10^{-14}	1.64×10^{-12}